High Resolution Organic Vapor Jet Printing of Phosphorescent Organic Light Emitting Diode Arrays

by

Gregory J. McGraw

A dissertation submitted in partial fulfillment
of the requirements for the degree of
Doctor of Philosophy
(Applied Physics)
in The University of Michigan
2013

Doctoral Committee:
- **Professor Stephen R. Forrest, Chair**
- **Professor Iain D. Boyd**
- **Professor Joanna M. Millunchick**
- **Professor Bradford G. Orr**
- **Associate Professor Max Shtein**

This thesis is dedicated to my mother. I am grateful for the sacrifices she made to provide for my education. Without her support, this document would certainly not exist.

Acknowledgements

I would like to thank Mike Arnold for mentoring me during the early phases of this project. He set a high standard for determination, skill, and creativity in the laboratory. I also thank my collaborators at Universal Display Corp., including Siddharth Harikrishna Mohan and Paul Burrows, for providing expertise and resources to further this work.

I thank Diane Peters and Ruizi Chen for the engineering expertise they lent to this project. I am also grateful to OCM alumni Chris Giebink, Richard Lunt, and Yiru Sun for useful discussions and guidance setting up and performing experiments. I thank Jeramy Zimmerman for his expertise with vacuum equipment and Razi Haque for his advice on MEMS processing techniques. I also wish to thank Prof. Ian Boyd for providing the MONACO gas dynamics modeling code.

I am grateful to the LNF staff, particularly Pilar Herrera-Fierro, for helping me fabricate micronozzle arrays. I would also like to thank the staff of the Physics Instrument Shop, particularly Julian Broad.

I thank Eva Ruff for providing administrative support and for proofreading this thesis. I am also grateful to Mary McGraw for proofreading my thesis.

I thank the members of my doctoral committee for the feedback they provided to improve this thesis. Finally, I would like to thank my advisor, Prof. Stephen Forrest, for his guidance, patience, and support during this endeavor.

Table of Contents

List of Figures

Chapter 1:

Chapter 2:

Chapter 3:

Chapter 4:

Chapter 5:

Chapter 6:

Chapter 7:

Chapter 8:

Chapter 9:

Chapter 10:

Chapter 11:

Chapter 12:

Appendix A:

Appendix B:

Appendix C:

Appendix D:

Appendix G:

Appendix H:

List of Tables

Chapter 1:

Chapter 3:

Chapter 10:

List of Appendices

List of Abbreviations

AFM	Atomic Force Micrograph
Alq_3	tris(8-hydroxyquinoline) aluminum
BCP	Bathocuproine
Bphen	4,7-diphenyl-1,10-phenanthroline
CBP	4,4'-Bis(9H-carbazol-9-yl)biphenyl
C-D	converging-diverging
CFD	computational fluid dynamics
CIE	Commission Internationale de l'Eclairage
C-R	converging-relieved
CRI	color rendering index
C-T	converging-tapered
DSMC	direct simulation Monte Carlo
EBL	electron blocking layer
EDP	ethylenediamine pyrocatechol
EML	emissive layer
EQE	external quantum efficiency
ETL	electron transport layer

FIr6	Ir(III) bis(4’,6’-difluorophenylpyridinato)tetrakis(1-pyrazolyl)borate
FWHM	full width at half maximum
HBL	hole blocking layer
HOMO	highest occupied molecular orbital
HTL	hole transport layer
$Ir(ppy)_3$	tris(2-phenylpyridinato) iridium(III)
Irppz	fac-tris(1-phenylpyrazolato,N,C2′)iridium(III)
ITO	indium tin oxide
ISC	intersystem crossing
LCD	liquid crystal display
LED	light emitting diode
LUMO	lowest unoccupied molecular orbital
mCP	1,3-Bis(*N*-carbazolyl)benzene
MFC	mass flow controller
MLCT	metal to ligand charge transfer
NPD	N,N'-di(1-naphthyl)-. N,N'-diphenylbenzidine
NTC	non-time counting collision algorithm
NTSC	National Television Standards Committee
OLED	organic light emitting diode
OVJP	organic vapor jet printing
OVPD	organic vapor phase deposition
pqIr	iridium(III) bis(2-phenylquinolyl-) acetylacetonate
PVD	physical vapor deposition

S-C	simple converging
SEM	Scanning electron microscope
TFT	thin film transistor
VTE	vacuum thermal evaporation

List of Symbols

a	nozzle aperture width
A	mass transport parameter
b	distance of closest approach
c	particle velocity
F	force
f	density function
g	nozzle aperture to substrate separation
h	characteristic dimension, height
H	enthalpy
I	spectral power distribution
j	current density, organic vapor flux
J	organic flux
K	thermal conductivity
K_B	Boltzmann Constant
Kn	Knudsen Number
l	length, orbital quantum number
m	molecular mass
N	Number of collisions

n	particle density, principal quantum number
N	Number of particles, N_A is Avogadro's number
p	momentum, dimensionless pressure
P	probability, pressure
Pe	Peclét Number
q	carrier gas flux, dimensionless flow rate
Q	carrier gas flow rate
R	ideal gas constant
Re	Reynolds number
s	spin quantum number
S	singlet spin state
T	triplet spin state
T	Temperature
u	characteristic velocity, velocity component in center of mass frame
v	bulk fluid velocity, velocity component in of mass frame
V	Volume
V	voltage, normalized eye response function
w	microchannel width, velocity component in center of mass frame
W	Power
X	red tristimulus value
Y	green tristimulus value
Z	blue tristimulus value
α	accommodation coefficient, thermal diffusivity

β	reciprocal thermal velocity
δ	identity tensor, rarefication parameter
ϵ	azimuth of collision plane, emissivity
η	dimensionless organic vapor generation rate
η_p	power efficiency
λ	mean free path, wavelength
μ	dynamic viscosity dipole moment
ρ	gas density
φ	heat flux
χ	spin wavefunction, collision deflection angle
ψ	spatial wavefunction
Ψ	total wavefunction

Abstract

Organic light emitting diodes (OLEDs) are widely used in mobile devices due to their thin form factor, wide color gamut, and high efficiency. The introduction of OLEDs into televisions and monitors has been slowed, in part, by the difficulty of patterning organic thin films over large areas at micron-scale resolutions. A practical patterning technology must also be compatible with efficient device architectures, such as phosphorescent OLEDs (PHOLEDs). Organic vapor jet printing (OVJP) is an approach for depositing and patterning the emissive layers of OLED displays in a scalable manner. An inert carrier gas is used to mix organic vapor from multiple material sources. The vapor mixture is then distributed to a Si micronozzle array that collimates it into multiple jets to deposit well-defined thin film features onto a chilled substrate. This technique is capable of printing features smaller than 20 μm and arrays of 100 μm wide multicolor PHOLED segments. An experimentally validated deposition model predicts that full color (red-green-blue) pixel pitches of 150 μm are obtainable without cross-contamination of dopants between adjacent sub pixels. Green PHOLEDs with an external quantum efficiency of 8.0±0.7%, comparable to that achieved with standard techniques, were fabricated with OVJP. Since the micronozzle array is fabricated using standard Si processing techniques, this approach is readily scalable. Based on the performance of the laboratory system, a production OVJP tool has the potential to print a full color OLED emissive layer onto Gen 8 (4 m^2) substrate in as little as 250s.

Chapter 1

Introduction

1.1 Motivation

Organic light emitting diodes (OLEDs) are a rapidly emerging technology for use in lighting and display applications. Displays incorporating OLEDs have already found widespread acceptance in the mobile device market due to their light weight, thin form factor, and high power efficiency. Examples of OLED displays currently and soon to be available to consumers are shown in **Figure 1-1**. Adoption in large area applications, such as televisions and computer monitors has been much slower, due to the difficulty of fabricating patterned arrays of multicolor OLEDs on large substrates. Lighting fixtures incorporating multicolor OLED segments have also been hampered by similar difficulties.

This thesis evaluates an approach to solving one of the remaining barriers to the economical fabrication of large area OLED displays and lighting. Patterning of organic thin films is currently an expensive process that is difficult to scale to large area substrates. Organic vapor jet printing (OVJP) is a technique that combines organic thin film deposition and patterning into a single, scalable step that is compatible with high efficiency OLED architectures. To better understand the requirements of the OVJP process, it is necessary to understand the manner in which OLEDs operate.

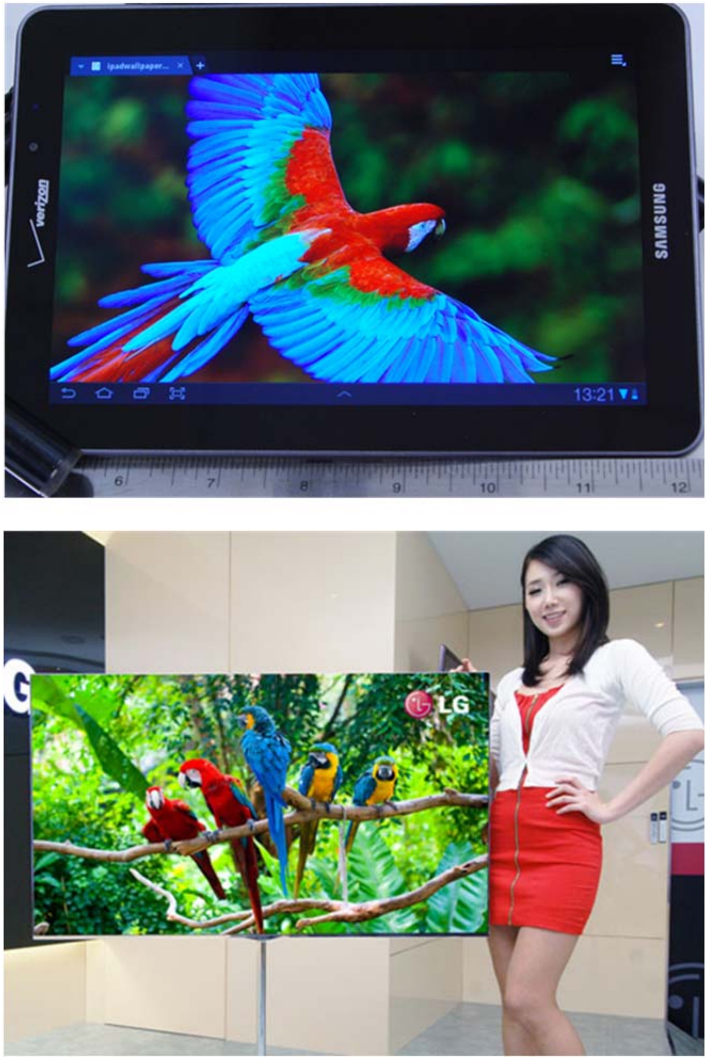

Figure 1-1: Examples of phosphorescent OLEDs in consumer products. (top) The Samsung Galaxy Tablet uses an 8 inch active matrix OLED display. (lower) LG plans to release a 55 inch flat screen OLED television in 2013. (Image from oled-info.com)[1]

1.2 Principles of OLED Operation

The basic structure of an OLED consists of thin layers of organic material sandwiched between a pair of electrodes. One or more of the organic layers is electroluminescent, producing light in response to an applied current. The cathode has a low work function to facilitate the injection of electrons into the organic material. Conversely, the anode has high work function, allowing it to inject holes efficiently. Due to its low work function, the cathode is most commonly reflective. The anode is usually a transparent material such as indium tin oxide (ITO). Architectures for OLEDs can be classified as bottom emitting[2] or top emitting[3] depending on whether light leaves through a transparent substrate or through a semi-transparent contact deposited over the organic film. Both contacts emit light in a transparent OLED.[4] Normally, the anode serves as the substrate for organic thin film growth, however the cathode serves this purpose in inverted devices.[5]

Organic layers can be comprised of "small molecules" that generally have a well-defined molecular mass < 1000 g/mol and lack a repeating molecular structure.[2] Alternately, they can be made from polymers[6] that feature electronically active moieties similar to small molecules bound together by a long, usually inert, repeating backbone. Similar physical processes govern the behavior of small molecule and polymer devices,[7] so the following discussion applies to both. Electrons and holes recombine to produce light when an electron-hole pair meets on the same molecule within the organic thin film. This forms a Frenkel exciton. The electron becomes bound in the lowest unoccupied molecular orbital (LUMO) of an electroluminescent molecule.

The hole produces an electron vacancy in the highest occupied molecular orbital (HOMO) of the same molecule.[8]

Single organic layer electroluminescent devices, as portrayed in **Fig. 1-2a**, are possible, although they are very inefficient.[9] Holes generally have much higher mobility than electrons in organic materials, so the recombination region of a single layer device is skewed towards the cathode. Holes can migrate directly to the cathode without recombining with an electron. Leakage can be mitigated through the introduction of one or more organic-organic heterojunctions. This approach was first demonstrated by Tang and Van Slyke, **Fig. 1-2b,** who fabricated what is considered the first step to a practical OLED.[2] The material covering the anode serves as a hole transport layer and the material adjoining the cathode is an electron transport layer. The hole mobility of the common hole transport material 1,4-bis(1-naphthylphenylamino)biphenyl (NPD) is approximately 10^{-3} cm^2/Vs, while its electron mobility is negligible. The common electron transport material Tris(8-hydroxyquinolinato)aluminium (Alq_3) has an electron mobility of 10^{-5} cm^2/Vs, while its hole mobility is three orders of magnitude lower.[10] As a result, holes do not penetrate far into the electron transport layer and electron-hole recombination is confined to the organic heterojunction, away from the contacts. The electron transport material Alq_3 emits light in a Tang & Van Slyke device.

Many refinements on this basic structure have subsequently arisen. A dedicated emissive layer can be deposited between dissimilar hole and electron transport layers, forming a p-i-n diode-like structure, **Fig. 1-2c**.[11] Blocking layers that create an energetic barrier to the motion of a charge carrier or exciton past a heterojunction can also be added to the stack to improve device efficiency.[12] Because holes are more mobile than electrons, the marginal benefit to adding a hole blocking layer, **Fig. 1-2d**, is greater than for an electron blocking layer, **Fig. 1-2e**.[13] Electron blocking layers are primarily useful for emissive layers with large HOMO-LUMO gaps. Without this blocking layer, the emissive layer in such devices is prone to transfer charge or energy to the hole transport layer, which can itself emit light.

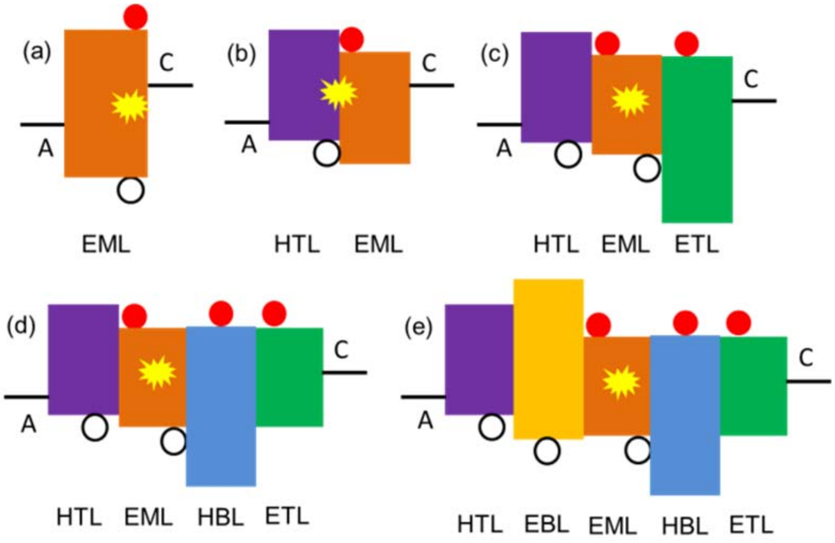

Figure 1-2: Layer architectures for OLEDs. In each diagram, the energy of LUMO and HOMO states in organic layers is indicated by the position of their top and bottom edges, respectively. States positioned higher are closer to vacuum level. The anode, A, on the left injects holes which appear as empty black circles. The cathode, C, on the right injects electrons which are solid red circles. Organic layers are abbreviated as follows: EML is emissive layer. HTL is hole transport layer. HBL and EBL are electron and hole blocking layers, respectively and ETL is electron transport layer.

In a properly designed device, holes and electrons combine to produce excitons in the emissive layer with close to unity efficiency.[14] Hole and electron distributions change smoothly over the emissive layer so that recombination is spread across its thickness. This lowers the exciton density and reduces multi-particle effects such as quenching. Emissive guest molecules can be doped into a non-emissive host in the emissive layer, allowing greater efficiency and more control over the color of emitted light.[15] The dopant material is excited by Förster or Dexter transfer of an exciton from the host material when there is a strong overlap between the host emission spectrum and the excited states of the dopant. If the spectral overlap is weak, but the electron and hole energy levels of the dopant are accessible to charge carriers in the host, direct electron-hole recombination on the dopant prevails.[16][17] A doped emissive layer facilitates standardization when fabricating multicolor OLED arrays, since different colors can be achieved by simply changing the guest material in differently colored segments.

A charge carrier has two possible spin states, |±½>. When the HOMO of a molecule holds two electrons, their spin wavefunction, χ, must be anti-symmetric to exchange, i.e. χ changes sign when particle identities are reversed. Therefore the ground electronic spin state is a singlet, with spin s=0, given by eq. 1.1. When an electron and hole combine to form an exciton, it has four possible spin eigenstates. Since the electrons do not share the ground state, the spin state can be either symmetric or antisymmetric. Only the first of these stages is a singlet, the other three, eq. 1.2, are triplets which are symmetric to exchange.[8] The argument that 25% of excitons in an electrically pumped small molecule organic film are singlets rests on the assumption that the spin of an electron added to the HOMO of a molecule and removed from its LUMO are uncorrelated. This distribution of exciton spin states has, however, been experimentally confirmed.[18][19]

$$\chi = \frac{1}{\sqrt[2]{2}}|+½\rangle|-½\rangle - \frac{1}{\sqrt[2]{2}}|-½\rangle|+½\rangle \tag{1.1}$$

$$\chi = \begin{matrix} |+½\rangle|+½\rangle \\ |-½\rangle|-½\rangle \\ \frac{1}{\sqrt[2]{2}}|+½\rangle|-½\rangle + \frac{1}{\sqrt[2]{2}}|-½\rangle|+½\rangle \end{matrix} \tag{1.2}$$

In order to emit light, an exciton de-excites to the ground state by emitting a photon. The spatial component of the electronic wavefunction ψ_n must now be considered, so that the total wavefunction, Ψ_n, of the frontier electrons of the molecule is given by eq. 1.3. Let n =0 for the ground state and n =1 for excited state. The probability, P, of a transition the ground state is proportional to eq. 1.4, where μ is the dipole operator that radiatively couples the excited and ground states.[20]

$$\Psi_n = \psi_n \chi_n \tag{1.3}$$

$$P \sim \langle \Psi_0 | \hat{\mu} | \Psi_1 \rangle = \langle \psi_0 | \hat{\mu} | \psi_1 \rangle \langle \chi_0 | \chi_1 \rangle \tag{1.4}$$

The dipole operator only acts on the spatial wavefunction of the electrons, and therefore leaves spins unchanged. Symmetry demands that the bra-ket on the far right in eq. 1.4 is only nonzero if χ_1 is a singlet. This type of a radiative transition, known as fluorescence, is only allowed for singlet excitons. Early OLED architectures were electrofluorescent, and electrofluorescence remains technologically relevant for short wavelength, i.e. blue, devices.

Unless the energy in triplet excitons is utilized, only a quarter of the exciton population generated within the emissive layer can produce light. Triplet excitons can be efficiently harvested by doping the emissive layer of an OLED with an emitter molecule containing an element of high atomic number. Excitons radiatively decay on the dopant molecules, producing electrophosphorescence.[21] The excited electron can exchange its particle spin *s* with the orbital spin *l* of an electron in a partially filled inner orbital of the heavy atom through a process of spin-orbit ($\hat{l} \cdot \hat{s}$) coupling.[8] These inner electrons effectively act as an angular momentum sink, allowing the triplet to couple to the ground state through emission of a photon. Interaction with these orbitals permit inter-system crossing (ISC) between singlet and triplet manifolds. The increase in phosphorescence quantum yield is termed the "heavy atom effect."

The electrophosphorescence process is illustrated diagrammatically in **Figure 1-3**. Holes and electrons meet in the emissive layer of an OLED, **Fig. 1-3a**, to form excitons. The first excited singlet state S_1, in which spins are antiparallel, has a higher energy than the triplet state T_1, in which spins are parallel, **Fig. 1-3b**. If a singlet exciton is present on the dopant molecule, it rapidly undergoes a non-radiative transition to a lower energy triplet state through intersystem crossing. It is therefore unlikely to de-excite directly to ground state S_0.[22] The only radiative transition is therefore $T_1 \rightarrow S_0$, giving the phosphorescent dopant a well-defined, single color emission spectrum. The evolution of this system is illustrated by the Jablonski diagram in **Fig. 1-3c**.[8]

Organometallic compounds, formed by conjugated organic ligands chelating a central transition metal atom, provide for extremely rapid and efficient phosphorescent emission of light. The central location of the metal atom leads to a high degree of overlap between its atomic orbitals and the frontier orbitals of the molecule. A metal-to-ligand charge transfer (MCLT) state is formed, that can have a phosphorescent lifetime as short as 10^{-6}s.[22] Short phosphorescent lifetimes are necessary for practical phosphorescent devices. Long lived triplets are prone to non-radiative decay and a large steady state triplet population leads to multi-body interactions that cause unwanted chemical reactions.[23] Iridium based compounds are particularly useful dopants, since Ir is hexavalent and possesses an extensive system of inner orbitals.[24][25]

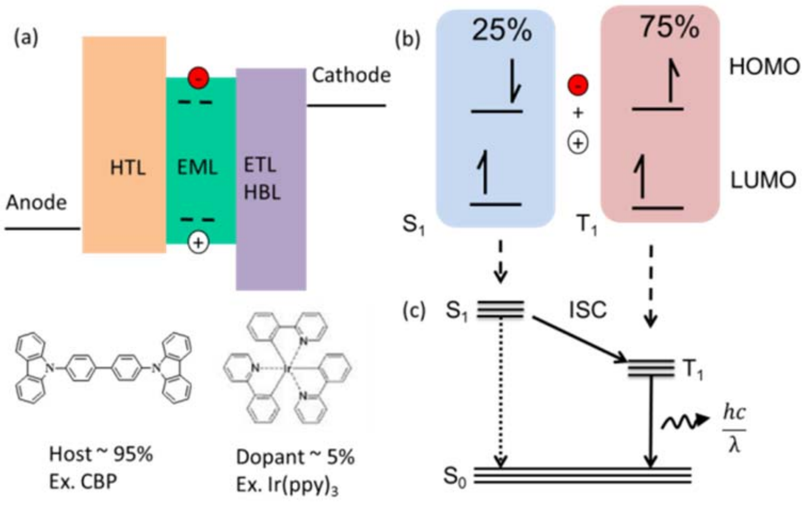

Figure 1-3: The electrophosphorescent process. (a) A Typical phosphorescent OLED architecture viewed in energy space, showing an anode, hole transport layer, emissive layer, electron transport layer, and cathode. The emissive layer contains a dopant with HOMO and LUMO levels lying inside of those of the host material. (b) Spins of singlet S_1 and T_1 excitons on the dopant. (c) Jablonski diagram showing evolution of system. Both S_1 and T_1 are populated by electrical pumping. Excitons follow the solid arrow path, with excitons beginning in the S_1 state transitioning to T_1. Excitons decay to the ground state S_0 from T_1 by emitting light. A direct transition $S_1 \rightarrow S_0$ is possible but highly improbable.

Organometallic dopants must be dispersed evenly throughout the emissive layer of an OLED to avoid concentration quenching due to the formation of excimers.[8] This both red shifts the emission peak and reduces quantum efficiency. There exists an optimal ratio of host to dopant, necessitating the capability to controllably mix the two materials.[26]

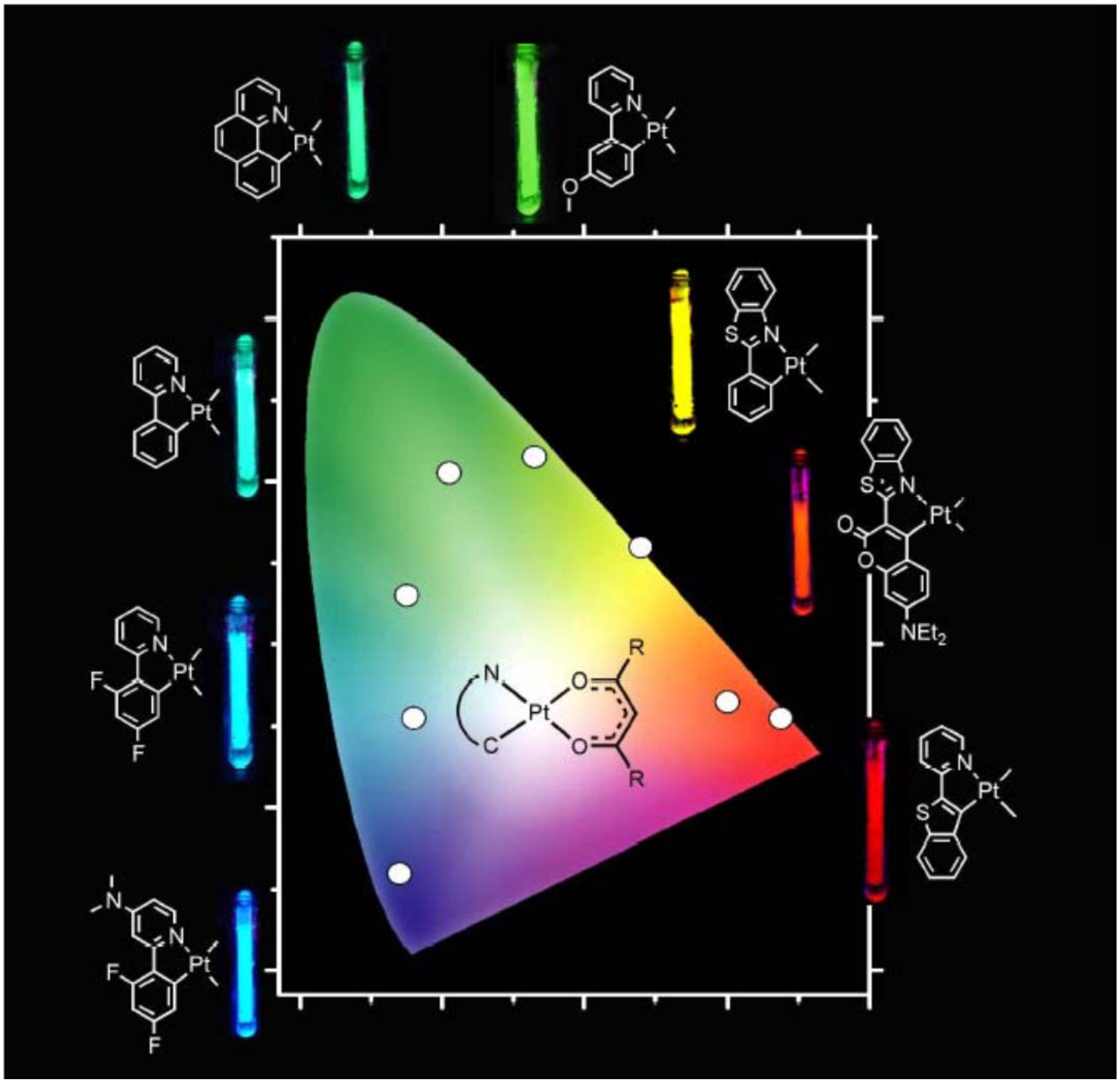

Figure 1-4: Color gamut of electrophosphorescent materials. A family of electrophosphorescent organometallic compounds illustrates large color gamut spanned by OLED materials. The apparent color of emission from each material is plotted on the CIE 1931[27] color gamut. Emission can be adjusted from deep blue to deep red by changing the organic ligands bonded to a central Pt group. Chemical data is from Brooks (2002).[28] (Image source: Shtein, *Organic Vapor Phase Deposition and Vapor Jet Printing for Electronic and Optoelectronic Device Applications* (2004))[29]

1.3 Application of OLEDs to Displays and Lighting

A large number of organic chromophores with high quantum efficiency exist. It is possible to find guest emitters covering the entire visible spectrum. This color palate can be further expanded by synthesizing an almost limitless number of derivatives of these compounds, as shown by **Fig 1-4**. By controlling the chemistry of thin film components, a designer is free to engineer not just the architecture of a device, but the properties of the materials within the device.[25]

Adjacent organic molecules are weakly bonded to each other through van der Waals interactions, rather than by chemical bonds. This is different from traditional semiconductors, in which atoms are covalently bonded in a massive crystalline network. The electronic properties of an organic film, such as the energy levels of the HOMO and LUMO, and the gap between them, are primarily determined by the molecular structures of the individual molecules. The color of an OLED can be changed by simply changing the chemical species of a dopant. Changing the color of III-V LEDs requires changing the components and lattice spacing to adjust the band gap of the material.[30] Electroluminescent organic films are typically amorphous. They do not need a lattice matched substrate to seed growth and can be readily fabricated on large substrates.

1.3.1 Multicolor OLED Architectures

Full color OLED displays can be achieved through a variety of pixel architectures. The most conceptually simple of these is an array of spatially separated red, green, and blue emissive segments, as shown in **Figure 1-5a**.[31] Each segment is driven by an element of an active matrix backplane that acts as a variable current source.

These segments form individual subpixels. This architecture has the advantage of a very broad color gamut and high power efficiency. Its primary drawbacks include both the difficulty of fabricating such a structure on large substrates and relatively low aperture ratios for each color emitter. This structure currently sees wide use in mobile devices such as Samsung's Super AMOLED display, however it lags behind other architectures for non-mobile applications, where ease of large area fabrication outweighs efficiency. An efficient process for fabricating such a structure, as is the goal of OVJP, would likely lead to its widespread adoption in large area displays.

Multicolor displays can also be fabricated from unpatterned OLED layers. A white emitting OLED can be split up into segments using a patterned electrode.[31]

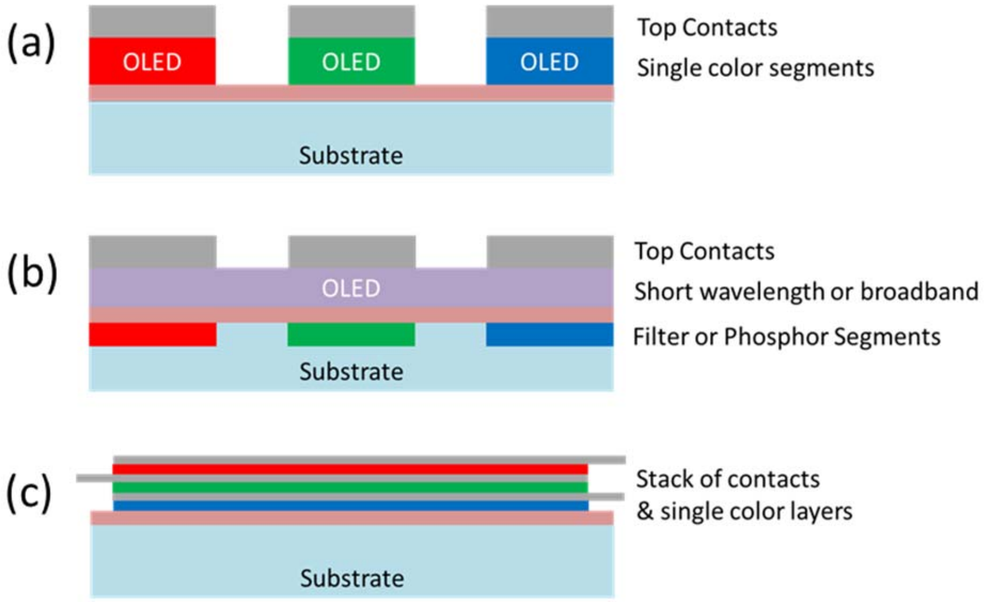

Figure 1-5: Architectures for a full color OLED display. Pixels render colors by mixing light from monochromatic sources of the primary additive colors red, green, and blue. This can be achieved by a spatially patterned array of single color device segments (a), by a single unpatterned OLED film placed behind an array patterned passive elements (b), or by stacking different single color devices (c). (Adapted from Burrows *et al.*)[31]

Arrays of red, green, and blue, filters can then be registered to these segments as shown in **Figure 1-5b**. Filtering of undesired wavelengths can be achieved by either molecular absorption or thin film interference. This method facilitates large area fabrication, since no patterning of the OLED layer is required. It achieves this at the expense of power efficiency, since color generation is subtractive. This approach is, therefore, best suited to stationary applications. LG's recently introduced 55 inch OLED television uses this architecture.[32] Multicolor devices can similarly be made using segments of a short wavelength emitting OLED film overlaid with optically pumped phosphors to produce longer wavelength light.

Finally, single color red, green, and blue OLED layers can be stacked in tandem between patterned thin film electrode layers as shown in **Fig. 1-5c**.[33][5] This architecture has the advantages of high efficiency and very high aperture ratio. Unfortunately, this device architecture is unsuitable for mass produced displays at present, but may show promise as a lighting source with a tunable spectrum.

1.3.2 Light Source Performance Metrics

Light sources are judged by figures of merit including power efficiency, external quantum efficiency, and CIE coordinates. The most straightforward of these is external quantum efficiency (EQE), which is the ratio of the number of photons emitted by the device to the number of electrons that pass through it. It is the product of internal quantum efficiency (IQE), which is the ratio of photons produced within the device per electron that passes through, and outcoupling efficiency, which is the fraction of generated photons that are able to radiate outward from the device.[34]

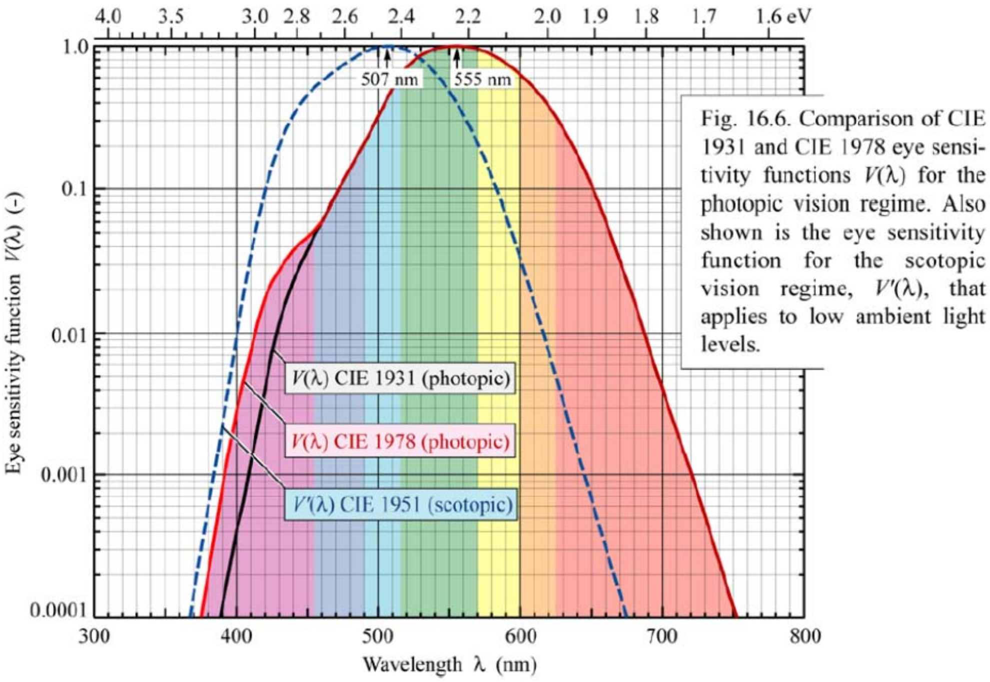

Figure 1-6: Responsivity of the human eye. Normalized responsivity of the eye under daylight (red) and low light (blue) conditions is plotted as a function of wavelength. ("Comparison of CIE 1931 and CIE 1978 eye sensitivity functions *V(λ)* for the photopic vision regime. Also shown is the eye sensitivity function for the scotopic vision regime, *V'(λ)*, that applies to low ambient light levels." Schubert, *Light emitting Diodes and their Use*, (2006))[35]

Power efficiency, η_p, relates the brightness of light perceived by the human eye integrated over the viewing angle, or luminous flux, to the power, *W*, consumed by the source. The response function of the eye is shown in **Fig. 1-6**. It has a maximum sensitivity of 683 lm/W at a wavelength of 555 nm.[35] The eye is significantly less sensitive to shorter and longer wavelength light within the visual spectrum. Equation 1.5 gives η_p, where *I* is the spectral power distribution of the light source and *V* is the normalized response function of the eye.[35] The eye is most sensitive to yellow-green light. Red and blue light sources, therefore, can have lower power efficiency than green sources, even when their EQE is similar.

$$\eta_p = (683\ lm/W)\frac{\int I(\lambda)V(\lambda)d\lambda}{W} \tag{1.5}$$

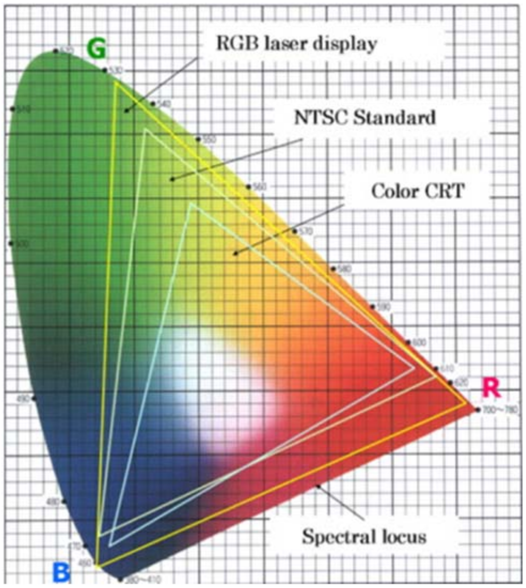

Figure 1-7: CIE Chromaticity diagram for displays. The diagram overlaid with the NTSC color gamut and sample display gamuts. (From Kubota *et al.*)[36]

The color of a light source is quantified by convolving I with the response functions of red, green, and blue receptors of a typical human retina. The most commonly used values for this are the CIE 1931 color space produced by the Commission Internationale de l'Eclairage.[27] Tabulated values of $\bar{x}$, $\bar{y}$, and $\bar{z}$ give the response of red, green, and blue sensitive cone cells, respectively, over the range of wavelengths λ. These are then used to compute tristimulus values X, Y, and Z, and find the luminance perceived by each cell type. If these values are normalized, a hue is uniquely specified by its CIE coordinate pair (x,y). The CIE gamut is shown in **Fig. 1-7**. Equations 1.6 and 1.7 are used to compute X and x. Other values are computed similarly.

$$X = \int I(\lambda)\bar{x}(\lambda)d\lambda \qquad (1.6)$$

$$x = \frac{X}{X+Y+Z} \qquad (1.7)$$

Highly saturated color sources are desirable for displays, since a display can only render hues on the CIE gamut that are contained within a triangle defined by vertices matching the coordinates of their component light sources, as shown in **Fig. 1-7**.[35] The color rendering capability of a display is expressed in terms of the ratio of the area of the gamut they can render to that of the idealized red, green, and blue sources of the National Television Systems Committee (NTSC) standard that have CIE coordinates (0.67,0.33), (0.21,0.71), and (0.14,0.08).[37] Most displays are capable of covering at least 70% of the NTSC gamut, while state of the art OLED displays are capable of 120%.[38].

Saturated monochromatic sources are undesirable for white lighting applications, since power efficiency is the primary figure of merit. Lighter blues and orange-reds appear brighter to the eye. The color of lighting from mixed monochromatic sources can be expressed in terms of CIE coordinates, with (0.33, 0.33) corresponding to pure white. It can also be expressed as color temperature; the temperature of the blackbody radiator that most closely approximates the appearance of a light source.

The spectrum of a light source determines the apparent color of the objects it illuminates. The color rendering index (CRI) of the source compares the ability of a light source to render color correctly in comparison to sunlight, which has a CRI =100.[39] A tradeoff exists between power efficiency and CRI, since a high CRI light source must emit a significant amount of short and long wavelength light. A CRI >80 is preferred for home lighting, while a CRI ≤50 is appropriate for applications like street lighting.

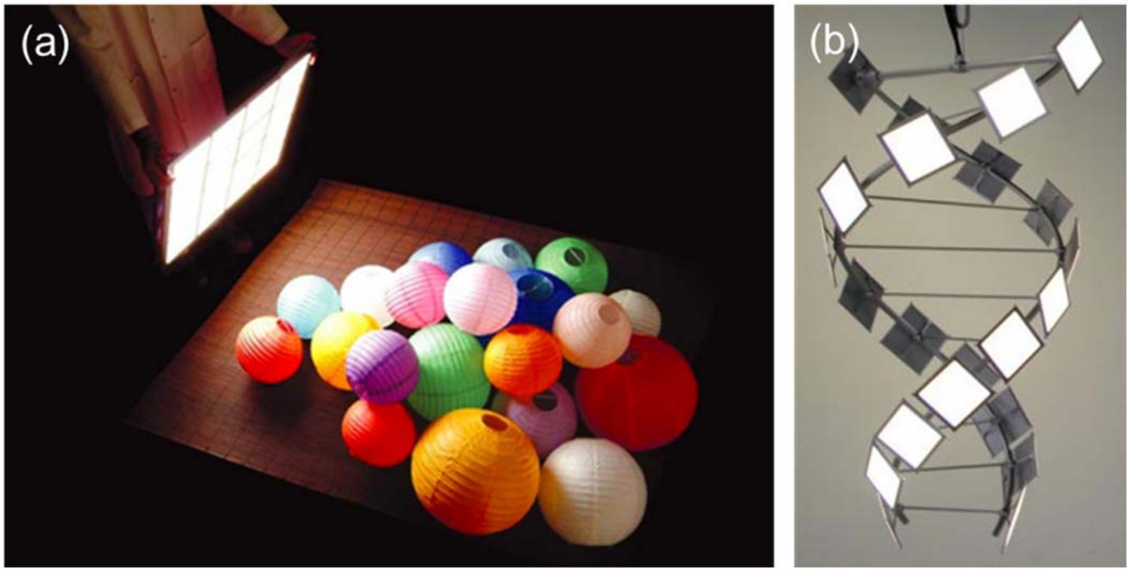

Figure 1-8: Examples of OLED lighting panels. (a) OLED lighting panels demonstrate a high color rendering index by illuminating colorful paper lanterns. (General Electric) (b) The form factor of OLEDs allows lighting to be integrated into aesthetically pleasing fixtures. (installation at Light + Building 2012)

Phosphorescent OLEDs optimized for lighting applications are capable of CRI >93 at an efficiency of 30 lm/W.[40] These devices are roughly twice as efficient as incandescent lighting. Efficiency greater than 100 lm/W can be obtained in demonstrator prototypes with a CRI =70 and panels with η_p =40 lm/W are commercially available.[41], [42] These efficiencies compare very favorably to other lighting technologies, such as compact fluorescent lamps and III-V LED lighting, as shown in **Table 1.1.** The color rendering capabilities of OLED lighting panels are illustrated in **Fig. 1-8a**. Novel fixtures, like the one in **Fig. 1-8b,** can be constructed around OLED panels due to their extremely thin form factor.

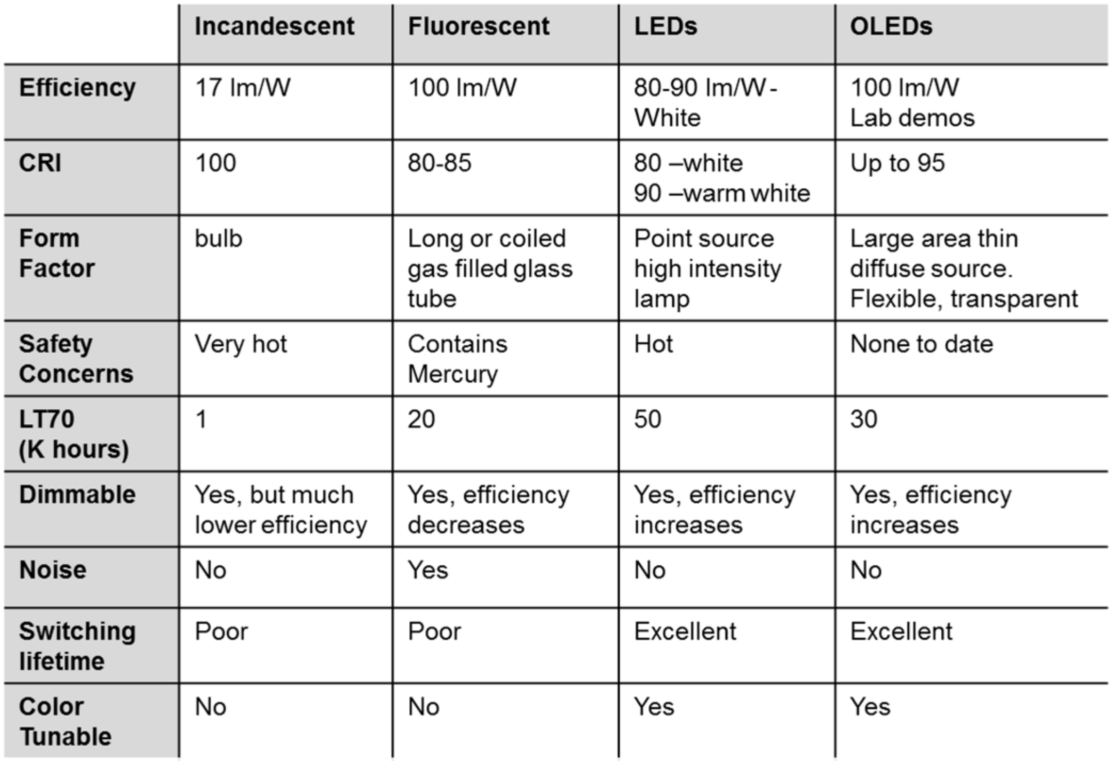

	Incandescent	Fluorescent	LEDs	OLEDs
Efficiency	17 lm/W	100 lm/W	80-90 lm/W - White	100 lm/W Lab demos
CRI	100	80-85	80 –white 90 –warm white	Up to 95
Form Factor	bulb	Long or coiled gas filled glass tube	Point source high intensity lamp	Large area thin diffuse source. Flexible, transparent
Safety Concerns	Very hot	Contains Mercury	Hot	None to date
LT70 (K hours)	1	20	50	30
Dimmable	Yes, but much lower efficiency	Yes, efficiency decreases	Yes, efficiency increases	Yes, efficiency increases
Noise	No	Yes	No	No
Switching lifetime	Poor	Poor	Excellent	Excellent
Color Tunable	No	No	Yes	Yes

Table 1.1: Comparison of Lighting Technologies. The properties of incandescent bulbs, fluorescent lamps, III-V LEDs, and OLEDs compared.

1.3.3 Substrates and Backplanes

The use of OLEDs in displays is facilitated by the appropriation of technologies developed for fabrication of liquid crystal displays (LCD). The infrastructure required to make large "mother glass" substrates has already been developed for the LCD industry. Economies of scale can be realized if thin film processing steps are performed on large substrates that are later diced into individual displays. Substrates used for LCD fabrication are classed into generations based on size. A state of the art LCD fab uses Generation 10 substrates, which are 3 meters on a side.[43] Generation 5.5 substrates,

Figure 1-9: Generations of mother glass for flat panel display fabrication. Gen 5, fifth from front, is currently used for mobile device applications. A Gen 8 substrate, shown at rear, is needed to economically fabricate large displays. A person standing in front of the Gen 8 glass provides a sense of scale. (image from www.hometheater.com)

which have dimensions 68 by 88 cm,[43] are currently used to fabricate most mobile device displays. Generation 8 substrates, which are 187 by 220 cm, are required to economically fabricate large OLED displays such as televisions and computer monitors.[44] Expansion to this standard is a near term goal for the OLED display industry. **Figure 1-9** gives a sense of scale for mother glass sizes used in OLED processing.

Displays using OLEDs also benefit from considerable effort spent on developing active matrix backplanes for large LCDs. Pixels within a display are addressed row by row using a two dimensional grid, with each column in a row refreshing simultaneously.

A passive matrix display in which each row is only active when addressed is impractical for displays with more than about 100 lines of pixels. The duty cycle of each line becomes too short to produce a bright image. An active matrix capable of remembering the state of a pixel between refresh events is necessary for larger displays.[45]

For LCDs, active control is generally achieved with amorphous Si thin film transistors (TFT).[45] When a row of pixels is addressed, a voltage is applied to the gate of each TFT in the row, allowing capacitors connected to each pixel in the row to be charged according to the column signal. Since the pixels of an LCD display are actuated by constant voltage, the line produces an image that persists until the next refresh cycle. Fabricating a transistor backplane array for large displays poses considerable engineering challenges and specialized processes have been developed.

A similar scheme is used for OLED displays. Since OLED intensity is better regulated by constant current as opposed to constant voltage, a more complex circuit requiring at least one drive transistor in addition to the switching transistor is required. The need to provide substantial current also requires that the backplane material have a mobility of 34 cm^2/Vs,[46] which is significantly higher than that of amorphous Si. Polysilicon TFTs are currently used for OLEDs applications,[46][47] although metal oxide transistors are being introduced.[48] Despite differences in the material sets, the high degree of similarity between the backplane technologies for LCDs and OLEDs substantially accelerates the scale-up of OLED displays.[45]

Minimal thermal load is placed on a substrate during OLED growth; therefore OLEDs are compatible with flexible plastic substrates. Roll-to-roll processing of OLEDs on clear plastic or metal foil may provide an inexpensive technology for white lighting,[49][50] or even displays.[51]

1.4 Summary

Organic light emitting diodes are already widely accepted for small mobile device displays and are currently being introduced for larger area applications like televisions, computer monitors, and lighting. The properties of OLEDs, such as their emission wavelength, follow directly from the molecular structures of their component molecules, permitting a huge design space in which OLEDs for various applications can be optimized. Organic devices match or exceed many of the performance metrics set by other lighting and display technologies and do so while retaining a thin, lightweight, and aesthetically pleasing form factor.

Much of the enabling technology developed for LCDs such as large mother glass substrates and large area TFT backplane arrays can be appropriated for OLED applications. An OLED fabrication technique that can economically pattern the very large arrays of colored subpixels required to fabricate full color displays on a Gen 8 substrate will take better advantage of this infrastructure. A practical fabrication process for high efficiency phosphorescent OLEDs must also permit fabrication of multilayer structures and co-deposition of evenly mixed host and dopant materials. Organic vapor jet printing is a promising approach to meet these requirements. It and other OLED fabrication techniques are introduced in the following chapter.

Chapter 2

Review of OLED Fabrication Technology

2.1 Requirements for OLED Fabrication

A viable OLED fabrication technology must meet three primary requirements. First, it must be compatible with high efficiency OLED architectures. This requires that the process must be capable of controlled co-deposition of the emissive layer and compatible with additional charge blocking and transport layers. Secondly, it must be capable of high resolution printing if the goal is to make a segmented structure as shown in **Fig. 1-4a**. A high resolution mobile display such as the Apple Retina® requires individually colored sub-pixels as small as 25 μm.[53] Even a 22 inch high definition television requires 80 μm sub-pixels. Thirdly and finally, the production method must be scalable. A clear path must exist to take it from a laboratory scale to a pilot scale and then to production scale. Since OLED fabrication will be performed on Gen 8 and larger substrates, this implies that an OLED deposition process must be compatible with a massive degree of parallelism. When viewed in the context of these three requirements, different OLED fabrication technologies each have strengths and weaknesses.

The lack of chemical contrast between organic semiconductors and common photoresist materials makes conventional photolithography impractical for patterning

OLED arrays.[45] Thin films used in OLED fabrication frequently become denatured or dissolved when exposed to water or organic solvents. Consequently, subtractive patterning is rarely used in OLED processing. Most OLED array fabrication techniques combine deposition and patterning of an organic thin film into a single step.

For purposes of this discussion, processing techniques can be split into two broad categories. The first is physical vapor deposition (PVD), which involves evaporating material so that it condenses on a substrate to form a thin film.[54] Condensed phase methods form a second category. They employ a liquid or solid carrier medium, such as a solvent or membrane, to transfer an organic material onto a substrate. Generally, PVD techniques can readily grow complex, multilayer device architectures, but patterning is difficult. Only small molecules can be used for PVD, since most polymers have very high evaporation temperatures and will chemically degrade if they are heated to that temperature. Organic vapor jet printing, which is the focus of this thesis, is a PVD technique. It seeks to combine the ability to grow complex multilayer structures with the scalable patterning capability of solvent based techniques like inkjet printing.

Condensed phase techniques facilitate patterning and are compatible with both small molecules and polymers. They generally offer less control over film thickness and morphology than PVD. It is difficult to make the multilayer structures required for efficient OLEDs with a high degree of consistency using solvent or stamping techniques. Furthermore, residual solvent in solvent deposited layers can reduce device lifetime.[45] The need for consistency, efficiency, and lifetime has led to the near universal adoption of PVD and a small molecule material set in the OLED display industry. Consequently, most research into commercial OLED materials has focused on small molecules.

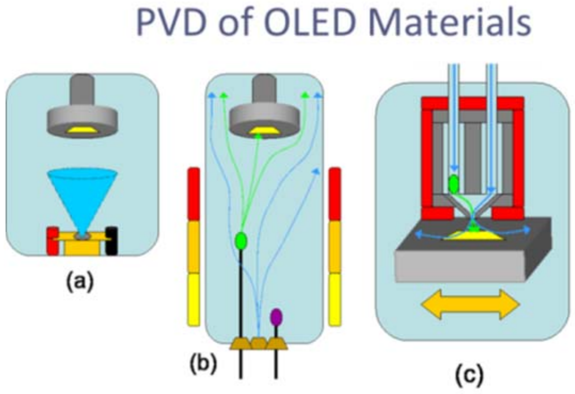

Figure 2-1: PVD of OLED materials. Physical Vapor Deposition (PVD) modes for small molecule organic thin films include (a) vacuum thermal evaporation (VTE), (b) organic vapor phase deposition (OVPD) in a hot walled reactor,[55] and (c) organic vapor jet printing (OVJP) using hot tubes to transport organic vapor to a substrate through a nozzle.[56]

2.2 Physical Vapor Deposition

2.2.1 Vacuum Thermal Evaporation

The most common way to deposit small molecule organic thin films is by vacuum thermal evaporation (VTE), shown in **Fig. 2-1a**.[45] Organic material within a resistively heated boat is evaporated inside of a high vacuum chamber. Molecules of organic vapor follow a ballistic path towards a substrate opposing the source where they re-condense into a thin, continuous film. Patterning is typically achieved by placing a thin metal shadow mask over a substrate to prevent organic material from depositing in regions where it is not desired.[33] Three sequential masking steps can be used to generate an RGB OLED array as depicted in of **Fig. 1-5a**.

Multilayer structures can be readily grown using VTE. Since it is a solvent free process in which films are grown at relatively slow rates of several Å/s, molecularly sharp interfaces between organic layers only tens of molecules thick can be grown. Vacuum thermal evaporation is the most widely used process in the OLED display industry, so it forms a baseline against which other deposition and patterning techniques must be judged.

Vacuum thermal evaporation has serious drawbacks in a production setting. High vacuum equipment is expensive to build and energy-intensive to operate. A large mother glass substrate requires large equipment, compounding this problem. A long relief distance between the source and substrate is required to ensure uniformity of the deposited film, especially when material evaporates from multiple sources, as in co-deposition. This has historically resulted in poor material utilization efficiency; however state-of-the-art linear sources are capable of efficiencies of 50% or greater.[57] A more significant inefficiency results from shadow masks. The material utilization efficiency for each color is limited to the fraction of the substrate surface it covers. The rest of the material simply coats and clogs the mask.

Shadow masks themselves pose a serious problem to the scale-up of VTE processing. Microfabricated metal structures generally have low aspect ratios.[58] A mask intended to deposit 30 μm features for a high resolution mobile display is itself no thicker than a leaf of foil. Such a thin structure quickly becomes unwieldy for large area substrates. The rigidity of a shadow mask is further reduced by the cutouts required to pattern organic material, limiting the printing density of conventional shadow masks to 7 pixels/mm.[59] Smaller "scanning masks" which cover smaller portions of a large substrate are often used, but registration and positioning pose considerable technical challenges.[60] Cleaning organic material that builds up on thin masks is also challenging.

2.2.2 Organic Vapor Phase Deposition

Some of the problems of VTE are addressed by organic vapor phase deposition or OVPD, shown in **Fig. 2-1b**. An inert carrier gas is used to entrain evaporated organic material and convectively transport it through a hot walled reactor and onto a substrate where it condenses.[55] The quality of deposited material is primarily dependent on the purity of the carrier gas input rather than the chamber base pressure. The OVPD process, therefore, only requires low vacuum, which is far easier to realize on a production line than high vacuum. Transport of organic material in OVPD is mediated by a carrier gas, so deposition rate does not depend on the position of sources relative to the substrate. Co-deposition is a straightforward issue of fluid mixing that does not place constraints on chamber geometry and materials utilization efficiency as it does in VTE. Material utilization efficiency can be very high since organic vapor does not condense on the heated walls of the chamber. A pilot scale OVPD system has demonstrated material utilization efficiency of 50%.[61] Features of 10 μm or less can be deposited by OVPD through shadow masks.[62] Substrates can face upward in OVPD to simplify masking; however the problems of applying, removing, and cleaning masks remain.

2.2.3 Organic Vapor Jet Printing

While similar to techniques like VTE and OVPD, organic vapor jet printing (OVJP) does not require shadow masks to deposit a patterned film, see Fig **2-1c**.[56]

OVJP seeks to combine the direct patterning capability and efficient material usage of inkjet printing with the capability of PVD to grow multilayer organic device architectures. The primary difference between the nozzles used in OVJP and a shadow mask used in OVPD is that the nozzles are both sealed to the organic material sources and heated. No material condenses onto the nozzles or flows around the substrate in OVJP. Also, there is no shadow mask to trap organic material. Material utilization efficiencies approaching unity can, therefore, be obtained.

Conceptually, the OVJP process can be broken into four steps illustrated in **Fig. 2-2.** In the first step, entrainment, organic material is evaporated at a constant temperature and entrained in an inert carrier gas that flows past a condensed material source. Secondly, different species of organic vapor from separate sources combine in a mixing channel to allow for co-deposition of host and guest materials. In the third step,

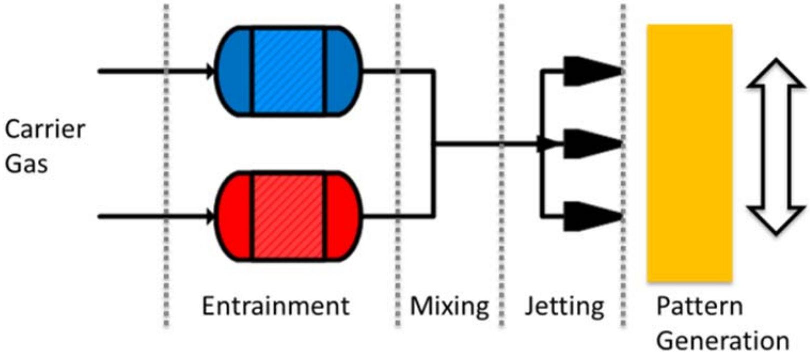

Figure 2-2: Basic steps of the OVJP process. The steps of the OVJP process are entrainment of organic vapor in carrier gas, mixing of vapors from different sources, formation of vapor jets, and deposition with pattern generation. (Figure from McGraw, Peters, and Forrest)[63]

the vapor mixture is distributed to an array of nozzles that collimates it into well-defined jets. In the fourth and final step, the jets impinge on a chilled substrate leaving deposits of condensed organic material. Patterns can be generated by moving the substrate relative to the nozzle array.[64]

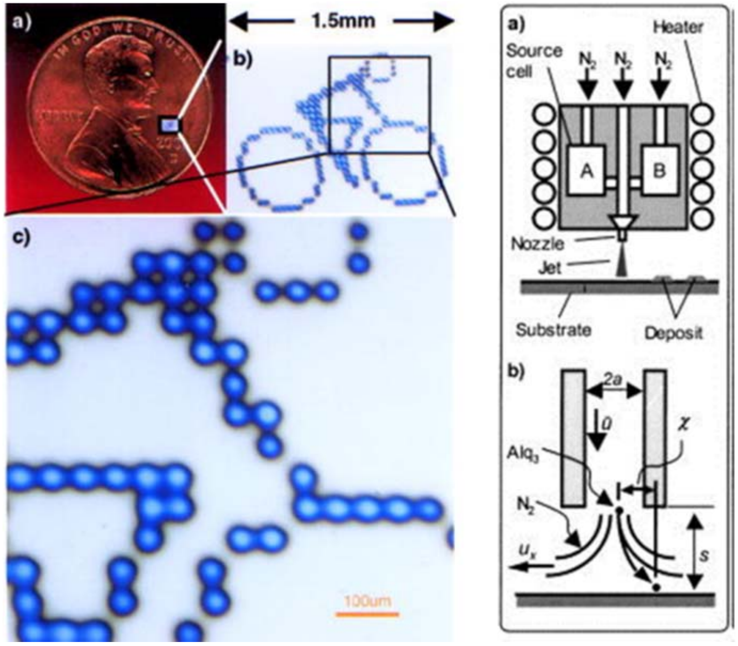

Figure 2-3: Patterning by OVJP using a single 20 μm diameter nozzle. A 1 mm long figure of a bicyclist is dawn from 20-30 μm dots. At right the OVJP tool is shown diagrammatically at top. Inert N_2 carrier gas accelerates organic material from source A or B through the nozzle onto the substrate. Carrier gas is deflected by the substrate, however heavier organic material does not scatter and lands in a well-defined pattern beneath the nozzle. (Figure from Shtein, *et al.*)[56]

The OVJP process was initially demonstrated by Shtein, *et. al* using a single 20 μm diameter laser drilled stainless steel nozzle to print patterns of neat organic material. Feature sizes of 30 μm were obtained, translating to printing resolutions of over 500 dots per inch.[56] An example of a printed pattern and the system geometry are shown in **Fig. 2-3**. The OVJP tool was used to draw continuous films of pentacene, used to make organic TFTs with hole mobilities of 0.2 cm^2/Vs, comparable to that achieved by VTE grown films.[65] Fluorescent NPD-Alq_3 OLEDs with EQE =0.84% were also grown by this method. The efficiency of the fluorescent OLEDs grown by OVJP was comparable to that of conventionally processed devices.[66] This simple system demonstrated the ability of OVJP to print electronic quality material at high resolution. Most implementations of OVJP require that deposition is carried out in a chamber evacuated to 1 Torr of absolute pressure or less. OVJP can, however, be used in atmosphere with an inert N_2 guard flow around the jet of depositing vapor. Fluorescent NPD-Alq_3 OLEDs with an EQE =1.36% were grown in this manner.[67]

Organic vapor jet printing offers some control over the morphology of deposited films. While amorphous films are desired for OLED applications,[25], the crystallinity and crystal orientation of an organic thin film can profoundly affect the performance of devices such as TFTs.[68] Carrier gas heated to 523K was found to promote the growth of bulk pentacene crystals with mobilities of up to 0.6 $cm^2/(Vs)$, while lower carrier gas temperature resulted in lower mobilities.[69]

Organic vapor liquid solvent (OVLS)[70] growth provides both an interesting example of both using an OVJP-like technique to control film morphology and a hybrid of PVD and solvent processing. A jet of organic material entrained in carrier gas is deposited onto a substrate wetted with solvent in an inert atmosphere. Deposition and solvent annealing therefore are combined into a single step. Ordered films of low solubility materials such as tetracene can be grown in this manner.[71]

To further develop OVJP for OLED fabrication, a bench scale system capable of printing up to three different colored OLED segments on a single substrate was developed. It demonstrated the capability to grow doped films for highly efficient phosphorescent OLEDs.[72] This system was intended to print segmented arrays for white lighting applications in which high resolution is not critical. It is further discussed in Chapters 3 and 4. Experience with this system guided development of a process incorporating arrays of microfabricated nozzles capable of printing multi-color features in parallel.[63] The principles underlying the operation of the multi-nozzle system[64] are discussed in Chapters 5 and 6, its construction is described in Chapters 7 and 8, and experimental results are presented in Chapters 9 and 10.[63][64]

The OVJP system described herein is designed to print lines of light emitting material. It can be readily used to print displays with stripe subpixels, in which the red, green, and blue subpixels are co-linear. This layout is generally used for large, high resolution displays, beginning with aperture grille cathode ray tube televisions such as the Sony Trinitron®.[73] Mosaic subpixel configurations, in which the positions of individual colored subpixels are staggered, allow emissive segments to be shared between pixels. This improves image quality for a given resolution or subpixel size.[45] It is therefore preferred for small displays. Mosaic subpixels, such as Samsung's Pentile® design, requires emissive material laid down in discrete segments rather than continuous lines. This contrast is illustrated in **Fig. 2-4.** To this end, Yun *et al.*, developed "digital-mode" OVJP (D-OVJP) to print features such as OLEDs and TFTs from discrete pulses of organic vapor. Cycle times as high as 80 Hz can be achieved by using a vent valve to rapidly de-pressurize the runline of the D-OVJP tool between pulses.[74]

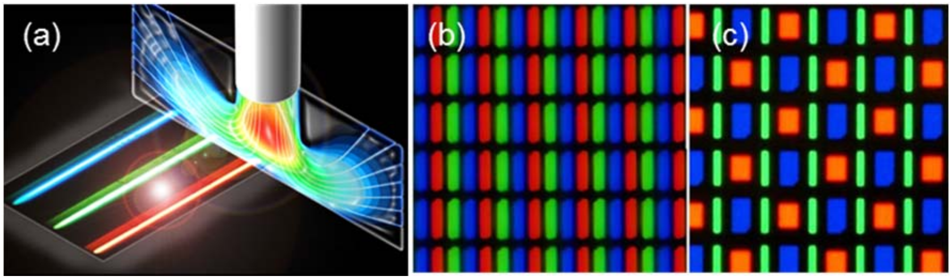

Figure 2-4: Sub-pixel layouts for full color displays. (a) An artist's impression depicts an OVJP system in line printing mode. Such a system can make the striped OLED pattern in (b) but not the Pentile® patterned display in (c). (a image courtesy of Michael S. Arnold, Ph.D., b and c Android® phones with OLED displays. www.andrioidauthority.com)

2.3 Condensed Phase Processing Methods

Condensed phase techniques use a solid or liquid transfer medium to distribute organic semiconductor material over a substrate at temperatures well below the evaporation temperature of the material. In solvent processing methods, the organic material is dissolved in a volatile liquid solvent. This solution is then applied to the substrate. The solvent evaporates, leaving behind a thin film of the organic material. Solvent processing is compatible with either polymer or small molecule materials. Blanket layers of organic material can be deposited using solvent techniques such as slot coating[75] or spin coating[76]. Some polymer films can then be patterned using photolithographic techniques. Light emitting polymers that behave like a negative photoresist and cross link in response to UV light have been developed.[77]

Patterned organic material can also be deposited using inkjet printing. Inkjet has the advantage of its relation to the widely used document printing technology. It is capable of printing features as small as 15 μm.[78] Its use of solvents, however, creates complications. Surface tension may limit printing resolution and lead to “coffee ring” effects and non-uniform film thicknesses, although this can often be mitigated with specialized drying protocols.[79] Substrate surface treatments that define wetted and non-wetted areas can also be used to address these issues.[80]

Nozzle printing is a simplified process, similar to inkjet, in which a solution of organic material is driven out of an array of micronozzles under steady pressure over a moving substrate.[44] Only stripe subpixel arrays can be fabricated using this method. This process has proven amenable to scale up and is currently being developed for mass production by Dupont.[81] All solvent processing methods are limited by very low (<1%) material utilization ratios, once solvents are considered. Electronics processing requires ultra-high purity solvents and these must be factored into a cost analysis.

Various methods exist to generate a pattern by dry transfer of an organic film. In micro-contact printing,[82] a stamp with features defined by photolithography is used to pattern an organic thin film. Patterning can be either additive or subtractive, depending on whether an organic thin film is added to, or removed from the substrate at the points it contacts the stamp.

Laser induced thermal imaging (LITI)[83] is an additive transfer technique. An organic thin film is coated onto a transfer medium that absorbs laser light and transforms it into heat. The coated face of the medium is brought into near contact with a substrate and a laser is scanned along the back side of the medium. The medium expands where it is illuminated and these portions apply pressure to the substrate. When a heated area of the medium cools and contracts, it leaves the organic thin film covering it on the substrate. The primary advantage of LITI is that it separates the formation of the organic emissive layer and its patterning into separate steps. The transfer films can be made more robust than thin metal shadow masks.[84] However LITI does not offer better material utilization efficiency than shadow masks since transfer films cannot be reused. The added expense of the transfer media must also be considered.

Molecular jet printing may be viewed as a hybrid between PVD and condensed phase techniques. An array of microheaters is fabricated on a porous plate, which is then loaded with organic material.[85] The array is then brought into close proximity with a substrate and microheaters flash-evaporate the organic materials onto a substrate to form well-defined dots. While bearing some similarity to dry transfer techniques like LITI, the final transfer of organic material to the substrate occurs in vapor phase. Despite being mechanically simple, issues like controlled doping remain problematic. This process is currently being developed by Kateeva.[86]

It is possible to combine PVD and condensed phase transfer techniques in a single device. This is trivially the case for virtually all solution processed or stamped OLEDs, since evaporated or sputtered top contacts are used. More complex combinations of evaporated, solvent-printed, or stamped organic layers are possible. Inkjet[87] and nozzle printing techniques can combine solvent-processed emissive layers with an evaporated electron transport layer to create patterned devices with sharp heterojunctions. Transport and emissive layers can be evaporated over a spin-coated hole transport layer that planarizes anodes with sub-optimal roughness for flexible devices.[88]

2.4 Summary

Organic thin films are difficult to pattern by conventional photolithography. They are therefore usually grown by processes that combine deposition and patterning into a single step. These techniques can be divided into two broad categories, PVD and condensed phase transfer. A high degree of control over film thickness and morphology makes PVD well suited to grow highly efficient multilayer structures. Commercial OLED fabrication is dominated by VTE, a PVD technique, since it can grow efficient, long-lived devices with a high degree of repeatability. Unfortunately, shadow masks are required to pattern thin organic films grown by PVD, making the process difficult to scale to large area substrates. Condensed phase printing techniques that employ solvents or dry transfer media facilitate patterning, albeit at the expense of control over film quality and device architecture.

Organic vapor jet printing is a PVD technique that seeks to combine the ability to grow precise multilayer structures with the scalable, high resolution patterning capability of solvent based techniques like inkjet printing. The OVJP process has the potential to meet all three requirements set out in the beginning of this chapter. First, it can print features with high resolution, comparable to that achieved by inkjet, as shown in **Fig. 2-3**.[56] Secondly, it is compatible with high efficiency phosphorescent OLED architectures, as will be shown in the next chapter. Thirdly, and finally, it will be able to achieve the previous two goals in a scalable fashion since arrays of micronozzles fabricated from Si by photolithography afford the OVJP process a high degree of parallelism.

Chapter 3

Single Nozzle OVJP

3.1 Overview

An expanded OVJP system was developed following the successful demonstration of the technique by Shtein *et al*.[65] This system was designed to be capable of depositing multiple colors as well as co-depositing organic host and dopant material in user-defined ratios. It could also grow overlapping patterns of different materials. These capabilities were gained at the expense of patterning resolution, since feature size was limited by the 1 mm diameter nozzle of this design.

This system was used to print a spatially repeating pattern of red, green, and blue phosphorescent OLED segments for white lighting applications. The printing resolution required to fabricate lighting is less than that required for displays. Light sources can be placed behind a diffuser and viewed in the far field. When viewed from a distance, the red, green, and blue subpixel emission blends to form white light.[72] This architecture, as depicted at the top of **Fig. 1-4a**, has many advantages. The array can be optimized for either high power efficiency or high color rendering index based on the choices of red, green, and blue emissive components. Optimal transport and blocking layers can be deposited for each color emissive segment. Color temperature can be controlled by the end user of an RGB lighting panel by placing each color of emitter on an independent, constant current power supply. Color change due to differential aging of devices fabricated from different emitters can also be remedied in a similar manner.

3.2 OVJP Tool Design

The OVJP tool had provisions for five independent material sources. A piping and instrumentation diagram indicating the placement of key elements is shown in **Fig. 3-1**. Material was stored in 6 mm diameter by 25 mm long quartz vials held within 12 mm inner diameter stainless steel tubes. Each material source was bounded at both ends by bellows valves to prevent migration of material when the source is not active. Flow of carrier gas into the tool was controlled by six mass flow controllers, one for each organic vapor source and another for a heated dilution flow. The sources are housed within a furnace that had a cubic interior of 60 cm on a side to provide baseline heating. Outside of the setup is shown in a wide angle photograph in **Fig. 3-2a**, and the inside of the furnace is shown in **Fig. 3-2b**. Supplemental electric heat tapes wrapped around source lines allowed each source and its surrounding valves to be held at different temperatures. The furnace had a series of cutouts for gas lines and valve actuators. Open space within these cutouts was packed with glass wool to retain heat.

All organic vapor sources and the dilution line emptied into a common 6 mm diameter runline that carried the heated carrier gas and organic vapor mixture from the furnace into a deposition chamber. The runline was approximately 2 m in length, measured from its junction with the last source. Resistive heat tapes were wrapped around the outer circumference of the runline, and portions of the runline outside of the furnace were wrapped in further layers of mineral wool and aluminum foil to ensure an even temperature distribution along the runline length. The runline was equipped with a heated relief valve to divert flow past the nozzle and directly into a vacuum pump. This provided a low impedance path through which the runline could be flushed under conditions of a high carrier gas flow rate (50 sccm) and low pressure (~1 Torr).

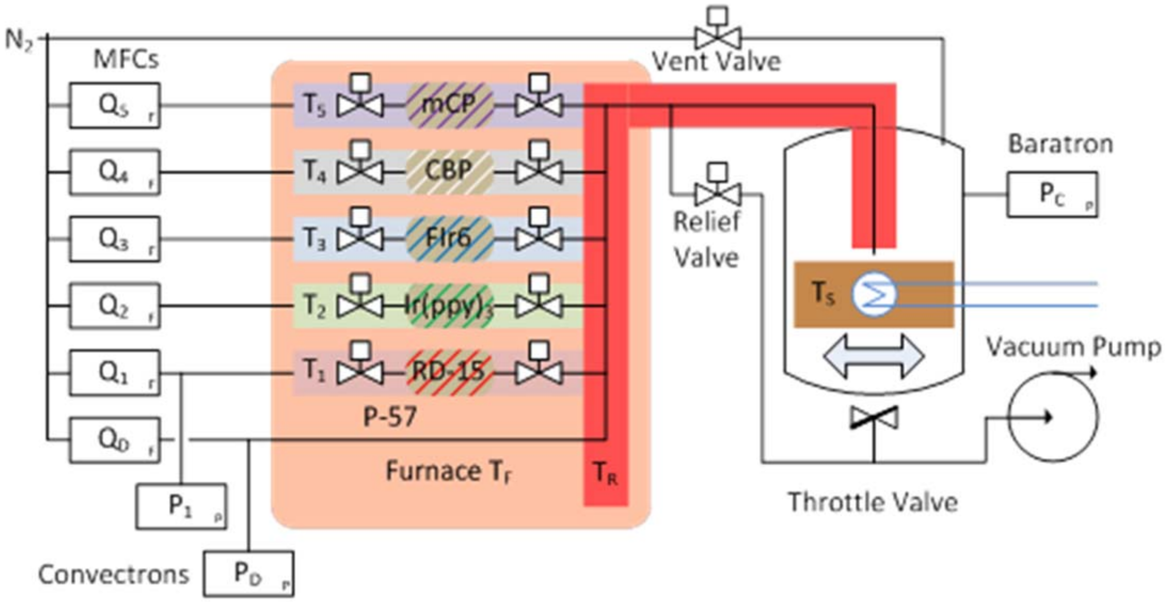

Figure 3-1: Piping and instrument diagram of the single nozzle OVJP tool. Flow of N_2 carrier gas is controlled by mass flow controllers (MFCs) for each color source and a dilution flow. Pressure upstream of the sources and in the deposition chamber is monitored by Convectron® and Baratron® sensors. Sources are located with a furnace that is heated to the sublimation temperature T_F of the most volatile organic material deposited. Supplemental heaters held material sources at temperatures T_1-T_5. The runline between the furnace and vacuum deposition chamber is heated by supplemental heaters to T_R, which is greater than the sublimation temperature of the least volatile organic material deposited. A single 1 mm Ø nozzle directs flow at the end of the runline, but this can be bypassed by a relief valve to facilitate rapid purging. The substrate is held on a chilled, moving holder.

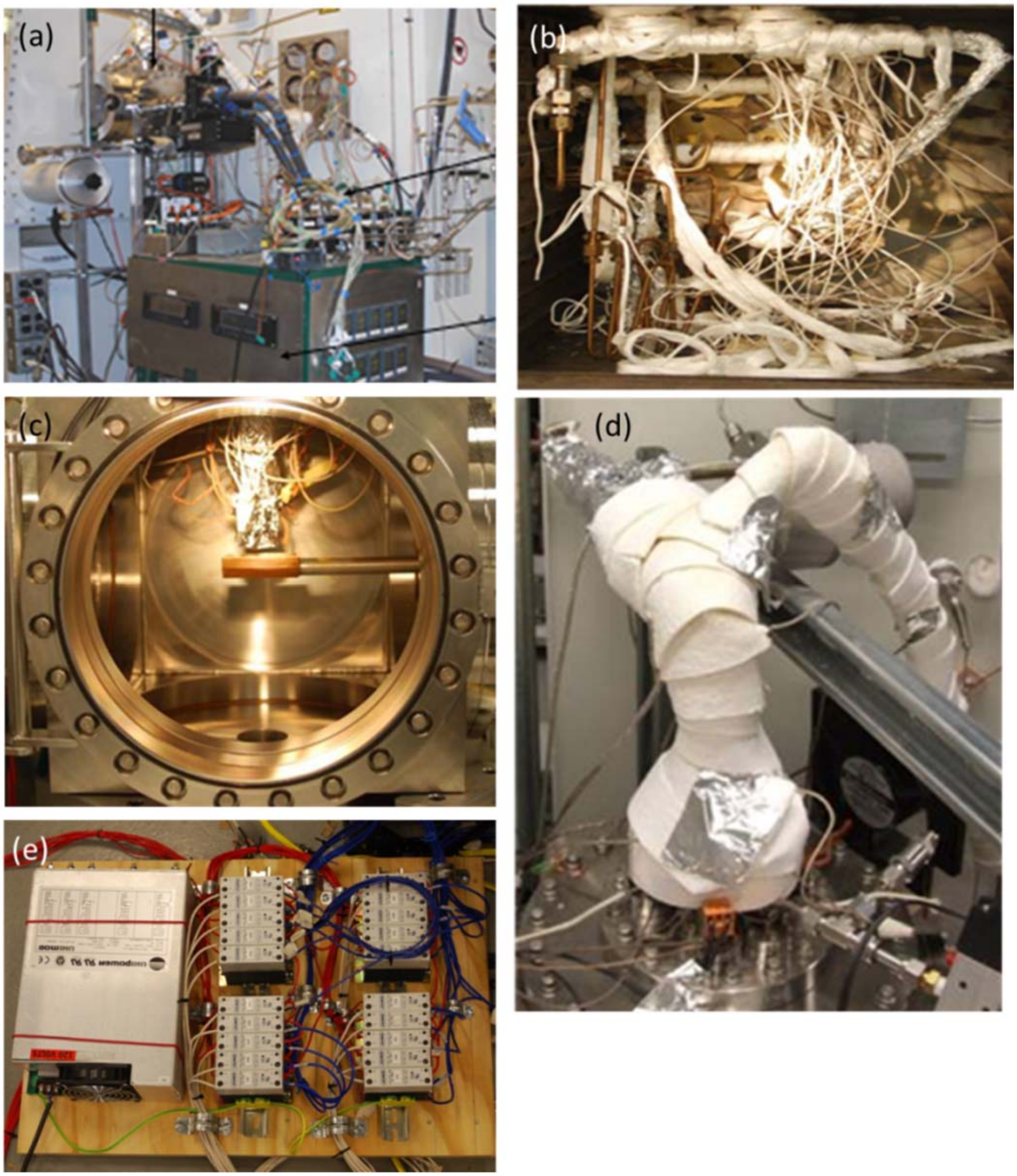

Figure 3-2: Photographs of the OVJP tool. (a) Front of tool viewed from outside. Furnace is visible at right. The utility cabinet is in the foreground. The deposition chamber with motorized tunnel feedthrough is visible behind it. An ultrapure N_2 glovebox is attached to it at right. (b) Inside of furnace, showing vapor source tubes with supplemental heat tapes. (c) Deposition chamber with heated nozzle and substrate stage. (d) Heated runline connecting the furnace to deposition chamber. The chamber feedthrough is at the bottom. (e) 20 channel, 2kW power supply for heaters.

The runline extended to a cubic vacuum chamber 25 cm on a side that served as a deposition chamber, **Fig. 3-2c.** After passing through a vacuum feedthrough heated to runline temperature, **Fig. 3-2d**, the flow of carrier gas was channeled into a single 1 mm diameter nozzle that was located approximately 700 μm above the substrate. A 15 cm length of runline inside of the vacuum chamber was heated using resistive heat tapes, while the nozzle itself was wrapped with glass wool and a Nichrome® wire heated by a DC power supply. All heated surfaces inside the deposition chamber were wrapped in aluminum foil to reduce radiative heat loss and eliminate particulate contamination inside the chamber from the fiberglass insulated heat tapes. The chamber was equipped with a motorized *x, y, z* tunnel feedthrough that supported a 20 by 30 mm chilled substrate holder on a cantilever. The chamber was evacuated by a rotary vane pump and had a base pressure of 50 mTorr. It could be accessed through a glovebox filled with ultrapure N_2 that could also be used to transfer substrates to other deposition tools without exposure to atmosphere. This glovebox is visible in the left corner of **Fig. 3-2a**. A utility cabinet provided electrical and pneumatic control. This was dominated by a large, custom built power supply for the supplemental heaters, **Fig. 3-2e.**

The OVJP tool was designed to print continuous stripes of differently colored electrophosphorescent material on a flat substrate, as illustrated in **Fig. 3-3a**. The size of printed features is approximately 1 mm wide, as demonstrated by logos for the University of Michigan and the Optoelectronic Components and Materials Group (OCM), **Figs. 3-3b** and **c**, printed with OVJP. The photoluminescent test pattern in Fig. **3-3d** demonstrates multicolor printing capability, with red, green, and blue phosphorescent lines.

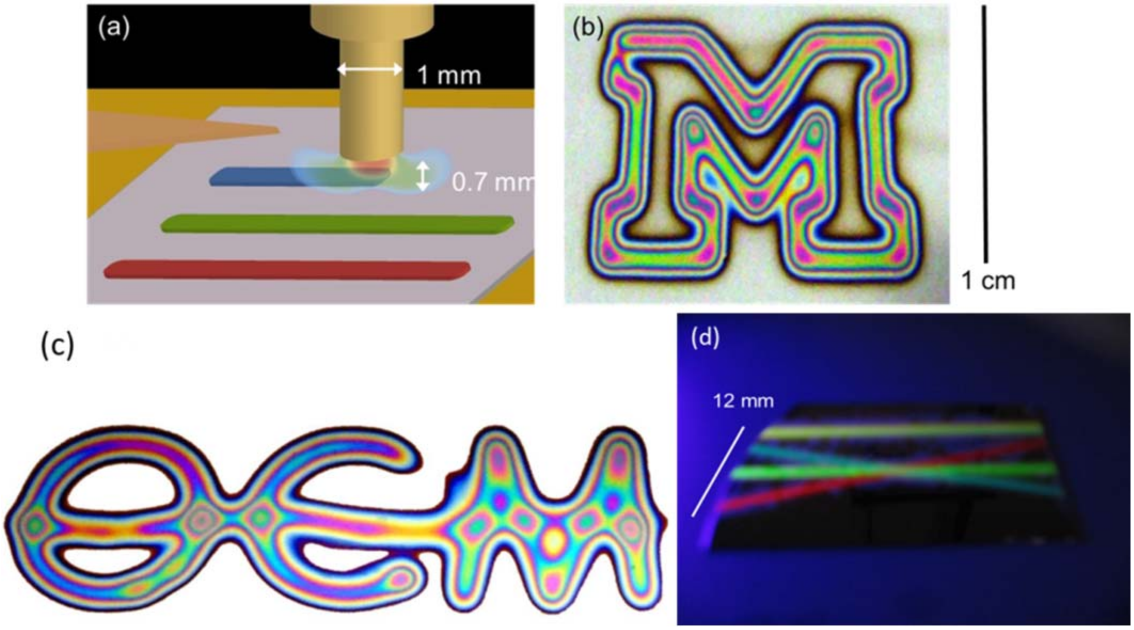

Figure 3-3: Examples of substrates printed with OVJP. (a) An artist's impression shows the OVJP tool printing a substrate with electroluminescent stripes. (b) University of Michigan and (c) Optoelectronic Components and Materials (OCM) group logos were drawn in organic thin film by OVJP (d) Phosphorescent lines of neat FIr6 (blue) and Ir(ppy)$_3$ (green) and RD-15 (red) doped in CBP were printed a an Si substrate and viewed under a UV lamp.

3.3 OLED Array Design

The highest possible power efficiency was desired to demonstrate that OVJP is a viable technique for fabricating OLED lighting. Since the light produced would be a composite of that emitted by three different spatially separated monochromatic segments, the architecture of each segment was chosen to optimize its quantum efficiency. An array of red, green, and blue phosphorescent OLED segments, surrounded by transport layers as depicted in **Fig. 1-d** and **e**,[12] was therefore desirable. The variety of available phosphorescent emitters offers significant freedom to optimize the color gamut of the device for lighting.[28] The architecture of the final device, however, was constrained by processing limitations. It is shown in **Fig. 3-4**. The green segment consisted of fac tris(2-phenyl pyridine) iridium(III) ($Ir(ppy)_3$) doped at approximately 6% by volume into a host layer of 4,4-N,N-dicarbazole-biphenyl (CBP). This host and dopant system was chosen since it is robust, well-characterized, and has a very high luminous efficiency.[26] It has an emission peak at a wavelength of λ =512 nm and CIE coordinates (0.27, 0.63).[26] The red emitter initially chosen was bis-2-phenylquinolyl-N,C2, acetylacetonate iridium(III) (pqIr). This material has a relatively short peak emission wavelength of λ =610 nm, making it appear orange.[13] This is desirable for a white light device, since its wavelength is closer to the peak sensitivity of the eye, as explained in Ch. 1.3.2. Unfortunately its low sublimation temperature relative to the host material, CBP (200°C vs 260°C) made its use in OVJP impractical. Universal Display Corporation's proprietary dopant, RD-15, with CIE coordinates (0.66,0.32) was found to be compatible with this process and was used instead.[72] This dopant has an emission peak at λ =623 nm, rendering it slightly less power efficient. The light blue dopant, iridium(III) bis(4',6'difluorophenyl-pyridinato) tetrakis (1-pyrazolyl)borate (FIr6) was chosen due to its relatively high power efficiency and compatibility with the OVJP process. The CIE coordinates of FIr6 are (0.19, 0.30).[72] Since it has a relatively large energy gap of 3.0 eV between the HOMO and LUMO,[17] FIr6 requires a 1,3-Bis(*N*-carbazolyl)benzene (mCP) electron and exciton blocking layer, with a HOMO-LUMO gap of 3.5eV, between itself and the hole transport layer.[17] This required a dedicated source, leaving no space for a host to use with FIr6. As a result, FIr6 was deposited as a neat film, leading to some loss of efficiency. The architecture of the blue emitting device provided a further demonstration of OVJP capabilities. The FIr6 and mCP layers were deposited as a two layer heterojunction patterned by OVJP. This demonstrates the capability of OVJP to optimize transport layers for each emitter. The mCP layer is unnecessary for red and green devices, and simply creates additional resistance.

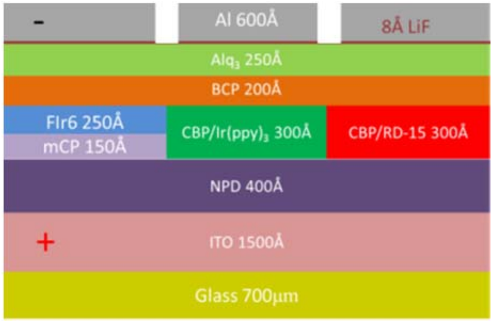

Figure 3-4: Segmented RGB OLED structure for lighting. Devices were grown on a soda lime glass substrate coated with a 15 Ω/sq ITO anode. NPD is a common hole transport layer. The blue segment consists of an emissive layer of FIr6 over a mCP electron blocking layer. The green and red emissive layers consist of Ir(ppy)$_3$ and RD-15, respectively, doped in CBP. BCP and Alq_3 are common hole blocking and electron transport layers. Each segment is contacted by an Aluminum cathode with LiF charge injection layer.[72]

3.4 Experimental Methods

The OVJP tool was calibrated in three steps prior to OLED growth. In the first step, source temperatures were set. Host source temperature was chosen such that a film of proper thickness could be deposited at a substrate feed rate of between 1 and 4 mm/s. Dopant source temperature was then chosen so that doping spans the range from under-doped to over-doped over the operating range of the dopant carrier gas mass flow controller. Secondly, after choosing source temperatures, the doping ratio was set by adjusting the ratio of host and dopant carrier gas flows. Optimal doping was verified with photoluminescence spectroscopy. Doping is optimized when the host emission is completely suppressed, but dopant concentration is sufficiently low that dimer emission from the dopant does not significantly red shift its emission peak, as seen for the CBP/ $Ir(ppy)_3$ calibration in **Fig 3-5a**. The volume doping ratios set by this method correspond

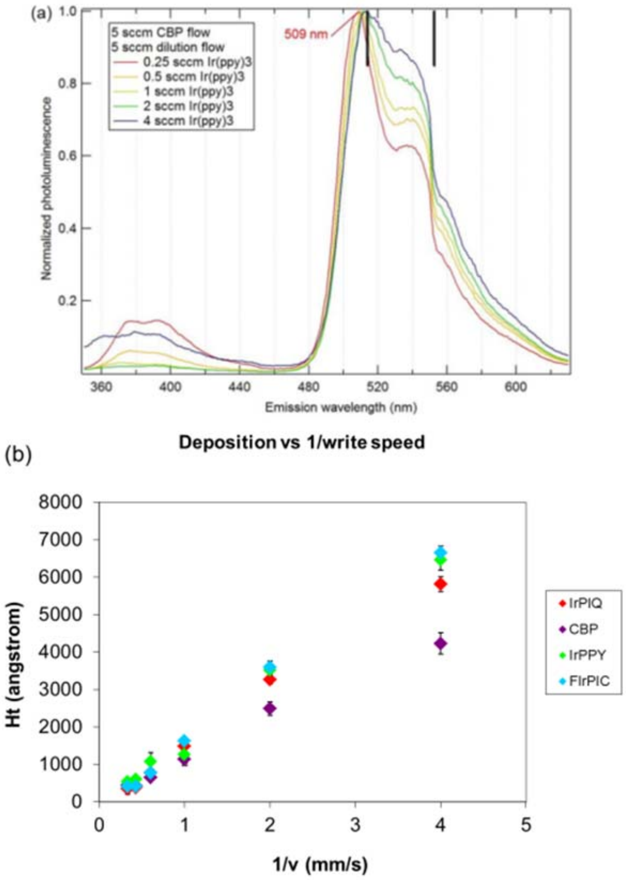

Figure 3-5: Typical calibration data for OVJP tool. (a) Doping ratio is calibrated by photoluminescence spectroscopy. A neat CBP film emits blue and UV light. Significant blue emission is observed if only 0.25 sccm of carrier gas flows through the $Ir(ppy)_3$ source. The host emission is fully quenched for 1 sccm of dopant flow. The film becomes overdoped for higher flow rates and a dimer emission peak at 530nm becomes more prominent as flow through the $Ir(ppy)_3$ source is increased. (b) Film thickness deposited by OVJP is plotted as a function of reciprocal substrate speed, measured by profilometry.

to 6% ±3% for $Ir(ppy)_3$ and 10% ±3% for RD-15 when compared with films grown by VTE.[72] In the third step, film thickness was calibrated. Thickness was measured by both stylus profilometry of individual lines and spectroscopic ellipsometry of continuous films drawn in multiple passes. Film thickness was adjusted by changing the rate at which the substrate was rastered underneath the nozzle, **Fig. 3-5b**, with slower speeds resulted in thicker films, since the residence time of the nozzle over each printed portion of the substrate was longer. The thickness of deposited films was relatively stable, with a typical variation of less than 10% between runs.

The emissive layer of three-color segmented OLED arrays were grown using the OVJP tool.[72] Devices were grown on a 1 mm thick glass substrate coated with 1500Å ITO. The substrates were covered in a 400 Å hole transport layer of NPD by VTE. Emissive layers were then applied using OVJP. A hole blocking layer of 200 Å 2,9-dimethyl-4,7-diphenyl-1,10-phenanthroline (BCP) and an electron transport layer of 250 Å Alq_3 was subsequently deposited by VTE. A cathode of 8 Å LiF and 600 Å Al was then deposited through a shadow mask using VTE.[72]

Emissive segments were sequentially deposited by OVJP. The runline was heated to 350°C for depositing red and green segments. The CBP source was heated to 240°C for both depositions, while $Ir(ppy)_3$ and RD-15 sources were heated to 235°C and 315°C, respectively. A flow of 5 sccm of ultrahigh purity N_2 carrier gas was fed through the dilution line, while the CBP, $Ir(ppy)_3$, and RD-15 sources are fed 5, 2, and 1.5 sccm of carrier gas respectively. Pressure within the material sources was 8 Torr and the chamber pressure was 220 mTorr. The nozzle was held at 700 μm from the substrate and the substrate holder was maintained at 30°C. Green and red sets of segments were deposited sequentially.[72]

Blue segments were deposited after red and green. The runline was cooled to 245°C to inhibit thermal decomposition of the blue material set. The mCP electron blocking layer was deposited first, and a neat film of FIr6 grown over top of it. The mCP source was heated to 175°C, and FIr6 to 235°C. Dilution and source carrier flows were 5 sccm in both cases. The substrate holder was chilled to 5°C.[72]

An extensive purging procedure removed contamination from the runline between each color growth. Organic material source valves were closed and the runline was flushed with 50 sccm of carrier gas for 5 min with all flow exiting through the nozzle and another 5 min with the relief valve open. The chamber was then purged to atmospheric pressure with N_2 and pumped down. This cycle was repeated three times between depositions.

3.5 OLED Array Performance

Red, green, and blue monochromatic phosphorescent OLED segments were successfully deposited on a single substrate using OVJP. A printed feature can be placed within 2 mm of a feature containing a different chemical species without apparent cross-contamination in its emission spectrum.[72] These devices are shown individually in **Fig. 3-6** and illuminated simultaneously in an RGB array shown in **Fig. 3-7a**. Adjacent 1 mm wide features are positioned on 2.5 mm centers without apparent color change. This is confirmed by spectra presented in **Fig. 3-7b**, which only show emission from one

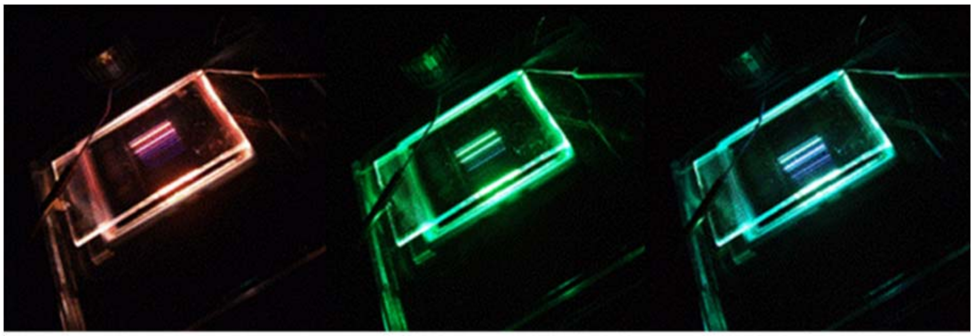

Figure 3-6: Red, green, and blue light emitting segments. This multicolor array of PHOLEDs was grown on a single substrate by OVJP.

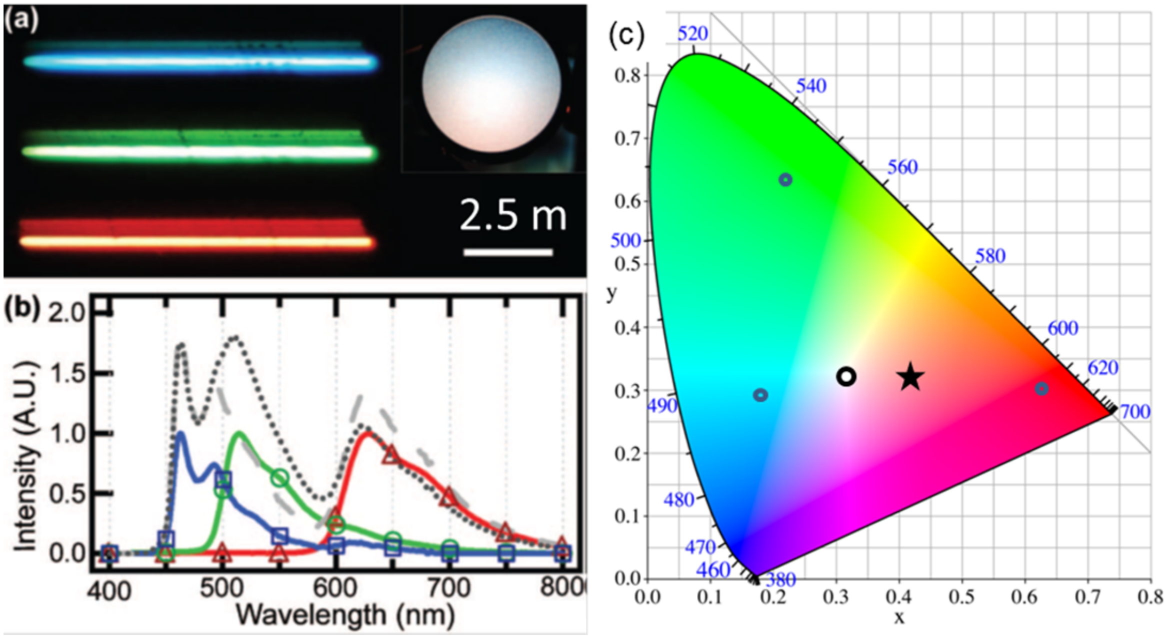

Figure 3-7: Color rendering of OVJP processed tricolor device. (a) Images of blue, green, and red OLED segments are shown simultaneously illuminated; both individually and behind a diffuser (inset) to produce white light. (b) Emission spectra of the individual monochromatic segments are shown in their respective colors. The spectrum of pure white light with CIE coordinates (0.33,0.33) is shown in dashes, while the dotted line shows an emission spectrum corresponding to a power efficiency of 11.9 lm/W and CRI of 80. The (c) Coordinates of the three component colors and the two white light combinations are shown on the CIE gamut. (Image from Arnold, *et al.*)[72]

phosphorescent emitter in each segment. As expected, the array produced white light when viewed from behind a diffuser, **Fig 3-7a (inset)**. The hue, efficiency, and color rendering index that could be produced by a light source employing this array were calculated from measurements on the individual segments. The CIE coordinates for each of the three emitters are shown in **Fig. 3-7c**, along with neutral white (0.33,0.33) and a setting for optimal color rendering. The neutral white point is near the border of color gamut of the array connecting the red and blue vertices. Neutral white light, therefore, would contain little green light, which adversely affects power efficiency, η_p, and CRI. Better efficiency and a CRI of 80 are possible if the operating point is shifted to CIE coordinates (0.40, 0.31), however the light source would appear to have a greenish tint. The spectra for neutral white and for optimal CRI are shown in **Fig. 3-7b.**

As shown in **Table 3-1**, blue and green segments had peak external quantum efficiencies that were within experimental error of those achieved by VTE grown control devices. Red segments had a peak power efficiency that was comparable to control devices. Based on the single color device data, and a 70% outcoupling enhancement from mounting the OLED array in a luminaire, it was calculated that it could produce neutral white light with CIE coordinates of (0.33,0.33) at a peak power efficiency of 8.4 lm/W. A light source operating at CIE coordinates of (0.40, 0.31) would have a peak power efficiency of 11.9 lm/W. At a typical brightness for OLED lighting of 400 cd/m^2, this light source would operate at η_p =11.4 lm/W.[72]

Color	Process	FFEQE (%)	FFPE (lm/W)	TEQE (%)	TPE (lm/W)
Red	OVJP	9.4 ±0.5	4.7 ±0.5	15.9 ±0.8	8.1 ±0.8
Red	VTE	12.6 ±0.1	4.9 ±0.1	21.4 ±0.1	8.3 ±0.1
Green	OVJP	8.6 ±0.7	16.5 ±1.2	14.6 ±1.2	28.0 ±2.0
Green	VTE	8.9 ±0.3	13.3 ±0.5	15.1 ±0.5	22.6 ±0.9
Blue	OVJP	5.4 ±0.6	4.2 ±0.5	9.1 ±0.9	7.2 ±.8
Blue	VTE	6.0 ±0.9	5.5 ±0.9	10.3 ±1.5	9.4 ±1.5
White	OVJP	7.0 ±0.3	4.9 ±0.2	11.9 ±0.5	8.4 ±0.4
White	OVJP	7.1 ±0.3	7.0 ±0.4	12.1 ±0.5	11.9 ±0.7

Table 3-1: Performance of OVJP patterned OLED lighting array. Elements of an OVJP processed array are compared with monochromatic VTE grown controls of the same architecture. FFEQE is forward facing quantum efficiency. FFPE is forward facing power efficiency. TEQE is total EQE and TPE is total power efficiency. Forward facing values of monochromatic sources are measured directly. Total values are calculated assuming a 70% outcoupling enhancement from a luminaire. Performance for neutral white light (upper) and optimal efficiency white light (lower) are also calculated. (From Arnold, *et al.*)[72]

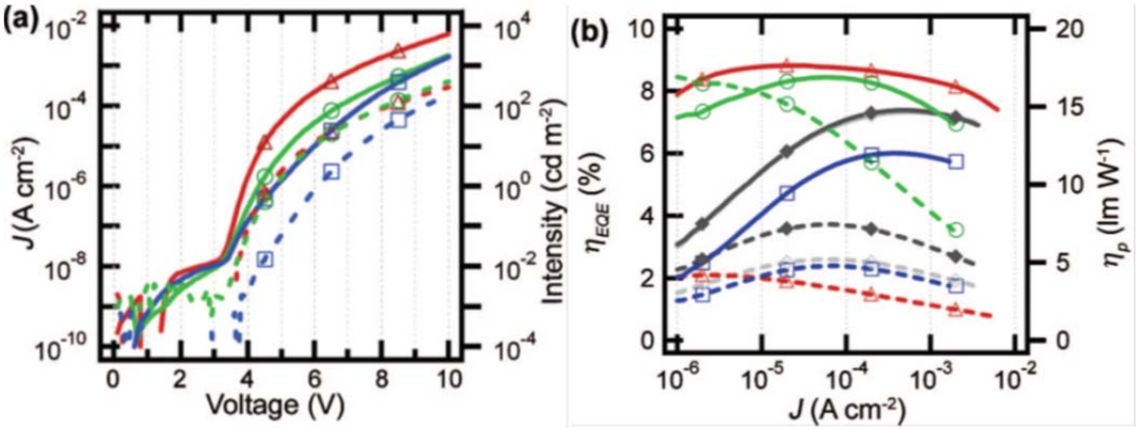

Figure 3-8: Performance characterization of OVJP processed tricolor devices. Monochromatic sources are shown in their respective colors. The left graph shows device current density (solid) and light intensity (dashed) as a function of applied voltage for each monochromatic source. Measured external quantum efficiency (solid) and power efficiency (dashed) are shown at right. Estimated efficiencies for a tricolor device producing neutral white light are also shown in light gray. Efficiency for white light with a color rendering index of 80 is shown in dark gray. (From Arnold, *et al.*)[72]

A plot of current density j and light intensity as functions of voltage V, shown in **Fig 3-8a,** reveals that turn on voltages for all devices were all approximately 3.5 V, comparable to VTE grown devices.[72] When η_p and EQE are plotted with respect to j, **Fig 3-b**, peak values comparable to VTE are observed. A tendency towards efficiency roll-off for j> 1mA/cm^2 is observed and will be further discussed in Chapter 9.

The performance of OVJP processed devices strongly depends on the substrate temperature during growth. Optimal substrate temperature was found to be 30°C for red and green devices, and 5°C for blue devices.[72] Devices grown above these temperatures were prone to crystallization and had poor quantum efficiencies. Devices grown at lower substrate temperatures tended to have high turn on voltages, low η_p, and poor lifetimes. This will be further discussed in Chapter 11.

3.6 Lessons Learned

This first experience with co-deposition and multiple colors using OVJP provided valuable experience upon which to improve the process. As described in Chapter 3.2, and illustrated in **Fig. 3-2d**, the organic material sources were physically separated from the deposition zone by 2 m of tubing. This entire runline had to be heated to a temperature approximately 30°C greater than the sublimation temperature of the least volatile component to reduce interaction between organic vapor and the walls. Heaters and gaskets required frequent replacement due to thermal cycling, and maintenance was complicated by the complex, interconnected, and irregular forms of the runline components, as shown in **Fig 3-2b**. High temperature valves also proved unreliable. Sealing was difficult. Chamber base pressure was limited to 50 mTorr, while the later version of the OVJP system described in Ch. 7-10 was able to achieve a base pressure an order of magnitude lower using the same pump.

The interaction between organic vapor and tube walls took two related forms. In the more extreme case, "cold spots" cause organic material to condense in regions of tubing cooler than its sublimation temperature. Cold spots could delay the onset of deposition for an hour or more, or prevent it entirely. Furthermore, since un-evaporated material remained in the runline after a deposition, it had the potential to contaminate subsequent depositions. Cold spots were observed in the bodies of pneumatically actuated valves and in junctions between adjacent heated zones. Pneumatic valves proved especially problematic, since their bodies required mechanical linkages to water cooled actuators. Supplemental heating of the valve bodies combined with a redesigned linkage remedied this.

The second kind of interaction proved both more common and more intractable. Organic vapor reversibly adsorbed onto the stainless steel walls of the runline at temperatures greater than its sublimation temperature. The rate of migration of organic material through the runline was found to increase with increasing runline temperature but was significantly slower than the rate of carrier gas flow in all cases. This behavior suggests that a thin layer of organic material must adsorb to the inner surface of the runline before it can "break through" and deposit on the substrate. This is analogous to behavior observed in a gas chromatography column as the media inside saturates. Increasing temperature changes the sorption isotherm to favor vaporized over adsorbed organic, reducing the amount of organic material required to saturate the column.[89] Since less organic material is required to saturate the column, the onset of deposition occurs more quickly. For example, there was a 500 s lag between opening the CBP source valve and the onset of deposition if the runline was heated to 325°C. This lag was reduced to 300 s if the runline was heated to 350°C. The sublimation temperature of CBP is approximately 250°C and the residence time of carrier gas in the runline is at only 0.6 s at a flow rate of 10 sccm. In both cases, CBP clearly interacts with the runline despite being heated to well above its evaporation temperature.

Attempts to replace the single 1 mm dia nozzle with an array of ten 100 μm or 30 μm straight walled nozzles cut into a stainless steel tube with 200 μm wall thickness, **Fig. 3-9**, led to considerable difficulty. It was found that at carrier gas flow rates of ~1 sccm, pressure in organic material sources quickly built up to atmospheric pressure and beyond.

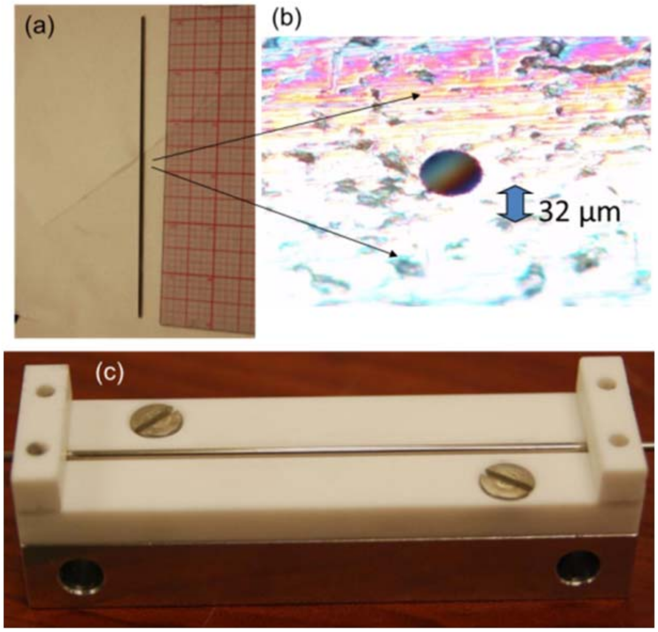

Figure 3-9: Nozzle array micromachined from a steel capillary. (a) A stainless steel tube carried organic vapor and carrier gas to (b) 30 μm micro-machined holes in its wall. This early nozzle array was affixed to the chamber by (c) a mica holder, and was resistively heated by current flowing along its length.

High pressure hindered the rate of organic material sublimation. Smaller flow rates also proved impractical, since difficulty sealing the runline leads to a considerable (~ 0.1 sccm) baseline leak rate. A process gas flow rate much higher than the leak rate is necessary to dilute and flush away contaminants. Severely degraded material is deposited when the carrier gas flow rate and leak rate are of comparable magnitude.

The 1 mm nozzle OVJP tool provided valuable lessons which pointed the way to a future design. The heated runline must be kept as short and mechanically simple as possible. It should incorporate no moving parts or metal gaskets. It should have minimal internal volume and surface area. Individual colors should each have a dedicated flow channel to eliminate the time consuming process of flushing the runline during multicolor depositions. There should also be a provision for storing organic material sources at low temperature when not in use to prevent degradation.

Impedance to flow must also be minimized, even for high resolution printing requiring very small nozzle apertures. As will be shown in Ch. 5-7, this can be achieved through nozzle microfabrication. Most importantly, OVJP must incorporate a multi-nozzle architecture in order to be expandable from laboratory to fabrication scale in a relatively straightforward manner. Photolithographic microfabrication facilitates the high degree of parallelism required.

3.7 Summary

Organic vapor jet printing was used to successfully fabricate an array of red, green, and blue phosphorescent OLEDs for use in white lighting applications. Each of the single color component devices in the array had quantum and power efficiencies comparable to conventionally processed, unpatterned devices of the same architecture. Efficient doped PHOLEDs with multilayer architectures can be grown with OVJP, demonstrating that it shares this key attribute of other PVD techniques. A full color PHOLED array capable of producing white light with a CRI of 80 at η_p=11.9 lm/W was fabricated using OVJP.

Unlike other PVD techniques, OVJP is also capable of directly printing a multicolor array of discrete monochromatic emitters without using shadow masks. A full color array of devices 1 mm in width can be printed on 2.5 mm centers without apparent cross-contamination. While this is adequate for lighting fabrication, higher resolution is desirable for displays. As will be demonstrated in later chapters, the size and spacing of printed features can be reduced by reducing the size of the nozzle aperture. Experience using OVJP for lighting fabrication informs how to best achieve this.

Chapter 4

Modeling Macroscopic Gas Flows

4.1 Overview

The observables in the OVJP process described in Ch. 3 were all either process conditions or the characteristics of finished printed substrates. Since deposition takes place under vacuum in a confined space near components at high temperatures, it is difficult to characterize deposition *in situ*. Modeling of the gas jet provides insight into the physical processes governing deposition. This, in turn allows operating conditions to be better related to the observed features on printed substrates.

Flow can be modeled in the continuum regime in a system with a ~1 mm characteristic length and a characteristic pressure of 1 Torr, but few simplifying assumptions can be made. Nonlinear equations for momentum and energy transport must be solved simultaneously using computational fluid dynamics (CFD) software. The equations governing the flow of the carrier gas jet and the transport of organic material through the jet are developed in this section. The results of this modeling study are then discussed. The doping uniformity tolerances that can be expected from the OVJP process, as well as the effect of deposition chamber pressure on the jet shape, are modeled.

4.2 Generalized Continuum Flow Equations

Mass is conserved in a non-reacting steady state fluid flow, therefore the fluid obeys the continuity equation, eq. 4.1, where $\vec{q}$ is carrier gas flux. This can expressed in terms of flow velocity as $\vec{q} = \rho\vec{v}$, where ρ is fluid density and $\vec{v}$ is flow velocity. A fluid element must also obey conservation of momentum, eq. 4.2. The time change in the momentum, $\vec{p}$, of a fluid element is equal to the sum of the normal forces, $\vec{F}_N$, and shear forces, $\vec{F}_S$, on its boundaries.

$$\frac{\partial\rho}{\partial t} + \nabla\cdot\vec{q} = 0 \tag{4.1}$$

$$\frac{d\vec{p}}{dt} = \vec{F}_N + \vec{F}_S \tag{4.2}$$

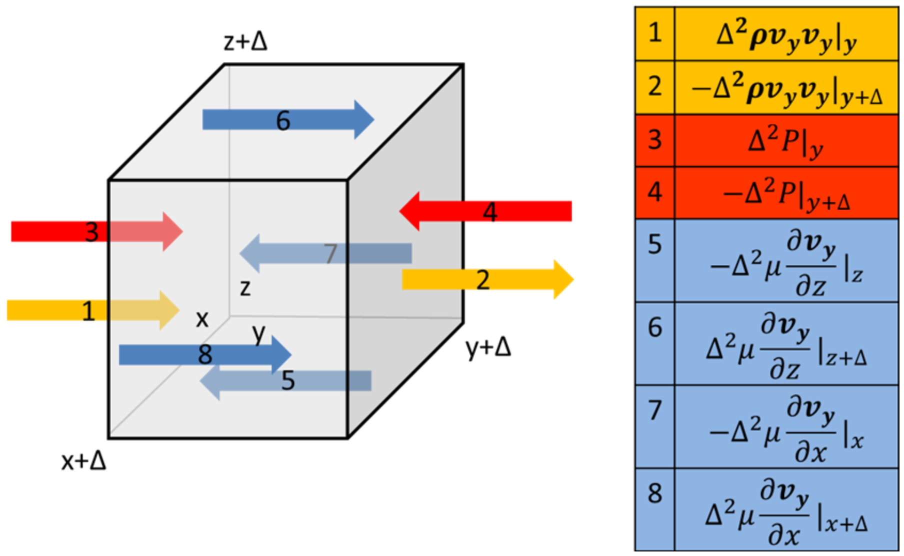

1	$\Delta^2 \boldsymbol{\rho v_y v_y}\vert_y$
2	$-\Delta^2 \boldsymbol{\rho v_y v_y}\vert_{y+\Delta}$
3	$\Delta^2 P\vert_y$
4	$-\Delta^2 P\vert_{y+\Delta}$
5	$-\Delta^2\mu\frac{\partial \boldsymbol{v_y}}{\partial z}\vert_z$
6	$\Delta^2\mu\frac{\partial \boldsymbol{v_y}}{\partial z}\vert_{z+\Delta}$
7	$-\Delta^2\mu\frac{\partial \boldsymbol{v_y}}{\partial x}\vert_x$
8	$\Delta^2\mu\frac{\partial \boldsymbol{v_y}}{\partial x}\vert_{x+\Delta}$

Figure 4-1: Momentum balance on a fluid element in steady state. Momentum in the *y* direction is considered here, but *x* and *z* can be treated identically. Flux of momentum in and out of the element (yellow) is balanced by normal forces from pressure (red) and shear forces from viscous dissipation (blue).

The left hand side of eq. 4.2 can be broken down into two components for a cubic fluid element with side length Δ. The first gives acceleration of fluid at that point, and the second component accounts for momentum fluxes through that point. This is referred to as convective acceleration.

$$\frac{d\vec{p}}{dt} = \Delta^3 \frac{\partial}{\partial t}(\rho\vec{v}) + \Delta^2\left(\rho\vec{v}_x^2|_x^{x+\Delta}\hat{x} + \rho\vec{v}_y^2|_y^{y+\Delta}\hat{y} + \rho\vec{v}_z^2|_z^{z+\Delta}\hat{z}\right) \tag{4.3}$$

A conceptual fluid element and the forces acting on it are illustrated in **Fig. 4-1**. Body forces on the fluid element, such as gravity, are negligible in the case of OVJP. Equations 4.4 and 4.5 give F_N and F_S, where P is pressure and μ is dynamic viscosity. Shear forces act on the element according to Newton's law of viscosity. Dividing by $\Delta^3$and applying the Stokes Transport Theorem, eq. 4.3 can be expressed as eq. 4.6.[90] Likewise, eqs. 4.4 and 4.5 can be expressed as eq. 4.7. The shear tensor τ for a Newtonian fluid is given by eq. 4.8, where δ is the identity tensor.[90]

$$F_N = \Delta^2 \textstyle\sum_{u=x,y,z} -P|_u^{u+\Delta}\,\hat{u}. \tag{4.4}$$

$$\begin{aligned}\frac{F_S}{\Delta^2} = \mu\frac{\partial v_x}{dy}|_y^{y+\Delta}\hat{x} + \mu\frac{\partial v_x}{dz}|_z^{z+\Delta}\hat{x} + \mu\frac{\partial v_y}{dx}|_x^{x+\Delta}\hat{y} \\ +\mu\frac{\partial v_y}{dz}|_z^{z+\Delta}\hat{y} + \mu\frac{\partial v_z}{dx}|_x^{x+\Delta}\hat{z} + \mu\frac{\partial v_z}{dy}|_y^{y+\Delta}\hat{z}\end{aligned} \tag{4.5}$$

$$\frac{1}{\Delta^3}\frac{d\vec{p}}{dt} = \vec{v}\left(\frac{\partial\rho}{\partial t} + \nabla\cdot(\rho\vec{v})\right) + \rho\left(\frac{\partial\vec{v}}{\partial t} + \vec{v}\cdot\nabla\vec{v}\right) \tag{4.6}$$

$$\frac{1}{\Delta^3}(F_N + F_S) = -\nabla P + \nabla\cdot\tau \tag{4.7}$$

$$\tau = \mu\left(\nabla\vec{\mathrm{v}} + \nabla\vec{\mathrm{v}}^T - \frac{2}{3}(\nabla\cdot v)\delta\right) \tag{4.8}$$

Combining eq. 4.6 with 4.8 and applying eq. 4.1, the most general form of the momentum balance in differential form, eq. 4.9 is obtained. Viscosity is independent of pressure, so it is constant in an isothermal flow and eq. 4.9 can be simplified to eq. 4.10. In the case of an incompressible fluid, this can be further simplified to the well-known Navier-Stokes equation, eq. 4.11.[90]

$$\rho\left(\frac{\partial\vec{v}}{\partial t}+\vec{v}\cdot\nabla\vec{v}\right)+\nabla P=\nabla\cdot\tau \qquad (4.9)$$

$$\rho\left(\frac{\partial\vec{v}}{\partial t}+\vec{v}\cdot\nabla\vec{v}\right)+\nabla P=\mu\nabla^2\vec{v}-\mu\nabla(\nabla\cdot\vec{v}) \qquad (4.10)$$

$$\rho\left(\frac{\partial\vec{v}}{\partial t}+\vec{v}\cdot\nabla\vec{v}\right)+\nabla P=\mu\nabla^2\vec{v} \qquad (4.11)$$

4.3 Coupled Heat and Momentum Transport with Diffusion

The momentum balance can often be simplified based on consideration of the Reynolds number, eq. 4.12. The characteristic length of the volume is h, and u is the characteristic velocity. The Reynolds number determines the ratio of convective acceleration to viscous acceleration. When the Reynolds number is much greater than unity, the viscous acceleration term can be set to zero. When it is much smaller than unity, convective acceleration can be neglected.

$$Re=\frac{\rho u h}{\mu} \qquad (4.12)$$

For typical flow of 10 sccm of N_2 carrier gas heated to 350°C through an OVJP nozzle where diameter h =1 mm, ρ =8x10^{-3} kg/m^3, μ = 3x10^{-5} kg/s*m, and u = 100 m/s,[72] Re =26, so the non-linear terms on the left of eq. 4.9 must be considered. Due to the large variation in pressure across the nozzle and the large temperature gradient between the nozzle and substrate, neither the assumptions of constant viscosity nor density are warranted. The momentum balance must stay in its general form, eq. 4.9. The flow field must be solved using a CFD package such as Fluent®, (ANSYS, Canonsburg, PA) that is capable of considering compressibility of flowing gases.

Organic material is assumed to be dilute in the carrier gas. The flow of carrier gas affects the motion of organic material due to convection. Organic vapor, however, neither affects the flow of carrier gas nor its transport properties. Transport properties of the carrier gas are computed from kinetic theory, assuming an ideal gas equation of state and a hard sphere model with particles of diameter d =3.55 Å. Molecular mass m =0.028/N_A kg, where N_A =6.02 x10^{23}, approximating N_2. Viscosity is given by eq. 4.13 where R is the ideal gas constant and T is the gas temperature.[91]

$$\mu = \frac{5m}{16d^2}\sqrt[2]{\frac{RT}{\pi}} \tag{4.13}$$

Due to the large temperature gradient between the nozzle tube and substrate, the viscosity is calculated for each cell of the model using eq. 4.13. Heat flux in the flow field must also be considered. The thermal conductivity of an ideal gas is $K = \frac{15}{4}R\mu$.[92] Flow of heat through an ideal gas in steady state is given by eq. 4.14.[90] The left hand term represents convective heat transfer while the first term on the right side treats conductive heat transport. The derivation of eq. 4.14 parallels that of the momentum balance in Ch. 4.2; with the transported quantity being scalar energy. Because flow is compressible and transonic, two additional terms, a sink and source of thermal energy within a fluid element, must be considered. The middle term on the right side accounts for energy lost as mechanical work done by the fluid element as it expands. The final term addresses heating due to viscous dissipation, where Φ is a dissipation function dependent on the strain tensor of the flow.[90] Eq. 4.14 must be solved simultaneously with eq. 4.9, since the flow field is affected by T both through the value of μ and through ρ, assuming an ideal gas equation of state, $\rho = mP/(RT)$.

$$\rho \hat{C}_p \vec{v} \cdot \nabla T = \mathrm{K}\nabla^2 T + \vec{v} \cdot \nabla P + \mu\Phi \tag{4.14}$$

Transport of organic vapor through the carrier gas is governed by the convection-diffusion equation, eq. 4.15.[90] Fluent® solves eq. 4.15 using the velocity field it calculates from coupled eq. 4.9 and 4.14. The binary diffusivity of organic material is given by eq. 4.16 where reduced mass $m_r = \frac{m_1 m_2}{m_1 + m_2}$ and collision cross section $\sigma = \pi\left(\frac{d_1+d_2}{2}\right)^2$.[93] Representative values of molecular mass m_2 =0.5 kg/N_A and molecular diameter d_2 =1 nm are assumed for the organic vapor, while m_1 and d_1 are the molecular mass and diameter of N_2. Diffusivity was calculated from eq. 4.16 for each cell of the Fluent® simulation by a user defined script.

$$\frac{\partial c}{\partial t} + \vec{v} \cdot \nabla c = D\nabla^2 c. \tag{4.15}$$

$$D = \frac{3kT}{16\sigma P}\sqrt{\frac{2\pi kT}{m_r}} \tag{4.16}$$

4.4 Simulation of an Organic Vapor Jet

Flow was modeled under conditions of a far field pressure of 150 mTorr, with an inlet pressure of 3 Torr chosen to produce a flow rate of 10 sccm through the 1 mm inner diameter nozzle. The nozzle was 300°C and the substrate was 0 °C. The simulation volume was cylindrically symmetric and 5 mm in radius to minimize edge effects on the simulated nozzle flow.

The flow of carrier gas is accelerated by expansion as it leaves the nozzle tip. The central portion of the jet achieves sonic velocity, as seen in **Fig. 4-2a**, due to the large pressure ratio (>2) between gas within the nozzle and the chamber. Supersonic flow cannot be achieved without a diverging nozzle to shape the expanding jet. The straight walled nozzle abruptly terminates, allowing an uncontrolled expansion of the choked

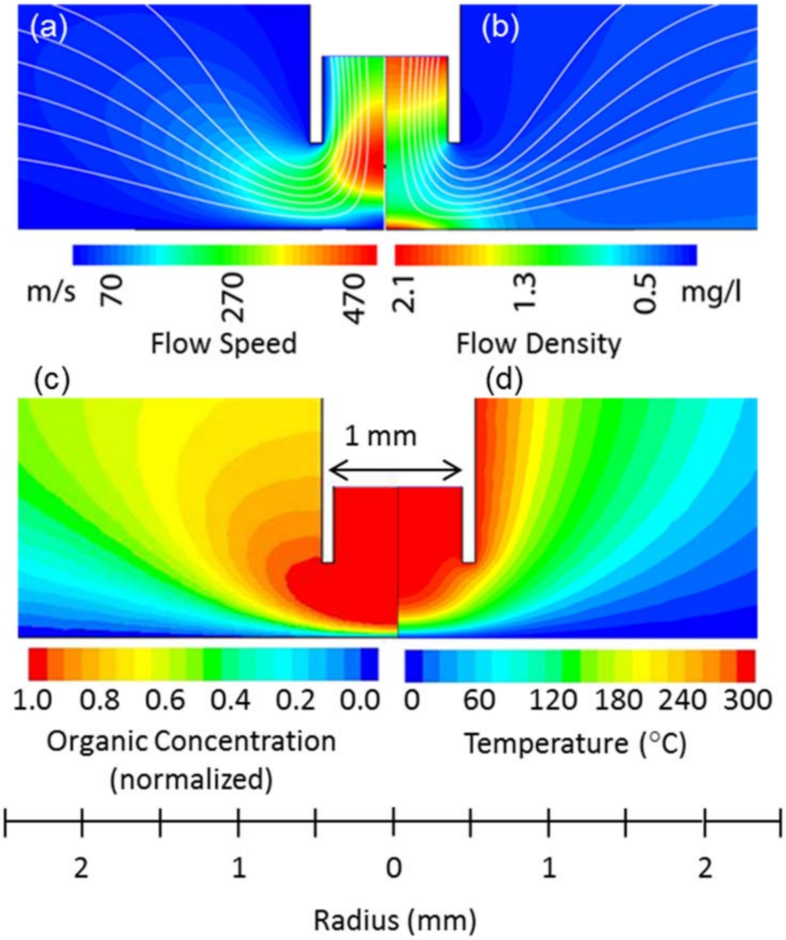

Figure 4-2: Modeled flow field for OVJP deposition. A 1 mm diameter nozzle 700 µm above a substrate was modeled in cylindrical coordinates using Fluent®. Due to symmetry, the two sides of each plot are used to show a different field. (a) Flow speed, (b) fluid density, (c) normalized organic vapor concentration and (d) fluid temperature are plotted. Streamlines on the upper plots show flow direction.

flow of gas at its tip. Due to the choked flow condition, the mass flow rate through the nozzle can be increased by raising the pressure within the nozzle to increase the density of the jet; however the velocity of the jet will not increase.[94] The abrupt change in carrier gas density past the nozzle tip, indicating expansion, is clear in **Fig. 4-2b.** Due to this expansion, flow following the outer streamlines has relatively large radial velocity outward. Organic material is convectively carried away from the centerline, leading to broadened features. The outermost streamlines of flow have positive axial velocity and do not bring the organic material they carry into contact with the substrate. A plume of organic material rising vertically from the nozzle tip is clearly apparent in **Fig 4-2c.**

Due to a combination of the rapid vertical deceleration imposed on the jet by the substrate and cooling of the carrier gas, as shown in temperature profile **Fig 4-2d**, there is a region of high density carrier gas immediately above the substrate and below the nozzle. This has the effect of slowing diffusive transport of organic vapor from the carrier gas to the substrate, thereby increasing convective broadening.

Organic material is ejected from the nozzle with substantial downward velocity, on the order of 300 m/s. This is significantly higher than the thermal velocity of molecules impinging on a substrate during vacuum thermal evaporation. For comparison, CBP sublimed at 250°C travels at 66 m/s. It was initially thought that this difference may lead to morphological changes in deposited films. A more detailed analysis reveals that this is not the case. Organic vapor is expected to thermalize with cooled carrier gas in the previously noted dense region underneath the nozzle in **Fig. 4-2b**. Since relaxation is mediated by molecular collisions, the relaxation length for hyperthermal organic molecules will be comparable to their mean free path in the carrier gas. The mean free path of an organic molecule is given by eq. 4.17.[92]

$$\lambda_o = \frac{1}{n\sigma}\sqrt{\frac{3\pi m_1}{8(m_1+m_2)}} \tag{4.17}$$

Assuming ρ =2 mg/l and T =300K, as indicated in **Fig. 4.2**, the mean free path of an organic molecule is 4.3 µm. Organic molecules may require multiple collisions with carrier gas molecules to thermalize, therefore the relaxation length is of order 10 µm. This is still significantly shorter than the flight path of organic material through the zone of high density, which is approximately 200µm. While energy can be stored as rotational and vibrational motion within organic molecules, this normally does not significantly impede relaxation.[92] This is consistent with a lack of observed differences between OVJP and VTE grown films of OLED materials studied by atomic force microscopy, scanning electron microscopy, and x-ray diffraction. It is also consistent with the experiences of Groves, *et al.* who noticed no differences in film morphology between copper films deposited by conventional e-beam evaporation and films grown from copper vapor entrained in a fast moving jet of carrier gas by the process of Directed Vapor Deposition.[95]

The Fluent® model was used to compute the flux of organic material onto the substrate as a function of radius from the nozzle centerline. This was used to generate simulated deposition profiles. The full width at half maximum (FWHM) of features scaled roughly as 1.3*g* where *g* is the nozzle-to-substrate distance.[72] This translates to a feature size of slightly over 1 mm in the actual tool, which is consistent with observations. It should be noted that the thickness cross section of a printed line and radial deposition rate map are not equivalent. The thickness of a printed line at distance *r* from its center is proportional to a path integral over the radial deposition map along the chord parallel to the direction of nozzle motion set distance *r* from its center.

The shape of deposition profiles predicted by Fluent® is largely independent of the diffusion coefficient of organic material in the carrier gas. This implies that organic material is brought to the surface primarily by convection from the jet, rather than by diffusion between streamlines. The Péclet number (*Pe =uh/D*) for the jet,[93] which gives the ratio of convective to diffusive transport, is 50. Convection dominated mass transport is preferable when depositing a doped film. Host and dopant materials may have different diffusivities that could create local variations in the doping ratio from the centerline to the edge of a printed line. To verify even doping, a pre-factor of 5×10^{-5} m^2 $K^{-3/2}$ Pa/ s was calculated for diffusivity of the common organic host material, CBP. This was used with eq. 4.16 to calculate diffusivity of organic vapor for each volume element

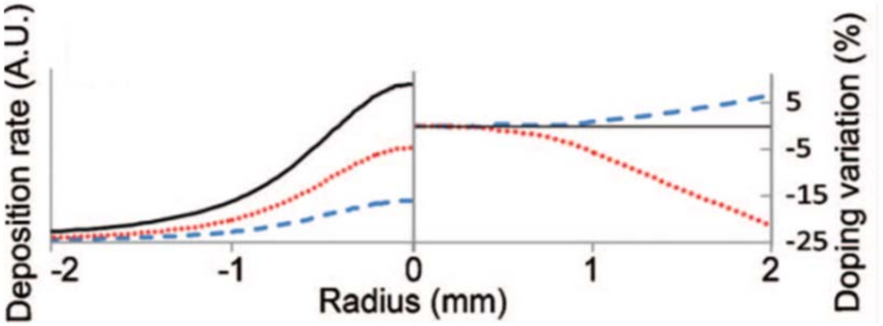

Figure 4-3: Deposition profile and doping ratio for printed features. Normalized simulated feature thickness profiles are plotted as a function of distance from the nozzle centerline for an organic host material (black), and materials with 2x (red) and 0.5x (blue) host diffusivity in N_2 carrier gas. The variation in doping ratio for dopants with 2x and 0.5x host diffusivity is also given as function of radius. (From Arnold *et al.*)[72]

of the Fluent® simulation as a function of pressure and temperature. This pre-factor was then varied by a factor of four to account for variations in the molecular mass and diameter within the set of organic dopant materials likely to be used with OVJP. The shape of the deposition profiles for each of these simulated materials was similar, and is shown in **Fig. 4-3.** They are Gaussians with approximately the same width. The doping ratio is expected to vary by less than 5% over a 1 mm radius if the diffusivity of the dopant material in N_2 is between 50% and 200% of that of CBP.[63]

4.5 Control of Jet Shape

Since not all streamlines exiting the nozzle cast organic material in a downward direction, a portion of material does not land on the substrate and material usage is less than unity. The Fluent® simulation indicates that if the nozzle is positioned 700 μm from the substrate, then 60% of organic material lands within a 2 mm radius its centerline. While optimizing material usage is beneficial, contamination of the substrate and chamber by unused material has proven to be a larger practical problem. Shaped nozzles combined with regulation of chamber pressure is a possible solution, as is an annular guard flow.[67] Universal Display Corporation achieved good results by equipping an OVJP tool with a chilled getter surrounding the nozzle to collect stray organic vapor.

Universal Display Corporation's growth laboratory is equipped with an OVJP tool similar to the one depicted in **Fig. 3-1**. This tool is equipped with a quartz crystal monitor that allows real time measurement of the deposition rate. The deposition rate measured by the monitor increased by a factor of two as chamber pressure was raised from 0.01 Torr to 0.2 Torr. The shape of the vapor jet under these conditions was

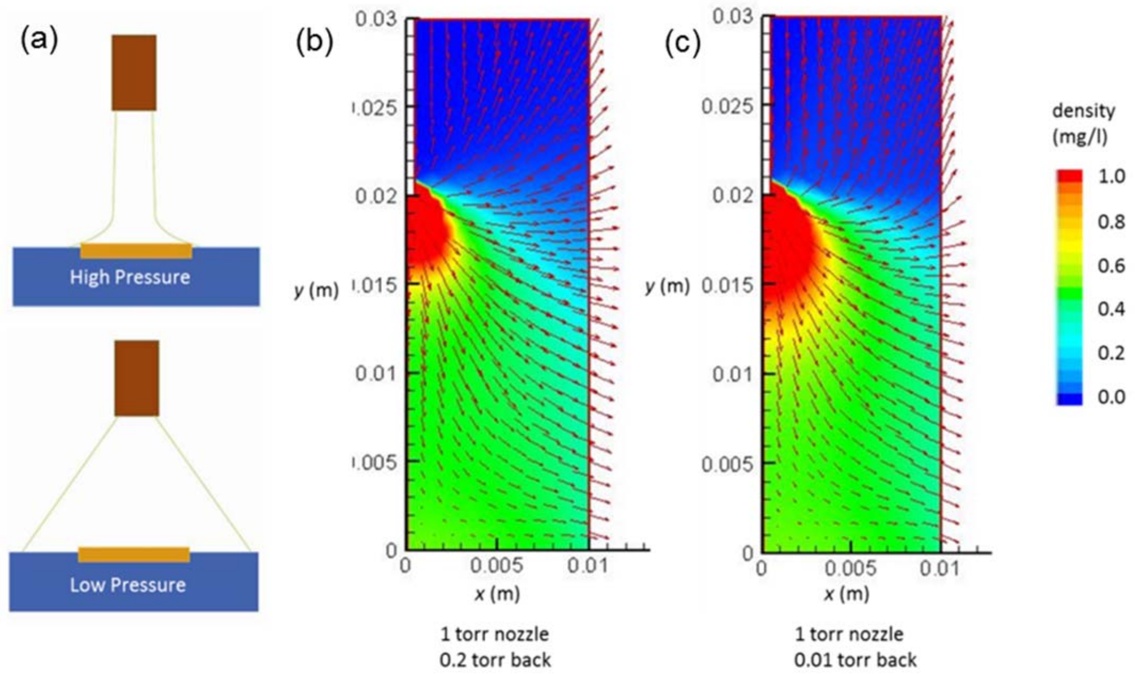

Figure 4-4: Expansion of the jet for varying ambient pressure. (a) High background pressure in the deposition chamber serves to restrict expansion of the jet. Assuming the same amount of material is ejected from the nozzle, more material will land on a centerline target in the high pressure case than the low pressure case. The jet expands and becomes more diffuse when the background pressure is low. This is supported by experimental studies using a quartz crystal deposition rate monitor. (b) and (c) Density and velocity plots are caluclated by MONACO for a nozzzle to substrate gap g = 20 mm. A higher background pressure of 200 mTorr results in a more confined jet than 10 mTorr.

modeled using MONACO Direct Simulation Monte Carlo code as shown in **Fig. 4-4**. The jet is more confined and collimated at higher chamber pressure, producing a more focused region of deposition over the detector. At lower chamber pressure, the jet expands more, so the amount of material falling on a sensor of the same area is reduced. A similar effect is encountered in the design of multi-stage rockets, in which rocket nozzles must be optimized to produce a collimated stream of exhaust over a specific range of ambient pressures.[96]

4.6 Summary

A full CFD treatment was required to model the millimeter scale OVJP system. The equation of motion of the carrier gas must account for a compressible flow undergoing significant viscous and convective accelerations. This equation was coupled to an energy balance that accounted for the large temperature differential between the nozzle and substrate. The motion of organic material was calculated by solving the convection-diffusion equation over the carrier gas flow field solution.

A feature size of approximately 1 mm is predicted for the system described in Ch. 3, which is consistent with experimental observation. Organic material must pass through a relatively dense zone of stagnant carrier gas directly underneath the nozzle to deposit on the substrate. The organic material is therefore thermalized before it reaches the substrate. The doping ratio was found to be consistent over the width of the printed features. Material utilization is non-unity, since some organic material is ejected away from the substrate by the expansion of carrier gas through the straight nozzle tip. The expansion of the gas jet depends on the ambient pressure of the deposition chamber.

The macroscopic system illustrates key aspects of the OVJP process, however the relatively large length scale of the modeled system makes it ill-suited to high resolution printing. A tool for the fabrication of displays must feature nozzles with a much smaller characteristic length. The assumption of continuum flow breaks down at these length scales. The following chapter will discuss the modeling micronozzles.

Chapter 5

Microscopic Gas Flows

5.1 Overview

Microfabrication techniques make it possible to remedy many of the deficiencies noted in Ch. 3.5. Because of its inherent scalability, microfabrication also offers a way to scale up the OVJP process from laboratory to production implementations. Since gas can behave in a counterintuitive manner at small length scales, modeling played a key role in the design of microstructures for fabrication.

Modeling gas flows through features of small characteristic dimension often requires consideration of the particle nature of the gas. A gas can be characterized by the Knudsen number, $Kn = \lambda/h$,[93] which is the ratio of the mean free path of a gas particle λ, given by eq. 4.17, to the characteristic dimension of the feature h. For $Kn < 0.1$, gas particles equilibrate rapidly due to frequent collisions with neighbors. Field properties such as such as density, bulk velocity, temperature, and solute concentration are well defined and change continuously in space. A continuum model provides a good solution in this regime. For $Kn > 10$, a free molecular flow model in which particles follow ballistic trajectories between the boundaries of the system, is appropriate. For intermediate values of Kn between 0.1 and 10, both the ballistic motion of particles and the continuum-like behavior created by collisions between particles in a flow field must be considered.

Microchannels can be used to distribute vapor to an array of micronozzles, thereby minimizing both the distance which organic vapor travels and the volume of its heated runline. This reduces adverse effects such as latency and chemical degradation of organic vapor. The microchannels used for an OVJP print head are 1 mm wide by 100 μm deep. They have *Kn* ~0.1 and can be modeled as a one-dimensional system in the continuum regime as described in Ch. 5.2.

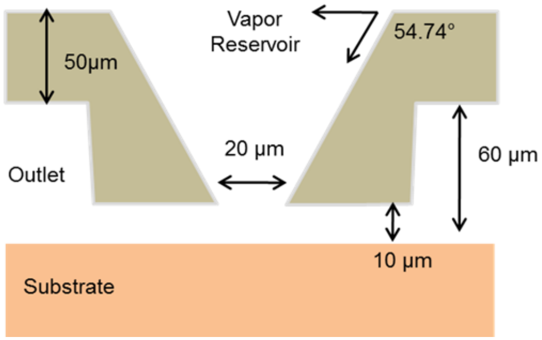

Figure 5-1: Cross-sectional diagram of a typical micronozzle. The nozzle is 200 μm long in the direction of the page.

Arrays of microfabricated nozzles are designed so that flow restriction is minimized for a given aperture size. Micronozzles are fabricated from a silicon membrane. They have a relatively wide inlet of 130 x 320 μm that tapers to an outlet aperture of 20x200 μm on the underside of the membrane. A typical nozzle is shown in in **Fig. 5-1**. The aperture is less than a micron thick at its narrowest point, shaping a confined jet while adding minimal flow resistance. The long dimension of the nozzle aperture is parallel to the direction of line printing. This increases the area of substrate that is under a depositing nozzle aperture at a given time and therefore increases printing speed while maintaining a small feature size. Nozzles are separated by a narrow gap from a chilled substrate onto which they deposit organic material. Due to the short length scale and low pressure of these nozzles, *Kn* near unity is often encountered, and it becomes necessary to model a transition flow. Methods for achieving this are discussed in Ch. 5.3 and 5.4. Flow conductivity, heat transport, and deposition performance can be calculated by modeling the micronozzles in two dimensional cross sections perpendicular to their long dimension. Specific simulated micronozzle geometries and process parameters affecting their performance are discussed in Ch. 5.5.

5.2 Compressible Unidirectional Flow in the Continuum Limit

Flow within the channels used to feed vapor to the nozzle array can modeled in the continuum limit. The microchannel based system has a characteristic dimension h =100 μm. Under typical operating conditions of 600K and 30 Torr, the mean free path of carrier gas is λ =10 μm. Therefore, *Kn* =0.1. To solve this channel flow, it is acceptable to assume a steady state flow in which all motion is in the x direction. Let v be the velocity in the x direction. Further assume that the pressure gradient is parallel to the direction of gas flow. Equation 4.10 can be used as a starting point with the assumptions of steady state, $v_x = v$, and $v_y = v_z = 0$ to yield eq. 5.1. Typical values of these terms for OVJP process gas are $\rho = 8\text{x}10^{-3}$ kg/m^3, $\mu = 3\text{x}10^{-5}$ kg/s*m, u = 30 m/s and $h = 10^{-3}$ to 10^{-4} m. The Reynolds number for this flow is from 8 to 0.8, so neither viscous nor convective acceleration terms can be discarded *a priori*.

$$\rho v \frac{\partial v}{\partial x} + \frac{\partial}{\partial x} P = \mu \left(\frac{\partial^2 v}{\partial y^2} + \frac{\partial^2 v}{\partial z^2} \right) \tag{5.1}$$

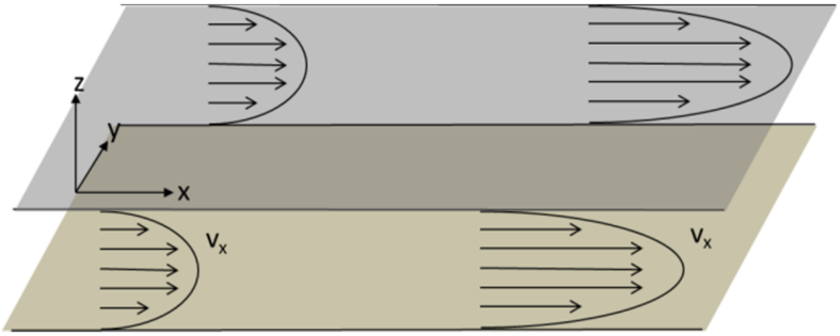

Figure 5-2: Unidirectional compressible flow between parallel plates. Gas velocity follows a parabolic profile with respect to channel height, however the gas accelerates as it rarifies near the low pressure end of the plates.

If the *z* cross sectional dimension of the channel is assumed to be much smaller than the *y* dimension, the channel can be assumed to be infinite in the *y* direction. The continuity equation, 4.1, can be rewritten as eq. 5.2. Furthermore, if an ideal gas equation of state is assumed, $\rho = mP/(RT)$ where *m* is molar mass of N_2, *R* is the ideal gas constant, and *T* is gas temperature of 300°C, eq. 5.1 yields eq. 5.3. The variable term in the bracket is far less than unity for typical operating conditions, and it can be ignored to good approximation. The remaining terms give a simple Poiseuille flow. The solution is fit to a no slip boundary condition at walls *z* =0 and *z* =*h*, given by eq. 5.4.

$$v \frac{\partial \rho}{\partial x} = -\rho \frac{\partial v}{\partial x} \tag{5.2}$$

$$\left(1 - \frac{m}{RT} v^2\right) \frac{dP}{dx} = \mu \frac{\partial^2 v}{\partial z^2} \tag{5.3}$$

$$v = \frac{1}{2\mu}\frac{\partial P}{\partial x} z(h - z) \tag{5.4}$$

Average gas flow velocity across the channel cross section is given by eq. 5.5, and eq. 5.6 gives the gas molar flow rate, *Q*. Since *Q* is constant, eq. 5.7 relates pressure and flow for a channel of length *l* and width *w*.

$$\langle v \rangle = \frac{h^2}{12\mu}\frac{\partial P}{\partial x} \tag{5.5}$$

$$Q = \frac{h^3 w}{12\mu}\frac{P}{RT}\frac{\partial P}{\partial x} \tag{5.6}$$

$$Q = \frac{h^3 w}{24\mu l}\left(P(0)^2 - P(l)^2\right) \tag{5.7}$$

Flow rate scaling with the square root of pressure is an exact solution in this regime and remains a good approximation well into the transition regime. This scaling has been experimentally observed for nozzle arrays injecting collimated gas beams into high vacuum chambers.[97]

5.3 Transition Flow

Carrier gas typically has a pressure on the order of 10 Torr as it enters a nozzle inlet. Given a characteristic length of 10 μm for nozzle structures, *Kn* =1. In the transition regime of 0.1 <*Kn* <10, the behavior of molecules is not dominated by either interaction with boundaries or other molecules, so both must be considered. This requires solving the Boltzmann equation, eq. 5.8.[91] The density function, *f*, gives the probability that a particle has a position $\vec{r}$ and a momentum $\vec{p}$. The right hand side of the equation is the collision term. It gives the probability of a particle leaving state *f* due to a collision with another particle with density function *f'*. The frequency of a collision is proportional to n^2, where n is the number of particles per volume.

$$\frac{\partial(nf)}{\partial t} + \frac{\vec{c}}{m} \cdot \nabla(\mathrm{n}f) = \int_{-\infty}^{\infty} \int_{0}^{4\pi} n^2\, \sigma |\vec{c} - \vec{c}'| (f^* f'^* - f f') d\Omega dc' \qquad (5.8)$$

The Direct Simulation Monte Carlo, or DSMC, model for gas flow simulates a solution to eq. 5.8 by tracing the paths of an ensemble of particles that are representative of the groups of particles in the real system.[91] Approximately 10^{11} gas particles are present in and underneath the OVJP micronozzle at a given time, making a particle by particle simulation impractical. Instead, each simulated particle is assumed to represent approximately 10^6 real particles with similar position and momentum. The following section, 5.4, is a summary of the non-time counting DSMC algorithm proposed by Bird in his classic text *Molecular Gas Dynamics*[91] as it was adapted to solve the specific problem of carrier gas mediated organic vapor transport between a micro-nozzle and substrate.[63][64]

5.4 Direct Simulation Monte Carlo Modeling

5.4.1 Overview

Particles are stochastically generated to reflect the boundary conditions of the system. Simulated particles follow ballistic trajectories between interactions with other simulated objects. Possible interactions fall into two categories, collisions with walls and collisions with other particles. Walls act as reflectors, redirecting carrier gas particles back into the simulation volume. Simulated particles collide with other particles in a manner chosen to reflect the likely set of collisions a real particle would experience along its trajectory. Collision partners are generated from other simulated particles.

Collisions with walls and other particles affect the momentum of particles. These interactions change the trajectory of the element of position-momentum phase space occupied by each particle in the ensemble. In turn, this affects the future interactions of these particles. In this sense, DSMC techniques are inherently time dependent. A steady state system is simulated by imposing constant boundary conditions and running the simulation long enough to outlast the transient response created by the imposition of boundary conditions. The simulation converges when the occupancy of each element in phase space converges to a steady state value.

Phase space is coarse-grained, making numerical computation of eq. 5.8 possible. Position is explicitly coarse-grained by grouping particles into spatial cells to gather statistics and choose collision partners. Each simulated particle is representative of many particles with similar momentum, so momentum can be thought of as implicitly coarse-grained with each simulated particle occupying a finite volume of momentum space. The value of density function f at each coordinate in phase space is proportional to the number of simulated particles within a cell with similar velocity.

The algorithm runs through inner and outer cycles. The inner cycle first enforces the boundary conditions, adding particles from a stagnant gas reservoir at the nozzle inlet and removing particles that have left the simulation volume. Each active particle is moved one time step along its ballistic trajectory and collisions with walls are detected and handled. After all particles have been moved, a collision selection algorithm chooses pairs of particles within a cell to collide. After approximately 100 inner cycles are run, an outer cycle updates statistics maintained for each cell. These are used to determine the rate of future collisions within the cell. Field quantities like temperature, pressure, and bulk velocity are computed from ensemble averages in the outer cycle for simulation output. The algorithm follows this pattern, illustrated as a flowchart in **Fig. 5-3**, for

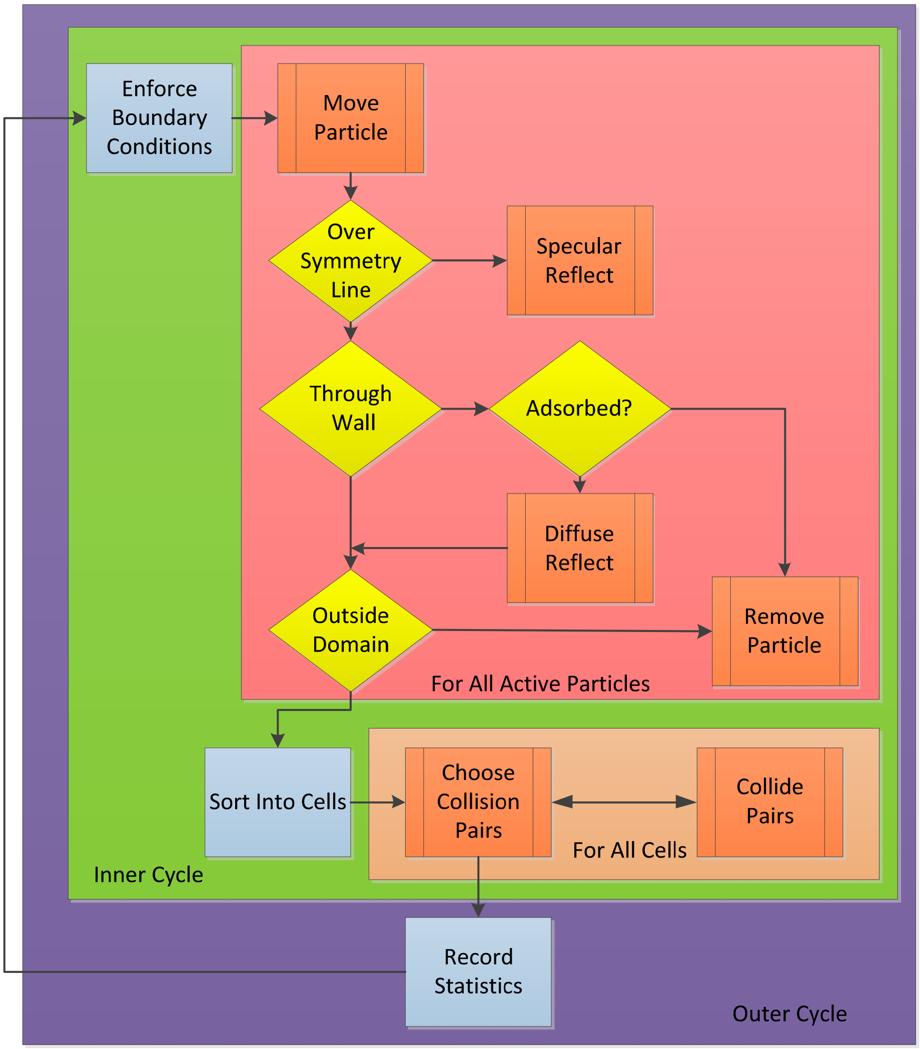

Figure 5-3: Flowchart of the DSMC algorithm.

10,000 or more outer cycles to build up a statistically significant data set of organic tracers adsorbed on the substrate.

5.4.2 Boundary Conditions

Inlet and outlet boundaries are treated as borders with a reservoir of stagnant gas. Particles cross such a boundary randomly along its length. The number of particles introduced per step is determined by the number that would be expected to cross the boundary per time step from a reservoir of given temperature and pressure. The velocity of the particle parallel to the boundary is stochastically chosen to match the Boltzmann distribution. The distribution function for the component of particle velocity normal to the reservoir boundary, c_n, is given by eq. 5.9, where A is a normalization constant. This accounts for the fact that a rapidly moving particle in an equilibrium ensemble will cross the boundary with greater frequency than a slower particle. The algorithm used to establish boundary conditions is discussed in greater detail in Appendix G.

$$f(c_n) = Ac_n exp\left(\frac{-mc_n^2}{2k_BT}\right) \tag{5.9}$$

Particles that cross over the inlet and outlet boundaries from inside the simulated volume are removed. Since more particles are introduced to the higher pressure inlet than the lower pressure outlet, a net flow is produced. Organic molecules are introduced at the inlet boundary in a ratio of 1:1000 with the carrier gas. This ratio was chosen to provide a statistically significant number of organic tracer molecules while not affecting the transport properties of the carrier gas. The actual ratio of organic to carrier gas in the OVJP system is on the order of 1:10^6.[98]

Walls can be treated as either diffuse or specular reflectors. The behavior of real walls can be approximated as a combination of these two limiting cases. A fraction, α, of incident particles reflect diffusely and 1-α of particles reflect specularly. Parameter α is referred to as an accommodation coefficient.[91] Most engineering materials have α close to unity, meaning that the gas molecules they reflect have thermalized with the wall. Materials such as crystalline sapphire, however, can be much lower.[92] For interactions between carrier gas molecules and simulation boundaries, it is assumed α =1. For organic materials, it is also normal to assume α =1. The sticking coefficient for deposited material is related to α, since a particle that thermalizes with a boundary cooler than its sublimation temperature is immobilized. An α of less than unity is used to model overspray, the deposition of small amounts of material beyond the intended dimension of a feature, due to incomplete condensation of organic material in the deposition zone. A study of pentacene deposited on SiO_2 over a range of incident kinetic energies suggests that α for thermalized organic material should be near unity.[99] Deposition onto an existing organic layer further promotes adsorption of organic vapor,[99] since an organic thin film is a soft, van der Waals material that adsorbs energy through inelastic collisions.

A diffusely reflecting wall behaves like a reservoir of stagnant gas at the wall temperature. When a carrier gas particle crosses a wall, its momentum is changed to reflect that of a particle leaving a reservoir with a border coincident to the wall. It is then moved back into the simulation near where it entered the wall. In the case of an organic molecule that thermalizes with a wall below its sublimation temperature, the particle is considered to have adsorbed. Its position is noted and it is removed from the simulation. In the case of a specular reflector, a particle collides elastically with the boundary.

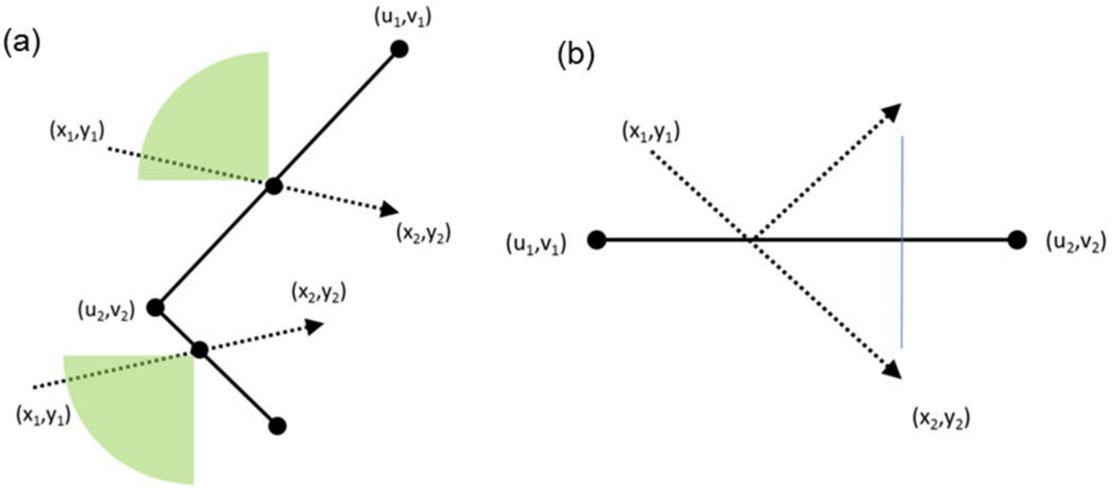

Figure 5-4: Comparison of wall collision types in the DSMC simulation. Walls are vectorized as segments with endpoints (u_n, v_n). A particle collides with a wall when its position (x_n, y_n) crosses a segment during a given time step. (a) Two walls joining to form a corner are depicted for the diffuse reflector. When the particle diffusely reflects off the wall, it is assigned a new velocity that is representative of the wall temperature. Reflected particles have the same velocity distribution as particles entering from a reservoir at wall temperature with a boundary coincident with the wall. The particle is restored to the point it crosses the wall and moves with its new velocity for the remainder of the time step. (b) The case of specular reflection is simpler. The coordinates and velocity vector of the particle are simply reflected over the boundary.

The parallel component of its velocity relative to the boundary does not change and the normal component changes sign. The symmetry line through the nozzle, normal to the substrate is treated as a specular reflecting surface. The difference between a specular and diffuse collision is illustrated in **Fig. 5-4.**

5.4.3 Intermolecular Collisions

Collisions between particles are chosen using the no time-counter (NTC) method for each particle. Rather than comparing collision periods with the time step, the NTC method computes a fixed number of collisions to test for each cell. A maximum collision probability between particles is calculated based on the highest relative velocity between two particles within the cell, $c_{r\ \max}$, using eq. 5.10. This gives the highest possible number of collisions, N_{max}, that can occur between a simulated particle and the F_N real particles occupying positions in phase space nearby to each of the other simulated particles in same cell. The collision cross section, σ, is defined as in eq. 4.16. Molecules are treated as hard spheres of fixed radius.

$$N_{max} = F_N \sigma c_{r\ max} \Delta t / V_C \tag{5.10}$$

When the N_{max} is calculated, it is assumed that all collisions are of the most probable type. Although N_{max} collisions are tested, the actual number of collisions modeled is smaller, since the other possible collisions have lower probabilities. Collision pairs are tested and accepted with a probability equal to the ratio of c_r for the collision pair to the maximum c_r for that cell. The maximum c_r for each cell is stored in memory. The initial value is set to that of the average thermal velocity of particles, but is continuously updated as collision pairs with higher c_r are detected by the simulation during collision tests. A low initial value for maximum c_r is quickly corrected as the simulation converges. An overly high value is computationally wasteful, since the simulation will test many collision pairs, each with a low individual probability of acceptance. Collisions between carrier gas molecules are selected separately from collisions between organic molecules and the carrier gas, since the two collision types have different σ and maximum c_r. Collisions between organic molecules are ignored due to their infrequency.

Collisions within the DSMC simulation change the velocities of a pair of particles from $\overrightarrow{c_1}$ and $\overrightarrow{c_2}$, eq. 5.11, before the collision to $\overrightarrow{c_1 *}$ and $\overrightarrow{c_2 *}$ afterward. It is helpful to transform velocities so that their changes are computed relative to a center of mass velocity $\overrightarrow{c_m}$, eq. 5.12, which is unchanged by the collision. If the collision is assumed elastic and internal molecular degrees of freedom are ignored, the kinetic energy of the particles is preserved. It is necessary to compute the change in relative velocity, eq. 5.13, between the particles, given by u_r, v_r, and w_r before the collision and their starred counterparts thereafter.

$$\overrightarrow{c_1} = \overrightarrow{c_m} + \frac{m_2}{m_1+m_2}\overrightarrow{c_r} \quad \overrightarrow{c_2} = \overrightarrow{c_m} + \frac{m_1}{m_1+m_2}\overrightarrow{c_r} \tag{5.11}$$

$$m_1\overrightarrow{c_1} + m_2\overrightarrow{c_2} = (m_1 + m_2)\overrightarrow{c_m} \tag{5.12}$$

$$\overrightarrow{c_r} = \overrightarrow{c_1} - \overrightarrow{c_2} \tag{5.13}$$

The post collisional velocities of both particles are six unknowns, and conservation of momentum and energy give four constraints, so two more parameters are required to uniquely specify the collision. Since each particle represents many particles with the same momentum in a cell, the exact orientation of the colliding particles is randomly generated. The distance of closest approach between molecular centers, b, is chosen from a randomly generated value obtained from a square root distribution normalized to the collision diameter. In the hard sphere collision model, the deflection angle χ is related to b by eq. 5.14, where d_{12} is the sum of the radii of the collision pair. The angle ε between the reference plane and the post-collision particle trajectories is also randomly assigned. Coordinates b and ε define the point at which the spheres meet upon impact, which in turn determines their post collisional velocities. The coordinate system used in the collision is depicted in **Fig. 5-5**.

After u_r^*, v_r^*, and w_r^* are calculated, eqs. 5.15-17, the transformation to center of mass coordinates can be reversed to find the new velocities, $\overrightarrow{c_1 *}$ and $\overrightarrow{c_2 *}$ of the colliding particles. The positions of both particles are unchanged by the collision. Changes in momentum due to the collision, however, affect the paths of both particles in future iterations.

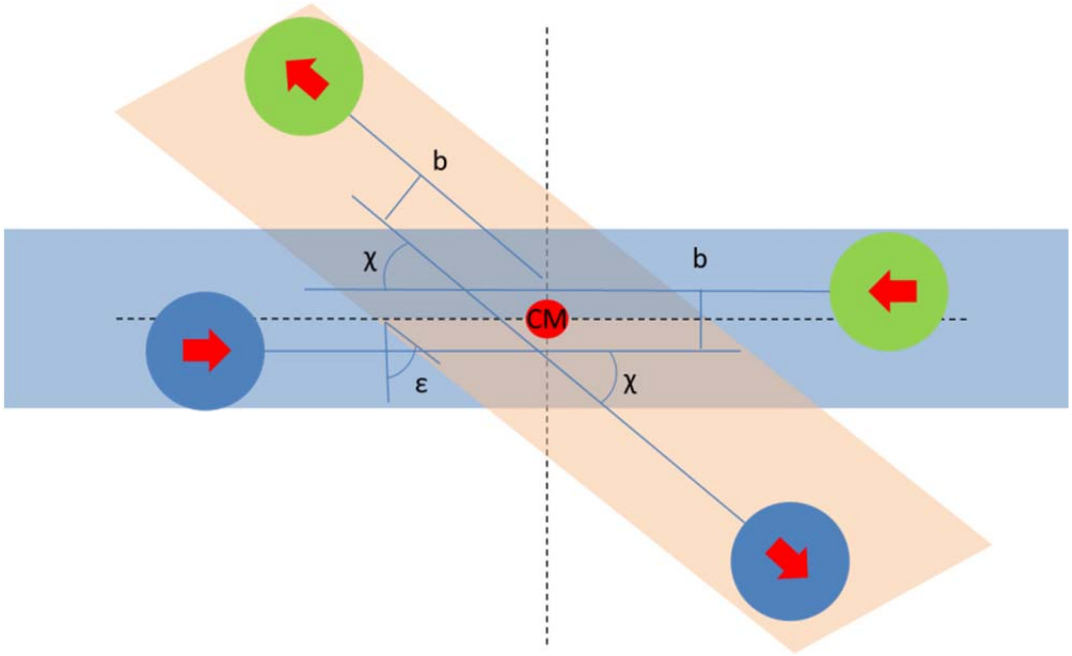

Figure 5-5: Center of mass coordinate system for colliding particles. Particle velocities before the collision are defined by the simulated particles chosen to collide. The closest approach of particle centers b is a randomly chosen variable that defines deflection χ. The angle ε between the reference plane of the simulation and the plane of the collision is also randomly chosen.

$$b = d_{12} cos(\chi/2) \tag{5.14}$$

$$u_r^* = cos(\chi)u_r + \ sin(\chi)sin(\varepsilon)\sqrt{v_r^2 + w_r^2} \tag{5.15}$$

$$v_r^* = cos(\chi)v_r + \ sin(\chi)\big(c_r w_r cos(\varepsilon) - u_r v_r sin(\varepsilon)\big)/\sqrt{v_r^2 + w_r^2} \tag{5.16}$$

$$w_r^* = cos(\chi)w_r - \ sin(\chi)\big(c_r v_r cos(\varepsilon) + u_r w_r sin(\varepsilon)\big)/\sqrt{v_r^2 + w_r^2} \tag{5.17}$$

5.5 Simulated Nozzle Array

The apertures of micronozzles are 200µm along the direction of parallel to the printing direction and much smaller perpendicular to it. Therefore, a nozzle can be approximated as the two dimensional structure by cutting it into cross-sections along its long axis. The cross section for one of the evaluated nozzle geometries, with a converging inlet and straight walled relief trenches, is depicted in the upper left corner of **Fig. 5-6**. The substrate is positioned beneath the nozzle. Key dimensions are the nozzle aperture width *a*, nozzle aperture-to-substrate gap *g*, and gap length *l*. The simulated volume is symmetric about the nozzle centerline, which is modeled as a specular reflector. The body of the nozzle is heated to 600K and the substrate is at 300K.

The simulation volume is split into square cells 2 µm on a side for calculating ensemble statistics and collision selection. A time step of 1x10^{-9} was chosen so that a simulated particle requires several cycles to cross a cell. The ratio of simulated to real particles was chosen so that approximately 80 particles are present in each cell along the inlet boundary. The mean free path of carrier gas particles is of order 10 µm. Under these conditions, there will be 2-3 intermolecular collisions per cell per time step.

5.5.1 Effect Process Parameters on Deposition

Gas does not significantly expand underneath the aperture for small values of *g*, but instead makes a turn at relatively constant speed and accelerates as it enters the relief trench. This is because the gap itself provides greater resistance to flow than the aperture. The carrier gas jet accelerates downward to a greater degree as nozzle to

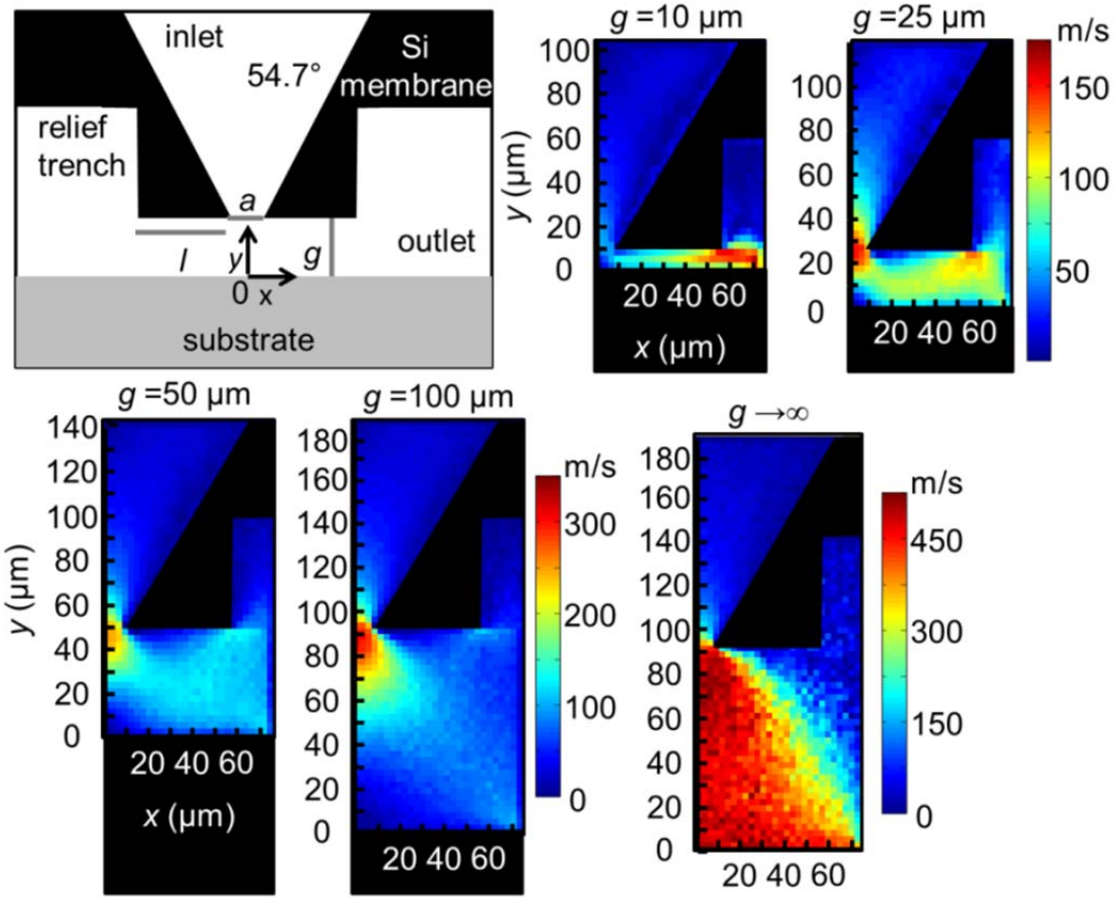

Figure 5-6: Micronozzle flow fields for range of nozzle to substrate separations. The figure on upper left shows the simulated volume of the nozzle (black) and substrate, (gray) system. Key dimensions such as aperture width *a*, nozzle to substrate gap height *g*, and gap length *l* are illustrated. Other images depict velocity profiles for this nozzle for a range of *g*. Flow rate *Q* =0.2 sccm/nozzle.

substrate separation increases. In the limiting case where the substrate is removed, it expands as a jet at sonic velocity, as seen in the modeling of Chapter 3. These trends are illustrated in **Fig. 5-6**.

Simulated feature thickness profiles, **Fig. 5-7**, indicate that the expected thickness cross section of printed features is roughly Gaussian. A full width at half maximum (FWHM) of 18 µm for is expected features printed at g = 10 µm. As g is increased, printed features become larger and more diffuse. The minimum obtainable feature size varies linearly with g, scaling as roughly $w = 1.4g + a$ for a flow rate of $Q = 0.2$ sccm/nozzle where w is the full width at half maximum (FWHM) of the feature thickness

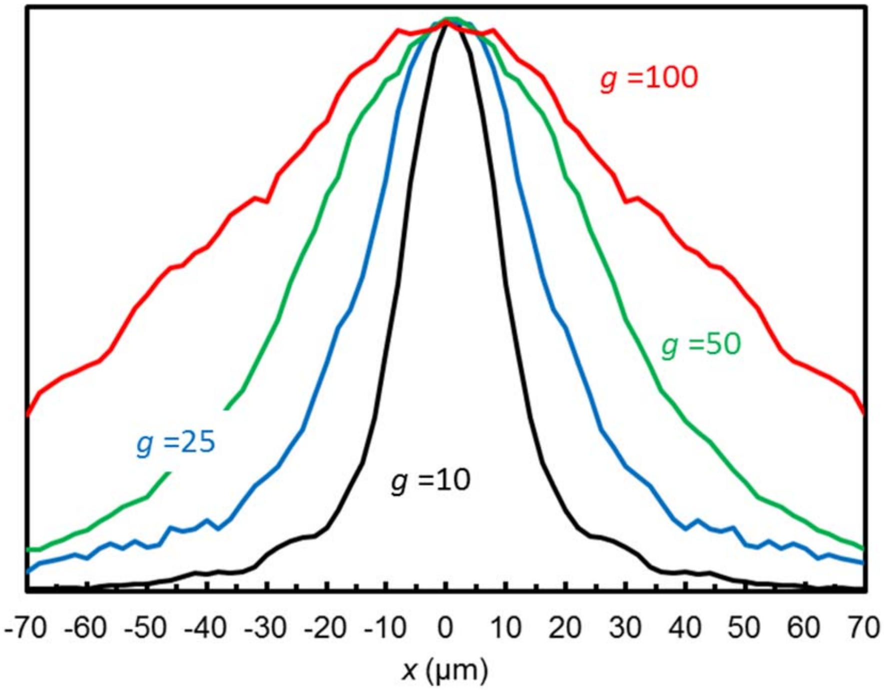

Figure 5-7: Thickness profiles of features for a range of nozzle to substrate separations. Normalized, simulated thickness is plotted as a function of distance x from the nozzle centerline. Plots show nozzle to substrate gaps, g, of 10, 25, 50, and 100 µm. Nozzle flow is Q =0.2 sccm. Nozzle width is 20 µm.

profile.[63] Feature size is independent of carrier gas flow rate for $g > 25$ μm. For $g = 10$ μm, an increase in carrier gas flow rate Q leads to increased feature size,[63] as shown in **Fig. 5-8**. This is due to the faster and denser carrier gas convectively dispersing organic material beyond the desired deposition zone. Both of these trends have been experimentally observed, as will be discussed in Chapter 9.

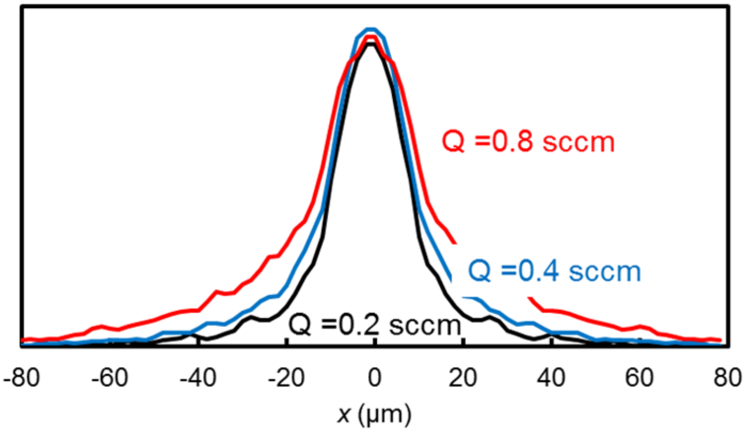

Figure 5-8: Thickness profiles of features versus carrier gas flow. Normalized simulated feature thickness is plotted as a function of distance x from the nozzle centerline. Profiles are plotted for flow rates of $Q = 0.2$, 0.4, and 0.8 sccm/nozzle. Nozzle to substrate gap width g is 10 μm. Nozzle width is 20 μm.

5.5.2 Effect of Nozzle Shape

Convection of the carrier gas is necessary to bring organic material through the nozzle inlet and into the deposition zone. Once carrier gas passes through the nozzle aperture, however, it accelerates outward from the nozzle centerline and imparts lateral velocity to organic molecules as it exits. This broadens the profiles of printed features. High resolution printing can be best achieved by a nozzle design that brings a slow moving stream of organic vapor laden carrier gas into proximity with the substrate near the nozzle centerline. If the vast majority of organic material has already adsorbed onto the substrate upstream of the zone where the carrier gas begins to accelerate, convective broadening of the printed feature is minimized.

The need for organic material to deposit in a zone of relatively stagnant flow conflicts with a requirement that flow restriction be kept low so that pressure in the source cells is minimal for a given carrier gas flow rate. The reason low pressure is desirable will be further discussed when the flow model is combined with a model for vapor production in Chapter 6. Flow restriction can be minimized by etching tapers or reliefs into the underside of the nozzle array, although these also increase the lateral velocity of carrier gas under the nozzle membrane. The optimal design of a nozzle will likely reflect many variables including the desired deposition rate, feature size, and the volatility of the materials deposited.

Four different nozzle geometries were simulated by DSMC. The first is simple converging (S-C). It features a funnel-shaped inlet that tapers over a 100 μm thickness to an aperture of 20 μm in width, **Fig. 5-9a**. The taper minimizes flow restriction for a given aperture size. The underside of the nozzle is simply a planar surface. This keeps organic material close to the nozzle aperture and substrate, but impedes the flow of exiting carrier gas. Two nozzle geometries with relief trenches to facilitate the venting of spent carrier gas were also simulated. Converging-relieved (C-R) nozzles, **Fig. 5-9b,** are characterized by a converging inlet with 50 μm deep, straight-walled relief trenches cut in the underside of the nozzle membrane located 60 μm from the nozzle centerline. Simulation results for this nozzle were previously given in **Figs. 5-6 to 5-8**. Converging-tapered (C-T) nozzles, **Fig. 5-9c,** have a tapered outer nozzle surface that is parallel to the converging inner surface. This minimizes the length over which the flow of carrier gas is confined to the narrowest portion of the gap with height, *g*. A fourth nozzle geometry, converging-diverging (C-D), **Fig. 5-9d,** has a constricted throat midway between its inlet and outlet. Organic material accelerates in the nozzle throat and then decelerates as it approaches the substrate. All of these structures can be physically realized by anisotropic etching of Si as will be discussed in Chapter 7.

Simulated field quantities such as carrier gas speed, pressure, and temperature are shown in **Figs. 5-9** to **5-11**. A two-dimensional geometry, symmetric about its left boundary is used. The long dimension of the nozzle goes into the page and is assumed to be infinite.

Flow is accelerated in a micronozzle by one of two processes. The first is due to constriction of flow. Gas flow must move more quickly to maintain constant mass flow rate through a decreasing cross section. Flow speed, **Fig. 5-9**, increases but pressure, **Fig. 5-10**, remains roughly constant. This occurs near the throat of the C-D nozzle and near the tip of the other nozzle geometries. The second and larger effect is acceleration due to expansion of a gas jet from a region of high pressure to low pressure. In this case, velocity increases as pressure decreases, indicating that carrier gas is entering a lower impedance region of the nozzle. This occurs farthest away from the region of deposition in the case of the S-C nozzle. Its slow carrier gas flow produces the sharpest deposition profile with the least overspray, as shown in **Fig 5-12**. Gas accelerates as it enters the relief trench in both the C-R and C-T geometries. In the case of the C-R nozzle, the plume of expanding gas is uncontrolled, and somewhat reminiscent of the tip of the 1 mm nozzle discussed in Chapter 3. As a result, this nozzle tends to produce more overspray than an S-C nozzle. The location of the relief trench with respect to the nozzle outlet affect the width and magnitude of the overspray tail of the deposition profile. When the trench is brought into close to the substrate, resistance to flow decreases, but organic material is not given an adequate opportunity to adsorb on the substrate before it is dispersed by the acceleration of carrier gas as it expands to fill the relief trench. The outer slope of the C-T nozzle provides a degree of shape to the exiting gas plume, reducing the motion of residual organic vapor away from the substrate and reducing overspray compared to the C-R nozzle as shown in **Fig. 5-12.** The length *l* of the nozzle-to-substrate gap can be as small as 20 μm for a C-T nozzle while producing relatively little overspray.

Flow in the C-D nozzle undergoes two expansions. The first occurs at its throat. Pressure in the diverging portion is lower than at the inlet, so flow accelerates as it enters the diverging portion. Although a choked flow can be achieved through the nozzle throat, the obstruction created by an underlying substrate prevents carrier gas from achieving supersonic velocity within the diverging portion of the nozzle, **Fig. 5-9d.** Due to the confining effect of the substrate, this nozzle can be thought of as two C-D nozzles in series when the behavior of the outer surface of the nozzle is considered. The proximity of the substrate pushes carrier gas and organic vapor towards the lip of the diverging nozzle, producing a cat head shaped deposition profile in **Fig. 5-12.** A significant region of stagnant flow is present along the nozzle centerline over the substrate, creating a zone of thinner deposition near the centerline. Carrier gas is accelerated again as it enters stricture formed under the lip of the diverging nozzle.

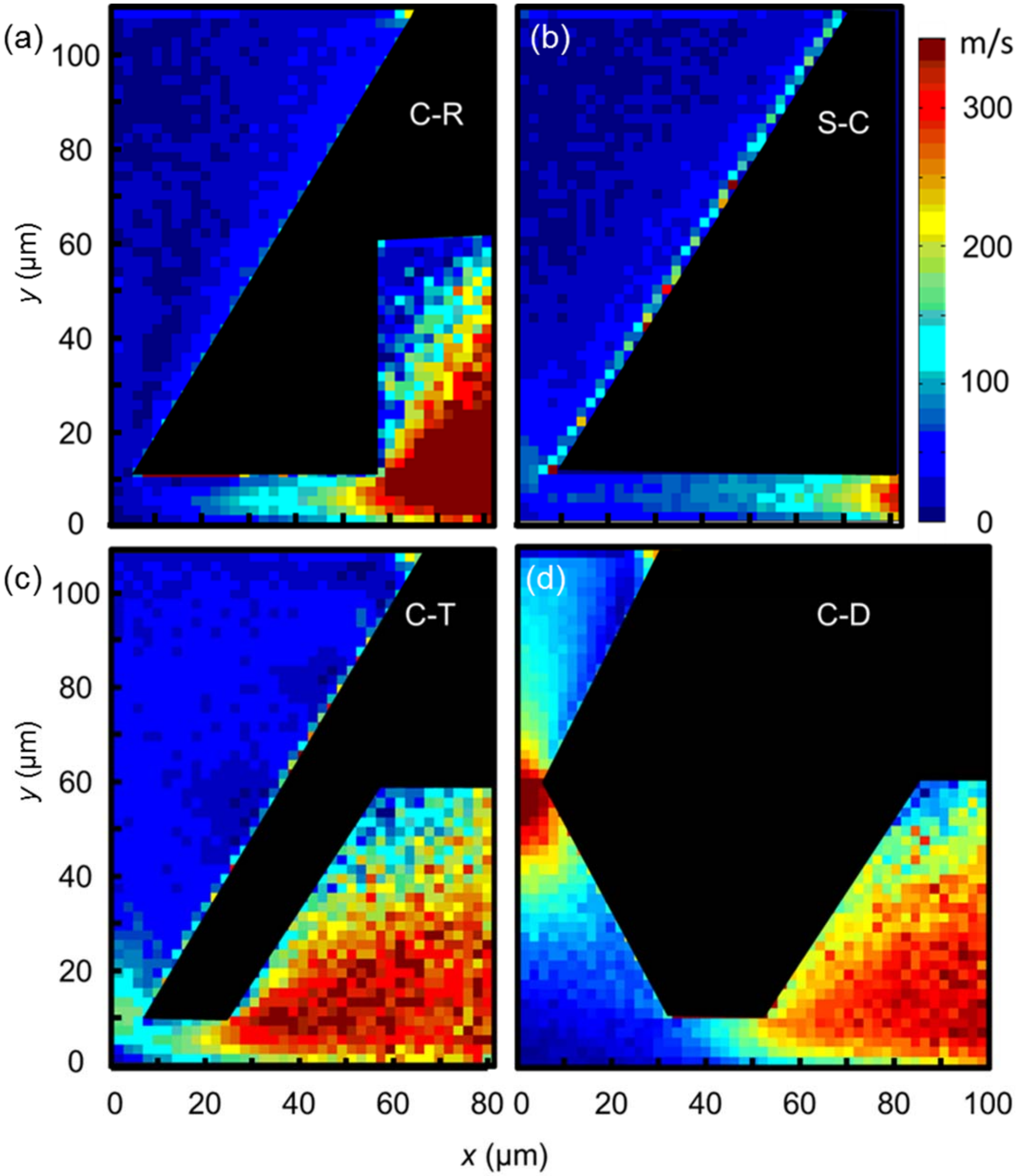

Figure 5-9: Velocity field for micronozzles of differing geometry. Color plots show the speed (norm of velocity) of the carrier gas for (a) converging-relieved (b) simple-converging (c) converging-tapered and (d) converging-diverging nozzle geometries at a constant inlet pressure of 3500 Pa. Outlet pressure is assumed negligible.

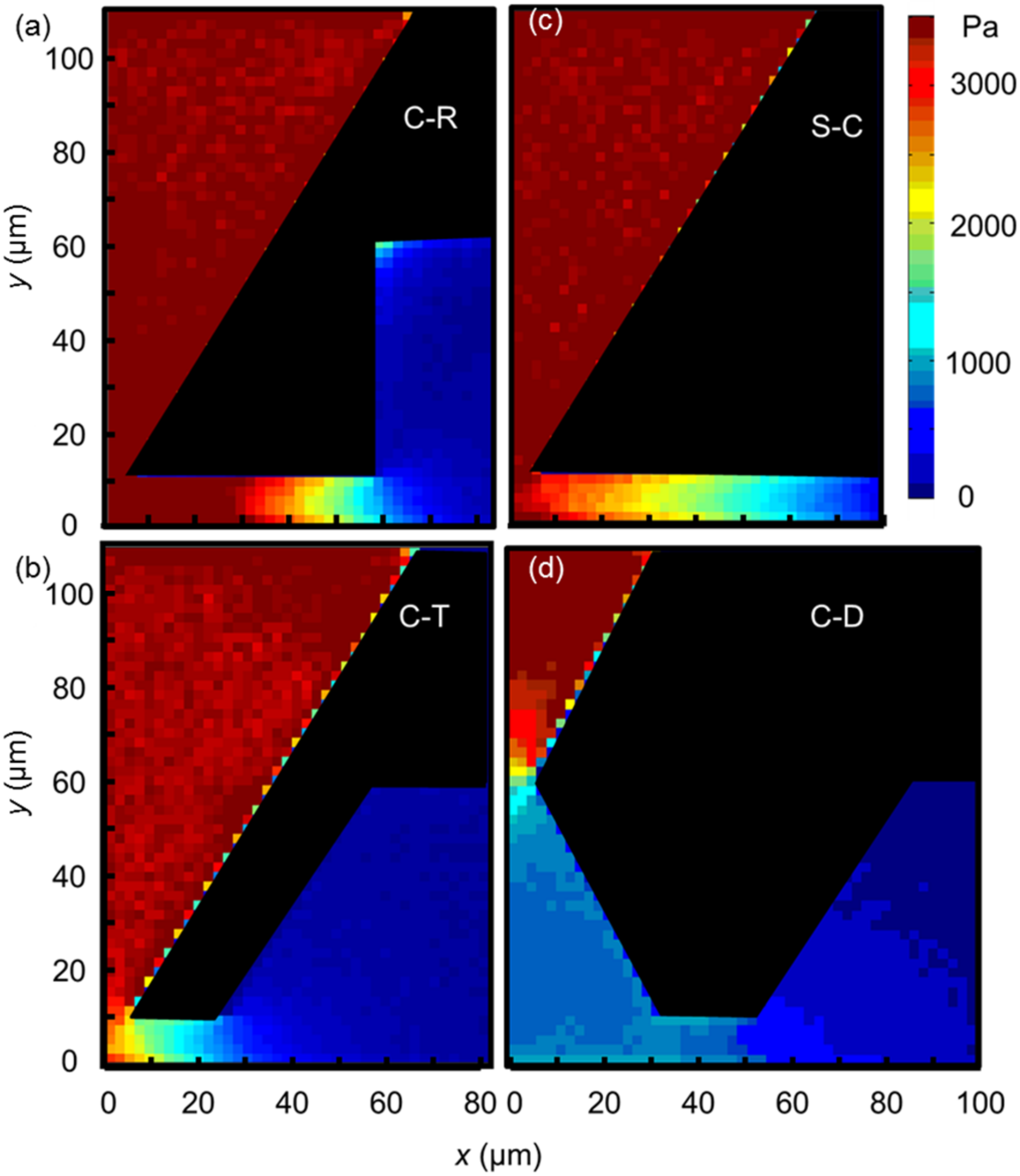

Figure 5-10: Pressure field for micronozzles of differing geometry. Color plots show the pressure distribution of the carrier gas in (a) converging-relieved (b) simple-converging (c) converging-tapered and (d) converging-diverging nozzle geometries at a constant inlet pressure of 3500 Pa. Outlet pressure is assumed to be negligible.

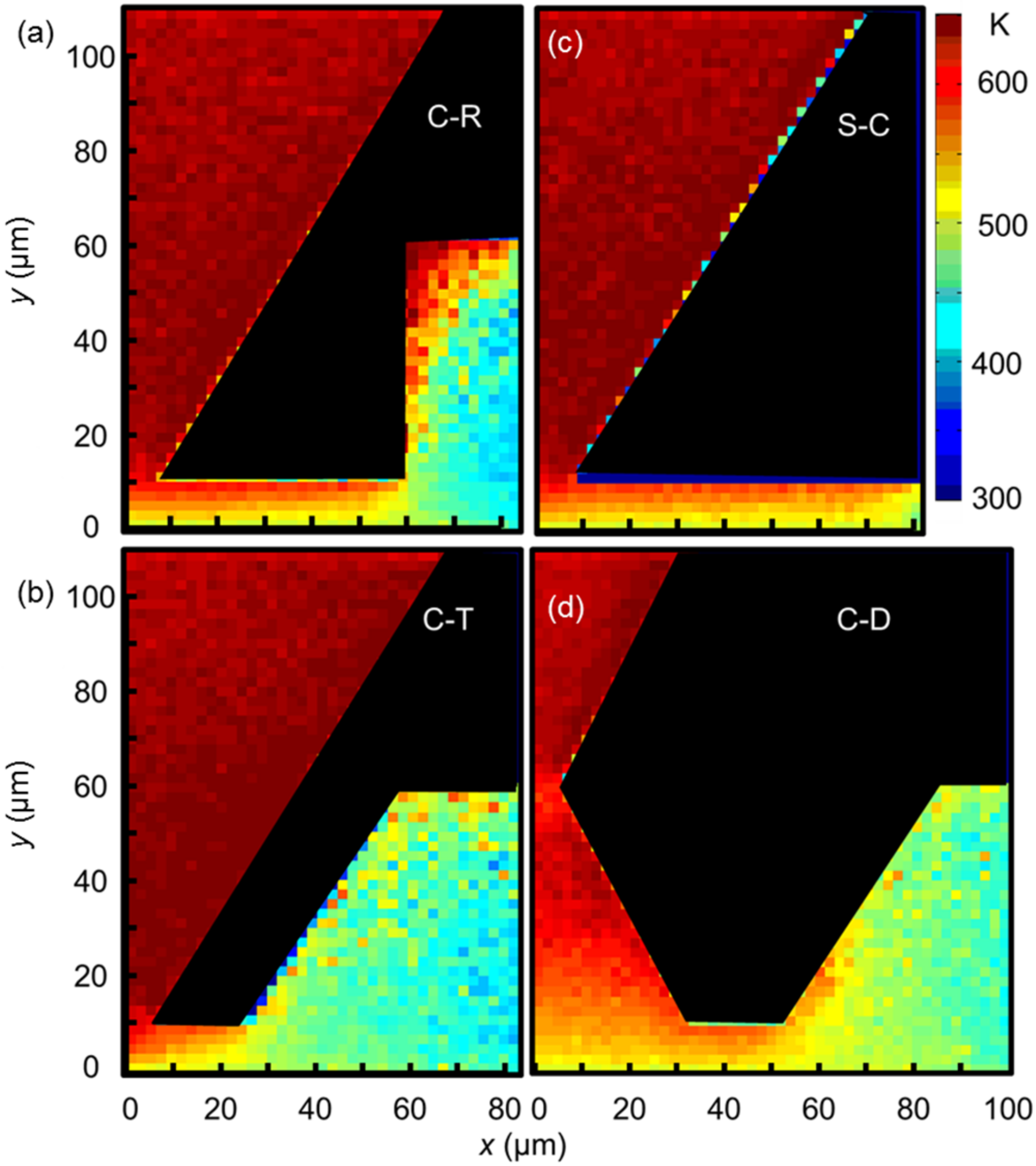

Figure 5-11: Temperature field for micronozzles of differing geometry. Color plots show the temperature of the carrier gas for (a) converging-relieved (b) simple-converging (c) converging-tapered and (d) converging-diverging nozzle geometries. The print head is assumed to be 600K, while the substrate (bottom surface) is 300K.

Most of the organic vapor deposits in the vicinity of this stricture. Carrier gas is further accelerated as it enters the lowest pressure region on the outside of the nozzle. Since some organic vapor is still present in the resulting jet, this expansion makes the outer edge of the deposited feature less sharp.

A major motivation for evaluating different nozzle geometries was to determine if a geometry that produces features with mesa-like cross sections, i.e. flat top with sharp sidewalls, exists. These are desirable for OLED applications, since features with uniform light emission properties can be grown in a single pass. While none of the tested designs have been completely satisfactory, there is still a largely unexplored parameter space in which nozzle design can be optimized. Further engineering of the nozzle shape by

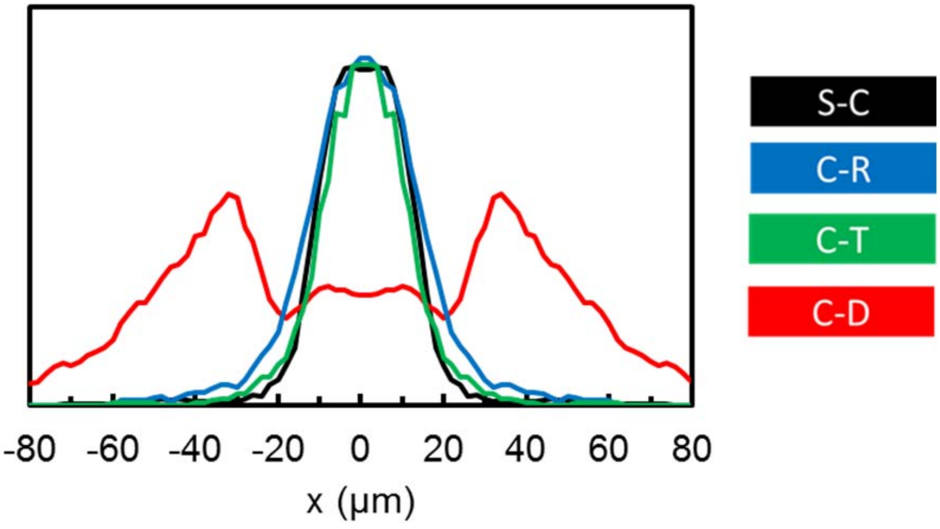

Figure 5-12: Profiles of features printed with different micronozzle geometries. Simulated profiles are plotted as a function of distance from the nozzle centerline. Nozzle tip to substrate gap *g* =10 μm and the inlet pressure is 3500 Pa. Outlet pressure is negligible.

adjusting the throat, aperture, and gap width, as well as by putting multiple shaped nozzles in tandem may allow for the mesa shaped features desirable for OLED emissive layers to be printed in a single pass.

5.5.3 Effect of Carrier Gas Characteristics

Carrier gas has two characteristics in the context of these DSMC simulations. Gas particles have mass and a molecular radius. The molecular radius primarily influences the rate of collision with other carrier gas molecules. Organic molecules are sufficiently wide, ~ 1 nm, that differences in the radius of the carrier particles do not significantly change the collision diameter of an organic-carrier gas collision.

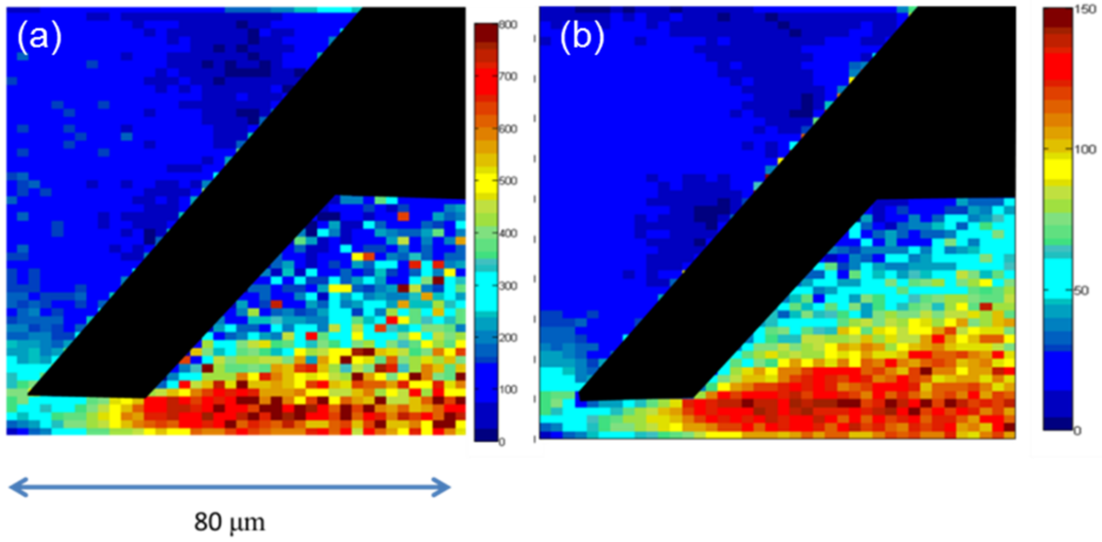

Figure 5-13: Velocity field for micronozzles with different carrier gas species. C-T nozzles heated to 600K with (a) He carrier gas and (b) Xe carrier gas are shown. Because He is lighter, the jet of carrier gas accelerates to significantly higher velocity as it escapes from beneath the nozzle. Inlet pressure is 3500 Pa.

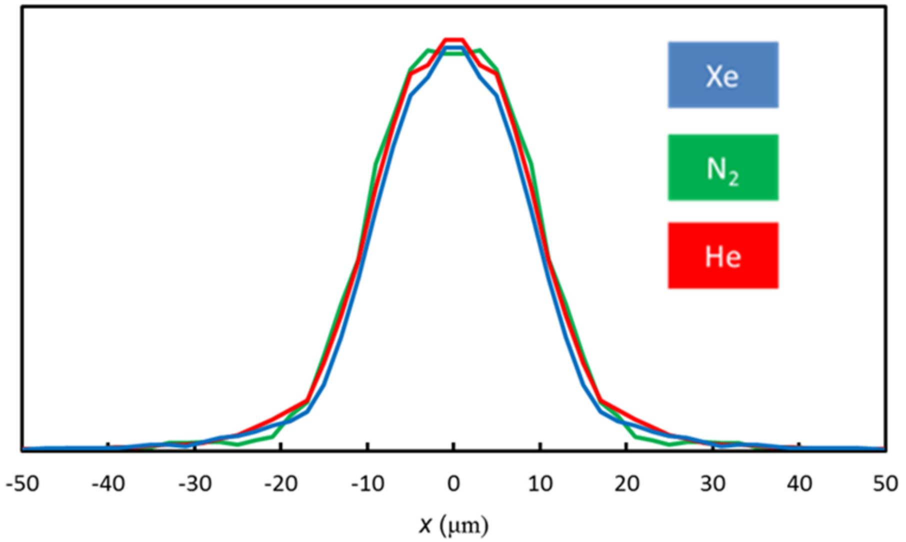

Figure 5-14: Thickness profiles of printed features for different carrier gas species. The plots show features printed by a C-T nozzle at g = 10 μm using carrier gases He, N_2, and Xe. Inlet pressure is 3500 Pa.

Molecular mass affects the behavior of the carrier gas in two ways. First, it affects the characteristic velocity of particles in the gas. Lighter particles move faster at a given temperature, as shown in eq. 5-18.[92] At a macroscopic level, this translates to a higher speed of sound in the gas and therefore higher velocities in jets of expanding gas, which have roughly sonic velocities. This is illustrated in **Fig. 5-13**. Since particles move faster, the collision rate also increases as implied by eq. 5.9. Secondly, while the thermal velocity of each particle is higher for a lighter carrier gas and collisions are more frequent, particles carry less momentum. Each collision is, therefore, less effective at imparting momentum to the organic molecules. Assuming that the rate of momentum transfer between the carrier gas and organic molecules is proportional to the product of the collision rate and the average momentum of a carrier gas molecule, eq. 5.19, the effectiveness of a carrier gas at imparting momentum to organic vapor molecules is independent of its mass. This is, of course, a crude approximation, but it explains the lack of significant differences in deposition profile observed in **Fig. 5-14**. It should also be noted that acceleration of organic material due to expansion of the carrier gas jet is minimal directly under the aperture of an S-C nozzle, which is where most of the organic material deposits. Since changing the species of carrier gas primarily affects the flow of an expanding jet, it can be expected to more noticeably affect deposition in nozzle geometries that allow the carrier gas jet to expand upstream of the deposition region.

$$\langle|\vec{c}|\rangle = 2\sqrt{\frac{RT}{m\pi}} \tag{5.18}$$

$$N_C\langle|\vec{p}|\rangle \sim m\langle|\vec{c}|\rangle^2 = 2\sqrt{\frac{RT}{\pi}} \tag{5.19}$$

Simulated feature thickness profiles are given for He, N_2, and Xe carrier gasses in **Fig. 5-14**. A slight degree of broadening is observed for lighter carrier gasses, implying the greater velocity of the carrier gas outweighs its decreased momentum in a more detailed model.

5.5.4 Effect of Sticking Coefficient

Because dopant materials have varying volatility, it is necessary to revisit the earlier assumption that α =1 and organic material condenses on contact with the substrate. If a portion of the organic material impinging on the substrate is allowed to specularly reflect rather than adsorb, a deposition profile with wide tails, as shown in **Fig. 5-15,** results. The persistence of this overspray tail is exacerbated by the fact that a reflected organic molecule is moving away from the substrate and requires collisions with either the print head or carrier gas molecules to redirect it back onto the substrate. Since the outer regions of the simulated volume have a low density of carrier gas, an organic molecule can translate a significant distance in the *x* direction before it returns to the substrate. The utilization efficiency, defined as the fraction of particles introduced into the simulation that adsorb inside of the control volume, decreases with non-unity α. It is likely that when unused material comes to rest in a real system, it contaminates adjacent printed features. While the sticking coefficients of organic materials used with OVJP are close to unity, as will be shown in Chapter 10, very minute levels of contamination by a dopant with a low lying triplet energy level can change the emission color of printed OLEDs.

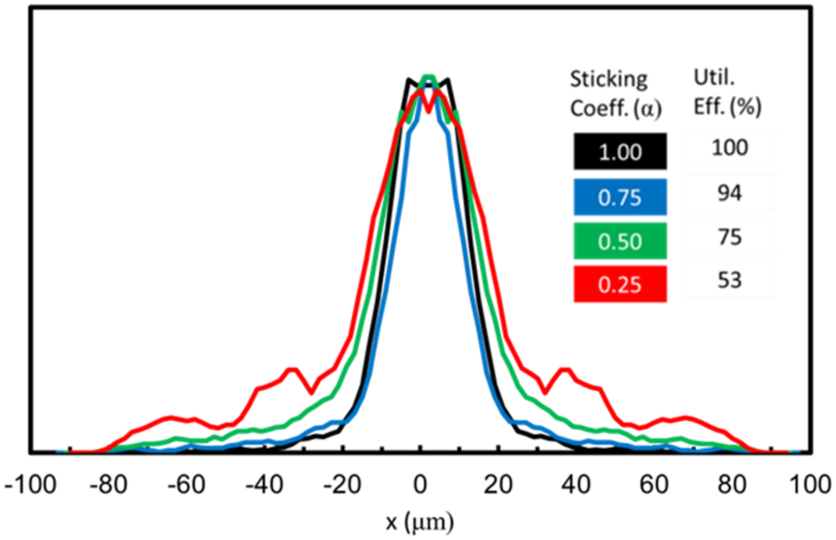

Figure 5-15: Thickness profiles of features for different material sticking coefficients. Features are printed by a simple converging nozzle at separation *g* = 10 μm from the substrate using material with varying sticking coefficient α. Inlet pressure is 3500 Pa and outlet pressure is negligible. Utilization efficiency is defined as fraction of organic material landing within the simulated volume.

5.6 Substrate Barrier Structures

Cross contamination between printed pixels can be reduced by fabricating barrier structures onto substrates prior to organic thin film deposition. A barrier structure 2 μm high and 10 μm wide was simulated on the substrate with its inner edge 20 μm from the nozzle center. The barrier is visible along the bottom boundary in **Fig. 5-16**, which depicts them used with a C-T nozzle**.** This barrier structure proved effective at minimizing deposition beyond its 20 μm inner edge when used with S-C nozzles held close, *g* =10 μm, to the substrate. The barrier casts a long shadow on the substrate, catching organic material that is moving transverse to the substrate and preventing it from

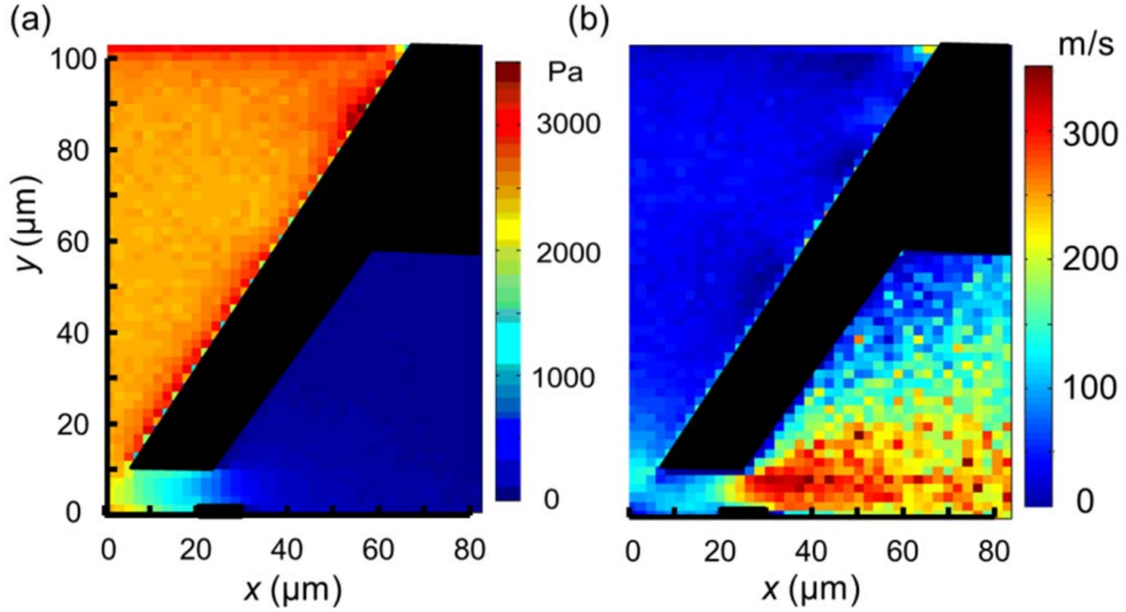

Figure 5-16: Velocity and pressure fields for nozzle and substrate barrier structure. (a) Pressure and (b) velocity profiles are plotted for a simulated converging-tapered nozzle with a 2 μm high, 1 μm wide barrier. The velocity profile shows that the barrier directs the jet of expanding carrier gas upward and away from the substrate. This inhibits deposition downstream from the barrier.

depositing further downstream. No deposition was observed between x =30 and 40 μm from the nozzle centerline, as seen in **Fig. 5-17**. There is a small amount of stray deposition beyond 40 μm, however as we will see in Chapter 10, even this could be sufficient to adversely affect a neighboring device. The length of the shadow cast by the barrier becomes less for g =20 μm, only extending from x = 30 to 35 μm and becomes non-existent for g =50 μm. Barriers become less effective with increasing g because organic material can approach the substrate from a steeper angle of incidence if the nozzle aperture is elevated.

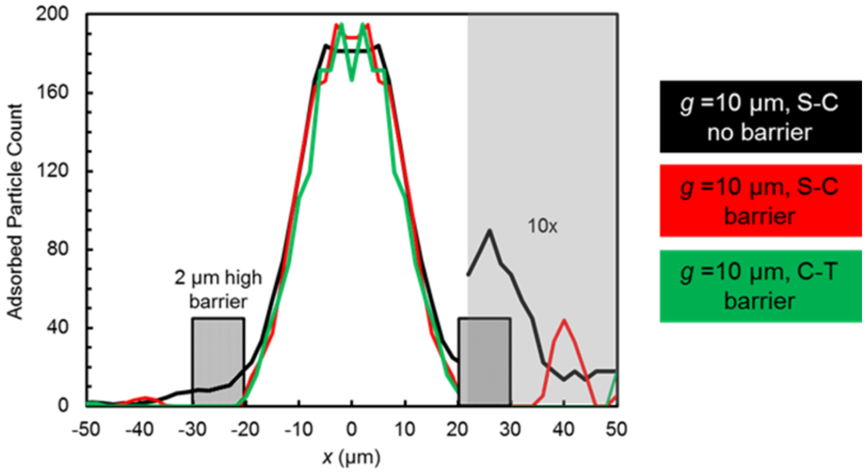

Figure 5-17: Thickness profiles for features printed between substrate barrier structures. The thickness of features printed in a groove between two 2 μm high, 10 μm wide barriers fabricated on 50 μm centers is plotted as a function of distance from the nozzle centerline. Simple converging (S-C) (red) and converging-tapered (C-T) (green) nozzles are modeled at g =10 μm with barriers. An S-C nozzle used without barriers is shown for comparison (black). The count of adsorbed organic tracer particles (vertical axis) is multiplied by 10x in the shaded region to highlight small absolute differences in thickness downstream of the boundary.

Increasing the height of the barrier does not significantly increase the width of the shadowed region for g =10 μm. The downstream deposition is therefore likely due to material reflecting off of the underside of the nozzle membrane. This can be mitigated by increasing the separation between the substrate and membrane past the barrier. To this end, a C-T nozzle was simulated with the barrier structure. Negligible overspray beyond the barriers was observed in this case, **Fig. 5-17** (green line). Since there is still organic underneath the print head, a method for removing it would enhance the effectiveness of these barriers. Otherwise, organic material would precipitate further downstream. A possible approach to this is discussed in Chapter 12.

5.7 Summary

A model for the flow of carrier gas and organic vapor through an array of micronozzles has been developed. The model is capable of predicting the size and shape of features printed by several different nozzle designs that can be fabricated from a silicon membrane, as discussed in Chapter 7. The microchannels that feed gas to the nozzle array can be modeled in the continuum flow regime. A more complex, Direct Simulation Monte Carlo model is used to model the micronozzles themselves, since they operate in the transition regime.

The model indicates that the width of printed features scales linearly with nozzle-to-substrate separation g, and depends on carrier gas flow rate at small values of g. Simple-converging (S-C) nozzles with a planar underside were found to minimize feature size and overspray, since they have low flow velocity in the deposition region and create minimal convective broadening. The profiles of printed features are relatively insensitive to the species of carrier gas used when flow through the deposition region is slow.

Although little material escapes from under the nozzle when the sticking coefficient is unity, overspray becomes significant if the organic material deposited has a smaller sticking coefficient. Materials with a sticking coefficient close to unity should be chosen for use with OVJP. Application of barrier structures can help to mitigate the small amount of overspray that cannot be eliminated through proper material choice, nozzle design, and process conditions.

Although the development of a micronozzle array is a critical element of this work, it is only one part of a larger system. The flow model developed here can be combined with a model for the organic vapor sources to characterize the performance of an OVJP tool employing a micronozzle array. This combined model is developed in the following chapter.

Chapter 6

System Level Modeling of OVJP

6.1 Overview

The design of a micronozzle array affects aspects of the OVJP process besides feature size. The model for microchannel and micronozzle flow developed in the previous chapter can be combined with a model for mass transport in organic vapor sources to relate process parameters such as source temperature and flow rate to observables such as deposition rate and doping ratio. This combined model provides insight into how to best design and control and OVJP tool.

Material sources in OVJP operate in a different regime than sources in OVPD due to the presence or a restrictive nozzle array. The assumptions used in characterizing the OVPD process must therefore be revisited before applying a similar analysis to OVJP. While the DSMC model of a micronozzle permits a detailed analysis of gas flow, it is very computationally intensive. Since it does not yield a closed form solution, this model also provides little guidance regarding how changes the system's parameters affect its operation. The DSMC model is also difficult to link to the organic vapor source model. A semi-analytical one-dimensional model for nozzle flow in the transition regime is developed to remedy these shortcomings. Closed form expressions relate pressure and flow rate at each step of the OVJP process. This can be incorporated with the organic vapor source model to predict deposition rate and doping ratio. The configuration of the OVJP tool is briefly described to help motivate development of the model. Mechanical and thermal design calculations for the micronozzle are also discussed in this chapter.

6.2 System Configuration

The overall configuration of the OVJP tool is shown in **Fig. 6-1**. It is discussed in greater detail in Chapters 7 and 8. The microfabricated nozzle membrane is sealed to a manifold containing multiple vials of different organic materials in heated tubes. Carrier

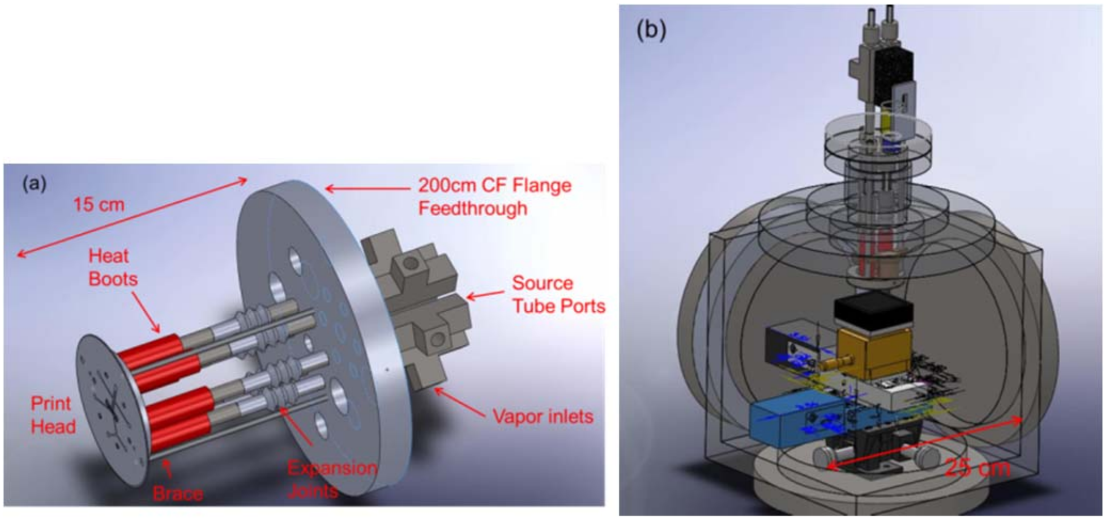

Figure 6-1: CAD renderings of OVJP tool. (a) The print head is mounted on a heated manifold containing multiple organic vapor sources. The manifold is fed carrier gas a large feedthrough at its other end. (b) The feedthrough sits on top of a cubic deposition chamber. The substrate sits on a chilled holder on a multi-axis motorized stage underneath the print head.

gas feeds are present for host and dopant materials. A dilution flow was judged to be counterproductive at these length scales, since increased flow volume results in increased pressure buildup. The manifold is itself mounted on a vacuum feedthrough that sits atop a high vacuum chamber. Carrier gas flows through the manifold, picks up evaporated organic material, and carries it to the micronozzles. The gas mixture passes through glass microchannels that distribute it to the micronozzle array in one version of the print head, discussed in Chapter 9. In a later version discussed in Chapter 10, conventionally machined channels distribute vapor to the nozzle membrane.

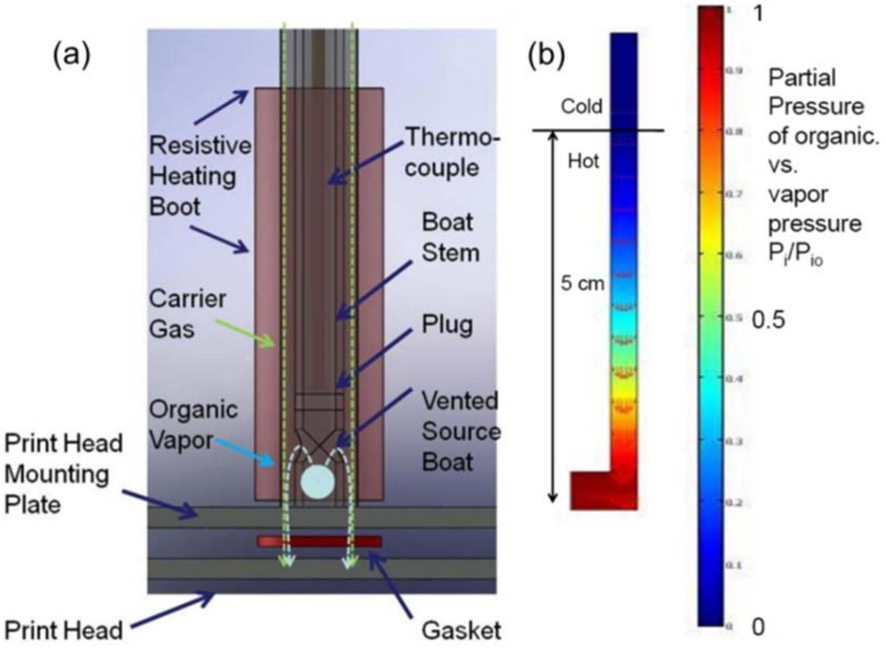

Figure 6-2: Detail of an organic vapor source cell. (a) The organic vapor source cell consists of an ampule of condensed organic material inside of an 8 mm diameter heated tube sealed to the print head with a gasket. (b) Plot of modeled organic vapor concentration in the source cell with a carrier gas flow of 0.5 sccm. Organic material does not back-stream to the cooler, upper portion of the source due to convection in the flow of carrier gas.

A detail of a source and its junction with the print head is shown in **Fig 6-2a**. Sources consist of a vented organic capsule at the downstream end of a uniformly heated tube segment. Organic vapor diffuses through holes in the capsule and into the carrier gas stream. Finite element modeling of the diffusion of organic vapor was performed to verify no appreciable backstreaming occurs at typical flow rates of 0.5 sccm, **Fig 6-2b**.

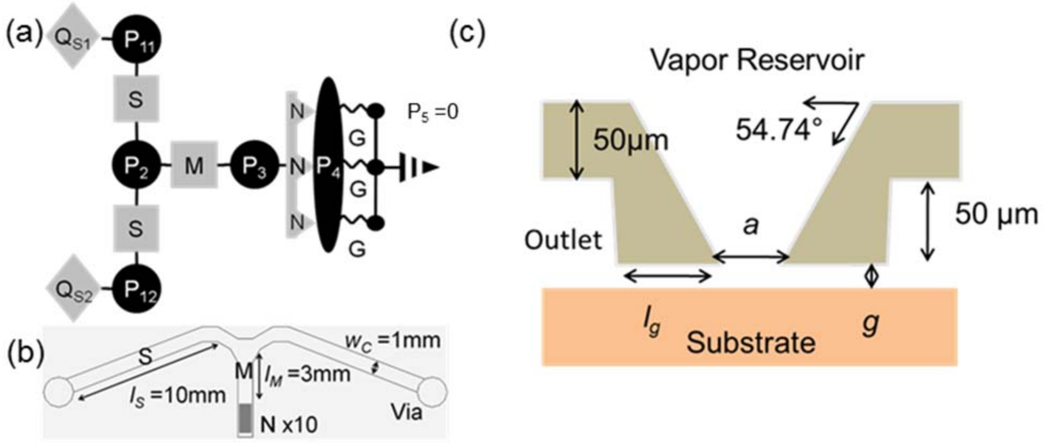

Figure 6-3: Diagram of semi-analytical OVJP flow model. (a) Elements Q_{S1} and Q_{S2} correspond to constant flow carrier gas sources. S and M are source and mixing microchannels. Elements N are an array of nozzles and G are the gaps between the nozzle and substrate. P_{11} to P_4 are pressures driving flow between these elements. (b) Physical layout of nozzle array chip. Source channel length, l_{S}, =10 mm, mixing channel length l_M =3mm, channel width w_C =1mm, and the depth of the channels h =100 μm. The array contains 10 nozzles. (c) Geometry of nozzle element N in this model. It is a C-R type nozzle with aperture a = 20μm and gap width l_g =50 μm. Gap height g is variable. The long dimension of the nozzle (into the page) w_N= 200 μm. (From McGraw and Forrest)[64]

6.3 Semi-Analytical Flow Model

Closed form relationships for pressure and flow are developed using tabulated dimensionless mass flow rates presented by Sharipov and Seleznev,[100] in which the

Boltzmann equation (eq. 4.8) is numerically solved for simple elements such as rectangular channels and orifices. An equivalent circuit, shown in Fig. **6-3a** is constructed from these elements to predict gas flow through the print head, substrate system.

This model addresses the case of a print head in which organic vapor is distributed to the nozzle array through microfluidic channels. Source channels bring host and dopant vapors from their respective sources to a central mixing channel. The mixing channel then distributes vapor to the nozzle array as shown in **Fig. 6-3b**. Upstream of the mixing channel, the analytical model given by eq. 5.7 is adequate. Downstream from the mixing channel, flow through the nozzle array is characterized by an intermediate Knudsen number. Gas dynamics are determined by a superposition of continuum and free molecular scaling laws in proportions determined primarily by gas density.

The molar flow rate of gas through each micronozzle aperture, Q_N, is approximated as flow through a slit aperture, given by eqs. 6.1 to 6.3. The gas flow has pressure, P_4, downstream of the nozzle aperture. Coefficients C_N and F_N correspond to the continuum and free molecular components to the carrier gas flow, respectively. The short dimension of the rectangular nozzle aperture is *a,* and the long dimension is w_N (see **Fig. 6.3c**). Here, the reciprocal molecular velocity is $\beta = \sqrt{(m/RT)}$, where *m* is molar mass of the carrier gas.[64]

$$Q_N = (C_N P_3 + F_N)(P_3 - P_4) \tag{6.1}$$

$$C_N = 0.171 \frac{a^2 w_N}{\sqrt{\pi}\mu RT}, \tag{6.2}$$

$$F_N = 1.073\frac{a\beta w_N}{\sqrt{\pi}m}. \tag{6.3}$$

The gap between the nozzle orifice and substrate forms the final restriction to the flow of carrier gas through the print head. This region corresponds to element G in Fig. **6-1a**, and has dimensions of gap height g and length l_G as shown in **Fig. 6-1c**. Flow rate, Q_G, through the gap is given by eq. 6.4.:

$$Q_G = C_G P_4^2 + \left(8 - 2ln(\delta)\right) F_G P_4, \tag{6.4}$$

$$C_G = 0.07\frac{g^3 w_N}{\mu l_G RT}, \tag{6.5}$$

$$F_G = \frac{g^2 w_N \beta}{5 l_G m}, \tag{6.6}$$

and where $\delta = g\beta P_4/\mu$ is the dimensionless rarefaction factor. Pressure is assumed to be negligible at the downstream opening of the gap.[64]

Continuum and free molecular flow scaling laws are recovered at the low and high pressure limits of eq. 6.4. In the case of high P_4, the term with coefficient C_G dominates. It is proportional to P_4^2 and g^3, as expected for a continuum flow between parallel plates (eq. 5.7). At lower pressures, F_G dominates, and the rate scales as expected for free molecular flow.[101] For small P_4, such that $\delta < 1, Q_G$ scales linearly with h^2 as well as P_4. Note that $P_4 ln(\delta) \rightarrow 0$ as $P_4 \rightarrow 0$.

Equation 6.4 and its coefficients are based on the dimensionless mass flow rate, G_P, which have been tabulated for specific values of δ. The tabulated values for $0.1 < \delta < 10$ can be fit by eq. 6.7. Equation 6.7 is then substituted into eq. 6.8 to yield the flow within the nozzle-to-substrate gap at position, x. This expression is integrated over the length of the gap to yield eq. 6.4.

$$G_P = 0.27\delta - 0.4ln\delta + 1.2. \tag{6.7}$$

$$Q_N = \frac{-a^2\beta}{m} G_P \frac{dP}{dx}, \tag{6.8}$$

This model was experimentally verified by measuring the pressures generated in the organic vapor source of the OVJP tool over a range of carrier gas flow rates and values of g. The pressure, P_I, required for a total flow rate Q_M through the print head is plotted in **Fig. 6-4** (data points). For g = 10, 25, 50, 100 µm, and ∞, P_I^2 is approximately proportional to Q_M. Restriction to flow is at a minimum for g →∞, and increases inversely with g. This increase becomes significant for g <50 µm. For example, the pressure when $Q_M = 2$ sccm increases from P_I =30 Torr for $g \to \infty$, to P_I =46 Torr for g = 50 µm, and P_I =79 Torr for g = 10 µm.[64]

Agreement between experiment and the semi-analytical model was obtained for the limiting cases of g =10 µm and $g \to \infty$, as shown by the solid lines in **Fig. 6-4**. The conductance of the source channel, S, was calculated using eq. 5.7 to be 3.6×10^{-3} sccm/Torr^2 at room temperature, in agreement with its measured value. The model proved less accurate for predicting P_I at intermediate values of g, where the two dimensional character of the nozzle-to-substrate gap is more accurately determined using a computationally intensive DSMC model.

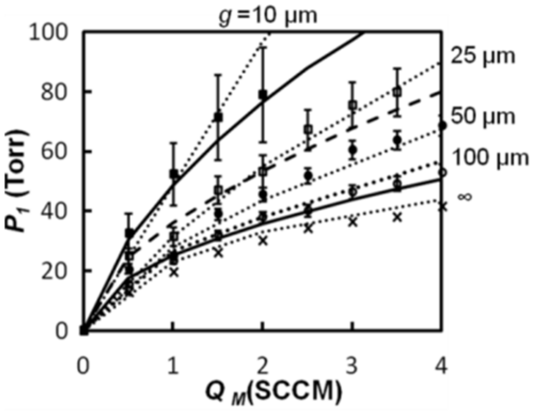

Figure 6-4: Modeled and measured pressure versus flow restriction. Pressure in organic vapor sources is plotted as a function of total flow through the print head. Analytical results for a C-R nozzle is shown in black for *g* =10 µm and ∞ and the dashed line shows a C-T nozzle for *g* =10 µm. DSMC results for a C-R are shown with dotted lines. (From McGraw and Forrest)[64]

6.4 Organic Vapor Source Cell Model

A closed form solution relating pressure and carrier gas flow in the OVJP system facilitates modeling vapor generation and transport. This allows prediction of deposition rates and doping ratios, as well as a better understanding of how to control them in a practical system. This combined model also provides insight into how to optimize OVJP.

The source design can be modeled as a layer of saturated organic vapor near the condensed organic material at the base of a capsule that diffuses into a nearly stagnant volume of carrier gas within the capsule. A portion of this material then diffuses through vents and becomes entrained in the flow of carrier gas flow surrounding the capsule. Material transport can be viewed as a purely diffusive process through a stagnant barrier in series with a purely convective process in which effluent gas is assumed to be well mixed. The series of diffusive and convective transport steps would be common to all source cell designs, however the depth of the diffusive barrier in the general case depends on the velocity of gas flow as dictated by boundary layer theory.[90] This model, however, is appropriate for the relatively simple source geometry used in a laboratory scale OVJP tool and illustrates trends common to more complex source geometries.

The partial pressure of organic vapor within the capsule is given by P_V'. Organic vapor accumulates within the capsule by evaporating at rate kP_V^*, where k is a kinetic constant and P_V^* is the equilibrium vapor pressure of the organic material. Coefficient k relates the flux of organic vapor away from a condensed source, given by eq. 6.9, to its equilibrium vapor pressure.[92] The surface area of the source is A_S, n_v is the equilibrium molar density of organic vapor, $<c>$ is the average velocity of effusing organic molecules, and m_v is molecular mass. The equilibrium vapor pressure is given by the Clausius-Clapeyron equation, eq. 6.10. The Arrhenius dependence of eq. 6.10 reflects

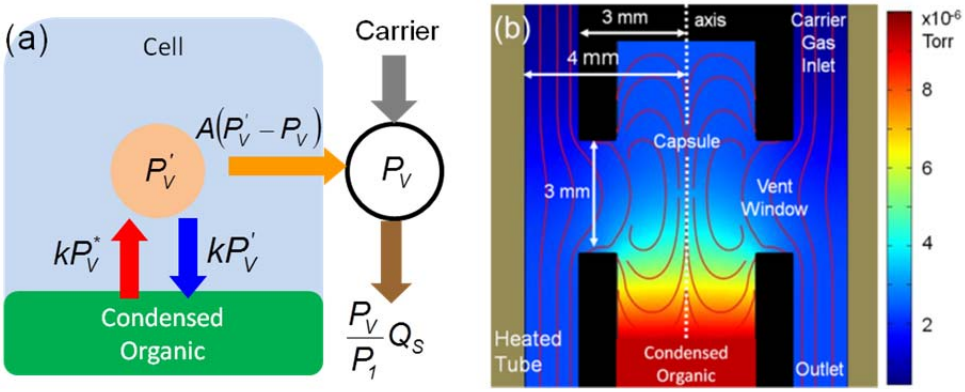

Figure 6-5: Organic vapor source cell model. (a) A diagram represents the modeled fluxes of organic vapor in the cell. (b) A finite element simulation models carrier gas flow and the transport of organic vapor through a source cell geometry used in the OVJP system. (From McGraw and Forrest)[64]

the equilibrium at temperature T between evaporated and condensed organic molecules. Molecules must overcome enthalpy of evaporation ΔH^{VAP} to leave surface of the condensed source, while molecules in vapor phase give up ΔH^{VAP} upon condensing. Organic vapor around the source has two fates, it can re-condenses at rate kP_V'.[98] It can also cross a diffusive barrier to become entrained in the gas flow surrounding the capsule. It does this at rate $A(P_V'-P_V)$, given by Fick's law. The partial pressure of organic vapor in the outbound carrier gas flow is P_V. These fluxes are shown in **Fig. 6-5a.** The flux of organic vapor from the source J is given by eq. 6.11, where P is the source cell pressure and Q is the molar flow rate of carrier gas.[64]

$$kP_V^* = A_S \cdot \frac{1}{4} n_V \langle c \rangle = A_S P_V^* \frac{1}{\sqrt{2\pi m_V k_B T}} \tag{6.9}$$

$$P_V^* = P_0 e^{\frac{\Delta H^{vap}}{RT}} \tag{6.10}$$

$$J = P_V^* \frac{k}{Q\left(1+\frac{k}{A}\right)+kP} Q \tag{6.11}$$

$$A = \frac{A_C D}{l_c} = \frac{3A_S k_B T}{16 l_c \sigma P} \sqrt{\frac{2\pi k_B T}{m_r}} \tag{6.12}$$

Mass transport coefficient A is proportional to binary diffusivity D of organic vapor in the carrier gas, as shown in eq. 6.12, where A_C is the cross sectional area over which diffusive transport occurs and l_c is the characteristic length of the stagnant gas layer through which organic vapor diffuses. The value of D can be calculated from kinetic theory using eq. 4.16. Reduced mass m_r and collision cross section σ are defined in Chapter 4. Mass transport coefficient can therefore be expressed as $A = A_0/P$, where A_0 is a constant dependent on temperature, the geometry of the source cell, and the properties of both the organic vapor and carrier gas. For the source cell geometry shown in **Fig 6-5b**, $A_0 = 0.16$ sccm was determined using the Chemical Reaction Engineering module of COMSOL Multiphysics® (COMSOL, Burlington, MA) finite element analysis software, assuming an organic species with a molar mass of 500 g/mol and a molecular diameter of 1 nm in an N_2 carrier gas at 240˚C.[64]

Equation 6.11 can be reduced to dimensionless form to yield eq. 6.13, where $\eta = J/(kP_V^*)$, $q = Q/A_0$, and $p = kP/A_0$. The dimensionless rate of organic vapor generation, η, is plotted in **Fig. 6-6**. As suggested by eq. 5.7, flow rate q approximately scales as p^2 due to the resistance to flow downstream from the vapor source. Diagonal lines expressing this relationship are plotted. These lines depict the operating points available to print heads characterized by varying conductance.

$$\eta = \frac{q}{(q+1)p+q} \tag{6.13}$$

If $q \propto p^2$, then η is maximized for $q = 1$, in which case $\eta = 1/(2p+1)$.[64] For, $q < 1$, increased carrier gas flow increases the rate of convection of organic vapor out of the source cell. For $q > 1$, this effect is offset by slower diffusive transport of organic vapor into the gas stream due to increased pressure. Organic vapor is entrained at an optimal rate for $Q = A_0$. The rate at which organic vapor is produced depends on the pressure required at the material source to drive a flow of Q through structures downstream of the source. Less pressure is required to drive carrier gas through a print head that is more conductive to flow, therefore a more conductive print head can deposit material more rapidly. The gas flow model developed in eqs. 6.1-6.8 can also be incorporated into the mass transport model to generate a system of equations that can be solved numerically.

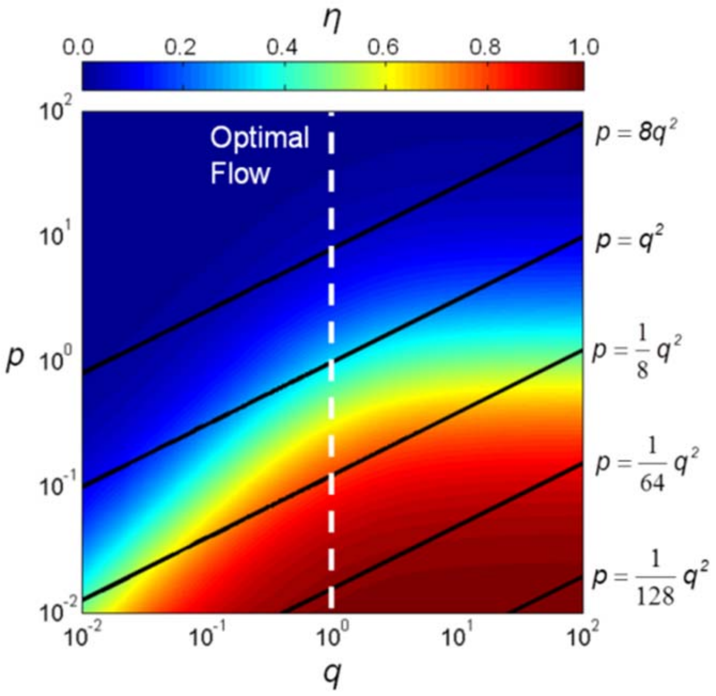

Figure 6-6: Vapor generation as function of source cell pressure and flow rate. The dependence of non-dimensional organic vapor generation rate η on the non-dimensional pressure p and flow rate q is given by eq. 6.10. Optimal flow rate is depicted by the white line. Operating lines showing the p required to drive a flow rate q through print heads with different conductivty c are shown in black, assuming a scaling of $q = cp^2$. (From McGraw and Forrest)[64]

6. 5 Deposition Rate Model

The more complex flow model described by eqs. 6.1-6.8 can be joined to the vapor generation model in eq. 6.11 to create a system of equations that can be solved numerically. These equations can be used to predict deposition rate and doping ratio for an OVJP system, generating an operating envelope, **Fig. 6-7**, in terms of host and guest source carrier gas flow rates. For the system used in this study, with a fluidic network as described in **Fig. 6-3** and a source geometry described in **Fig 6-5**, a deposition rate is 1.8 x 10^{-10} mol/s for g =10 μm at flow rate Q_S =0.18 sccm in both source cells. This is close

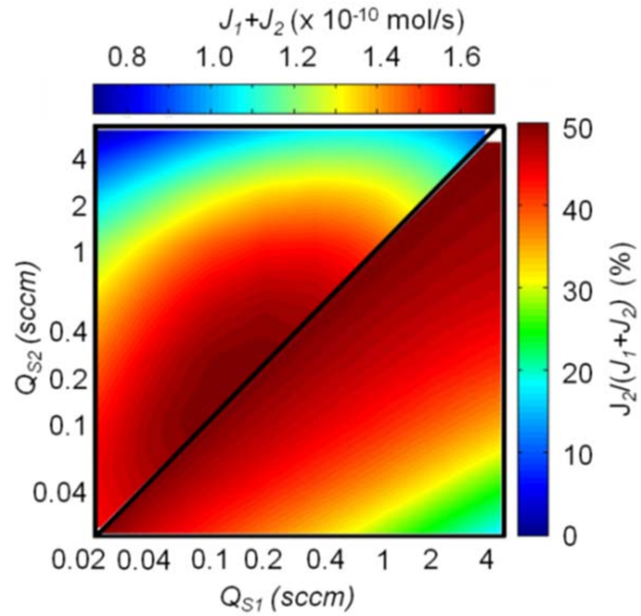

Figure 6-7: Operating envelope for OVJP. Calculated rates of deposition (top left) for a host, J_1, and guest, J_2, are determined using the flow model developed in eqs. 6.1 to 6.8 and the mass transport model in eq. 6.11. Values were calculated assuming that both the host and guest had P^*_V of 10^{-5} Pa at deposition pressure, creating a symmetric system. The guest to host doping ratio produced for a given set of Q_{S1} and Q_{S2} is shown in the lower right. (From McGraw and Forrest)[64]

to the value of $Q_S = A_0 = 0.16$ sccm predicted by the simple scaling of $Q_S \alpha \ P_1^2$. The predicted deposition rate of 1.6 x 10^{-10} mol/s at Q_{S1} = 1.5 sccm and Q_{S2} = 0.5 sccm is considerably higher than the observed deposition rate of 7 x 10^{-11} mol/s. This factor of two discrepancy is reasonable considering differences between the actual thermodynamic properties of CBP and Ir(ppy)$_3$ and the generalized organic material properties used for the calculation.[64]

Since the maximum obtainable deposition rate is $\eta = 1/(p+2)$, minimizing the pressure drop through the print head is essential. The analytical model can be used to identify regions of high flow resistance. The pressure drop through the microchannels constitutes nearly 30% of the total. Relatively shallow, 100 μm deep channels were chosen for ease of fabrication, although deeper channels are possible. Increasing channel depth can dramatically reduce resistance to flow due to the dependence of Q_S on h^3, as shown in Eq. 5.7. The pressure drop across the converging nozzle array itself is minimal. Pressure drop across non-converging nozzles is, however, significant. A pressure drop of P_3-$P_4 \approx 20$ Torr would be required to achieve a flow rate of $Q_M = 2$ sccm through an array of ten straight walled nozzles with 20 μm wide, 100 μm deep inlets.

High-resolution printing requires positioning nozzles within a distance approximately equal to the smallest feature size. A narrow gap of $g \sim 10$ μm is required for high resolution printing, in which case most of the pressure drop occurs within the nozzle-to-substrate gap. One strategy to reduce flow restriction is to etch an outer taper around the nozzle apertures that is parallel to their inner taper, as in a C-T nozzle, thereby reducing l_G to 20 μm or less. The relationship of P_1 versus Q_M for such a nozzle geometry at $g = 10$ μm is shown in **Fig. 6-4**.

The rate of organic vapor production can be coarsely controlled by adjusting the temperature of the sources. Equilibrium vapor pressure P_V^* and therefore vapor production rate J are related to source temperature T by eq. 6.10.[98] The enthalpy of vaporization, ΔH^{VAP}, and coefficient, P_0, are material specific. Organic vapor pressure changes rapidly with T, approximately doubling for every 10 °C increase. Adjusting the carrier gas flow to control deposition rate is largely ineffective, since the operating points of the print head are nearly tangent to the contours of constant organic vapor generation rate, **Fig 6-6**. The result of this is clear in the upper left corner of **Fig 6-7**. Deposition rate is relatively insensitive to carrier gas flow rate over its range of operation and does not change monotonically. Instead, it reaches a maximum value when host and dopant source flow rates are both equal to A_0. Fine control of J is perhaps best achieved through the use of a variable geometry source that can adjust the value of A_0. This could be realized through a movable curtain between the organic material and carrier gas stream.

For g =10μm, the majority of the pressure drop is downstream from the mixing channel; therefore P_l in the vapor source is primarily determined by the sum $Q_{S1}+Q_{S2}$. Consequently, the fraction of material 2 in the deposited film can be controlled by adjusting Q_{S2} for a fixed value of Q_{S1}, provided that $Q_{S2} < Q_{S1}$. A modest change in Q_{S2} adjusts the rate at which vapor leaves that source without significantly changing its diffusivity. This effect can be observed in the lower right section of Fig **6.7**.

6.6 Dynamical Model

When dealing with very small rates of flow, it becomes crucial to minimize the volume of regulated gas flow in order to make a controllable system in which evaporated organic material has a reasonably low residence time. The residence time of carrier gas and entrained organic is approximately $\tau = N/Q$ where N is the quantity of carrier gas within the volume of the print head and organic vapor source cells and Q is the carrier gas mass flow rate. If carrier gas is governed by an ideal gas law, eq. 6.14 results, where V is the volume of controlled carrier gas flow and T is its temperature. If Q $=CP^2$ as implied by eq. 5.7, then the result is eq. 6.15, where C is a proportionality constant.

$$\tau = \frac{VP}{QRT} \tag{6.14}$$

$$\tau = \frac{V}{CPRT} \tag{6.15}$$

Two major practical considerations arise from the finite time constant τ at which this system responds to changes in gas flow. The first is that the volume over which gas mass flow is controlled must be kept as small as possible. Therefore, mass flow controllers should be brought close to organic vapor source cells. Secondly, a "Eustachian tube" vent line, that connects the organic vapor cell upstream of the nozzle membrane with the deposition chamber, is required to provide a low impedance pathway to evacuate organic vapor source cells as the chamber pumps down. Otherwise, a damaging pressure differential can form across the nozzle membrane.

6.7 Mechanical Model

The mechanical design of the print head accounted for stresses from three major sources. The first of these was sealing a removable print head to vapor sources that are a permanent part of the deposition chamber. The high temperatures required for deposition necessitated a hard perfluoroelastomer such as Dupont Kalrez®. Kalrez O-rings require 12-18% compression for a proper seal, that in turn corresponds to a clamping pressure of approximately 1 MPa.[102] A robust metal backing for the micronozzle array is required to apply this pressure.

Thermal stress of the layered nozzle membrane, a borosilicate glass interlayer, and metal backing were considered next. Kovar® controlled expansion steel was chosen as a backing material, since its coefficient of thermal expansion of 4.9×10^{-6} K^{-1}[103] is well matched to both Si, 2.6x10^{-6} K^{-1}, and borosilicate glass, 4.0 x10^{-6} K^{-1}[54] over the range of operating temperatures of the print head. If the nozzle membrane is mounted to its backing by a bond formed near operating temperature, the stack will be flat at operating temperature. The metal backing provides compressive stress at room temperature. The nozzle array is positioned near the center of the structure, both to ensure that the variation in height over the nozzle array due to curvature is minimized, and the nozzle array is not obstructed from contact with the substrate.

Finally, the ability of the nozzle membrane itself to withstand the pressure of the carrier gas must be considered. The silicon nozzle membrane is modeled as a one dimensional beam of infinite width fixed at its two ends and bearing an evenly distributed load. The expected beam deflection is given by eq. 6.16.[101] The Young's modulus for Si is E =130 GPa.[104] A l =1 mm wide, h =50 μm thick membrane is expected to have a maximum deflection of 50 nm at its center at an operating pressure of 70 Torr. Pressure of the carrier gas does not significantly affect its shape. The burst strength of such a Si membrane is estimated to be on the order of an atmosphere, making a Eustachian tube a necessary precaution.

$$w = \frac{Pl^4}{12Eh^3} \tag{6.16}$$

6.8 Summary

The rate at which organic vapor is generated by sources depends on both carrier gas pressure and flow rate through each source. Closed form expressions relating pressure drop and carrier gas flow rate were derived by breaking the flow path in the OVJP print head into individual fluidic elements and developing a semi-analytical model for each element. Elements were then linked together in an equivalent circuit. The flow conductivity predicted by this model agrees with that experimentally observed in the OVJP tool. The closed form solution for carrier gas flow is then combined with the material source model to develop expressions for deposition rate and doping ratio.

Carrier gas flow rate Q through the print head scales approximately with the change in the square of pressure $\Delta(P^2)$. Assuming this scaling and diffusion limited transport of organic vapor in the source cell, the maximum rate of organic vapor generation is achieved when carrier gas flow through a source $Q_S = A_0$, where A_0 depends solely on the geometry of the source cell and the thermodynamic properties of the material deposited. Controlling Q_S does not provide much leverage over deposition rate, however doping can be controlled by adjusting the ratios of Q_S between the host and dopant source for constant total flow rate. Overall deposition rate can be best controlled by organic vapor source temperature.

The nozzle membrane requires finite time to adjust to changes in chamber pressure or carrier gas flow rate, since it significantly impedes the gas flow between the sources and chamber. This latency can result in pressure buildups during chamber venting and pump down that can damage fragile membranes in the print head. Consequently, the volume of the organic vapor source cells should be kept as small as possible to minimize this latency time. A low impedance valved connection between the organic vapor sources and deposition chamber further mitigates this problem.

Chapter 7

Micronozzle Array Construction

7.1 Overview

Photolithographic microfabrication techniques provide a path to obtaining the small features and scalability necessary for practical OVJP nozzle fabrication. Micron scale tolerances can be maintained over tens of square centimeters. Microfabrication techniques also allow chemically inert materials with low coefficients of thermal expansion such as Si and borosilicate glass can be used in OVJP nozzle arrays. Microfabrication by photolithography is inherently scalable, since the marginal cost to adding additional features to a mask is negligible and large numbers of nozzle dies can be produced in batches. Using various etch techniques, nozzles themselves can be designed with a microstructure to minimize resistance to flow for a given aperture size. As shown in the last chapter, low resistance to flow is critical for achieving high printing speeds.

A nozzle array fabrication process must solve two basic problems. First, it must allow features to be micro-machined into the front and back of a delicate Si membrane. This is solved through the use of "handle" wafers. The membrane begins the process as the device layer of a silicon-on-insulator (SOI) wafer. Its face is then sealed to a Pyrex® wafer as described in the process flow summary in **Fig. 7-1**. The second issue that must be addressed is "chip to world" interfacing; the microfabricated structure must seal to a conventionally machined fixture. The anodic bonding can be used to make a glass to metal joint between a microfabricated die and its carrier plate. A gold eutectic solder joint offers a more general solution suitable for joining Si directly to metal.

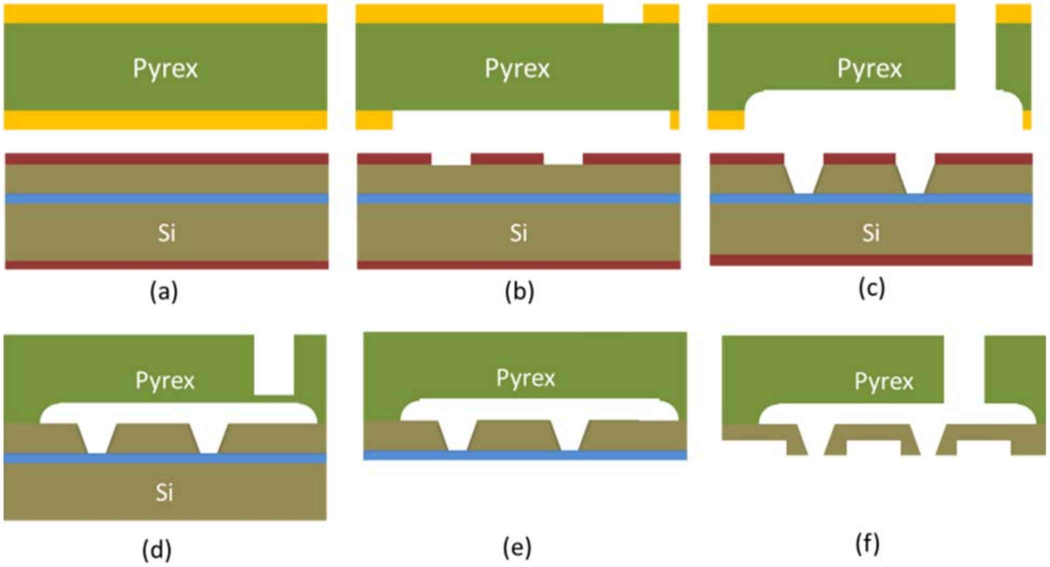

Figure 7-1: Overview of nozzle membrane fabrication process. (a) Nozzle membranes begin as two wafers coated in hard masks. One is a 500 µm thick Pyrex® flat, the other is a Si on insulator (SOI) wafer with a 100 µm device layer. (b) Hard masks are etched. (c) Nozzle inlets, microchannels, and vias are etched. (d) Hard masks are removed and wafers are bonded to form sealed channels. (e) Handle layer of SOI wafer is removed. (f) Relief channels are etched into the underside of the nozzle membrane. These steps are elaborated in Ch. 7.2.

7.2 Integrated Nozzle and Microchannel Fabrication Process

A hard mask consisting of a 100 nm thick layer of Si_3N_4 is deposited on a 100 mm diameter silicon-on-oxide (SOI) wafer with a 100 µm thick device layer. Wafers are RCA cleaned prior to deposition as is required for CMOS processing.[105] Low pressure chemical vapor deposition is used to deposit Si_3N_4 at a rate of 50 Å/min. Film thickness was confirmed using spectroscopic reflectrometry.

The hard mask was patterned with an array of 135 by 315 μm rectangles using photolithography. The wafer was spin-coated with SPR 220-3.0 photoresist at 3,000 RPM and soft baked at 90°C for 90s. The mask pattern was transferred to the wafer with a 12 s exposure in a mask aligner set to soft contact mode. Resist was then developed by a 35 s spray of AZ-300 MIF developer in the ACS 200 tool. The Si_3N_4 layer was then etched in the MNF_Nitride_1 recipe in the LAM 9000 tool for 150s.

The patterned SOI wafer was etched using a KOH solution to selectively attack the <100> crystal plane of Si while leaving the <111> plane intact.[106] The resulting trenches are tapered inward at an angle of 54.7° from the <100> plane. A bath of 50% wt. aqueous KOH solution was heated to 85°C. The solution was covered with 3 cm of isopropanol to prevent the molarity of the etch solution from changing due to evaporation. Material is removed until the etched trenches extend to the insulator layer of the SOI wafer which acts as an etch stop. Etch progress is monitored by stylus profilometry and its completion is confirmed by observing the insulator layer, **Figs. 7-2a** and **b,** through an optical microscope. A 100 μm thick silicon membrane requires 120 min to etch to completion. The tapered inner surface produced by this etch is evident in the scanning electron micrograph in **Fig. 7-2c**.

A hard mask of 200 Å Cr and 5,000 Å Au was deposited on both sides of a 100 mm dia, 500 μm thick borosilicate glass wafers by e-beam evaporation. A second film of 200 Å Cr and 5000Å Au was then deposited on each side. The second film served to reduce pinhole defects and also to mask portions of the wafer covered by the clamp holding it during the first deposition. A second adhesion layer was included to reduce strain in the deposited film.[107] Prior to deposition, the glass wafers were cleaned for

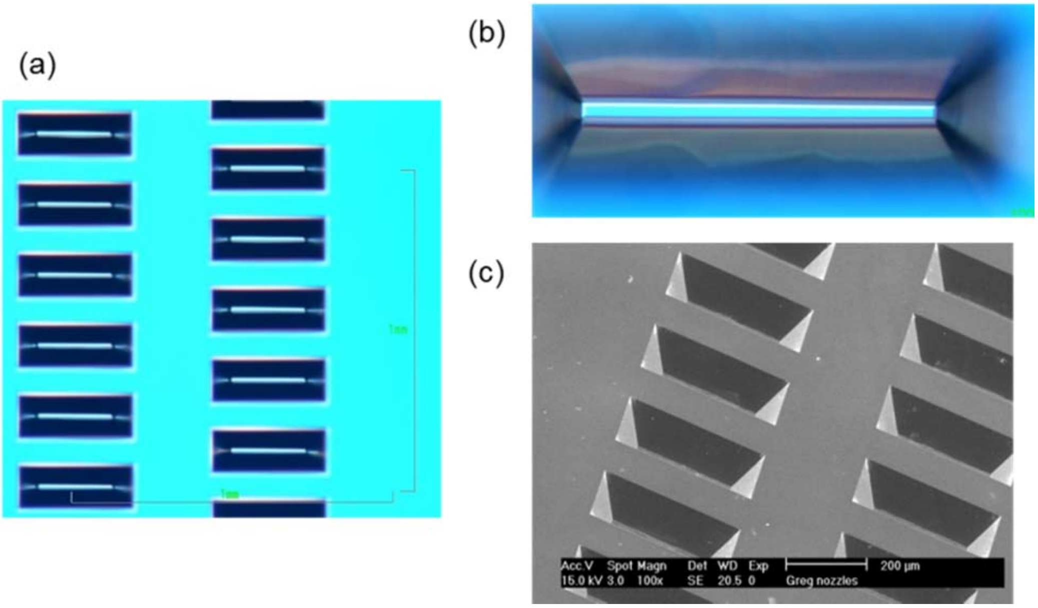

Figure 7-2: Anisotropically etched nozzle inlets on a Si membrane. (a), (b) The tapered sidewalls surrounding the insulator layer etch stop are visible by in optical micrographs and (c) A scanning electron micrograph clearly shows the tapered sidewalls of the nozzle inlets.

20 min in a 4:1 H_2SO_4:H_2O_2 solution. The wafer was then spin-coated with AZ-9260 Photoresist at 3000 RPM, leaving a 9 µm thick resist layer. The channel and via patterns were transferred to the wafer by a 60 s soft contact exposure. Channels were patterned without alignment on a centered contact aligner chuck. The wafer was then developed by a 90 s soak in AZ-400K developer and hard baked at 110°C for 20 min. The reverse side of the wafer was spin coated, exposed, developed, and baked as before. The pattern for gas entrance vias on the back of the wafer was aligned to fiducial markings on the channel side using a Karl Suss MA/BA-6 mask aligner with backside camera.

The outer layer of Au and Cr was removed by dipping in Transene GE-8148 for 3 min and Cyantech CR-14 for 1 min. This series was repeated to remove the inner layer of Au and Cr from both sides of the wafer. Photoresist was not removed since it provides additional protection against HF.[107] Wafers were immersed in a solution of 1:1 HF:H_2O for approximately 12 min to etch 100 µm deep channels. Etch progress was monitored by stylus profilometry. After a 100 µm etch was achieved, the channel side of the wafer was bonded to a dummy wafer with paraffin wax and the vias were etched to completion, requiring approximately 40 min. An etched glass flat is shown with and without its hard mask in **Fig. 7-3**. The wafers were cleaned in boiling trichloroethylene to remove wax and ultrasonicated in acetone to remove photoresist. Remaining portions of the hard masks were removed by a series of dips in GE-8148 and CR-14 etchants.

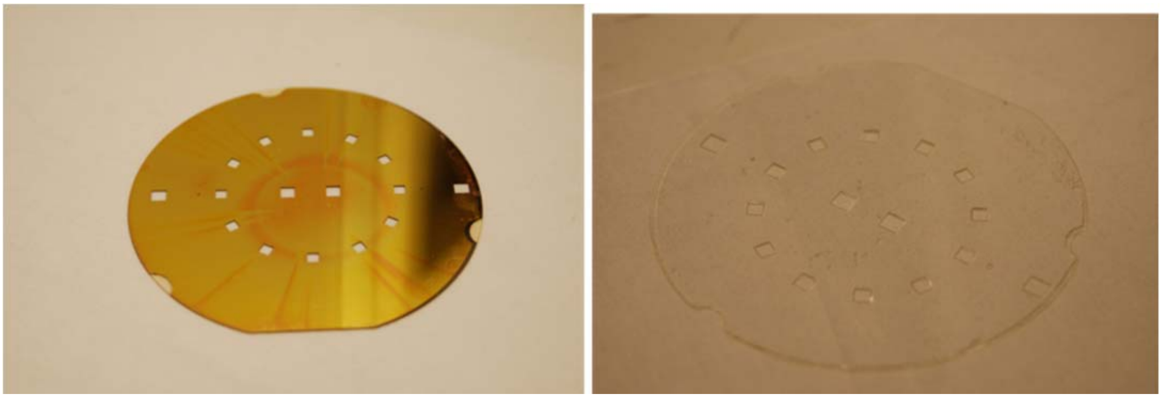

Figure 7-3: Deep etched Pyrex® flats. Microchannels and vias were etched into Pyrex® wafers using HF and a mixed Cr-Au-photoresist mask (shown at left).

The glass and SOI wafers were cleaned and then joined by anodic bonding under conditions of 400°C and 800V.[108] The wafers were cleaned with a 4:1 H_2SO_4:H_2O_2 solution and the Si wafer was dipped in dilute HF to minimize its native oxide prior to bonding. After bonding, the handle wafer was removed by deep reactive ion etching (DRIE).[109] The DRIE process selectively etches Si over SiO_2, allowing the insulator layer of the SOI wafer to again serve as an etch stop. The Surface Technology Systems Pegasus tool is capable of removing Si at 10 µm/s. Before the Pegasus became available, wafers were thinned using an HF-Nitric-Acetic acid "trilogy" etch.[110] Trilogy has poor Si to SiO_2 selectivity, so it was followed by a slower DRIE finishing step to remove the last 50µm of the handle layer. An example of a glass wafer bonded to a released membrane is shown in **Fig. 7-4**.

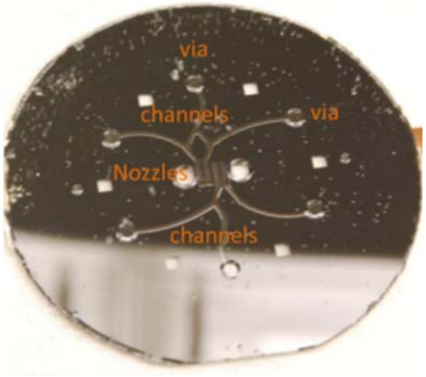

Figure 7-4: Nozzle membrane and channel plate. A glass wafer with micro-channels is bonded to a released Si membrane containing a micronozzle array.

Relief trenches were etched into the underside of the Si nozzle membrane after the handle layer was removed. After cleaning, the wafer was spin-coated with AZ-9260 photoresist at 3000 RPM. Thick resist was preferred since it provides an effective mask for DRIE, allowing it to supplement the SiO_2 etch stop that may be damaged during the wafer thinning process. It is also less prone to seep into the nozzles, which may be open prematurely during processing. The AZ-9260 is patterned using the same procedure as described for the Pyrex® layer, and the remaining SiO_2 layer is patterned by a 600 s plasma etch in the LAM 9000 tool using MNF_Oxide_1 recipe. Relief trenches are then etched 50 μm deep with DRIE to form C-R nozzles shown in **Figs 7-5** and **7-6a**. Depth is confirmed by stylus profilometry. Photoresist is then removed and the wafer is etched with 10% HF solution to remove remaining SiO_2. Finally, the wafers are cut into 50x25 mm dies, as shown in **Fig. 7-7.**

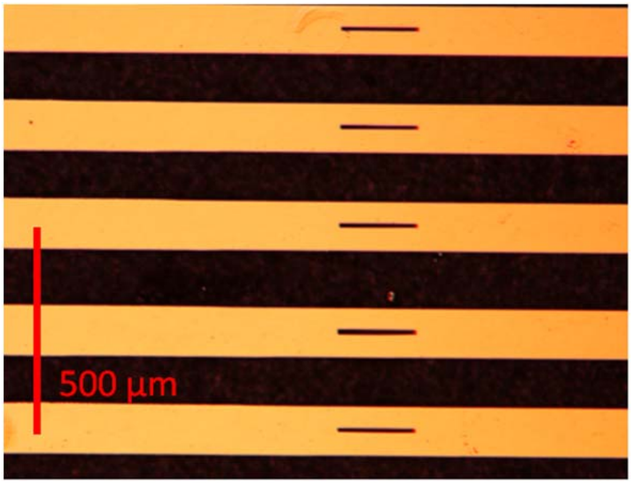

Figure 7-5: Micrograph of converging-relieved nozzles. Apertures are visible along centers of bright raised features. Dark regions between these features are straight walled relief trenches.

Features with tapered sidewalls can be fabricated on the underside of the membrane using ethylenediamene-pyrocatechol (EDP) etchant to make C-T nozzles, **Fig. 7-6b.**[111] Relief trenches between nozzles can be etched with a taper that matches the inner taper of the nozzles, reducing resistance to flow without sacrificing mechanical strength. Alternately, converging-diverging, or C-D, nozzles can be fabricated by etching the underside of the wafer with EDP, shown in **Figs. 7-8** and **9**. The <100> plane of Si is attacked by EDP in a manner similar to KOH, allowing it to produce a tapered outer nozzle surface parallel to the inner surface. EDP is a more viscous solution and the

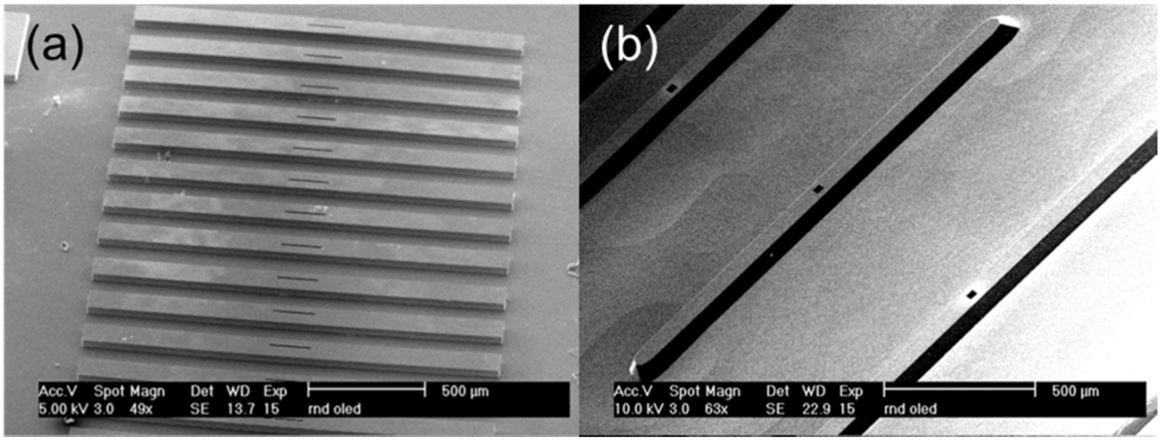

Figure 7-6: Nozzle membrane undersides prepared with different etch techniques. Scanning electron micrographs show the difference between (a) C-R nozzles with straight walled relief trenches, and (b) C-T nozzles with tapered relief trenches surrounding the nozzle apertures. Note that in this example, the C-T nozzles have square, rather than rectangular apertures.

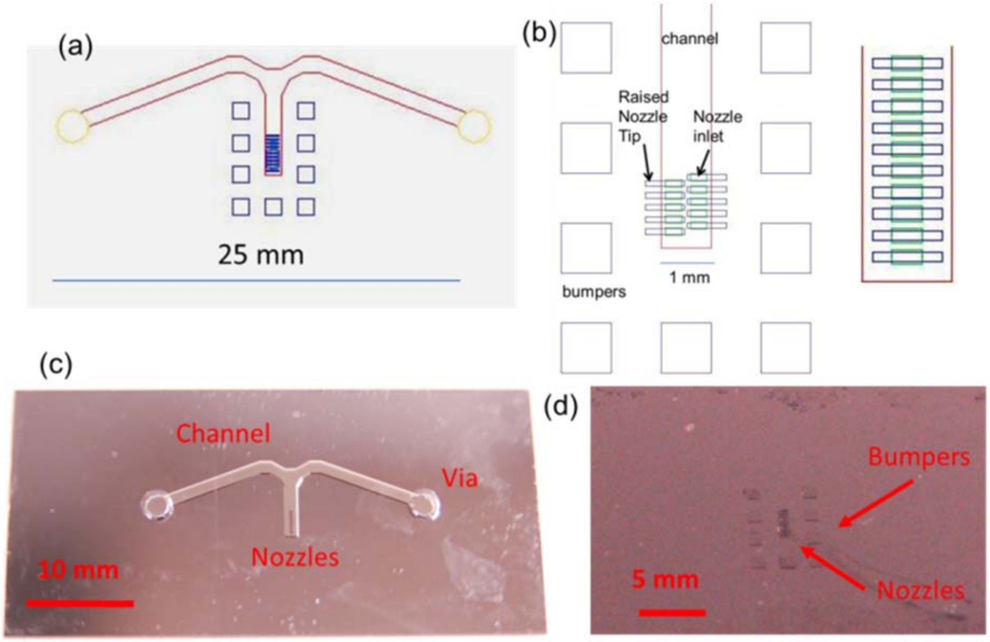

Figure 7-7: Layout of a micronozzle array die. The microchannels, vias, and nozzle inlets and outlets are defined photolithographically using mask patterns, such as those shown in (a) and (b). Photographs show the channel side (c) and nozzle outlet side (d) of a finished die.

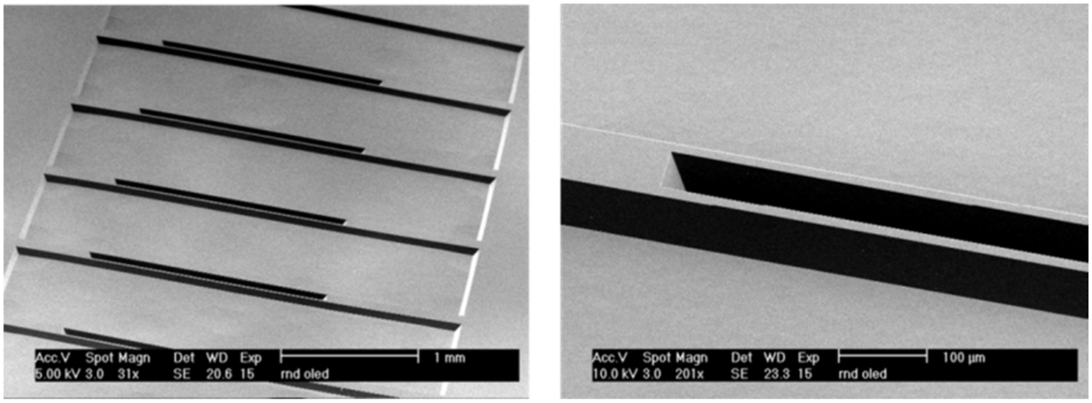

Figure 7-8: SEM of converging-diverging nozzle outlet. The outer aperture is 70x500 µm.

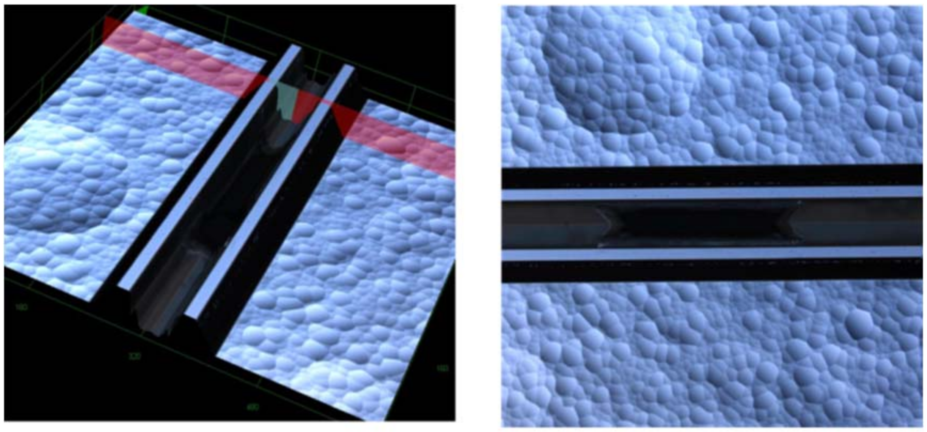

Figure 7.9 Rendering of a converging-diverging nozzle by optical profilometry. The 20x200 µm throat inside the aperture is apparent in the top view.

reagents have a higher degree of steric hindrance than KOH. Convex corners are aggressively attacked by KOH, which removes all unmasked Si not laying on a <111> plane. Since EDP does not open up new etch planes as aggressively, it is more suitable for etching convex corners into Si. Protection structures that mask additional material around convex corners to prevent them from being etched are still required.[112]

Tapered outer nozzle surfaces can be formed by etching the glass and Si wafer for 90 min in a 115°C refluxed bath of 192 ml deionized water, 600 ml ethylenediamine, 192 g pyrocatechol, and 3.6 g pyridine. The back surface of the nozzle membrane must be protected from this etchant. Furthermore, photoresist cannot be used in place of the SiO_2 layer mask to protect Si structures since EDP is an alkaline solution.

7.3 Packaging

In order to interface with the manifold containing the organic vapor sources, the die must be mounted on a robust holder that can be used in a high vacuum chamber. Developing a method for this proved perhaps the single most challenging aspect of the project. The first approach was to clamp the microfabricated channel and nozzle plate to an organic vapor source manifold with a high temperature elastomer seal between the two. This proved impractical due to both the brittleness of the microfabricated dies and geometric constraints imposed on the clamping hardware so that it does not interfere with substrate positioning. The next method used to attach dies to the organic vapor source manifold was to use high temperature epoxy (Cotronics, Brooklyn, NY). While the system was operable and it was possible to get initial patterning and device data,[63] concerns about outgassing from the epoxy motivated the search for a more satisfactory sealing process.

7.3.1 Anodic Bond

The first of these was to perform a second anodic bonding step that attached the wafer to a metal plate that is sufficiently robust to form an O-ring seal with the organic vapor source manifold.[113] Anodic bonding joins an electrolyte bearing glass to a metal or semiconductor that readily forms an oxide. The formation temperature of anodic bonds is relatively low compared to methods such as fusion bonding. An anodic bond can also be heated to its formation temperature repeatedly without losing strength. High platen pressures are not required for anodic bonding, so it is not only more tolerant to small deviations in thickness of the bonded pieces[114] but it is also less destructive to substrates with raised surface topography.

To form an anodic bond, the two materials to be fused are placed in a press and heated to between 300 and 400°C, sufficient to mobilize Na^+ in the glass. A potential of 800-2000V is then applied to the metal or semiconductor component, causing ions in the glass to migrate away from the bonding surface. Opposite charges on the two surfaces attract and pull them into intimate contact. The migration of Na^+ leaves dangling O^- on the bonding surface of the glass. These negative ions oxidize the anode material on the adjacent surface to form a permanent chemical bond. To bond effectively, both materials must have similar coefficients of thermal expansion over a range from room temperature to the bond formation temperature.[115]

The metal carrier plate for the nozzle array was fabricated from hot rolled Kovar® plate stock to minimize residual stress. After the piece was drilled with vias and bolt holes, its surfaces were ground to a flatness tolerance of ± 15 μm. The bonding surface was then lapped with 12 μm calcined aluminum oxide slurry over a slotted iron plate until an even matte finish was achieved. This required approximately 90 min with the lapper jig applying 5 kg weight and the plate spinning at 30 RPM. The plate was subsequently lapped with 9 μm and 3 μm slurries for 30 min each, under the same conditions. The plate was then polished with 1 μm slurry and a polishing pad until an even specular finish was achieved, requiring approximately 90 min. Following polishing, the plate was ultrasonicated, boiled in a 2% NH_4OH solution and solvent cleaned.[64] The dies containing the nozzle membranes are RCA cleaned prior to bonding to remove Na_2O precipitates from the glass surface formed by the previous bond.[116] Qualification by AFM, **Fig. 7-10**, showed that the plate had an RMS roughness of less than 10 nm.

The nozzle membrane and channel plate dies were bonded to the Kovar® carrier plate at 300°C, with voltage ramped at 50°C/min from 300 to 1,200V. A slow voltage ramp helped to reverse the electrolyte migration created by the previous bonding step and to minimize arcing of current across the electrolyte depleted glass due to dielectric breakdown.[117][64] Despite the slow ramp, some degree of arcing was unavoidable, as shown in **Fig-7.11**. A working bond requires minimal arcing, since arcs are sites of resistive heating, and thermal expansion can initiate cracks. The oxidation potential of the Fe in Kovar® is less than that of Si.[116] Therefore a glass-to-metal anodic bond can be formed after the glass-to-Si bond without reversing the oxidation that formed the first bond.[118]

Glass-to-metal anodic bonding is a die level bonding technique.[119] An example of a successful bond is shown in Fig. **7-12a**. Attempts to expand it to join large (> 10 cm^2) channel plates to carrier plates were not fully successful due to the persistence of cracks. Glass channel plates large enough to accommodate multicolor printing could not be reliably joined to metal carrier plates. To achieve multicolor printing, a simplified print head fabrication process was devised. The holder was also redesigned to minimize the surface area of die-to-metal bonding required.

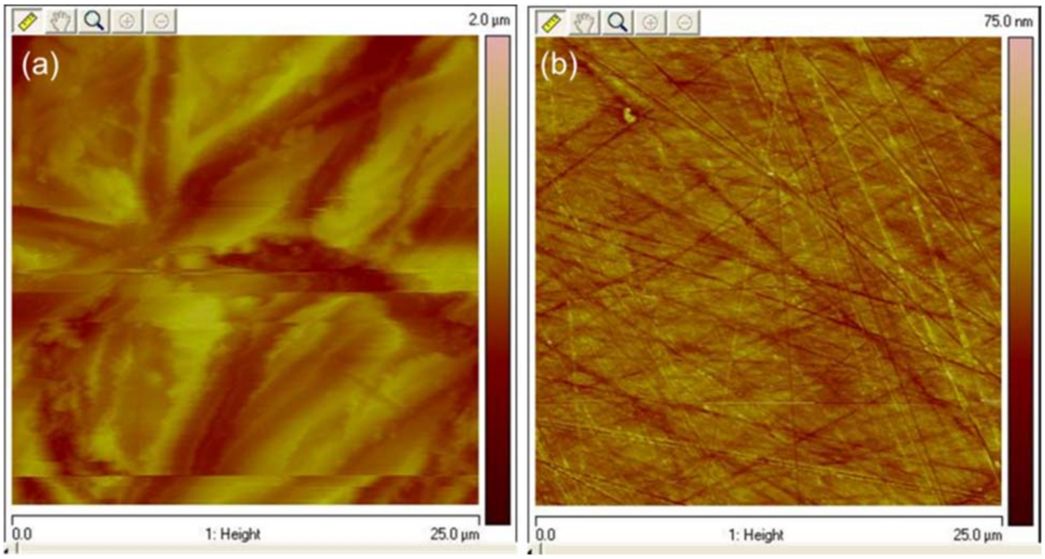

Figure 7-10: Surface roughness of the metal carrier plate. (a) A ground Kovar® plate has micron scale surface features plate prior to finishing. (b) The RMS roughness of a lapped and polished plate before bonding is less than 5 nm.

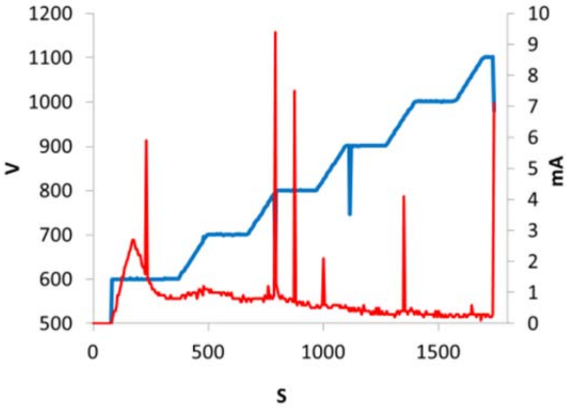

Figure 7-11: Current and voltage log from a glass to metal anodic bond. Voltage (blue) and current (red) through the die change as a function of time during the bonding process. Voltage is slowly ramped in steps and average current decreases as the bond goes to completion. Arcing of current through the glass, as indicated by current spikes, persisted despite slow voltage ramp.

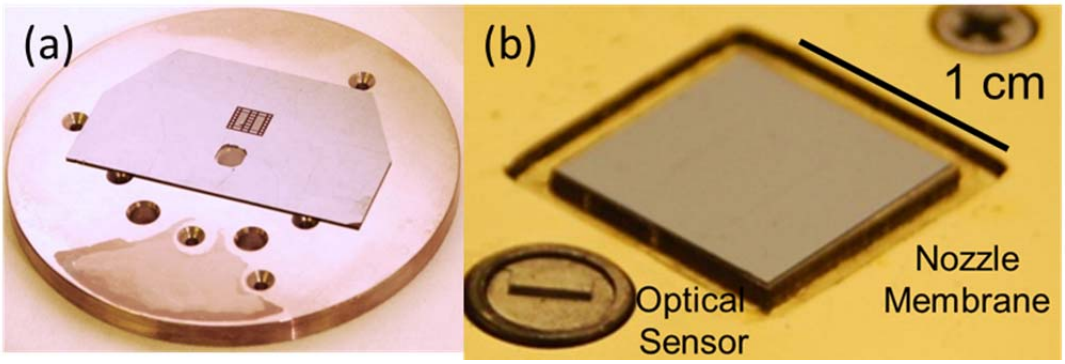

Figure 7-12: Mounted OVJP print heads. (a) A nozzle membrane with integrated microchannels is anodically bonded to a polished Kovar® disc with vias to permit flow of carrier gas to the microchannels. (b) A nozzle membrane without microchannels is mounted to a carrier plate by Au eutectic bonding.

7.3.2 Soldered Nozzle Membrane

Enclosed cavities were machined directly into the Kovar® carrier plate to serve as source and mixing channels for two separate host and dopant material sets. Host and dopant channels, 2 mm in diameter, transported and mixed organic vapor vapor. The channels connect to trenches that distribute vapor to the nozzles. This setup will be further described in Chapter 8. The plate was machined with two sets of channels and trenches so that two colors could be printed simultaneously. The nozzle membrane was reduced to only $(1\ \text{cm})^2$ and contained two rows of nozzles, each corresponding to a trench on the carrier plate. A bonded nozzle membrane is shown in **Fig. 7-12b**.

Nozzle membranes are fabricated using the same procedure as before. Etched microchannels, however, are not required. The SOI wafer is anodically bonded to a blank glass flat to provide mechanical strength prior to removing the handle wafer. After dicing and prior to bonding, the borosilicate back is removed from a diced nozzle membrane square with a 120 min 1:1 $HF:H_20$ etch. The Kovar® plate and Si die are soldered together in a heated press using an Au-Ge layer of eutectic composition. Each mating surface is coated with a 20 nm thick Cr adhesion layer and a 30 nm thick Pt diffusion blocking layer to prevent diffusion of Au atoms into the Si membrane.[120] Two sets of alternating 266 nm Au and 160 nm Ge layers, and a 133 nm thick Au capping layer are then deposited by e-beam evaporation. Thicknesses of Au and Ge are chosen to match an 88% Au by weight eutectic alloy that melts at 361°C. The plate and nozzle membrane are joined under high vacuum at 400°C and 3 MPa platen pressure for 60 min. Platen pressure is then released and the bonder is vented and air cooled.

The contrast between the unheated metal stack in **Fig. 7-13a** and the soldered joint in **Fig. 7-13b** is clear. The metal solder anneals into a uniform film that joins the two surfaces. The eutectic creates a liquid layer capable of reflow to accommodate non-

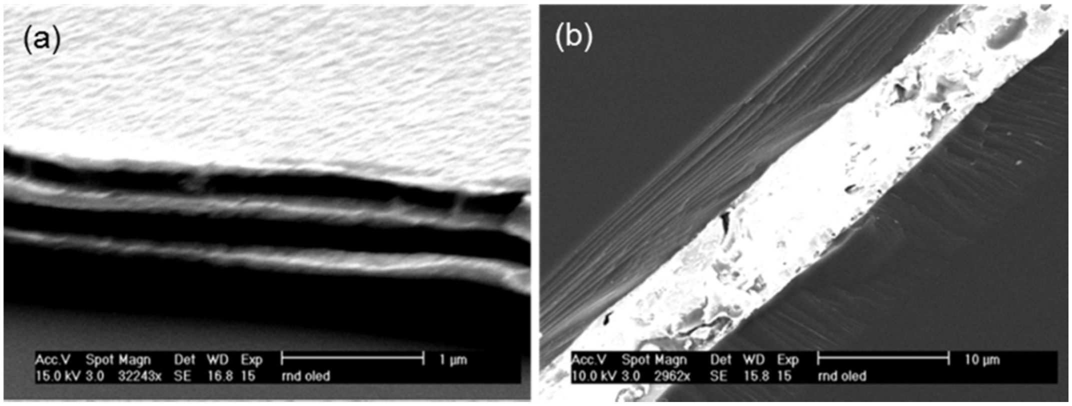

Figure 7-13: Deposited metal layers and soldered joint. (a) A scanning electron micrographs shows a stack of alternating Au and Ge layers deposited on a Si test die. (b) Two Si dies were soldered together at 400°C and 3 MPa pressure. The joint was imaged by cleaving the joined dies. Note that joint is approximately 2 μm wide, but appears wider due to viewing angle.

uniformities between surfaces. Reflow can be observed in a 5 μm thick ripple of solder approximately 1 mm from the edge of the die. The absence of a fillet close to the die suggests that solder is wicked underneath the die as it cools. A thinner joint may be possible if piston pressure is maintained throughout the cooling process.

Eutectic bonding is widely used for applications such as joining integrated circuits to heat sinks. One drawback of eutectic bonding is that surface topography on the nozzle membrane can lead to unevenly applied bonding force. Regions of poor bonding can form due to locally low pressure. Eruptions of eutectic liquid through trenches in the Si membrane can also occur due to an absence of pressure to reinforce it. While this was observed at bonding pressures of 5 MPa and greater, it was not a problem at 3 MPa. In fact, a membrane sparsely populated with raised features, as shown in Fig. **7-14** was successfully soldered to a Si base layer. The bonded die was cleaved prior to imaging.

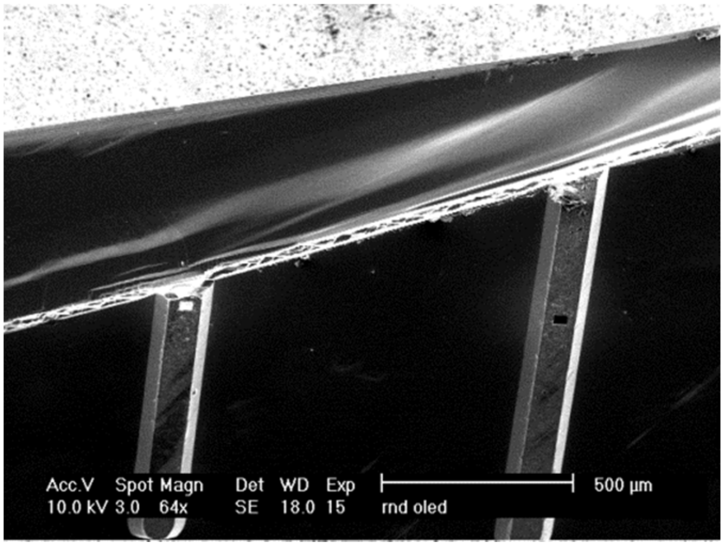

Figure 7-14: Nozzle membrane soldered to silicon wafer. A consistent bond is formed despite the uneven pressure placed on the joint during by the surface topography of the membrane.

Note that the cleave of the membrane follows the cleave of the Si base layer, indicating that the soldered joint has comparable strength to the base material.

7.4 Summary

Arrays of micronozzle inlets were etched into a 100 μm thick Si membrane formed by the device layer of an SOI wafer. Flow restriction was minimized for a given aperture width by using a KOH solution to anisotropically etch converging inlets. The membrane was then transferred from a sacrificial Si handle wafer to a glass flat using anodic bonding. Nozzle outlets, relief trenches, and other features then fabricated on the opposite face of the membrane using a variety of anisotropic etch techniques to produce different surface topographies that influence carrier gas flow.

Two basic designs of nozzle arrays were fabricated. The first type featured a glass layer with etched microchannels to distribute organic vapor to the nozzles. This glass and Si structure was affixed to a metal carrier plate by either an adhesive or an anodic bond. This method could not be scaled to seal multicolor nozzle arrays, leading to the development of second nozzle array architecture. This consisted of a single layer Si membrane diced into 1 cm squares and sealed with a gold eutectic solder joint to a metal fixture containing integrated distribution channels for organic vapor. In both designs, the nozzle array and its carrier plate combine to form a print head that can be integrated with a high vacuum deposition system described in the next chapter.

Chapter 8

The OVJP Chamber

8.1 Overview

A significant aspect of micronozzle based OVJP is the need to interface a microscopic system, an array of photolithographically fabricated nozzles, with the macroscopic printer system. Hardware designed to handle rarefied gases has a large characteristic dimension and designing a “chip to world” interface capable of bridging these scales while operating at temperatures in excess of 300°C is a significant challenge. The sealing techniques described in the previous chapter mate the OVJP nozzle membrane to a robust metal carrier plate that can be installed in a high vacuum deposition system. The deposition system must provide the print head and its organic vapor sources with regulated carrier gas flow and multiple independent zones of temperature control. It must also be capable of sensing the distance between the substrate and nozzle array and positioning the substrate precisely. The design and construction such a deposition system is described in this chapter.

Specialized hardware is also required to characterize substrates fabricated by OVJP. The construction of a high spatial resolution linescanner capable of measuring the emission spectrum from an array of micro-printed OLEDs is also described.

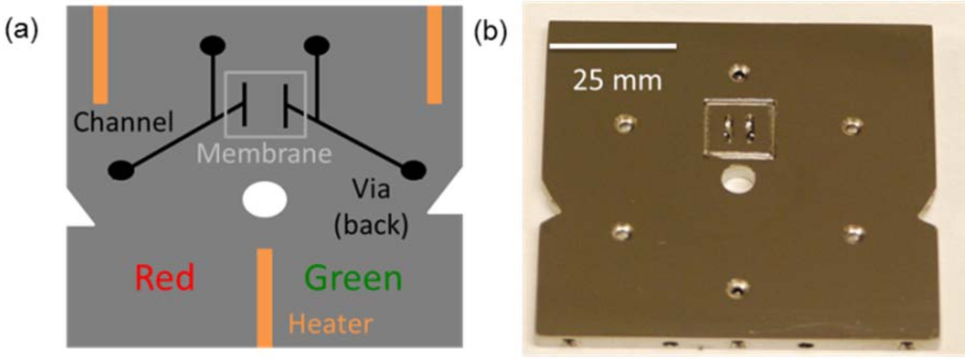

Figure 8-1: Metal carrier plate for nozzle membrane. (a) The plate contains two sets of drilled host and dopant channels that terminate into feed trenches over which the nozzle membrane is affixed. It also contains integrated heaters. (b) The nozzle membrane is fabricated from Kovar®. The trenches and surrounding fiducial markings are visible.

8.2 Carrier Plate

The nozzle membrane was bonded to a carrier plate fabricated from 6 mm hot rolled Kovar® plate as described in the previous chapter. Together, these two pieces, the nozzle membrane and plate, comprise the OVJP print head. Two different plates were used. The first, shown in **Fig. 7-11a**, was used with nozzle membranes featuring microchannels. It was sized to fit dies as large as 100 mm in diameter. It contained six drilled vias for organic vapor, and a cutout for mounting an optical displacement sensor.

The second type of carrier plate was used with silicon membranes attached by Au eutectic bonding, as described in the Ch. 7.3.2. This was also fabricated from 6 mm hot rolled Kovar® plate. Gas flow was distributed from the organic vapor sources to the micronozzle arrays through a pair of 1 mm wide conventionally machined trenches. The two trenches provided separate host and dopant mixtures to the two arrays on the nozzle membrane. The trenches were each connected to a 2 mm diameter mixing channel formed by the intersection of a host and dopant source channel on each side, **Fig. 8-1a**. Vias on the reverse side of the plate allowed vapor to flow into the channels. The print head also contained integrated ports for resistive cartridge heaters and thermocouples, as well as a central cutout for the optical displacement sensor. A fiducial rectangle cut into the sealing surface guided placement of the nozzle membrane, **Fig. 8-1b.** The sealing surface was raised 0.3 mm relative to the rest of the plate in later versions to facilitate surface preparation and reduce heat transfer between the print head and substrate holder.

The print head is sealed to a vapor source manifold by Dupont Kalrez® perfluoroelastomer O-rings thermally rated to 350°C. The O-rings were compressed by a six bolt circle connecting the carrier plate to the manifold, as shown in **Fig. 8-2**. Each of the six 8 mm source tubes on the manifold was sealed by a separate #14 O-ring.

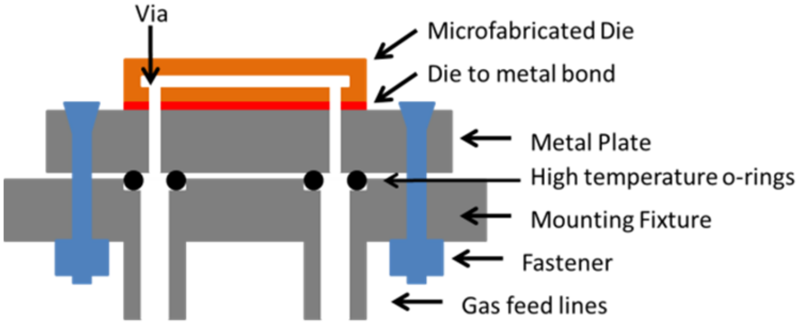

Figure 8-2: Diagram of sealing mechanism between the print head and chamber.

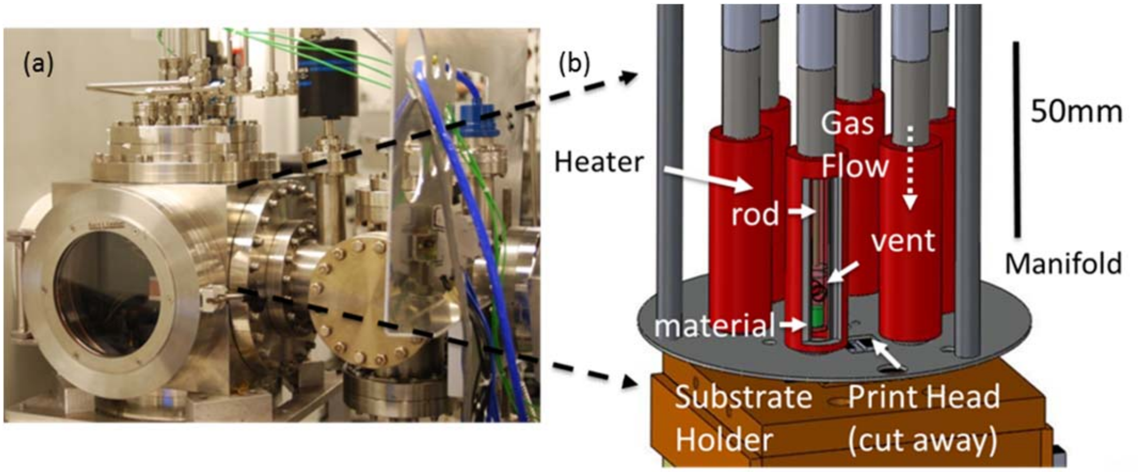

Figure 8-3: The Organic Vapor Jet Printing tool. (a) A photograph shows the exterior of the deposition chamber. The feedthrough holding the print head and manifold is visible at its top. (b) A computer rendering shows the organic vapor source manifold inside the chamber that connects the print head to the feedthrough. Portions of the vapor source cell and flange are cut away.

8.3 Deposition Chamber

The print head operates inside a vacuum deposition chamber **Fig. 8-3a**, with a base pressure of $1\text{x}10^{-5}$ Torr. The typical operating pressure of the chamber under deposition conditions is $4\text{x}10^{-4}$ Torr, with spent carrier gas being rapidly swept out of the chamber by a turbomolecular pump. The print head is attached to the chamber by an organic vapor source manifold that contains sublimable organic material, **Fig. 8-3b**. The manifold consists of six tubes, each containing a separate organic vapor source, that are laser welded at their bases to a circular Kovar® flange containing attachment points for the print head. Each source consists of an 8 mm diameter stainless steel tube wrapped with resistive heat rope. Supplemental resistive heat rope was also applied to the upper surface of the flange when required. Print heads containing glass microchannels were heated in this manner. Temperature was measured from a thermocouple port on the manifold in this case.

Organic material is contained in vented vials mounted at the end of 6 mm dia. Pyrex® tubes. The vials have two 3 mm diameter drilled vents on opposite sides. A 2 mm long pinched region in the glass tube creates a vacuum seal that isolates the vial from the rest of the tube. A thermocouple is inserted into the far end of each tube so that it is in thermal contact with the pinch point on the atmospheric side. When combined with the heaters, these thermocouples permit independent temperature control for each organic vapor source. A cutaway rendering of this organic vapor source is shown in **Fig. 8-3b.** The manifold is shown in **Fig. 8-4** with potted Nichrome® source heaters, prior to installation in the chamber.

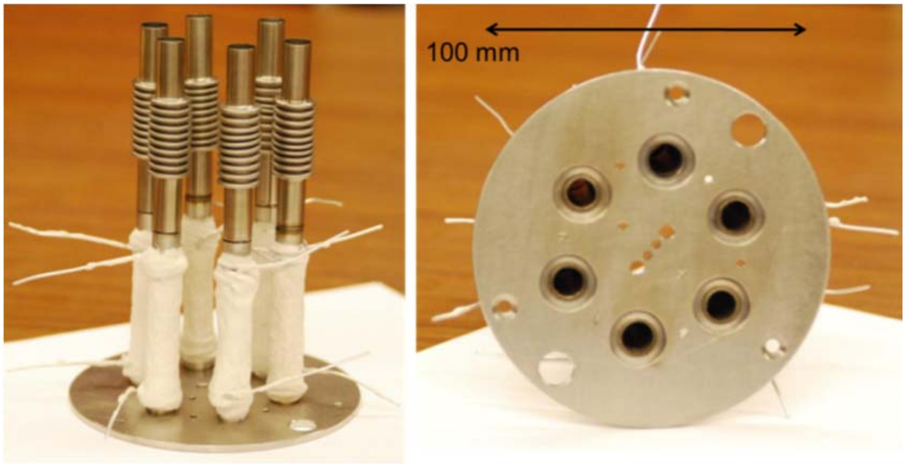

Figure 8-4: Side view and sealing surface of vapor the source manifold. Note resistive heaters near base of source tubes.

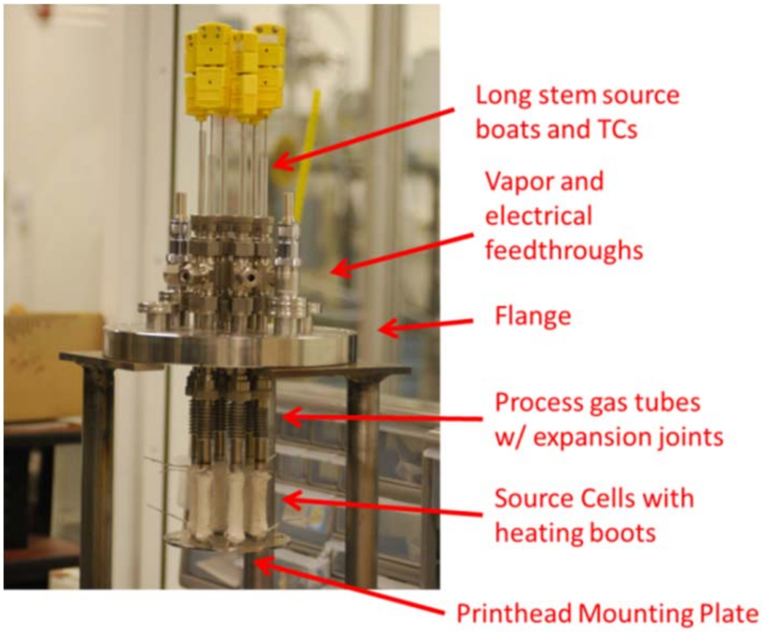

Figure 8-5: Vapor source manifold and feedthrough removed from chamber.

The manifold is provided carrier gas service by a multiport feedthrough on the top flange of the deposition chamber shown in **Fig 8-3a**. Three steel pillars provide rigid attachment to the feedthrough. Each tube is sealed to a corresponding port on the feedthrough by a Swagelok Ultra-Torr® fitting. Bellows near the upstream end of each tube serve as thermal expansion joints. The feedthrough connects each tube to a Swagelok Tee on its atmosphere side. The side port of the Tee connects to a mass flow controller for carrier gas. The top inlet is connected to an Ultra-Torr® fitting that serves as an attachment for the stem of a Pyrex® source vial. The vials can be easily removed for refilling. The feedthrough flange and manifold are shown assembled in **Fig. 8-5.** The top flange also contains feedthroughs for temperature measurement and heater power.

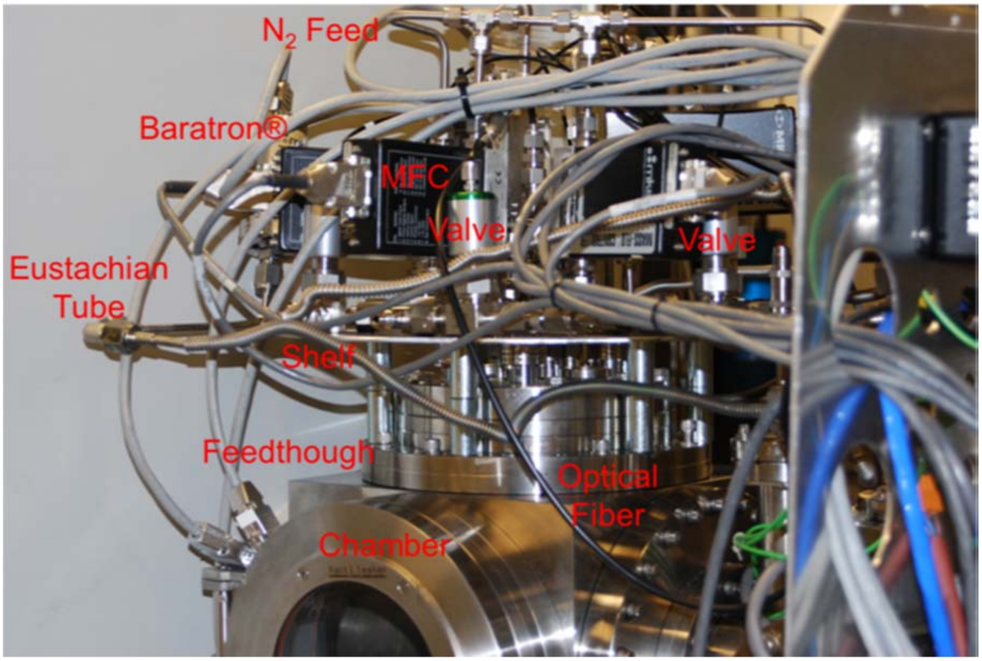

Figure 8-6: Utilities over top of the deposition chamber. The top feedthrough of the OVJP chamber is fitted with mass flow controllers, valves, vent lines, thermocouple and power cables, and other peripherals.

Carrier gas was provided to each organic vapor source tube by a dedicated mass flow controller (MFC). The MFCs are positioned directly over the feedthrough to reduce source cell volume as discussed in Ch. 6.6. Sources are each equipped with a vent line connecting to the interior of the deposition chamber to equalize pressure during chamber venting and pump down. These "Eustachian tubes" are fitted with default open valves that are only closed during deposition. Each source also has a Baratron® capacitance manometer to measure pressure. A piping and instrumentation diagram can be found in Appendix A. These chamber components are clearly visible in **Fig. 8-6**.

Data is collected from Baratrons and valves are controlled using a National Instruments DAQ® card and a LabView® code. The print head thermocouple is also monitored by the DAQ® and the LabView® code controls the output of a DC power supply using a proportional-integral (PI) algorithm to maintain a set temperature. LabView® also controls carrier gas flow and organic source cell temperature through RS-232 data links to local controllers.

8.4 Substrate Motion

The substrate sits underneath the print head on a movable stage, as shown in **Fig. 8-3b**. On the top level of the stage is a ground copper chiller plate with heat exchange loop containing either isopropanol or liquid N_2. The plate has dowel pins for mounting copper trays that are used to load and unload substrates through an attached ultra-high purity nitrogen-filled glovebox using a transfer fork. The stage is shown in **Fig. 8.7**. Planar motion of the stage is provided by precision x and y actuators. The thickness of printed stripes depends on substrate velocity and accurate lateral positioning of colored stripes is necessary to ensure that different emissive segments are properly addressed. Consequently, an x-stage capable of moving at a wide range of speeds and a high precision y stage are required. The x stage is a Physik Instrumente M 683 unit capable of velocities from 0.01 to 25 cm/s. The y stage is a Physik Instrumente M 112, capable of moving with micron resolution.

The nozzle-to-substrate gap is measured with a Philtec RC-25 fiberoptic reflectance compensated displacement sensor. This instrument measures the degree of coupling between a light source and two different photodetector channels at the end of an optical fiber bundle. The sensor calculates the distance between the fiber tip and the reflector based on the strength of the return signal. The sensor accounts for differences in

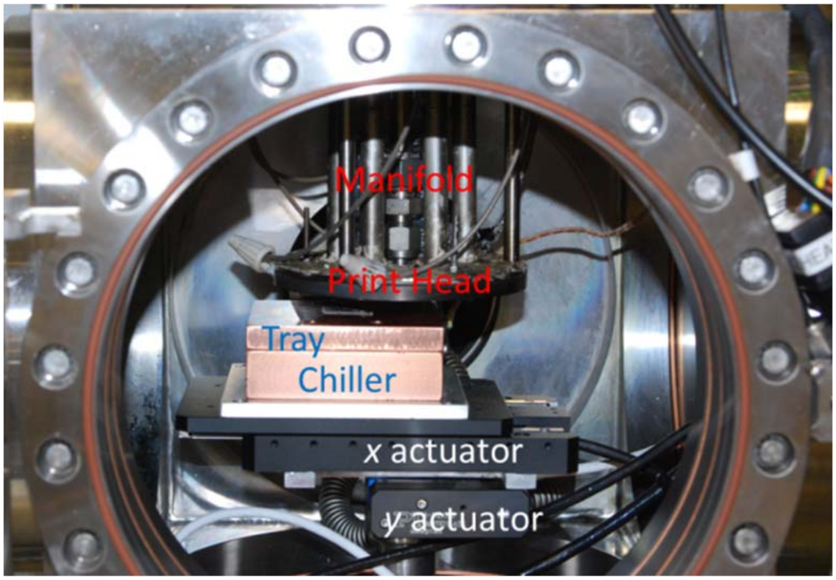

Figure 8-7: Two axis stage inside deposition chamber. The copper sample tray and heat exchange block are visible on the top. The upper actuator moves the substrate in the *x* direction. It is capable of velocities of up to 25 cm/s. The lower actuator moves in the *y* direction. It is slower, but capable of micron precision.

the albedo of target surfaces by using two different return signals. The sensor has a full range of approximately 700 μm and an accuracy of 2 μm under operational conditions. It can be used with metal and Si targets. It can be used with 700 μm thick ITO coated glass. Although the substrate is transparent, the back surface is out of the sensor's range. Thinner ITO glass, however, produced unreliable results. The sensor fits through a hole through the center of the print head. Its fiber optic cable is clamped at two ends by Swagelok® fittings, one affixes the tip to an adjustable positioning rod, while the other serves as a vacuum feedthrough.

The elevation of the stage is controlled by a PI algorithm implemented through Labview® that compares the analog output of the displacement sensor with the value expected for the set height. The stage is actuated by a stepper motor that drives a

Newport dual pantograph LabJack®, allowing positioning at 2 μm increments over a 25 mm range of motion. Stage rotation was controlled by a stepper driven rotary table situated on top of the *z* actuator. This θ actuator can be used to broaden printed lines by skewing the long dimension of the nozzle relative to the direction of printing.

The in-chamber stage components are connected to this lower actuator stack by a 25 mm diameter stainless steel pillar that passes through a Swagelok Ultra-Torr® fitting at the chamber base, forming a vacuum feedthrough. The lower stage actuator stack and the pedestal holding the chamber are shown in **Fig. 8.8**.

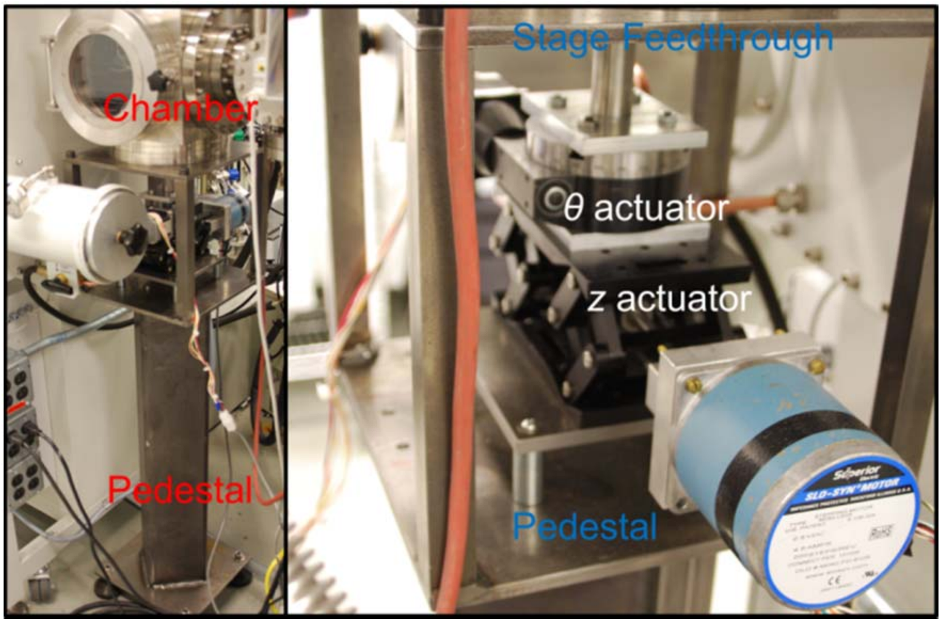

Figure 8-8: Stage components below the deposition chamber. The OVJP deposition chamber is supported by a heavy duty steel pedestal with vibration damping machine feet. The pedestal contains a shelf that holds the *z* and θ actuators for the substrate stage. These actuators are connected to the in-chamber components by a pillar passing through a feedthrough at the base of the chamber.

The stage was leveled using a feeler gauge to compare the gap between the print head and substrate holder tray along its front, back, left, and right edges. Coarse adjustment of leveling was performed by adjusting the platform supporting the *z* actuator. Fine adjustment was permitted by using bolts on the top feedthrough connecting the print head to the chamber to adjust the compression on an elastomer o-ring. The displacement sensor was zeroed by "kissing," i.e. lightly contacting a reflective substrate with the tips of the nozzle array following a slow approach. Contact or near contact could be confirmed by a pressure increase in the organic vapor source cells for a given flow rate. Despite the claimed performance of the displacement sensor, corrections were occasionally necessary for substrates with different reflectivities.

8.5 Measurement Hardware

Electroluminescence of the printed patterns was measured using a motorized micrometer line scanner. An optical fiber placed at the image plane of a low numerical aperture 10x objective coupled light into an Ocean Optics HR-4000 spectrophotometer, yielding a spatial resolution of 40 μm. Spectrum acquisition was synchronized to scanner motion with a Labview® script. The setup contained two probes for electrical testing of devices mounted on a vertical actuator that also held samples so that focus could be adjusted without breaking electrical continuity. The vertical actuator was fixed to an optical table while the optical components moved to reduce vibration experienced by the substrate. A high resolution CCD camera could be mounted in place of the optical fiber for taking pictures and the objective can be replaced with a calibrated photodetector for making efficiency measurements. This setup is shown in **Fig. 8-8**.

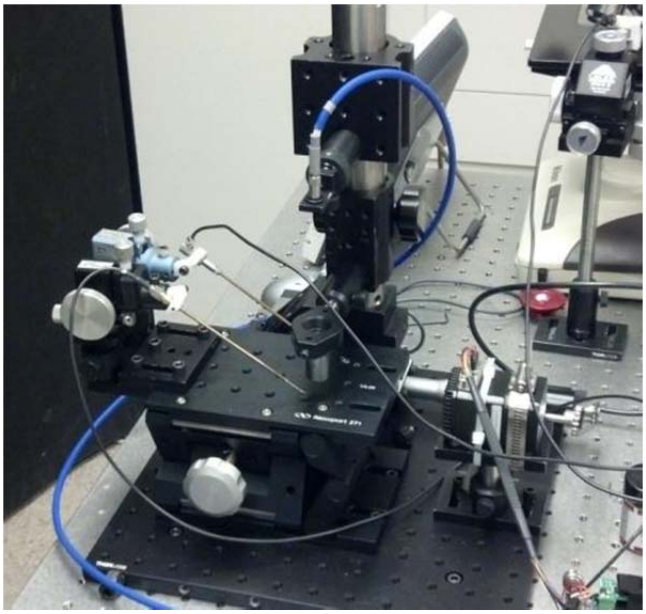

Figure 8-8: Electroluminescence Linescanner. Substrates were addressed using probes visible at left. Probes moved with the substrate to facilitate focusing. A microscope objective and optical fiber were mounted on a post with a motorized scanning axis.

8.6 Summary

Interfacing a microfabricated nozzle array to a vacuum deposition tool proved to be a major engineering challenge. Solving this challenge required solving two distinct problems. First, methods to mount a micronozzle array to a robust carrier plate and form a print head were developed, as described in the previous chapter. Secondly, a manifold to hold the print head and the surrounding deposition chamber were designed to meet the requirements imposed OVJP process. The print head is sealed by high temperature O-rings to a manifold, allowing it to be removed if needed. The manifold and surrounding deposition chamber are designed so that different material sources are independently heated and can be maintained at different temperatures. Each source is fed carrier gas by a separate mass flow controller to maximize the degree of control over the deposition process. The chamber is evacuated with a turbomolecular pump to maintain a vacuum of 10^{-4} Torr despite the influx of carrier gas.

The substrate is positioned on a chilled holder below the print head on a four axis stage. A high speed x actuator and precision y actuator are inside the chamber. These actuators are supported by a pillar that passes through a feedthrough and connects at its base to z and θ actuators below the vacuum chamber. Substrate position in the z axis is a critical process parameter. It is therefore measured by an optical reflectance displacement sensor and maintained by a feedback control.

An automated linescaner with 20 μm resolution was developed to record the emission spectra of OLED arrays as a function of position. This capability was used to characterize multi-color OLED arrays fabricated by OVJP, as discussed in Chapter 10.

Chapter 9

Organic Vapor Jet Printing Using Micronozzle Arrays

9.1 Overview

As discussed in Chapter 2, a practical OLED fabrication process must achieve three major goals. It must first be capable of patterning features with high resolution and it must secondly be capable of processing highly efficient devices. Thirdly, it must be capable to meet the first two goals with technology that can be readily taken from laboratory to production scale. Work presented in this chapter shows that micronozzle based OVJP is capable of meeting both the resolution and efficiency goals. The third goal, scalability, follows from the photolithographic techniques used to fabricate the micronozzle array. Scalability will be discussed further in Chapter 12.

The OVJP tool is capable of printing features of 20 μm and smaller. It is also able to grow the emissive layers of devices that have comparable efficiency to control devices grown entirely by VTE. The initial evaluation of micronozzle-based OVJP measures printing resolution and device efficiency in separate experiments. The dimensions of printed features are characterized by metrology and photoluminescence, and electronic testing is done on continuous films deposited by OVJP. The performance of patterned devices and multicolor arrays will be discussed in Chapter 10.

9.2 Measurement of Printed Feature Size

An array of micronozzles fed by microchannels was fabricated as described in Chapter 7.2. The arrays used for the study had rectangular apertures of 200 μm in length and 10-20 μm in width. Nozzles were spaced at 240 μm center-to-center and arranged in either one row of ten or two staggered rows of 5. These were C-R nozzles with 50 μm deep, straight walled relief trenches surrounding the nozzles. Parallel printing of multiple features of deposited thick film Alq_3 was achieved, with the observed variation in thickness and width of deposited features being on the order of 10%. The smallest features printed had a width of 16 μm measured at its base, as shown in **Fig. 9-1**.

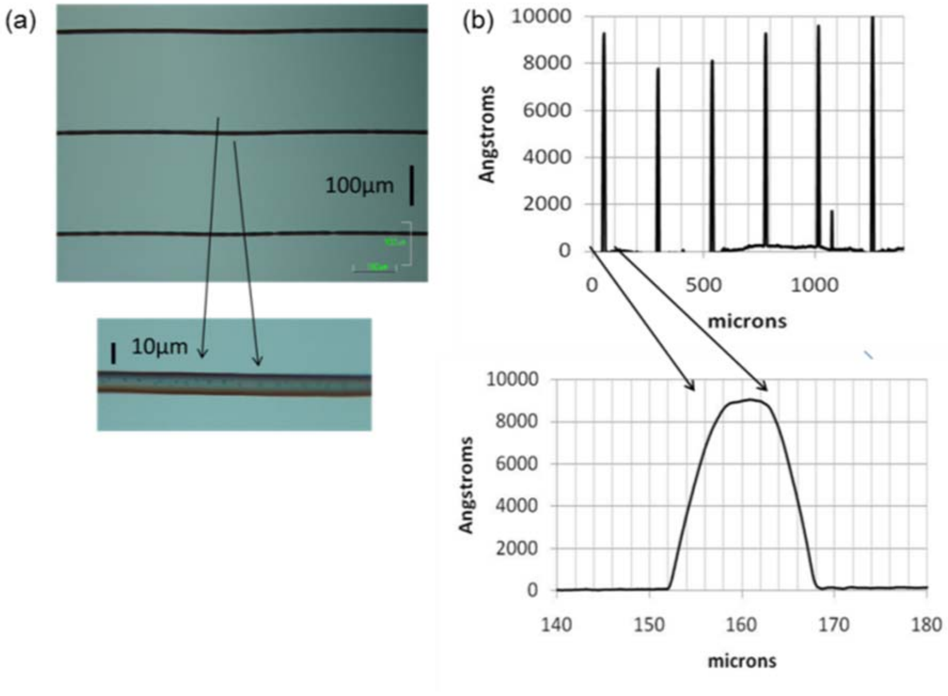

Figure 9-1: Images and profilometry for printed organic thick film lines. Micrographs (a) and stylus profilometry (b) show the dimension of a set of 800 nm thick lines of Alq_3 deposited by OVJP.

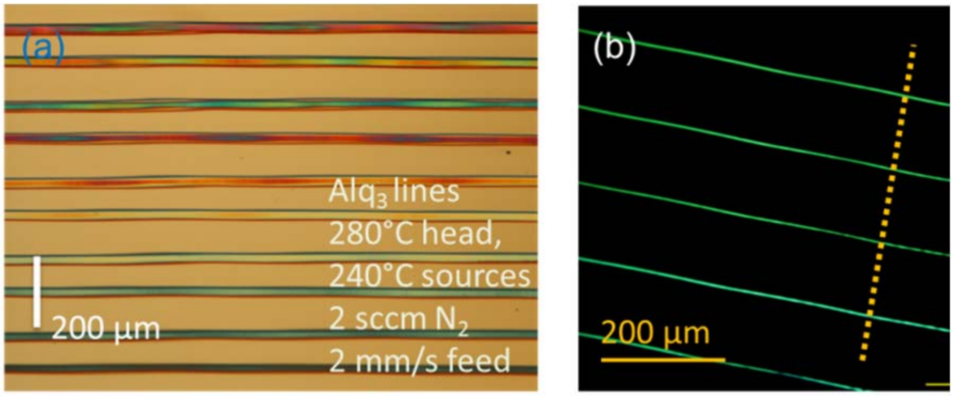

Figure 9-2: Array of printed thin film lines. (a) White light image shows an array of ~20 µm wide features deposited by OVJP in a single pass. (b) Fluorescence microscopy reveals even finer features on a different substrate.

Additional samples of multiple line patterns printed in a single pass by OVJP are shown under white light and fluorescence in **Fig. 9-2.** These were printed using a 10 µm nozzle positioned at a distance g =10 µm from the substrate. The features shown in **Fig. 9-1** were measured using stylus profilometry. While this measurement clearly indicates that OVJP can deposit organic material into printed features with a high degree of precision, it is relatively insensitive to the deposition of very thin films of material beyond the apparent boundary of the feature. This "overspray" of organic material is better measured with photoluminescence or electroluminescence. Overspray will become significant in Chapter 10.

A LSM 510-META (Zeiss, Jena, Germany) confocal microscope was used to characterize the width of printed thin film features by photoluminescence. A confocal microscope is normally used to generate three dimensional images of fluorescently stained biological systems using an iris to image a very thin focal plane.[121] Accordingly, the microscope is equipped with a 364 nm wavelength pump laser and a photomultiplier-tube based light detection system. When the iris was opened, detection of very weakly photoluminescent features was possible. Minute quantities of organic material deposited beyond the apparent boundary of printed feature, referred to as overspray, could be observed when it was present. An overspray detection limit of an approximately 1 nm thick film of Alq_3 was established.[63]

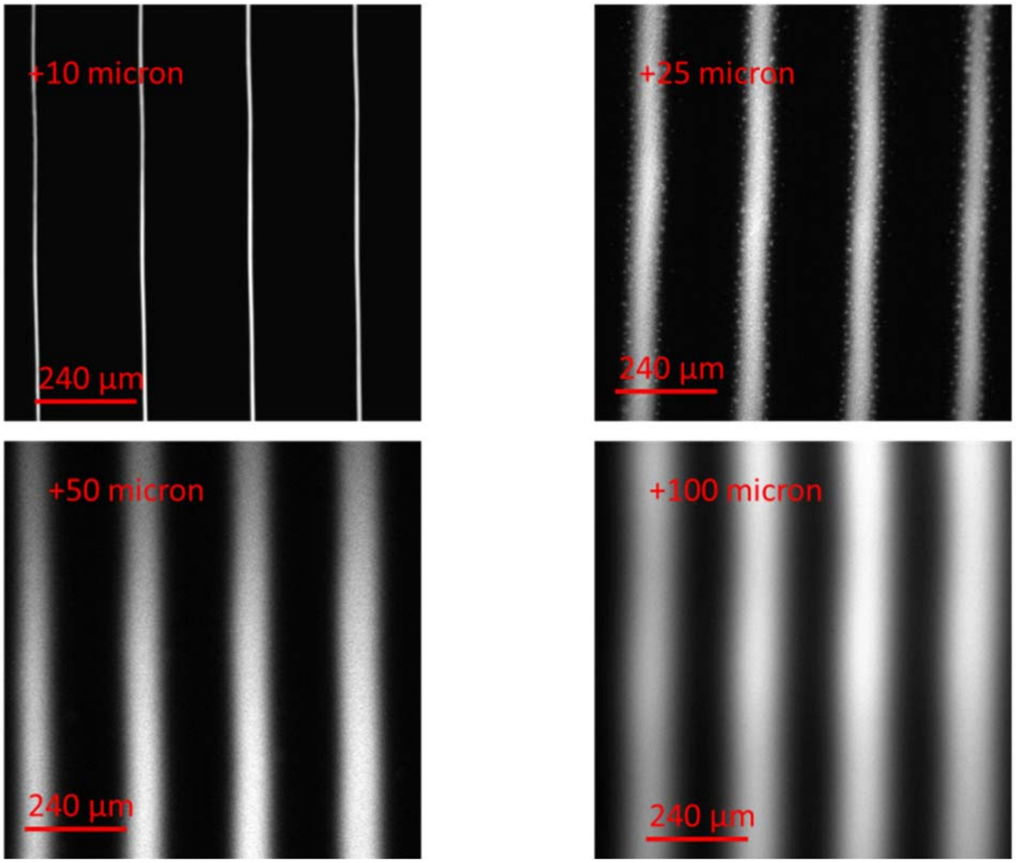

Figure 9-3: Photoluminescence images of printed features. Nozzle to substrate separations g = 10, 25, 50, and 100 µm are shown. Note that features become larger and have more diffuse edges with increasing separation. Images were taken using a confocal microscope for highly sensitive light detection.

The feature size produced by a nozzle array depends primarily on the width of the nozzle aperture and the nozzle-to-substrate separation, *g*. Very sharp lines are achieved at *g* = 10 μm, producing 20 μm wide features and no detectable overspray in regions between lines. As the nozzle moves away from the substrate, printed patterns become larger and more diffuse. This is apparent from both the series of images in **Fig. 9-3** and the photoluminescence profiles in **Fig. 9-4**. Feature size, measured as full width at half

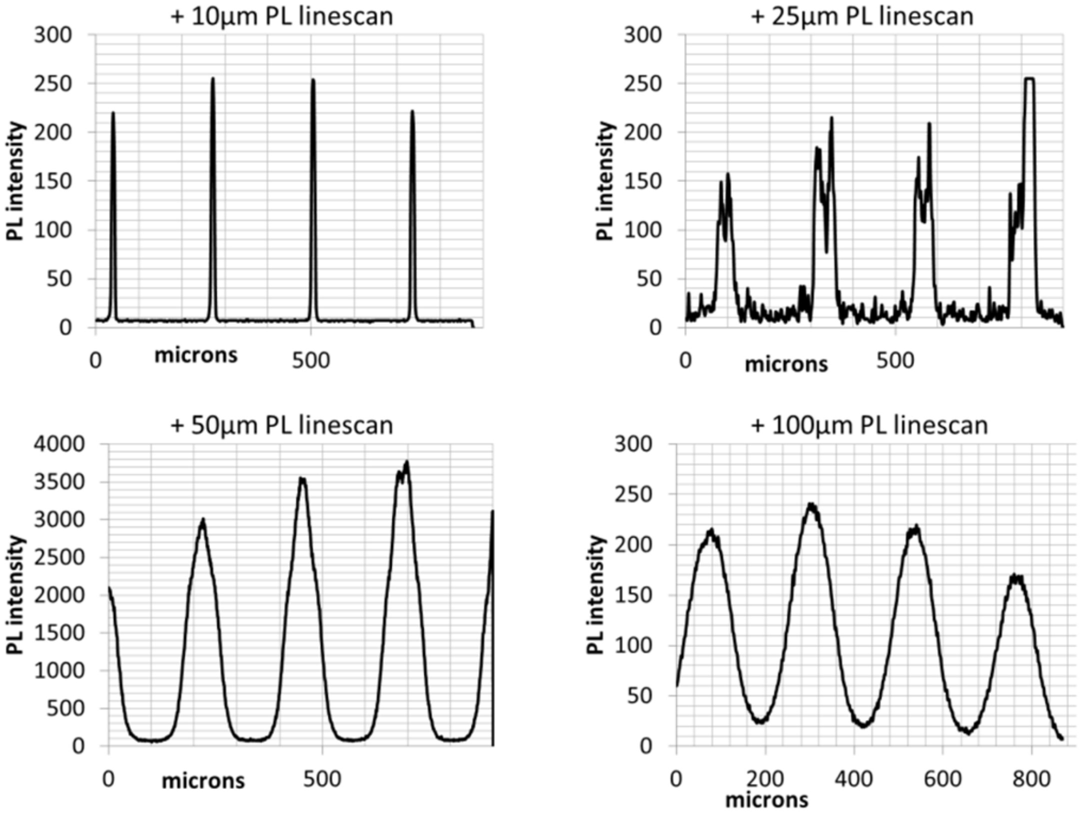

Figure 9-4: Plots of photoluminescence intensity across arrays of printed lines. Lines were imaged with a confocal microscope. Nozzle to substrate separations *g* = 10, 25, 50, and 100 μm are shown. Note that features have a wider full width at half maximum and more gently sloping sides with increasing *g*.

maximum photoluminescent intensity scales approximately as 1.5g +15. Feature size is relatively independent of carrier gas flow rate for large nozzle-to-substrate separations of g =50 and 100 μm. When the nozzle is closer to the substrate, the combination of faster flow and higher pressure underneath the nozzle reduces printing resolution. This is apparent at g =10 μm. Experimentally measured values for feature size are plotted as data points on **Fig. 9.5a**, with simulated feature sizes appearing as lines. Simulations reproduce the trends in feature size with respect to g and carrier gas flow rate to within experimental error in each case. The thickness of printed features measured with stylus profilometry as a function of distance from the nozzle centerline also agrees well with simulation predictions as shown in **Fig. 9-5b**.

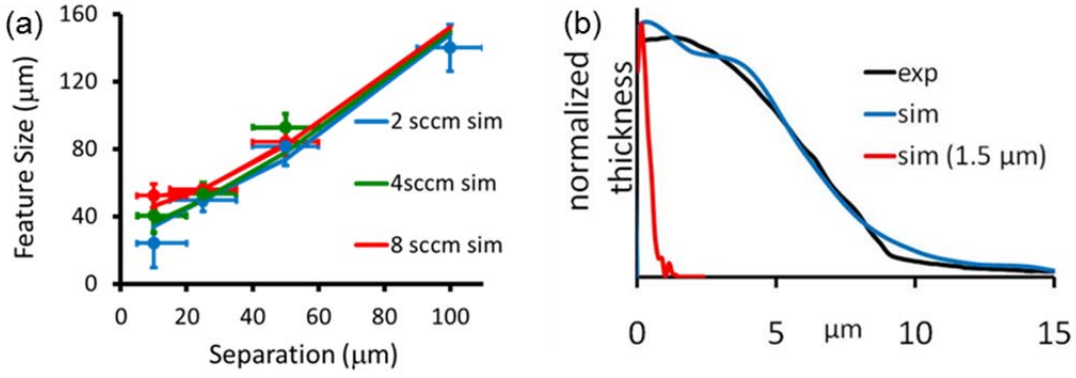

Figure 9-5: Measured and modeled size and cross section of printed features. (a) Feature size was measured by photoluminescence as a function of both nozzle to substrate separation g and total carrier gas flow rate through a ten nozzle array. Experimental values are plotted as data points and simulated values are shown by lines. (b) A feature deposition profile measured by stylus profilometry (black) closely matches that predicted by simulation (blue) for a 10μm wide aperture nozzle with g =10μm. Simulation of a 1 μm wide aperture nozzle with g =1 μm (red) is also shown. (From McGraw, Peters, and Forrest)[63]

Much smaller features than those shown in **Fig. 9-1** can be printed using the OVJP technique. Now that the deposition model had been experimentally validated, it was used to explore the case of a nozzle with a 1 μm aperture positioned 1 μm from the substrate. A feature with FWHM of 1.5 μm, shown by the red line in **Fig 9-5b**, was obtained. Even smaller features may be possible, as this feature size was chosen for ease of modeling rather than due to a fundamental limitation of the OVJP process.

9.3 Device Performance

The first batch of devices grown by OVJP consisted of phosphorescent OLEDs with continuous emissive layers. These devices were compared to OLEDs grown entirely by VTE. Doping ratio and tooling as established prior to printing using the procedure described in Chapter 3.3. During printing, the print head was heated to 250 °C. Source temperatures and flow rates were adjusted to maintain a deposition rate of 800 Å/s through the area of the nozzle orifices. A displacement of g=150 μm allowed neighboring lines printed by a staggered two by five nozzle array to blend into a continuous film. Devices were grown on 0.55 mm thick soda lime glass substrates coated with a 1500 Å thick layer of indium tin oxide. The device architecture was based on the high internal quantum efficiency architecture of O'Brien *et al.*,[12] to similar that depicted in **Fig. 1-2d**. A 400 Å thick hole transport layer of NPD was first deposited via VTE with a base pressure of 10^{-7} Torr. A 300 Å thick emissive layer of approximately 8 wt. % $Ir(ppy)_3$ doped into CBP was then deposited using either OVJP or VTE. Process conditions for OVJP are given in the following paragraph. All devices were subsequently capped by a 200 Å thick bathocuproine layer, a 250 Å thick Alq_3 electron transport layer, and an 8 Å LiF/700 Å Al cathode, deposited by VTE.[63]

Organic vapor jet printed devices had a maximum EQE of 8.8 ± 1.3%, compared to VTE-grown devices with EQE=9.1 ± 0.8%. The electroluminescence spectrum of the OVJP grown devices was consistent with the VTE OLEDs, with an emission peak at a wavelength of 523 nm. While performances of the two device sets were comparable at low current density, as shown in **Fig. 9-6**, the EQE of OVJP devices rolled off more significantly than VTE devices at current density $j > 10$ mA/cm^2.[63]

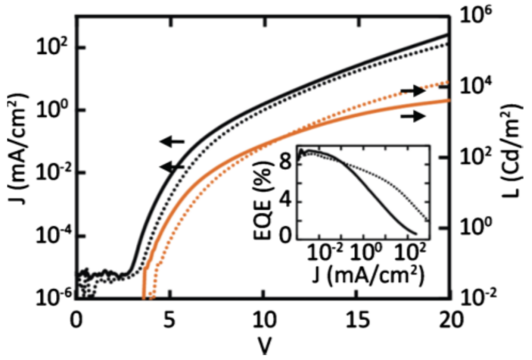

Figure 9-6: Initial device data for OVJP deposited OLEDs. Current density j and luminous intensity l for OLEDs grown by OVJP (solid) and VTE controls (dotted) are plotted as a function of voltage V. External quantum efficiency as a function of j is shown in the inset. (From McGraw, Peters, and Forrest)[63]

Micronozzle-based OVJP demonstrated both the capability to deposit electrophosphorescent devices and the ability to pattern features at a 10 micron scale. This original implementation, however, required high temperature epoxy to seal the vapor source manifold to the nozzle membrane. It is suspected that outgassing from the seal contributed to efficiency rolloff at high current densities. The epoxy seal was replaced with a glass to metal anodic bond as described in Ch. 7.3.1, and the efficiency of

OLEDs fabricated by OVJP increased to that of VTE grown control devices for a full range of drive current densities.[64]

This improved batch of devices had the same architecture as previously. The print head was heated to 300°C and both the host and dopant source cells were heated to 240°C, N_2 carrier gas was fed into the host and dopant sources at rates of 1.5 and 0.5 sccm, respectively. The substrate was translated along the primary axis of motion at a rate of 4 mm/s with a perpendicular step of 250 μm between each pass, resulting in a uniformly printed 25mm square area. The total OVJP deposition rate was approximately 7×10^{11} mol/s, corresponding to a growth rate of 700 Å/s within the zone of printing. This is within a factor of two of the predicted deposition rates in Chapter 6.4, which is reasonable agreement given uncertainties in the thermodynamic and transport properties of $Ir(ppy)_3$ and CBP.[64]

The PhOLEDs grown with a print head using the anodic sealing technique have a maximum EQE =8.0±0.7%, compared with 8.5±0.3% obtained for similar devices grown entirely by VTE. The power efficiencies of these devices are also comparable, with OVJP-grown devices peaking at 14.9±1.3 lm/W, and VTE devices at 15.5±1.3 lm/W. At j =10 mA/cm^2, the luminance of both sets of PHOLEDs is 1000 cd/m^2. Current density j and luminance l are plotted versus voltage, V, in **Fig. 9-7**, as are power efficiency and external quantum efficiency as functions of j, for representative OVJP and VTE devices. Devices grown at 0°C substrate temperature had peak EQE comparable to VTE control devices. Devices grown at 10°C substrate temperature had lower EQE but maintained a power efficiency equivalent to that of VTE grown devices over 6 decades of drive current density *j*.[64] The effect of substrate temperature on device characteristic will be discussed further in Chapter 11.

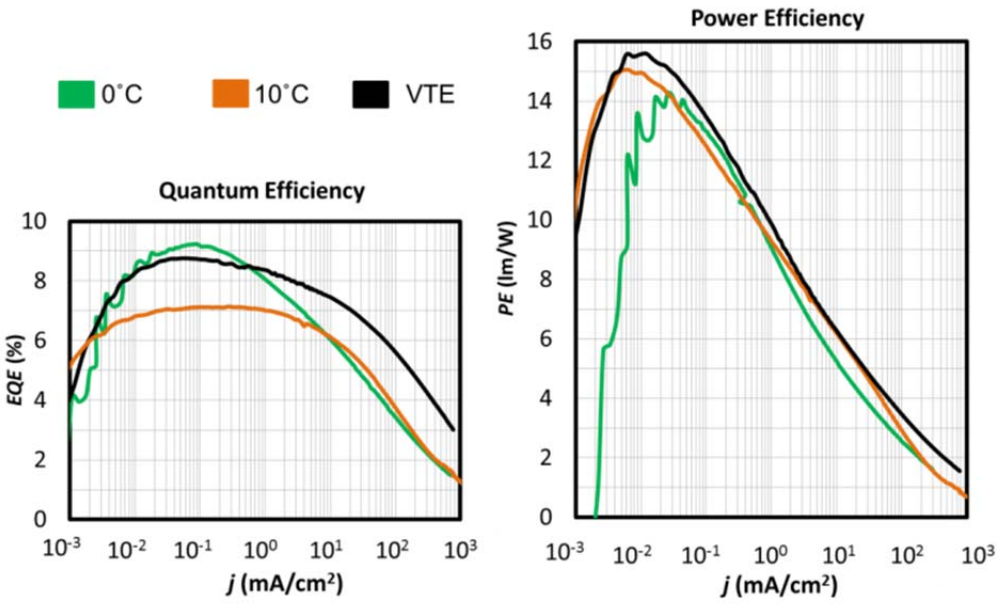

Figure 9-7: Device data for optimized OVJP deposited OLEDs. External quantum efficiency and power efficiency are plotted as a function of current density *j*. Orange and green lines indicate substrate temperature, 10° and 0°C, during growth. Curves for a VTE device are shown in black. (From McGraw and Forrest)[64]

The anodically bonded print head demonstrated that micronozzle based OVJP print head constructed from a proper material set is capable of matching the efficiency of VTE grown devices. Unfortunately, the nozzle membrane with integrated microchannels proved too fragile to be expanded to accommodate more than a single pair of host and dopant channels. It was therefore limited to single color printing. Multicolor printing, using the more robust soldered print head will be discussed in the next chapter.

9.4 Summary

Organic vapor jet printing demonstrated both the ability to print very small features and the ability to grow electronic quality doped films for phosphorescent OLED applications. Features of 20 μm and smaller were measured by both stylus profilometry and spatially resolved photoluminescence measurements. The size of printed feature that can be obtained varies linearly with the width of the gap between the micronozzles and the substrate. Feature size also depends on carrier gas flow rate when the gap is small. Experimental results for feature size as a function of process conditions are in good agreement with predictions from the model in Chapter 5.

The emissive layers of CBP/Ir(ppy)$_3$ PHOLEDs with peak EQE > 8% and η_p matching that of standard VTE devices were be grown by OVJP. In this case, OVJP was used to print a continuous, rather than a patterned film. The size and efficiency of the illuminated regions in single and multicolor OLED arrays patterned by OVJP are measured in Chapter 10. A deposition rate of $7x10^{11}$ mols/s was observed for the 10 nozzle OVJP used in this study. This is in reasonable agreement with the predicted deposition rate in Chapter 6, and provides a baseline for estimating the printing speeds that can be achieved by a production scale OVJP tool. This scale-up calculation is discussed in greater detail in Chapter 12.

Chapter 10

Organic Vapor Jet Microprinting of PHOLED Arrays

10.1 Overview

The ability of based OVJP to fabricate single and multicolor arrays of PHOLEDs that are efficient and well resolved is demonstrated in this chapter. The glass to metal seals used in early versions of the print head were unreliable, so they were only suited to simpler tests that treated feature resolution and device efficiency separately. Electroluminescence provides a more sensitive probe for the presence of printed emissive material than either profilometry or photoluminescence. Minute amounts of overspray around a printed feature that are not apparent by the previous methods may significantly change the size and color of the illuminated regions of a patterned OLED array. The only way to ensure that such overspray can be held to manageable levels is to print the emissive layer of patterned OLED arrays using OVJP. The gold eutectic soldering method described in Chapter 7.3.2 was crucial to developing the more robust print head that enabled this demonstration.

The improved print integrates multiple sets of channels, so that multicolor OLED arrays can be printed. Features of different color result from different chemical compositions, so it is also necessary to detect and mitigate overspray of material between printed features. Since minute amounts of contamination can change the emission spectrum and color of an OLED, virtually no cross-contamination between printed pixels is permissible. The extent of overspray around printed features defines the separation that is required between adjacent subpixels in a printed OLED display. It must, therefore, be quantified.

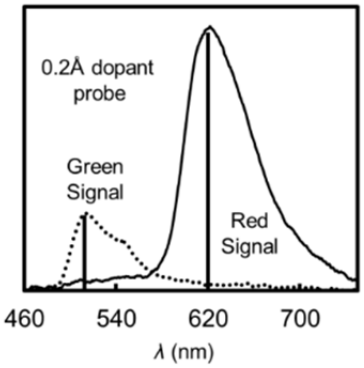

Figure 10-1: Electrophosphorecent emission signal from ultrathin dopant layers. The emission spectrum from a film of 0.2 Å of RD-15 deposited in place of an emissive layer of a top emitting OLED is measured test its effectiveness as an overspray probe (solid). The signal from 0.2 Å of Ir(ppy)$_3$ is also shown (dots). Signal for RD-15 is approximately 10x the noise floor for scanner settings used to generate data for **Figs. 10-2** and **10-3**, implying a much lower detection limit.

10.2 Overspray Probe and Multicolor Printing Methods

We begin by establishing a structure designed to probe for the presence of overspray in a phosphorescent OLED array with extremely high sensitivity. A top emitting structure was chosen for experimental convenience. The reflective displacement sensor measuring the vertical position of the substrate had difficulty differentiating between the top and bottom surfaces of 500 μm thick glass, necessitating the use of an opaque substrate. Furthermore, it was advantageous to be able to electrically probe devices and outcouple light from the same surface when taking spatially resolved emission spectra.

A top emitting device was grown on a Si substrate with a 300 nm thick Al and 20 nm thick Pt anode deposited over the entire surface by vacuum thermal evaporation (VTE) in a chamber with a base pressure of ~10^{-7} Torr. A 50 nm thick hole transport layer of NPD and a 10 nm thick Irppz electron blocking layer were deposited over the anode.[13] The Irppz layer was intended to block light emission by the hole transport layer in regions uncontaminated by dopant. An ultrathin layer 0.2 Å of the red dopant RD-15 (Universal Display Corp., Ewing, NJ.) was then deposited through a shadow mask. The shadow mask was removed and a 20 nm thick Bphen hole blocking layer followed by a 25 nm layer of Alq_3 electron transport layer were subsequently deposited on the substrate. Devices were then capped with a semi-transparent 1 nm thick LiF, 5 nm Al, and 15 nm Ag cathode.[122]

The electrophosphorescent intensity of RD-15 is ten times the detection threshold of the line scanner, as shown in **Fig 10-1**. Since host-to-dopant energy transfer is negligible for films much thinner than a monolayer, a neat film of dopant provides a useful gauge for the sensitivity of this probe structure for overspray detection and the signal is expected to scale linearly with the dopant concentration. This implies that the actual detection threshold is 0.02 Å of RD-15, or approximately 1/500 of a monolayer. A structure with 0.2 Å of $Ir(ppy)_3$ was also made for comparison, however the electroluminescence signal it produced was only 28% as bright. Since RD-15 has a narrower gap between its HOMO and LUMO energy levels then $Ir(ppy)_3$, it traps holes from the Irppz layer and electrons and excitons from the Bphen layer more efficiently.

A low level of RD-15 contamination is more readily visible than the same level of $Ir(ppy)_3$ contamination, making RD-15 a more effective overspray probe.

The OVJP tool was then used to grow OLEDs with patterned single and multicolor emissive layers deposited in place of the RD-15 tracer between the same set of transport layers. The EML consists of OVJP-printed stripes of the host material, CBP mixed with one of two phosphorescent dopants, either the green emitter $Ir(ppy)_3$, or the red emitter RD-15. Total deposition rate was controlled by the temperature of the organic source cells. The doping ratio was set by the fraction of total carrier gas flow sent through the dopant source cell,[64] and calibrated prior to deposition using photoluminescence spectroscopy as described in Chapter 3. Optimal volume doping ratios of 6 ±3% for $Ir(ppy)_3$[26] and 10% ±3% for RD-15[72] were set. The thickness of the emissive stripes was approximately 20 nm, measured with stylus profilometry. The $Ir(ppy)_3$ source was heated to 330°C, CBP sources were between 300°C and 340°C, and the RD-15 source was at 350°C. Ultrapure N_2 carrier gas was fed into each material source at flow rates of from 0.1 to 1 sccm, generating a pressure of between 3 and 10 Torr within the source. The print head temperature was maintained at 350°C to prevent downstream organic condensation, and the substrate stage was chilled to between 0 and -20°C. A gap, *g*, of between 20 μm and 100 μm was maintained between the nozzles and substrate. The substrate was translated relative to the nozzle array at between 8 and 12 mm/s along the printing axis. Both red and green stripes were printed simultaneously.

10.3 Size and Spacing of Printed Features

The full width at half maximum (FWHM) intensity for features printed with a S-C nozzle at g = 20μm is 94 ±18 μm, and the width to 10% of maximum intensity was 124

±18 µm. Table 10.1 lists the width to 50% and 10% of maximum intensity for electroluminescent features printed using C-D nozzles at *g* = 20, 50, and 100 µm. Red and green emitting features are narrowest and have defined edges for *g* =20 µm. Emissive features are larger and have diffuse edges at g =100 µm. **Figure 10-2** shows

g (µm)	G FWHM	G 10%M	R FWHM	R 10%M
20	97 ±22 µm	166 ±40 µm	127 ±13 µm	250 ±45 µm
50	200 ±59 µm	275 ±76 µm	214 ±12 µm	365 ± 7 µm
100	263 ±47 µm	408 ±31 µm	299 ±21 µm	550 ±50 µm

Table 10.1: Sizes of segments in microprinted red and green OLED arrays. Widths are expressed as full width to half of maximum brightness (FWHM) and 10% of maximum brightness (10%M) for green, G, and red, R, devices. Segments are printed at nozzle to substrate separations of *g* = 20, 50, and 100 µm.

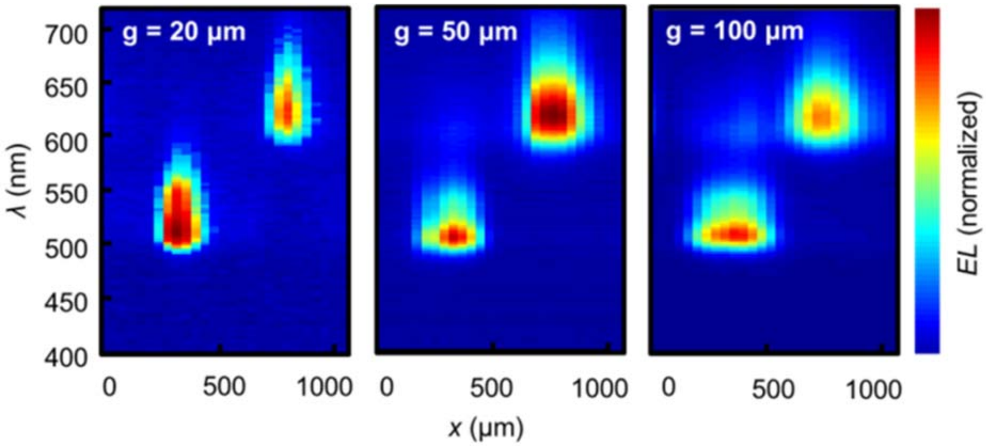

Figure 10-2: Spectrally resolved linescan of emission from a red and green OLED array. The scan direction, *x* axis, is orthogonal to the direction of printing. Wavelength is the *y* axis, and color indicates the strength of light emission at each wavelength and scan step. Scans are shown for nozzle to substrate gaps *g* =20, 50, and 100 µm. Regions of emission become larger and have poorly defined borders for larger values of *g*.

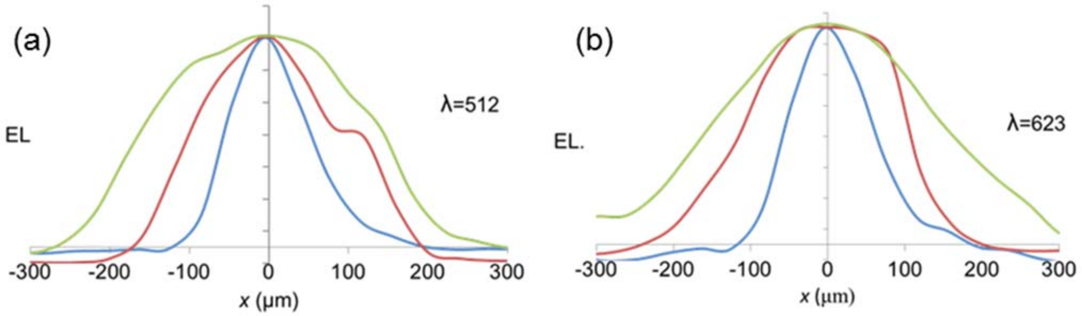

Figure 10-3: Spatially resolved light emission intensity from printed features. Normalized Intensity profiles for (a) green segments is taken at λ =512 nm and (b) at λ =623 for red segments. Intensity profile for patterns printed at g =20 μm is blue, g =50 μm is red, and g =100 μm is green.

signal from a spectrally resolved linescan taken perpendicular to the printed EML lines at each value of *g*. These scans indicate the spectrum of light emitted for each region of the printed pattern. This can be used to determine where red or green dopants are deposited. The intensity of electroluminescence across the width of both red and green printed features is roughly Gaussian, as shown in **Fig. 10-3**. The general trend of broader features and more diffuse boundaries with increasing *g* is apparent. For given conditions, the red and green pixels have a similar FWHM, implying the widths of printed features from each host and dopant mixture are similar.

Red pixels are significantly wider than the green pixels at their bases (i.e. their width measured at 10% of the maximum intensity). Since both $Irppy_3$ and RD-15 have comparable sublimation temperatures, this difference is due to the more intense emission from oversprayed RD-15 than from $Irppy_3$. Red emission can be detected at 61 μm beyond the FWHM on each side of a feature printed using a C-D nozzle at *g* =20. No cross-contamination between red and green features printed on 500 μm centers is detectible, as is evident from their emission spectra shown in the upper portion of **Fig. 10-4**. Green features printed at *g* = 20 have Commission Internationale de l'Éclairage (CIE) 1931 chromaticity coordinates[27] (0.27, 0.63), which matches that of discrete Ir(ppy)$_3$ OLEDs.[26] Also, red devices have coordinates of (0.66,0.33) that match the discrete value of (0.66, 0.32).[72] Conversely, for *g* = 100 µm, red emission can be detected across the entire array. This contamination is sufficient to shift the CIE coordinates of a neighboring green segment to (0.32, 0.61). This spectrum corresponds to approximately 0.03Å of red dopant contamination, demonstrating that even a minute amount of RD-15 can adversely affect the performance of the green OLED. In contrast, the CIE coordinates of the red segment is unchanged for *g*=100 µm, since transfer of triplet excitons from the red to green dopant is endothermic, and hence unlikely to occur.

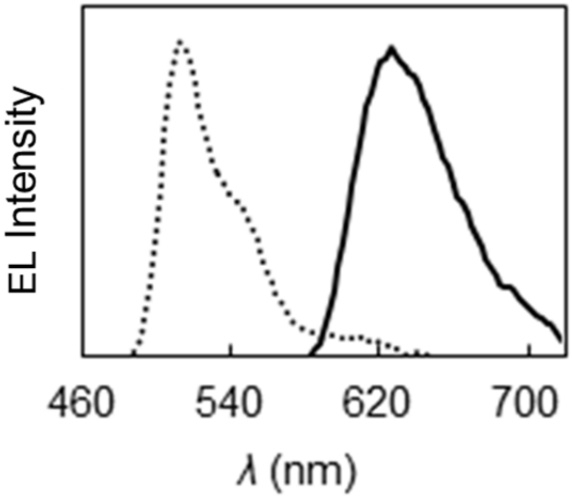

Figure 10-4: Electroluminescence of neighboring red and green printed features. Adjacent red (solid) and green (dots) emissive segments were printed on 500 µm centers with a C-D nozzle at *g* =20 µm. Note the absence of cross contamination in the emission spectra.

10.4 Printed Device Performance

Printed devices performed comparably with control devices of the same layer structure grown entirely by VTE. Green devices fabricated by OVJP had peak external quantum efficiency (EQE) of 4.9%, compared with 5.4% for VTE devices of the same architecture and aperture ratio (EML grown on 50% of the contacted area). While this EQE is only about half of what is expected for an Ir(ppy)$_3$ PHOLEDs,[26] this device was intended to evaluate patterning capability and indicate the presence of overspray. This particular top emitting architecture is estimated to have a ~49% lower outcoupling efficiency than a bottom emitting device,[123] accounting for the discrepancy. The fact that a patterned, OVJP deposited EML performed comparably to a similar device fabricated entirely by VTE implies that OVJP could be used to fabricate high efficiency devices with better outcoupling. Plots of current, voltage, luminous intensity, and EQE are shown along with a photograph of the green device array in **Fig. 10-5**. A series of red emitting devices printed over a range of *g* is shown in **Fig. 10-6**, illustrating both that sharp features are possible for small g and the broadened features at larger *g*. Representative multicolor OLED arrays are shown in **Fig. 10-7**.

10.5 High Density Printing

Assuming that the emission intensity from red contamination in a green device varies linearly with concentration, an array of alternating 100 μm wide red and green sub-pixels printed using C-D nozzles at *g* = 20 μm require a center-to-center spacing of at least 210 μm to avoid noticeable spectral shifts (as determined by 2% changes in their CIE coordinates). Higher feature densities can be obtained by reducing *g*. The red electrophosphorescent probe suggests that no more than 0.02Å thick layer of dopant

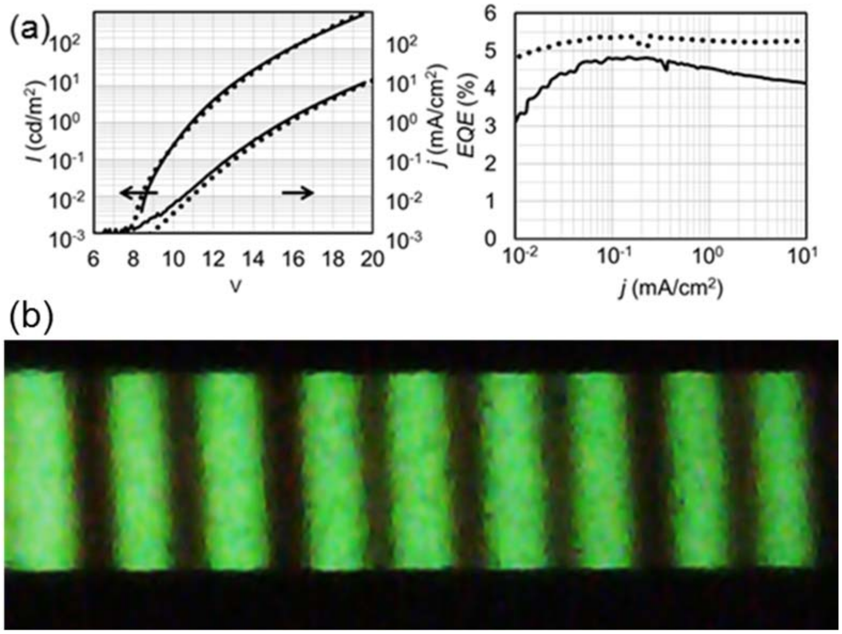

Figure 10-5: Device data and image for a printed green OLED array. (a) Light emission and current density as a function of voltage for an array of printed CBP/Ir(ppy)$_3$ OLEDs is shown at left. OVJP grown devices are shown in black and VTE grown control devices are shown with dotted lines. External quantum efficiency (EQE) for these devices is graphed at right. (b) A photograph shows an array of green devices like the one used for these measurements. It was printed using a simple converging nozzle at g = 20 µm,

overspray is tolerable in a printed feature. When interpreted in this light, the modeled deposition profile shown in figure 5.17 for an S-C nozzle with g=10 µm indicates that the minimum lateral sub-pixel spacing in this case is 70 µm for 25 µm wide features in a 200Å, 6% doped emissive layer. Wider pixels can be printed in multiple passes without increasing the width of the border required between features. For instance, 50 µm wide sub-pixels on 95 µm centers can be printed in two passes.

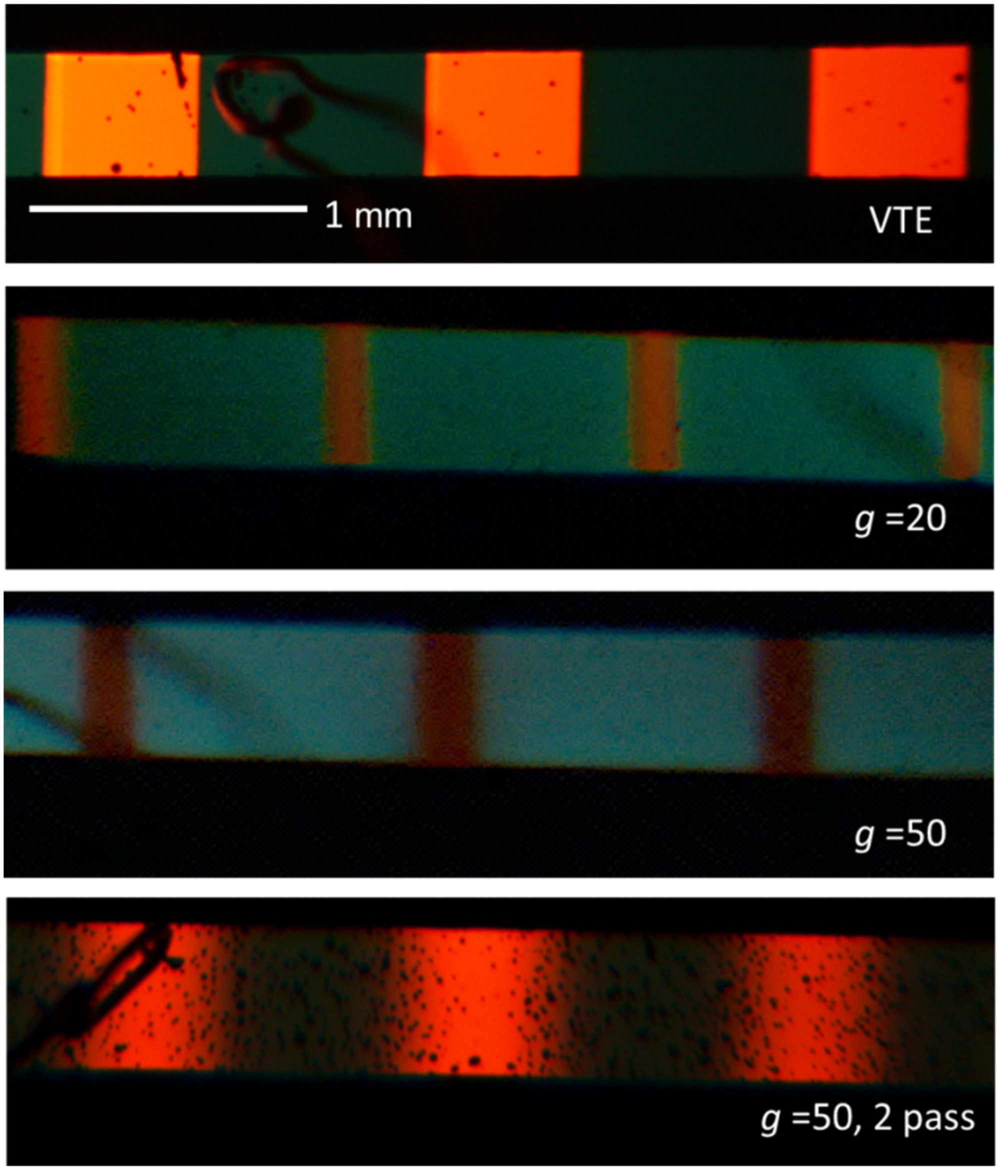

Figure 10-6: Images of printed red emitting arrays. A control array deposited by VTE using a shadow mask is shown at top. Below that is a pattern of sharp subpixels drawn by OVJP at g = 20 μm. Features become broader and more diffuse for g =50 μm as indicated in the third image. For the final image, pixels are drawn in two passes, staggered by 150 μm transverse to the direction of printing in an attempt to duplicate the 50% aperture ratio of the VTE device.

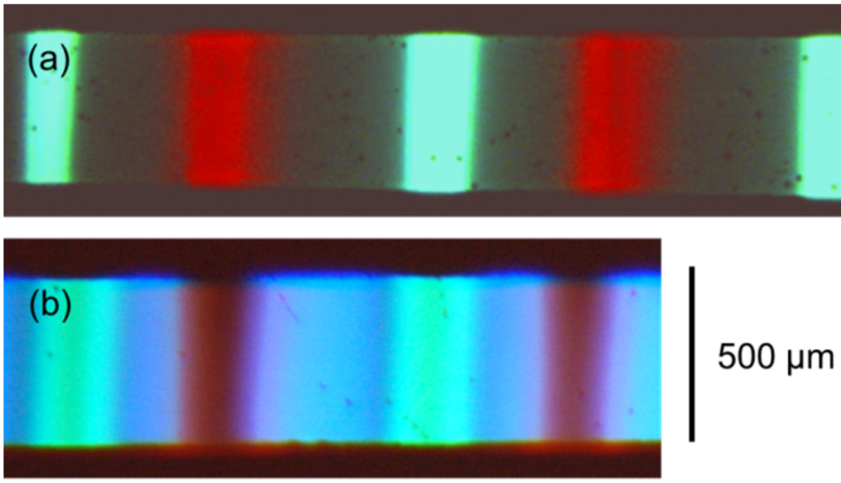

Figure 10-7: Multicolor OLED arrays printed by OVJP. Arrays were printed with a C-D nozzle at $g = 20$ μm. (a) The EML of the top device was grown using the Irppz-Bphen structure used previously in this chapter. (b) The Bphen layer was replaced by blue fluorescent emitter BAlq to produce a red-green-blue array.

To achieve an even closer pixel spacing, lateral spreading of contaminants can be reduced with inert barrier structures surrounding the pixel active area, analogous to wells used for inkjet printing.[124] An S-C nozzle, as discussed in Chapter 5.6, depositing onto a substrate with 2 μm high barriers separated by 40 μm at g =10 μm produces approximately 0.03 Å of overspray downstream of the barrier. This is just slightly more than the neighboring sub-pixel can tolerate. If a C-T nozzle is used instead, less organic material scatters off the underside of the nozzle membrane onto the substrate and overspray contamination can be reduced to an undetectable level. If 40 μm sub-pixels separated by 10 μm wide barriers are assumed, as in Chapter 5, a pixel pitch of 150 μm can be obtained. Further optimization of nozzle and barrier shapes (e.g. undercut barriers that trap organic material without re-directing free material upwards) to reduce overspray and increase the density of printed features may be possible.

10.6 Summary

The emissive layers for PHOLED arrays were patterned using with the OVJP print head. Both single and two color arrays were printed, with red and green emissive segments printed in a single pass for the latter. The electrode pattern over the OLED array covered both printed and non-printed regions, so the electroluminescence produced by the presence of overspray surrounding printed features was visible. Of the two nozzle geometries evaluated, S-C nozzles produce narrower luminous features with more sharply defined boundaries than C-D nozzles. The width, including overspray, of the illuminated region printed by S-C nozzles is 124 μm, compared 166 μm for C-D nozzles at growing $Ir(ppy)_3$ devices g =20 μm. Modeling in Chapter 5 suggests that sharper patterning is possible with S-C nozzles than C-D nozzles due to the lower velocity of carrier gas velocity under the S-C nozzle aperture. Adjacent red and green features printed on 500 μm centers with C-D nozzles show no cross contamination. Printed OLED arrays have quantum and power efficiency comparable to VTE grown devices of the same architecture and fill factor.

The red dopant RD-15 is a highly sensitive electroluminescent marker for the presence of overspray, with an estimated detection limit of only 1/500 of a monolayer. This electrophosphorescent probe allows the maximum tolerable levels of overspray between adjacent OLED subpixels to be quantified. This can be combined with the modeling in Chapter 5 to estimate the printed feature densities obtainable by OVJP. An array of alternating 100 μm wide red and green features on 210 μm centers without detectable cross contamination can be printed at g =20 μm using C-D nozzles. The required separation between adjacent red and green features reduces to 150 μm for S-C nozzles. Because the tolerance for cross contamination is so low, it is necessary to pre-pattern the substrate with barrier structures to achieve higher feature density. These barriers demarcate printed subpixels and inhibit the lateral motion of organic vapor past the desired feature boundary. Modeling suggests that an array of C-T nozzles printing 40 μm wide sub-pixels onto a substrate with 2 μm high barriers is capable of a pixel pitch as fine as 150 μm. This is comparable to the best achieved by conventional shadow masks.

Chapter 11

Substrate Thermal Effects in OLED Fabrication

11.1 Overview

Organic vapor jet printing inevitably puts a substantial thermal load on a substrate. Low volatility organic vapor is transported to the substrate by a jet of carrier gas that is significantly hotter than the sublimation temperature of the organic material. Since carrier gas is much more abundant than the organic molecules in the jet, heat is transferred to the substrate much more rapidly than it would be in vacuum thermal evaporation. Furthermore, radiative and residual gas mediated heat transfer between the print head and substrate becomes significant due to the proximity of the two structures.

In evaluating these thermal considerations, it is necessary to first understand the physics of heat transfer in OVJP. Heat transfer can be broken into steady state and transient components. Next it is important to understand the effect that substrate temperature during growth has on OLEDs and establish the range of temperatures over which efficient devices can be grown. To this end, performance is evaluated as a function of substrate temperature for multiple OLED deposition methods. These temperature targets can be related to a heat transfer model to determine the amount of thermal load that a substrate can tolerate.

11.2 Steady State Heat Transfer

Steady state heat transfer can be either radiative or due to the motion of carrier gas particles between the print head and substrate. Radiative heat transfer between the print head and substrate is independent of g, since the gap between these two surfaces is small relative to their area, resulting in a parallel plate geometry. Radiative heat transfer per area is given by the Stefan-Boltzmann equation, eq. 11.1, where $\sigma = 5.670373\times10^{-8}$ $W/(m^2K^4)$. The emissivity, ϵ, of Si is 0.5[104]. Assuming the print head is at 600K and the substrate is 300K, the difference in energy radiated by these two surfaces results in a radiative heat flux of 730 mW/cm^2.

$$\varphi_R = \epsilon\sigma T^4 \tag{11.1}$$

Assuming an approximate average pressure of 200 mTorr beneath the print head, the mean free path of N_2 carrier gas molecules, given by eq. 4.17, is λ = 500 μm. This is significantly longer than the separation between the print head and nozzle, even when features like relief trenches are included. Consequently, the motion of carrier gas molecules can be approximated as free molecular flow. Particles move freely between the print head and substrate surfaces. Equation 11.2 gives the flux, φ_G, of energy carried by particles diffusely reflecting from a planar surface at temperature T. The planes of the print head and substrate are separated in the z direction, and v_x, v_y, and v_z are particle velocities. Squared terms correspond to the kinetic energy of the molecule, while the E_{int} term accounts for the internal degrees of freedom of the molecule. For a diatomic molecule like N_2, $E_{int} = k_BT$.[92] The density function, f, that governs particle motion between the print head and substrate is assumed to be spatially invariant. It depends only on momentum, so eq. 11.2 can be expressed as eq. 11.3, where *n* is particle density and *m* is molecular mass.[92] Each planar surface is modeled as a reservoir of gas molecules at temperature *T*. Note that the density of particles effusing from a boundary is *n/2*, since only half of the particles in this reservoir are moving away from the boundary.[91] The limits of integration for eq. 11.3 are such that only positive values for particle velocity normal to the boundary, c_z, are considered. Other degrees of freedom are integrated over their full range. Assuming *f* obeys Boltzmann statistics, eq. 11.3 takes the form of eq. 11.4 and then simplifies to eq. 11.5 by the Equipartition Theorem.[125] Note that kinetic energy terms are grouped under variable *KE* and a normalization constant is expressed as *C* in these equations to avoid excessive length. Integration of eq. 11.5 yields eq. 11.6.

$$\varphi_G = \frac{1}{A}\int_{All\ Particles}\left(\frac{m}{2}\left(c_x^2 + c_y^2 + c_z^2\right) + E_{int}\right)c_z \qquad (11.2)$$

$$\varphi_G = \frac{n}{2}\int_0^\infty \iint_{-\infty}^{\infty}\int_0^\infty (KE + E_{int})c_z f(E_{int}) f\left(c_x, c_y, c_z\right) dE_{int} dc^2\, dc_z \qquad (11.3)$$

$$\varphi_G = \frac{n}{2}C\int_0^\infty \iint_{-\infty}^{\infty}\int_0^\infty (KE + E_{int})c_z exp\left((KE + E_{int})/k_B T\right) dE_{int}\, dc^2 dc_x \qquad (11.4)$$

$$\varphi_G = \frac{n}{2}(2k_B T)\sqrt{\frac{2m}{\pi k_B T}}\int_0^\infty v_z e^{-\frac{m v_z^2}{2k_B T}}\, dv_z + \frac{nm}{4}\sqrt{\frac{2m}{\pi k_B T}}\int_0^\infty v_z^3 e^{-\frac{m v_z^2}{2k_B T}}\, dv_z \qquad (11.5)$$

$$\varphi_G = \frac{3}{2} n k_B T\sqrt{\frac{2k_B T}{\pi m}} \qquad (11.6)$$

Assuming an average pressure of 200 mTorr between the print head and substrate and an average temperature of 450K, midway between a print head temperature of *T* =600K and a substrate surface temperature of *T* =300K, the particle density within this space is 2.1x10^{21} /m^3. The heat flux from the nozzle membrane predicted by eq. 11.6 is

1.8 W/cm^2 and heat flux from the substrate to the membrane is 620 mW/cm^2. The net rate of gas mediated heat transfer between the heated nozzle membrane and chilled substrate is therefore 1.2 W/cm^2.

Combining the radiative and carrier gas mediated heat transport, the steady state heat load of the print head is of order 1.9 W/cm^2. The surface temperature of a substrate under thermal load φ_S and thermal conductivity K can be modeled by applying the Fourier heat law, eq. 11.7,[90] and solving for a 1 dimensional substrate with thickness h, eq. 11.8. For a 700 μm thick glass substrate with K =1 W/(mK),[104] the steady state temperature difference between its front and back surfaces is 13° C.

$$\varphi_S = -K\nabla T \tag{11.7}$$

$$\varphi_S = -\frac{K}{h}\Delta T \tag{11.8}$$

This model suggests various approaches for reducing heat transfer between the print head and substrate. Heat transfer will decrease if the average density of gas between the print head and the substrate is reduced by the incorporation of relief trenches or vents into the print head. Radiative heat transport can be significantly reduced with low emissivity surface coatings such as Au (ϵ =0.02)[104]. Even without such measures, the temperature rise is moderate and substrate holder does not need to be aggressively cooled, provided the substrate is in good thermal contact with it. Thermally conductive materials like FujiPoly®[126] are vacuum compatible and can be used to mount substrates in research scale systems. More elaborate solutions, such as a He cooled electrostatic chuck may be required to expand OVJP to production scale.

11.3 Transient Heat Transfer

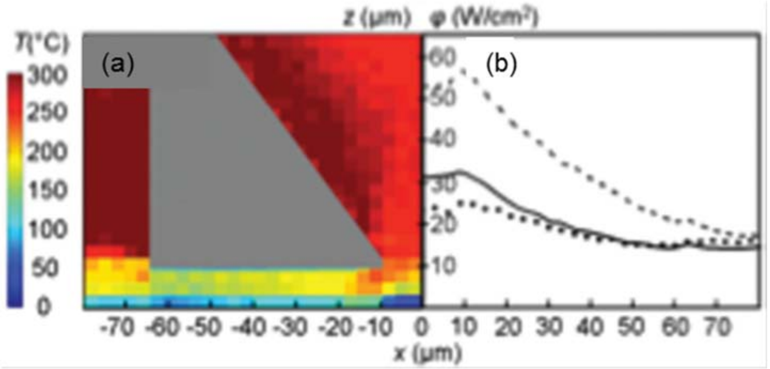

Figure 11-1: Temperature in micronozzle and heat flux to print head. (a) A color plot indicates the temperature of carrier gas around a micronozzle calculated by DSMC simulation. (b) Heat flux φ to substrate is plotted as function of distance from the nozzle centerline. The solid and dashed lines show φ for inlet pressure P_3 =15 Torr and 26 Torr for g =10 μm. The dotted line shows φ for g =25 μm and P_3 =15 Torr. (From McGraw and Forrest)[64]

The steady state thermal load on the substrate is relatively low, but the thermal loads generated by gas jets impinging on the substrate can be much higher. The rate of transient heat transfer to the substrate is best modeled using the Direct Simulation Monte Carlo (DSMC) code described in Chapter 5. Temperature distributions within the gas flow calculated by DSMC are shown in **Fig. 11-1**. When g =10 μm, gas inside the nozzle is in thermal equilibrium with the nozzle array, but it quickly cools as it flows toward the substrate. As indicated in Fig. 10.1, increasing g from 10 to 25 μm at constant nozzle aperture pressure P_3 = 15 Torr yields only a slight reduction in thermal load on the substrate, although the load is less sharply peaked near the aperture. The thermal load on the substrate is expected to be relatively insensitive to g, so long as g is comparable to the mean free path of carrier gas molecules. Conversely, increasing flow rate such that P_3 =26 Torr for g =10 µm significantly increases the substrate thermal load due to a proportional increase in the carrier gas molecular density.[64]

When the molecular mean free path of the carrier gas is of the same order as the nozzle-to-substrate separation, g, or greater, heat is transferred primarily by molecules following ballistic paths between the nozzle and substrate surfaces. As in the previous example of steady state heat flux in the free molecular regime, there are no intermolecular collisions to establish a thermal gradient. As a result, the rate of heat flux is primarily dependent on carrier gas density underneath the nozzle. This implies that the nozzle can be brought arbitrarily close to the substrate without increasing the thermal load on it.

Equation 11.9 is the heat equation in a solid, where α is the thermal diffusivity, $\alpha=K/\rho C_p$. The thermal conductivity of the solid is K, its density is ρ, and its heat capacity is $C_{p.}$ If the depth over which heat penetrates the glass is assumed to be small relative to the width of the jet, eq. 11.9 simplifies to eq. 11.10, which is solved using eq. 11.11.[93] The initial temperature of the substrate surface is T_0. Equation 11.1 is then fit to a surface boundary condition of total heat flux φ_T by eq. 11.12. Finally, the expression for surface temperature as a function of time, eq. 11.13, is obtained. Solving this expression for a typical thermal flux of 30 W/cm^2 and assuming typical values of k, ρ, and C_p for soda lime glass[104], the time required for the surface temperature to rise by 50°C when directly under the jet is 17 ms. Assuming a 200 µm long nozzle, this corresponds to a translation speed of 12 mm/s. Printing speeds of 12 mm/s were demonstrated in Chapter 10, and as will be demonstrated in the next section, 60°C is an acceptable substrate surface temperature for OLED growth. Assuming that the substrate can be cooled to a steady state temperature, $T \leq 10°\text{C}$, the time scale of heat transport is sufficiently long that the transient created by the nozzle passing over the substrate will not overheat the deposited film. Note that the thermal diffusion length in glass for a process with a characteristic time of 17 ms is 50 μm, which is much smaller than the thickness of a glass substrate and on roughly the same length scale as the width of the jet, supporting the validity of the approximations used here.

$$\frac{\partial T}{\partial t} = \alpha \nabla^2 T \tag{11.9}$$

$$\frac{\partial T}{\partial t} = \alpha \frac{\partial^2 T}{\partial z^2} \tag{11.10}$$

$$T = A \cdot \operatorname{erfc}\left(\frac{z}{\sqrt{4\alpha t}}\right) + T_0 \tag{11.11}$$

$$\varphi_T = -k \frac{dT}{dz}\Big|_{z=0} = \frac{2kA}{\sqrt{4\pi\alpha t}} e^{\frac{-z^2}{4\alpha T}}\Big|_{z=0} \tag{11.12}$$

$$T(0,t) = \frac{\varphi_T \sqrt{4\pi\alpha t}}{2k} + T_0 \tag{11.13}$$

11.4 Effect of Substrate Temperatue on Device Peformance

At low substrate holder temperatures, T_{sub}, devices grown by OVJP tend to have maximum external quantum efficiency *(EQE)* that is comparable to VTE control devices, but their *EQE* rolls off quickly with increasing current density, as shown in **Fig 11-2**. Power efficiency, η_p, is low, due to a combination of high turn-on voltage, rapid quantum efficiency roll off with increasing current density, j, and relatively large voltages required to drive a given j. The trend of low j and luminous intensity for a given voltage is clear in the T_{sub} =-20° and 0°C cases with the micronozzle OVJP in **Fig. 11-3**. Its effect of low T_{sub} on η_p is evident in **Fig. 11-4**. A similar reduction in EQE and η_p with low T_{sub} is apparent in **Fig. 11-5**, for the 1 mm dia. nozzle OVJP system described in Chapter 3. Devices in the "2012 APL" case grown at T_{sub} =10° using a print head affixed to its manifold by an epoxy sealant[63] are also presented in Figs. **11-2** to **11-4**. The properties of these devices are similar to those of devices grown at low T_{sub}. The epoxy sealant was replaced with a glass to metal seal due to concerns about contamination.[64]

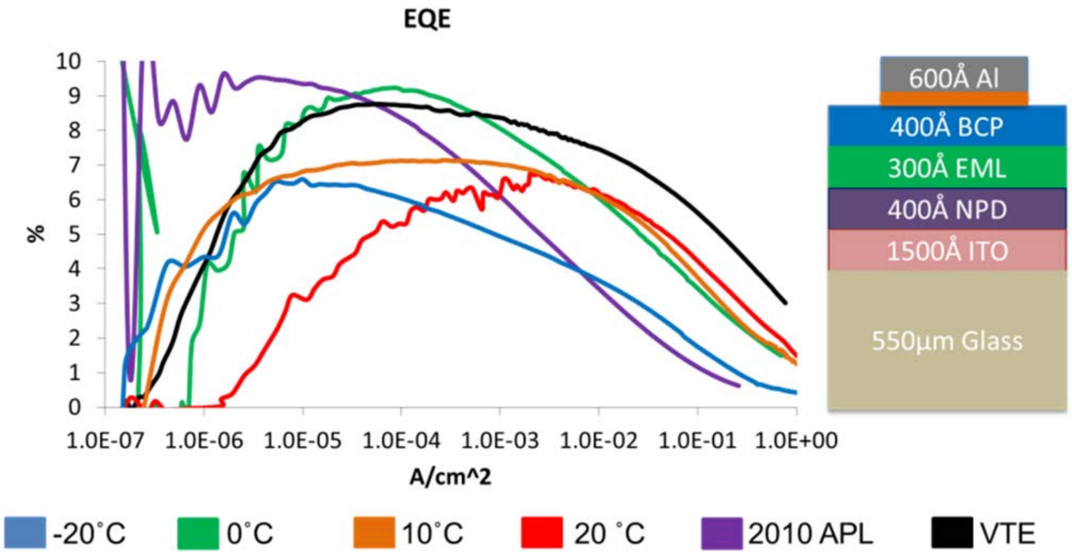

Figure 11-2: Quantum efficiency for OVJP grown OLEDs at multiple T_{sub}. External quantum efficiency is plotted over current density. Devices were grown at substrate temperature from -20 to 20°C. The device architecture used in this and other substrate temperature experiments is shown at right.

At higher substrate temperatures, turn-on voltage decreases and less voltage is required to obtain a given j as seen in the 10° and 20°C cases in **Fig. 11-3**. Quantum efficiency, **Fig. 11-2,** remains unchanged for the 10°C, and η_p, **Fig. 11-4** therefore, increases. A reduction in EQE at low values of j reduces η_p somewhat in the 20°C case,

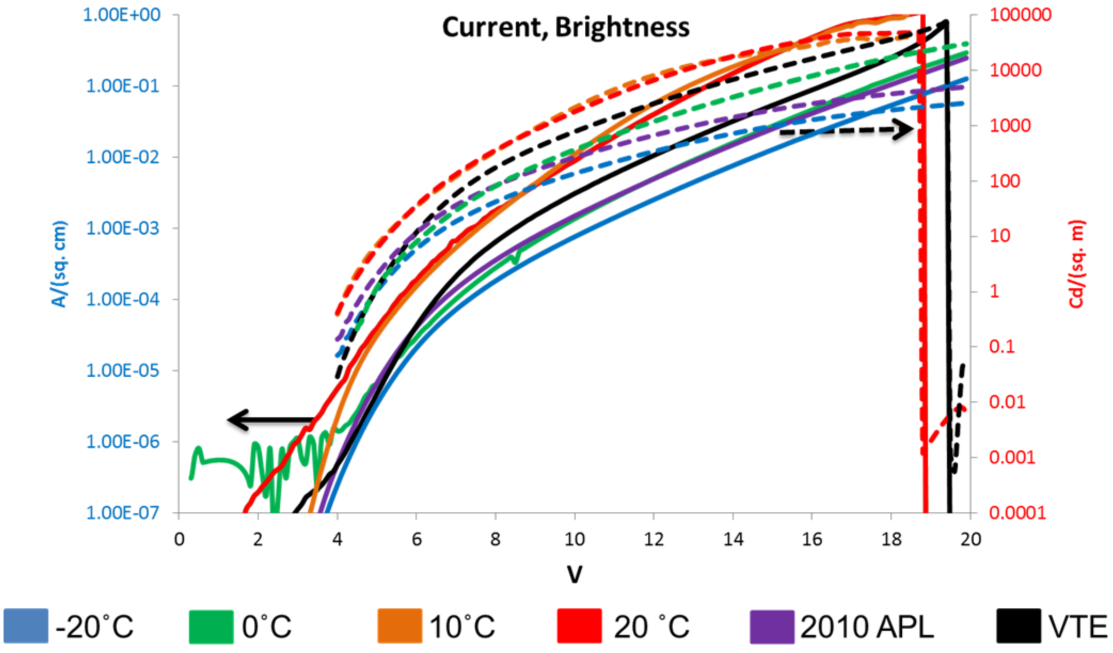

Figure 11-3: Device characteristics for OVJP grown OLEDs at multiple $T_{sub.}$ Current density and luminous intensity of OLEDs grown by micronozzle OVJP are plotted as a function of voltage. Devices were grown at a range of substrate temperatures from -20 to 20°C.

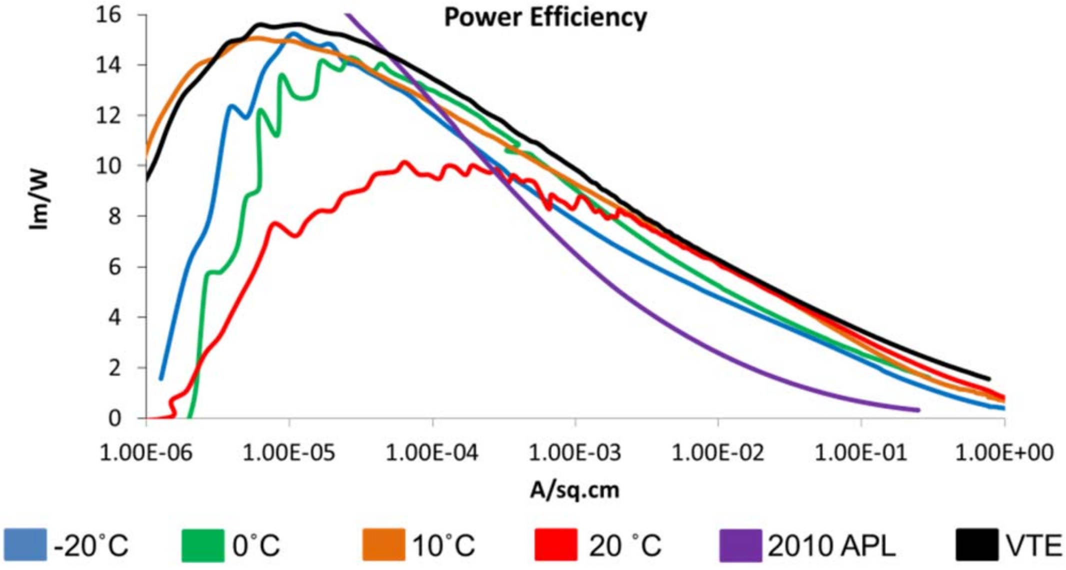

Figure 11-4: Power efficiency for OVJP grown OLEDs at multiple T_{sub}. The power efficiency of OLEDs grown by micronozzle OVJP is plotted over current density. Devices were grown at substrate temperatures ranging from -20 to 20°C.

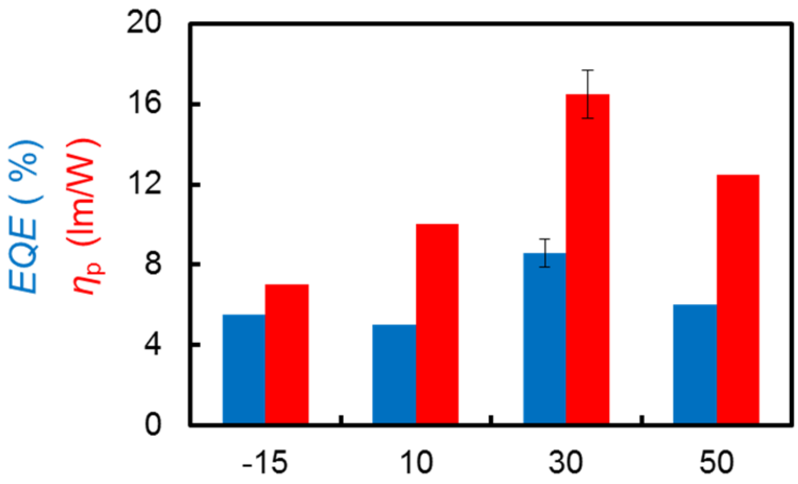

Figure 11-5: Efficiency of 1 mm Ø OVJP grown OLEDs at multiple T_{sub}. Maximum external quantum efficiency (*EQE*) and power efficiency (η_p) for bottom emitting CBP/Ir(ppy)$_3$ OLEDs fabricated using the OVJP tool from Ch. 3 are given for a range of substrate temperatures (°C) shown on the bottom axis.

however this effect disappears for j >1mA/cm^2. A similar trend toward increasing power efficiency at elevated temperature is observed for devices with identical architectures grown using the 1mm diameter nozzle OVJP, **Fig. 11-5**. For films grown at even higher temperatures, j continues to increase for a given voltage. By itself, this would further increase power efficiency, but quantum efficiency decreases due to the presence of apparent electrical shorts through the organic films. Devices grown on an overheated substrate are therefore very inefficient. This is the case for device growths at T_{sub}> 30°C for the micronozzle OVJP and T_{sub}> 50°C for the 1 mm dia nozzle OVJP.

The presence of carrier gas and convection-dominated organic vapor transport are distinctive features of OVJP. To determine if either is responsible for the dependence of device performance on growth temperature, sets of CBP/Ir(ppy)$_3$ OLEDs of the architecture depicted in **Fig. 11-2** were grown over a range of temperatures using OVPD to control for the presence of strong convection.[61] Carrier gas velocities are lower in OVPD and it can be operated in a regime where diffusion dominates vapor transport. Since the transport layers of OVJP devices were grown by VTE, only the emissive layers of the OVPD device set were grown by OVPD. Other layers were grown by VTE.

Another set of devices was grown by organic molecular beam deposition (OMBD)[127] to eliminate the carrier gas effects. Depositions by OMBD are performed at base pressures of 10^{-9} Torr, however they are otherwise analogous to VTE growths. The OMBD tool is equipped with a temperature controlled substrate holder to facilitate this study. There is a negligible thermal load placed on the substrate during OMBD due to radiative heating of the material sources. A doped film is deposited in OMBD by two 30 mm diameter Knudsen cells heated to ~250°C. The substrate is located 30 cm from these sources. Assuming the cells to be blackbodies and applying eq. 11.1, a heat flux of 0.5 mW/cm^2 is expected at the substrate. This corresponds to a temperature difference of much less than a degree for a 700 μm thick glass substrate.

Growth temperature affects the performance of OLEDs in a similar manner regardless of the mode of growth; however the extent can differ greatly. Devices grown at low T_{sub} are relatively resistive to current flow, and devices grown at higher T_{sub} permit larger j at a given voltage but may develop shorts. Quantum and power efficiency decreases at both temperature extremes, with a maximum between 0 and 60°C depending on the deposition technique. The effect is pronounced over a relatively narrow temperature range for OVPD (see **Fig 11-6**) for which there is a noticeable difference in power efficiency between -10, 0, and 40°C. Performance was severely degraded in the case of devices grown at 80°C. Conversely, the performance of OMBD grown devices is relatively constant over a range from -10 to 60°C, **Fig. 11-7**. Devices at 75°C and -186°C showed significant reductions in quantum efficiency, but the change was less dramatic than that observed in the 80°C and -20°C cases for OVPD. A set of devices grown at 100°C by OMBD did not function well enough to produce useful data.

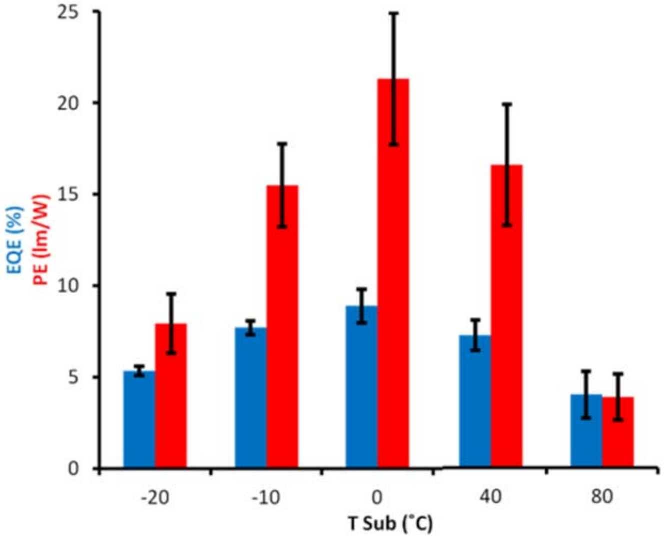

Figure 11-6: Efficiency of OVPD grown OLEDs at multiple T_{sub}. External quantum efficiency (blue) and power efficiency (red) at a current density of 1 mA/cm^2 are given for bottom emitting CBP/Ir(ppy)$_3$ phosphorescent OLEDs grown by OVPD over a range of substrate temperatures, T_{sub}.

Studies of undoped, single heterojunction, **Fig 1-2b**, fluorescent OLEDs have noted also the general trend of decreasing external quantum efficiency with increased T_{sub} during growth by VTE. Kwong et al, found that devices grown at 100°C had only 70% of the quantum efficiency of devices grown at room temperature, despite an absence of clear morphological changes in completed devices.[128] Current density, however,

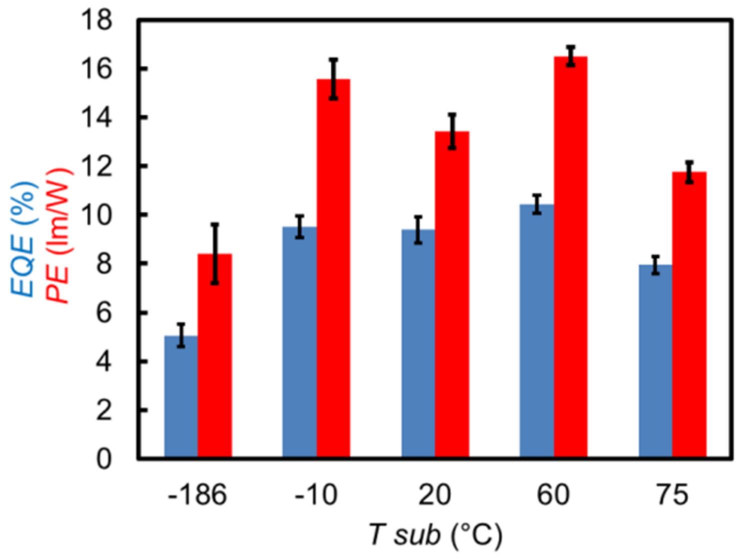

Figure 11-7: Efficiency of OMBD grown OLEDs at multiple T_{sub}. External quantum efficiency (blue) and power efficiency (red) at a current density of 1 mA/cm^2 are given for bottom emitting CBP/Ir(ppy)$_3$ phosphorescent OLEDs grown by OMBD over a range of substrate temperatures, T_{sub}.

follows an opposite trend and decreases with increased T_{sub} at a given voltage. A much greater temperature range was required to produce a significant change in the electronic characteristics of undoped devices. This suggests that growth of a doped film capable of efficient energy transfer between host and dopant is the most temperature sensitive aspect of OLED fabrication. Host and dopant material are only well mixed in an amorphous phase, since they separate upon crystallization. Signs of increased crystallization in deposited films, such as higher surface roughness, are seen at high substrate temperature in other T_{sub} dependent studies.[129][130] Since these studies were also done with neat films, the devices continued to operate with pronounced crystalline phases. Doped devices suffer a severe reduction in efficiency when crystalline phases are present. The photographs in **Fig. 11-8a** and **b** clearly show that crystal formation in devices with emissive layers grown at T_{sub}=80°C by OVPD, while **Fig. 11-6** indicates a significant decrease in device performance under these conditions.

In the case of micronozzle OVJP and OVPD, optimal EQE is obtained at 0°C. When transient heating and imperfect thermal contact are considered, the temperature at the upper surface of the substrate can be up to 40°C higher than the substrate holder. This was confirmed with thin film thermocouple measurements taken during OVJP deposition. A similar thermal load and degree of substrate heating is expected for devices grown by OVPD. The organic film thin film may be growing on a substrate surface heated to 50°C or more if T_{sub} =10°C. Growths by OVJP and OVPD T_{sub} =10°C would therefore correspond to T_{sub} =60°C results for OMBD.

Substrate holder temperature T_{sub} is a readily measured process variable. It is the substrate surface temperature, however, that directly affects film characteristics and this is difficult to measure *in situ*. Device performance rolls-off more rapidly with T_{sub} in the presence of carrier gas because the temperature of the upper surface of the substrate reaches a damaging value (~100°C) at a lower nominal value of T_{sub} than in its absence. Evidence of thermal damage is clear in the crystallized films in **Figs 11-8a** and **b**, while films grown at lower temperatures in **Figs. 11-8c** and **d** show no widespread crystallization and produce devices with satisfactory electronic properties.

It is worth noting that the film in **Fig. 11-8a** and **b** has two distinct crystalline phases. The smaller patches of crystal growth emit green light when viewed under UV, and are therefore most likely Ir(ppy)$_3$ that phase separated from the emissive layer. The larger, blue emitting crystals are spherulites, which are commonly formed from BCP.

Since BCP was deposited at room temperature by VTE following the OVPD deposition, this implies that defects in the emissive layer can nucleate crystal growth in the blocking layers.

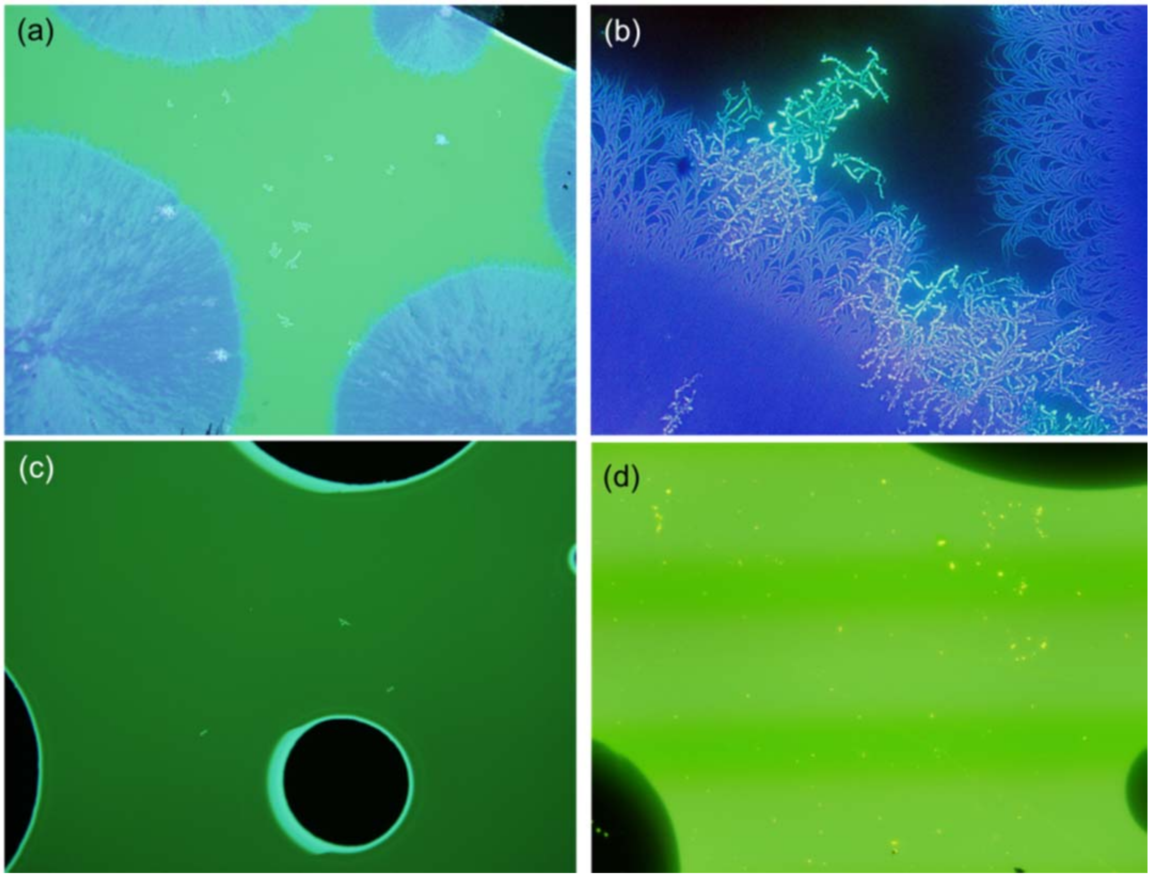

Figure 11-8: Fluorescence images of OVPD and OVJP grown films at multiple T_{sub}. Images (a) and (b) show a film grown at a substrate holder temperature of T_{sub} =80°C in OVPD. Two distinct crystalline phases are visible due to the high growth temperature. This can be compared to OLEDs with emissive layers grown by (c) OVPD and (d) OVJP at T_{sub} =20°C. Extensive crystallization is not apparent in the latter two cases.

The drop in η_p with decreasing T_{sub} in OVJP is most likely due to contaminants that condense onto the substrate. Deposition takes place in medium vacuum, (1 to 0.1 mTorr), meaning that low levels of water or hydrocarbons may be present. If a chilled substrate is the coldest part of the chamber, contaminants will tend to migrate there. The CBP/Ir(ppy)$_3$ film shown in **Fig. 11-9a** grown by OVJP at liquid N_2 temperature supports this hypothesis. Its mottled pattern is similar to that observed on organic thin films placed in contaminated cryostats. The mottling disappears at higher T_{sub} as shown in

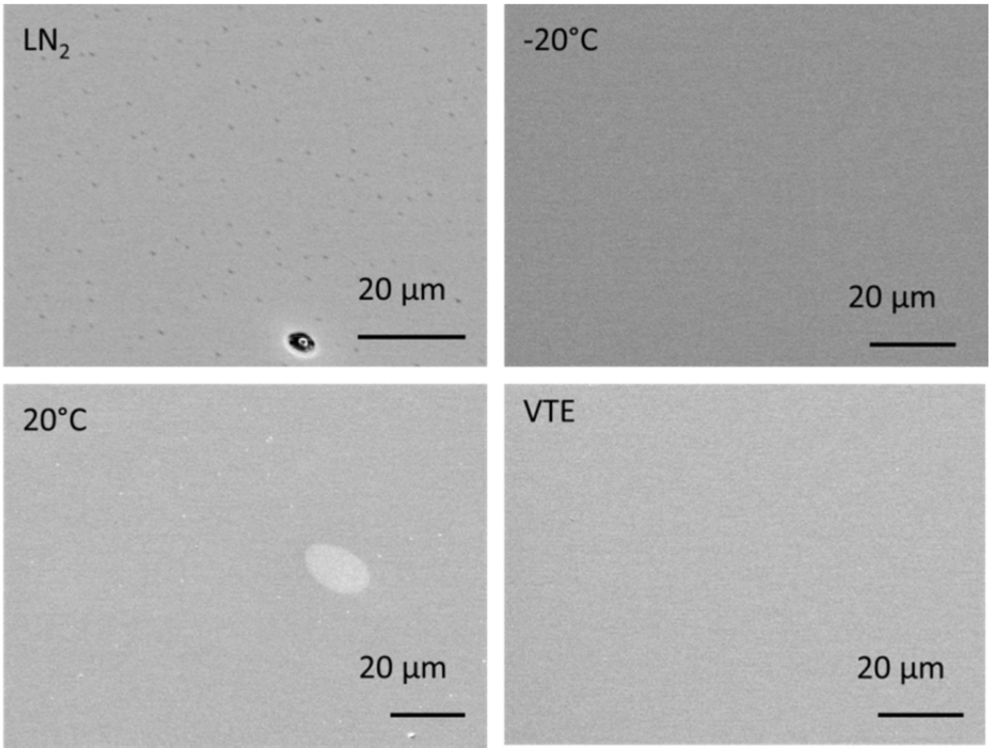

Figure 11-9 SEM images of OVJP films grown at multiple $T_{sub.}$ The emissive layers of CBP/Ir(ppy)$_3$ OLEDs were grown by OVJP at a range of substrate holder temperatures, T_{sub}, and compared with a VTE grown film. The film grown with liquid nitrogen coolant, T_{sub} =-186°C, shows a dimpled pattern which is not present in the other samples.

Figs. 11-9b and **c**. As noted earlier, devices grown at low T_{sub} behave similarly to devices grown by an epoxy sealed print head at higher T_{sub}. Since the epoxy sealant was itself a probable contamination source, this supports the hypothesis that films grown at low substrate temperature are affected by contamination from the chamber.

The analysis in the previous sections indicates that the substrate does not need to be cooled to T_{sub} <0°C. Steady state heating is manageable and transient heating can be controlled with a fast linear printing speed. Chilling the substrate, however, may be desirable to increase sticking coefficient of materials with a low sublimation temperature. In this case, a cold trap should be introduced into the chamber to sequester contaminants.

The low T_{sub} data for OVPD and OMBD are somewhat more puzzling. The performance changes in devices grown at T_{sub} in OVPD may be due to gas phase nucleation. Some organic vapor may condense prematurely and precipitate on the substrate as particulates due to cooling as it diffuses through the thermal boundary layer surrounding the substrate. No morphological changes, however, were apparent in low T_{sub} OVPD grown films under SEM or AFM. The hot walled chamber and relatively high (>100 sccm) flow rates of ultra-pure carrier gas should eliminate contamination from residual impurities in the OVPD chamber. The low *EQE* of devices grown at T_{sub} =-186°C in OMBD may be due to low surface mobility at cryogenic temperatures interfering with dissolution of dopant into the host to facilitate good energy transfer.

This study was primarily intended to establish a range of substrate surface temperatures conducive to efficient PHOLED growth. It was, therefore, relatively simple and definite conclusions about the role of temperature in formation of efficient doped films are beyond its scope. A more detailed investigation may be warranted.

11.5 Summary

The heat load placed on a substrate by OVJP has transient and steady state components. Both can be managed so they do not adversely affect OLED growth. The steady state thermal load placed by the print head on the substrate is on the order of 2 W/cm^2. Two thirds of this is mediated by residual carrier gas and the remainder is due to radiative heat transfer. This load creates a temperature difference of 13° C across a typical glass substrate, so heating can be readily managed with a cooled substrate holder. Heat transfer can be reduced by incorporating features such as low emissivity coatings into the print head.

Transient heat fluxes from vapor jets impinging on the substrate are more significant. A typical jet heat flux of 30 W/cm^2 increases the surface temperature of a glass substrate by 50°C in 17 ms. This rate of heating is acceptable if the linear print speed is sufficiently high, corresponding to 12 mm/s for a 200 µm long nozzle. Features can be printed in multiple passes if necessary to reduce peak temperatures due to transient heating. The magnitude of transient heat flux from a jet is nearly independent of nozzle-to-substrate gap g, in the limit of $g \leq \lambda$, where λ is the mean free path of carrier gas molecules under the nozzle. Consequently, g can be made arbitrarily small for high resolution printing without putting an excessive heat load on the substrate.

The characteristics of a doped thin film depend on the surface temperature of the substrate during growth. Highly efficient CBP/Ir(ppy)$_3$ devices can be grown by vacuum thermal evaporation at substrate surface temperature between -10 and 60°, with warmer or cooler substrates producing sub-optimal devices. The temperature of the substrate holder, T_{sub}, is far easier to measure during processing than the substrate surface temperature. Since the use of carrier gas in OVPD and OVJP places additional load on the substrate, the temperature gradient across the substrate must be considered when selecting T_{sub}.

Chapter 12

Conclusion

12.1 Status of OVJP with Micronozzle Arrays

In Chapter 10, it was shown that multicolor arrays of 100 μm wide interlaced red and green phosphorescent OLEDs can be printed by OVJP. Both the extent of and tolerance for overspray contamination between printed pixels in these arrays has been quantified. It is expected that a full color pixel density of 66 pixels/cm (170 pixels per inch) can be achieved with the proper nozzle design and substrate barrier structures. The ability of OVJP to print fine (<20 μm) features was demonstrated in Chapter 9, as was its ability to print continuous emissive layers for efficient bottom emitting PHOLEDs. This experimental work validates both the micronozzle model discussed in Chapter 5 and the whole system model developed in Chapter 6. These models inform a detailed understanding of OVJP and provide a path to developing a practical technique for fabricating full color OLED displays and lighting.

Lessons learned from the experimental implementation of OVJP can also be applied to future systems. Fabrication techniques developed in Chapter 7 allow both sides of a delicate silicon membrane to be chemically micromachined and then securely sealed to a conventionally milled plate, forming a print head that can be installed in a high vacuum deposition chamber. The design of that chamber, discussed in Chapter 8, includes novel features such as compact organic vapor sources and active control of the nozzle to substrate gap.

12.2 Future Work

The next step towards printing full color pixels at high density is to experimentally validate overspray mitigation practices developed through modeling. Processes for depositing efficient blue emitters must also be developed. Scale-up to pilot and ultimately production then becomes feasible. In addition to its application to OLED fabrication, OVJP also provides a starting point for more fundamental work, such as studying the dynamics of flowing organic vapor and nanoprinting small molecule thin films.

12.3 Overspray Mitigation

The primary barrier to adapting OVJP to display manufacture is the presence of detectable overspray. As seen in Chapter 10, some encouragement can be drawn both from the high sensitivity with which overspray can be detected and the relatively small plumes that are, in fact, detected. Using an array of C-D nozzles separated g =20μm from the substrate, overspray limits the pitch of a full color display printed by OVJP to 15-20 pixels/cm. While this would be consistent with a very large display, such as a 45 inch HDTV, higher feature densities are desirable for many applications.

The overspray characterization in Chapter 10 mainly used C-D nozzles, which, as discussed in Chapter 5, are expected to have the most severe overspray characteristics of the four nozzle geometries evaluated. Earlier attempts at multicolor printing used S-C and C-T nozzles resulted in unmanageable levels of overspray. The red dopant pqIr was used in these earlier experiments and it is much more volatile than RD-15. The overspray in that case was most likely due to a non-unity sticking coefficient for pqIr. The first step in a future study of overspray should be to pattern Ir(ppy)$_3$ and RD-15 device arrays with either S-C or C-T nozzles to determine if overspray plumes extending significantly beyond feature boundaries persist.

Overspray scales with nozzle to substrate gap *g*, so it can be controlled by further reducing this characteristic length. The width of the printed feature also scales with *g* and aperture width *a*. A feature of a given size can, therefore, be printed as a sum of narrower, laterally offset features while reducing the extent of the overspray border around it. A dense array of subpixels can be fabricated by either printing each subpixel in multiple passes or printing it in a single pass using multiple arrays of nozzles offset perpendicularly from the printing axis. Very fine control of nozzle height and leveling is required to realize this approach, which requires $g \leq 10\mu m$.

The barrier structures described in Ch. 5.6 are a practical method of reducing overspray once the minimum reproducible *g* is achieved for a given substrate size. Barrier structures serve as getters for some, but not all of the organic material leaving the deposition zone. Carrier gas flow must flow over the barrier, and this flow perturbation can redirect organic vapor molecules so that they move away from the substrate. Unless these molecules can be captured by a second getter, they will inevitably deposit on the substrate, albeit at a very low and possibly tolerable concentration. Maximum benefit from barrier structures can be realized by combining them with vents to allow organic vapor to travel up and out of the gap between the print head and substrate. **Figure 12-1** depicts a possible configuration of a print head with integrated vents and a chilled getter to catch unutilized organic material. An array of C-T nozzles fabricated from a Si membrane is anodically bonded to a Pyrex® plate. Both the Si membrane and plate are etched with vents between each nozzle that allows carrier gas and surplus organic vapor from the nozzles to clear the substrate by passing through to the other side. The plate also contains etched microchannels to distribute vapor from vias along its ends to the centrally located nozzle membrane. The ends of the plate are Au soldered to a heated Kovar® fixture that supplies organic vapor. A chilled getter runs through a gap between the metal fixture and the channel plate. The getter is thermally isolated from the fixture and can be cooled by either thermoelectric cells or a liquid cooling loop. The central

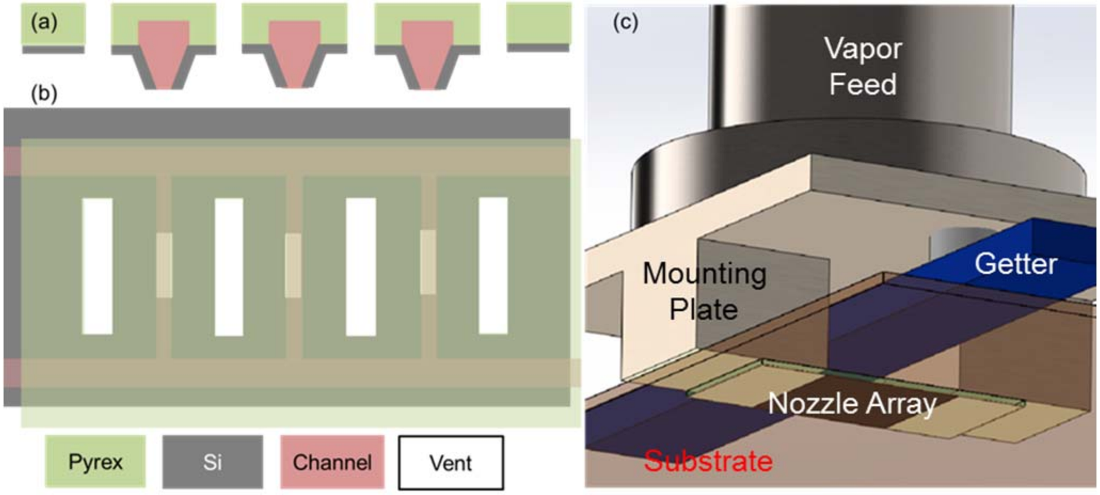

Figure 12-1: Print head with integrated vents and getter. (a) A cross sectional and (b) top view of a nozzle membrane and channel plate show a design featuring vents between nozzles to allow for the escape of un-deposited organic material. The nozzle membrane contains a series of C-T nozzles that is bonded to a Pyrex® channel plate. This plate is etched with both microchannels to distribute vapor to the micronozzles and vents between each nozzle to allow carrier gas and surplus organic material to pass through the plate. (c) The plate and nozzle array mount on a fixture that feeds carrier gas into the micro-channels of the microfabricated structure. A chilled getter traps unused organic material passing through the channel plate.

portion of the channel plate is not in thermal contact with the fixture, but it can be independently heated by passing an electric current through thin film heaters or even the Si membrane itself.

12.4 Full Color Printing

From a transport perspective, there is no barrier to expanding the OVJP process to print phosphorescent doped blue OLED segments, and thereby print a full color PHOLED display. A more challenging problem may arise from the chemistry of blue emitting phosphors. While highly efficient blue emitters for OLED applications exist,[131] they are extremely sensitive to processing conditions. Growing efficient blue devices using the OVJP system from Chapter 3 proved challenging due to issues including thermal degradation. The blue emitter FIr6 was chosen primarily because it was more compatible with OVJP than other blue phosphors.[72] Modifications to the OVJP process, such a noble carrier gas or inert coatings on metal surfaces to prevent chemical reactions at high temperature may be necessary to make it compatible with a wider palate of blue emitters.

12.5 Scale-up

Since the print head was fabricated using conventional semiconductor processing methods, scale-up to arrays of 100 or more nozzles is straightforward. An array of 500 nozzles intended to print at a 150 μm pixel pitch would be roughly 7.5 cm long, which is achievable though MEMS processing techniques. The present system can deposit up to 1.1 μg/s of organic material through ten, 20 μm by 200 μm orifices. Assuming three arrays of 500 20x800 μm aperture nozzles with each array simultaneously depositing a different color, a 300 Å thick, simultaneously patterned red-green-blue emissive layer can be deposited onto a Gen 8 substrate in approximately 250 s. Such a substrate could be diced to yield either six 55 inch or up to eighty 13 inch high definition displays. Nozzles can be arranged on separate carriers or integrated into a single multicolor print head as shown in **Fig. 12-2**. A single print head simplifies registration and allow a pixel triad to be printed in a single pass without loss of speed.[63]

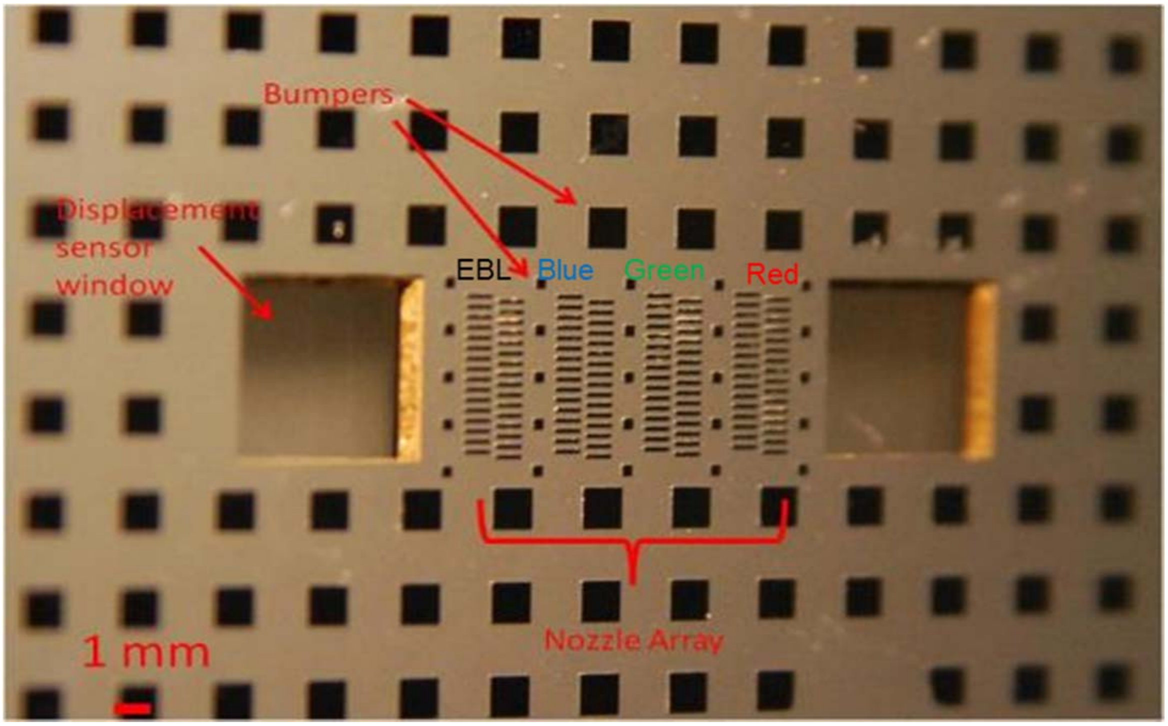

Figure 12.2: Array of 120 micronozzles for multicolor printing. Four separate arrays of 40 nozzles each allow for simultaneous deposition of four different material sets in a single pass. In this example, two collinear nozzle arrays on the left side deposit the electron blocking layer (EBL) and host-dopant mixture for blue devices. The middle-right array is vertically offset one sub-pixel width from the blue arrays and deposits green devices. The far right array is offset by another sub-pixel width and deposits red devices.

12.6 Compressed Organic Vapor

If a method to transfer organic material from condensed sources without the use of carrier gas can be developed, this might provide organic thin film growth and patterning capability far beyond that of OVJP. The presence of a sufficient carrier gas pressure to drive flow creates a diffusive barrier to the evaporation of organic material, as shown in Chapter 6. Furthermore, carrier gas within the nozzle-to-substrate gap mediates significant heat transfer. Carrier gas plays no role in the finished structure, since glassy, VTE-like films are optimal for OLED applications. While purified gasses are relatively inexpensive, their cost and the additional pumping capacity required to remove carrier gas from a deposition chamber must be considered as well.

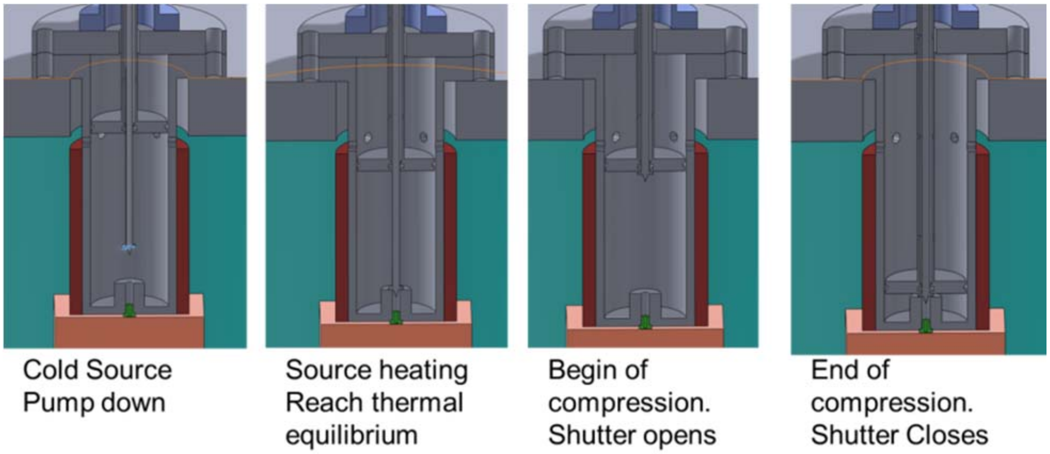

Figure 12-3: Proposed apparatus for compressing organic vapor. Organic material is evaporated directly into a cylinder where it is compressed by a piston. A stopper running coaxially with the piston controls the flow of organic vapor through a nozzle (green). The substrate sits on a chilled holder beneath the apparatus. (Figure courtesy of Cedric Rolin, Ph.D. University of Michigan)

It may be possible to eliminate carrier gas from the OVJP process by evaporating organic material into a heated volume which, upon filling, uses a piston to compress the organic material until it reaches a near-continuum flow condition. The organic material then flows through a heated nozzle membrane and deposits onto a substrate. This method, shown in **Fig. 12-3**, retains the patterning capability of micronozzle based OVJP and is also amenable to pulsed printing, allowing for more complex display patterns to be realized.

The feasibility of this process depends on the phase change behavior of organic material in the vicinity of its sublimation temperature over a range of pressures. The compression and transport of supersaturated vapors of low volatility organic materials is not well understood and may lead to unwanted gas-phase nucleation. Additionally, the incorporation of moving parts into an environment requiring high temperature and low contamination is a significant engineering challenge.

12.7 Nanoprinting

No theoretical limit to the resolution achievable with OVJP or related techniques has been identified. Indeed, DSMC modeling indicates that features of 1 μm or less are possible as shown in Chapter 9.[63] The nozzle array and substrate can be brought into close proximity without increasing heat transfer as demonstrated in Chapter 11.

The largest obstacle to nanoprinting would be one of mechanical control. The position and orientation of the nozzle with respect to the substrate, particularly gap g, must be controlled to nanometer precision. Sensors and actuators with this precision have been developed for applications such as atomic force microscopy. Adapting these technologies to a system like OVJP, where key components are in vacuum and held at temperatures > 300°C, is a considerable engineering challenge.

Fabrication of a membrane of silicon nano-nozzles must also be considered. The SOI-based etching technique described in Chapter 5 involves controlling a small feature, a 20 μm wide aperture, with a much larger, 135 μm wide inlet etched into a 100μm thick Si membrane. A small variation in the actual final dimension of the aperture exists due to factors like variation in etch bath selectivity and the exact orientation of crystal planes relative to the wafer flat. These sources of variation would become much more significant for a sub-micron aperture. Beginning with a thinner membrane reduces variability. Assuming these sources of error scale linearly, a 1 μm thick membrane would be desirable for producing nozzles with 200 nm wide apertures. Both SOI processing and Au soldering technique can be applied to such a thin membrane, however methods for handling this delicate structure must be developed. Finally, the flexibility and burst strength of thin silicon membranes need to be considered when designing a print head and predicting its operating envelope.

12.8 Conclusion

While the path to developing OVJP has been difficult at times, the overall outlook for this technology is positive. A relatively simple implementation of OVJP using micronozzles was able to produce phosphorescent OLEDs with efficiencies comparable to those achieved by VTE. It was also capable of printing resolutions within a range that is of interest to display patterning. Features on the order of 10 μm can be printed and arrays of interlaced 100 μm wide red and green OLEDs were patterned using OVJP. Cross-contamination between adjacent features must be considered when depositing dense arrays of electroluminescent material. Modeling using a direct simulation Monte Carlo code validated by experiment indicates that pixel pitches of 150 μm are obtainable with the use of barrier structures. This would make OVJP suitable for fabricating large area displays compliant with all current resolution standards.

Returning to the criteria laid out for a viable OLED patterning method in Chapter 2, a process must be, (i) capable of high resolution patterning, (ii) compatible with high efficiency device architectures, and (iii), highly scalable. The first two goals have been largely met by OVJP, as demonstrated by this work. High resolution feature printing has been achieved and a clear path exists to applying OVJP to the emissive layers of displays. Standard phosphorescent devices with performance comparable to other PVD methods can be fabricated using OVJP, making OVJP suitable to fabricate high efficiency OLED architectures. Since photolithographic processing was used to fabricate the micronozzle arrays, the third goal of scalability should follow from the inherent scalability of silicon processing techniques. Large micronozzle arrays for high resolution printing that are optimized for low flow impedance, rapid material deposition rate, and massively parallel patterning can be fabricated. Based on the performance observed in the laboratory system, a production scale OVJP may be able to print a full color OLED emissive layer onto a Gen 8 substrate in only 250 seconds.

Appendix A: Piping and Instrumentation Diagram

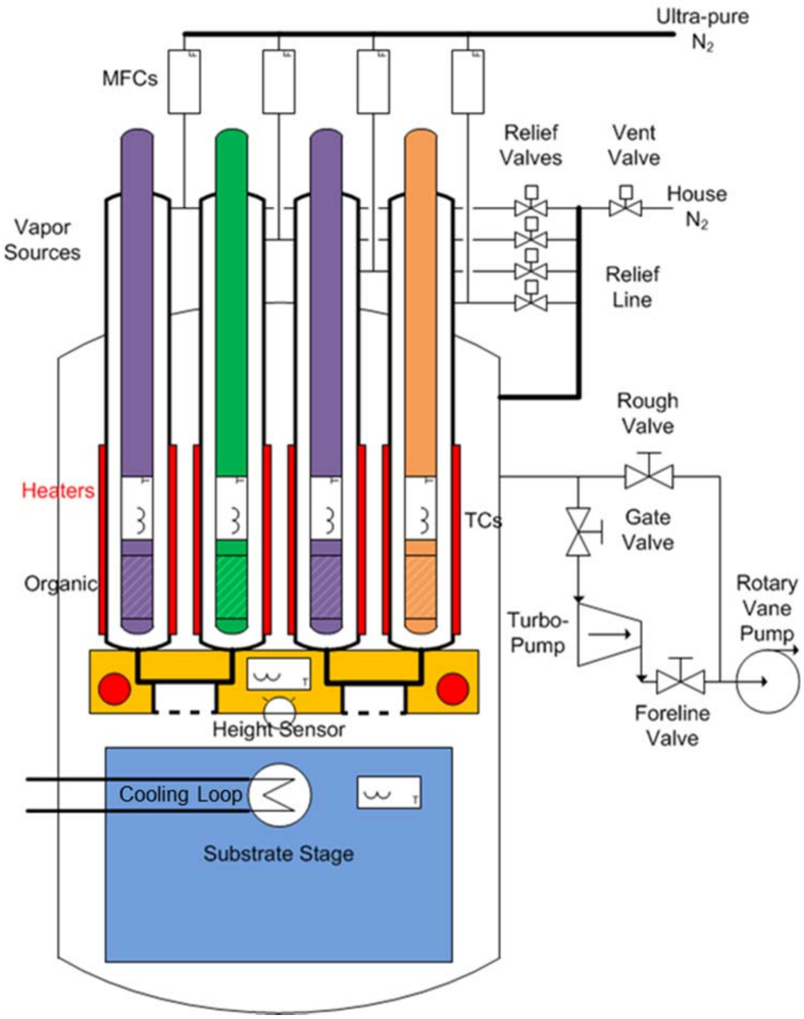

Figure A-1: Piping and instrumentation diagram for OVJP tool. This diagram shows all fluid components of the OVJP process with associated tubing, pumps, valves, heaters, and sensors.

Ultra-pure N2 carrier gas is metered into an array of organic vapor source tubes containing a vial of sublimable organic material. Each source has its own mass flow controller (MFC), heater (red), and thermocouple (TC). The carrier gas and vapor mixture from pairs of adjacent sources containing host and dopant material combine in the print head to feed a nozzle membrane covering a common trench. The print head is also equipped with heaters and thermocouples.

A relief line provides a low impedance gas flow path between the organic vapor sources and vacuum chamber. This prevents potentially damaging pressure buildups across the nozzle membrane during chamber pump down and venting. Organic vapor source tubes are each connected to a common relief line by normally open pneumatic valves. This valves isolate the sources and allow carrier gas pressure to build up and drive flow through the nozzle membrane during deposition, while allowing unimpeded flow between the source and chamber at all other times.

The chamber operates at medium vacuum ~10^{-4} Torr. Vacuum is maintained by a turbopump. The turbo can be isolated from the chamber with a manual gate valve and from the rotary vane pump by a manual bellows valve. A rough pump line connects the chamber to the rotary vane pump. This is also sealed by manual bellows valve.

Nozzle aperture to substrate gap is controlled by a PhilTec RC-25 fiber optic reflectance displacement sensor as described in Chapter 8 and Appendix B. The substrate stage is liquid cooled, with refrigerants ranging from chilled isopropanol to liquid nitrogen supplied externally. A thermocouple permits measurement of substrate holder temperature; however the temperature of the cooling liquid is regulated at its source.

Appendix B: Electrical Diagrams

The OVJP tool is controlled through a PC which communicates to the various components of the tool through a variety of interface protocols. The computer interfaces with some devices directly and with others through adaptors and via programmable control busses. The layout of the control network is depicted in **Fig. B-1.** The feedback loop for the substrate height controller is shown in **Fig. B-2**

The heater circuits for both the organic vapor sources and print head were largely custom made. Circuit diagrams are depicted in **Fig. B-3** and **4**. **Figure B-5** gives a cabinet wiring diagram for the OVJP tool.

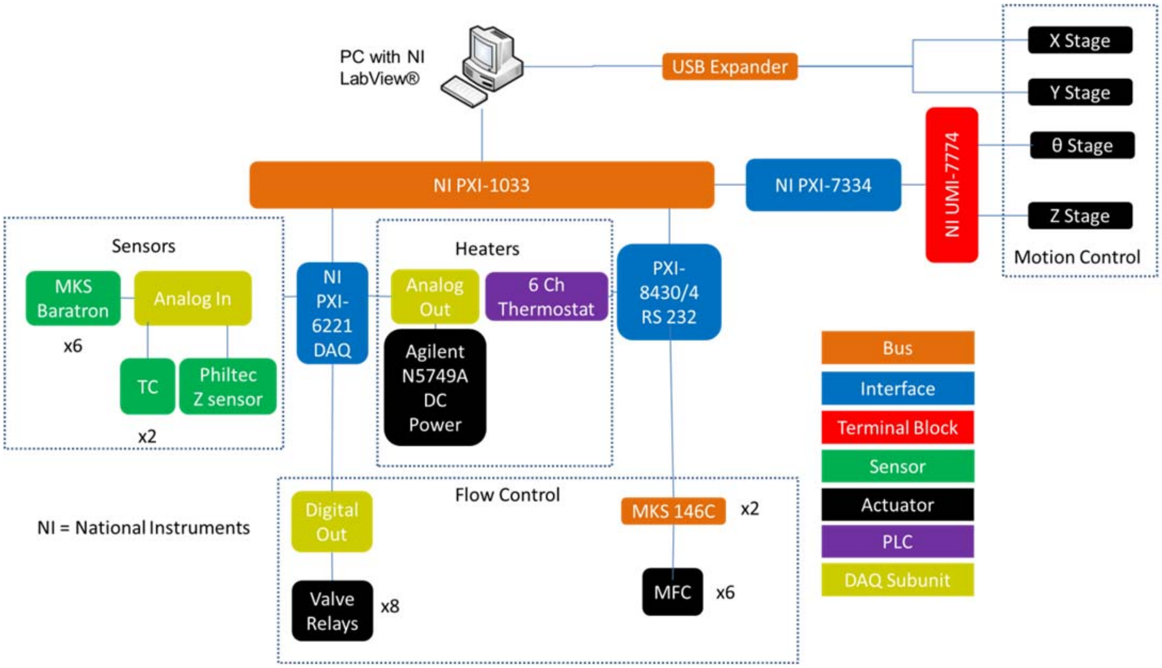

Figure B-1: Main control diagram for OVJP tool. The tool is controlled by a PC that connects to it with a PXI-1033 Bus. Functions on this bus are controlled through LabView.® The bus is equipped with motion control, serial communication, and CAN network communication cards. Thermostats and flow controller busses maintain set points established by the computer. The PXI-1033 bus is also equipped with a DAQ that senses analog inputs to measure temperature and pressure. It also communicates analog outputs to the print head heater circuit and digital output signals to control solenoid valves. A separate USB hub connected to the computer controls the x and y stages via Physik Instrumente MicroMove® software.

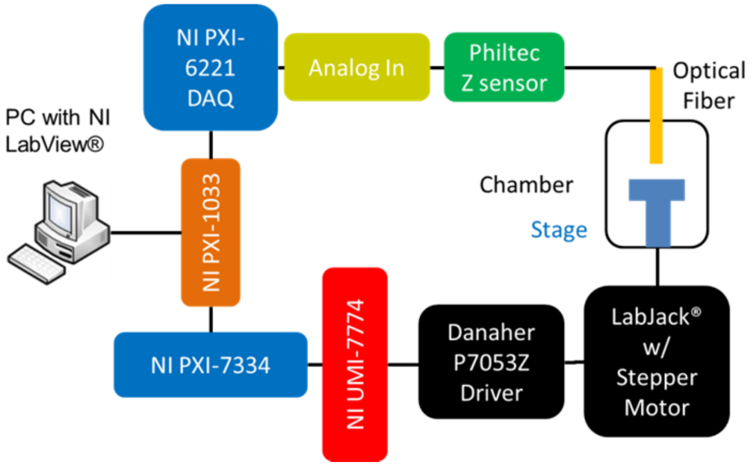

Figure B-2 Control system for substrate height in relation to print head. Height measured by an optical sensor. The OVJP control software compares the measured height to a set point and sends commands to adjust the *z* axis actuator accordingly by a proportional-integral (PI) control algorithm.

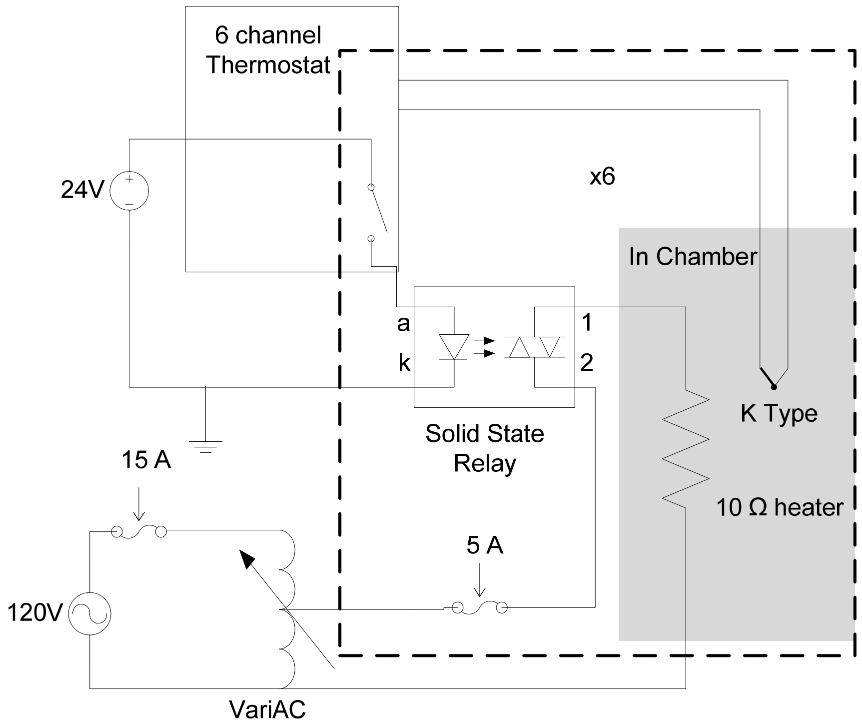

Figure B-3: AC power supply for organic vapor source cells. Sources receive power through a variable autotransformer set to ~10V. Power is switched by solid state relays which are controlled by a six channel thermostat connected to thermocouples in each heated zone. The thermostat turns each relay on and off according to the commands of an internal PID loop. Thermostat set points are programmable via an RS-232 connection with the computer.

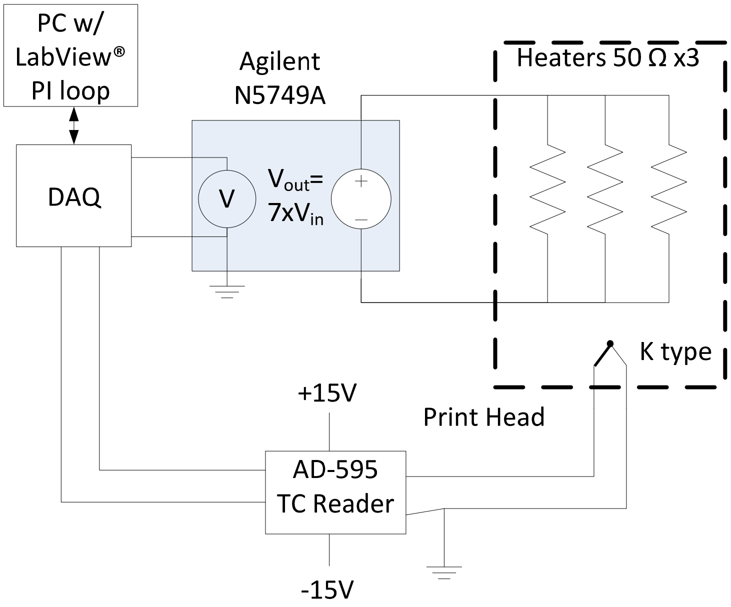

Figure B-4 Print Head Heater Circuit. Temperature is read by a K type thermocouple with a monolithic reader chip and logged by a Data Acquisition Card (DAQ). A software control loop in LabView compares these inputs with a set point and determines the proper current output through a PI algorithm. The desired power level is communicated to an Agilent DC power supply that is controlled by analog programming through the DAQ. Ethernet, USB, and RS-232 modes are also possible.

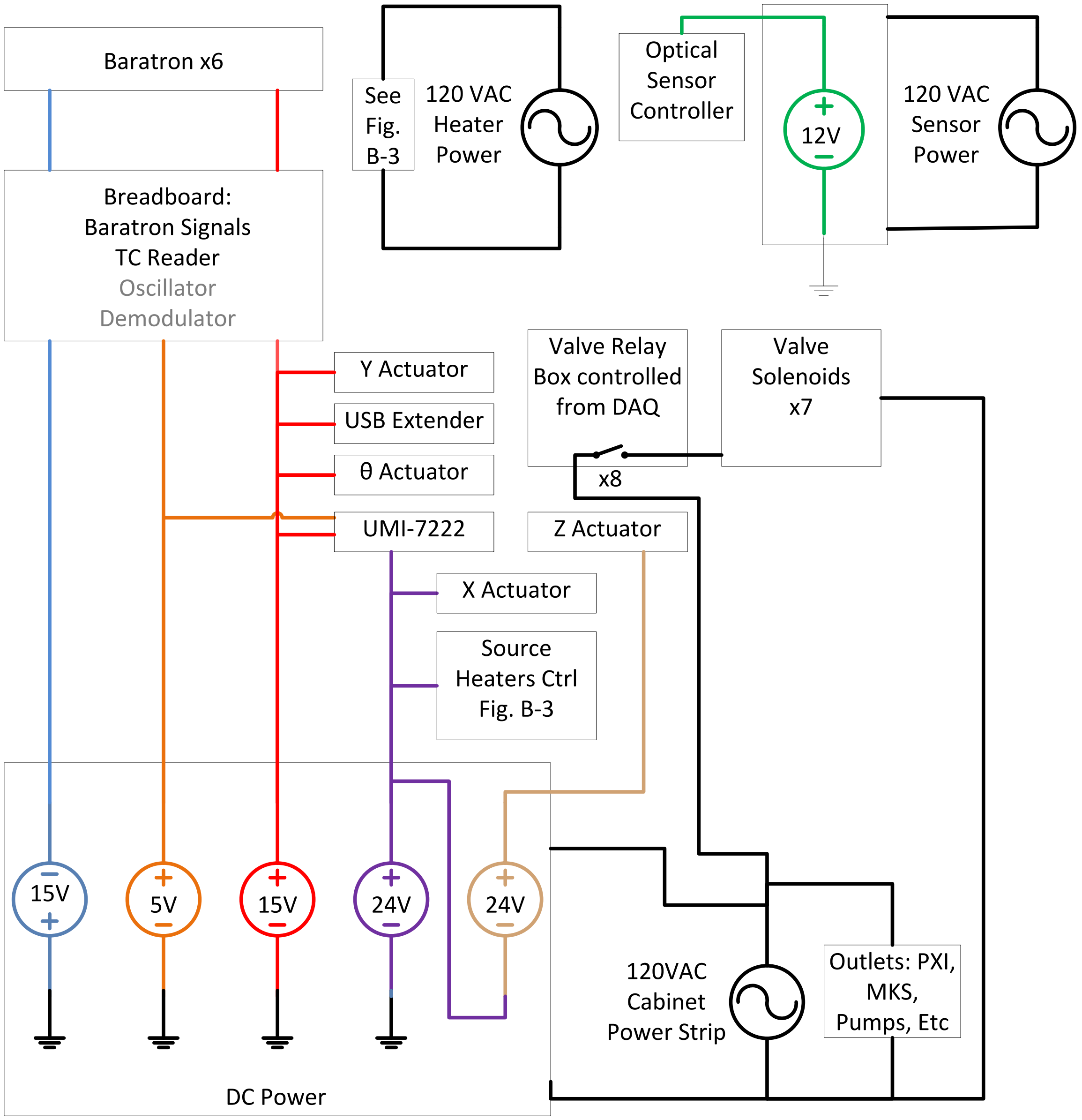

Figure B-5 OVJP cabinet power distribution system. The tool is powered by three separate 120V/20A circuits. Most of the equipment is run off of a single circuit through a power strip. Chassis power, both DC and AC is supplied through a single outlet on this strip. Instruments from vendors plug into other outlets. A multi-outlet DC power supply in the cabinet accommodates a variety of power needs. All DC powered equipment is connected to ground, even if not explicitly specified. A different circuit provides power for the organic vapor source heaters. The substrate chiller (not shown) connects to a third circuit.

Appendix C: Mechanical Drawings

There are dozens of mechanical drawings associated with the OVJP tool. Drawings for a few of the key assemblies are provided here. This reference is primarily to provide plans for parts requiring frequent replacement and give measurements for future chamber modifications. A complete set can be found on the Optoelectronic Components and Materials (OCM) group server.

Note that fabrication of the structure in **Fig. C-1** requires drilling narrow 2 mm dia. holes with an aspect ratio of 25:1 into Kovar® low thermal expansion steel. Kovar® is slightly less machinable than 304 Stainless Steel, which is itself sufficiently hard and ductile to make these features difficult to fabricate. Drilling is performed on a vertical mill at 1000RPM. The bit is advanced in 1 mm increments and chips are cleared between steps. It should also be liberally lubricated with tapping fluid between steps. Long diagonal channels are required to join the outside vias to the nozzle feed trenches. Notches should be machined into the sides of the plate to allow these drillings to begin from a plane normal to the intended channel. Channels can be plugged at their ends with 304 Stainless Steel dowel pins with heads fused to the channel plate using a TIG torch. The metals are miscible. Note that hot rolled plate should be used to minimize residual stress and the work piece should be surface ground on both sides and solvent cleaned before advancing to cleanroom fabrication as described in Chapter 7.

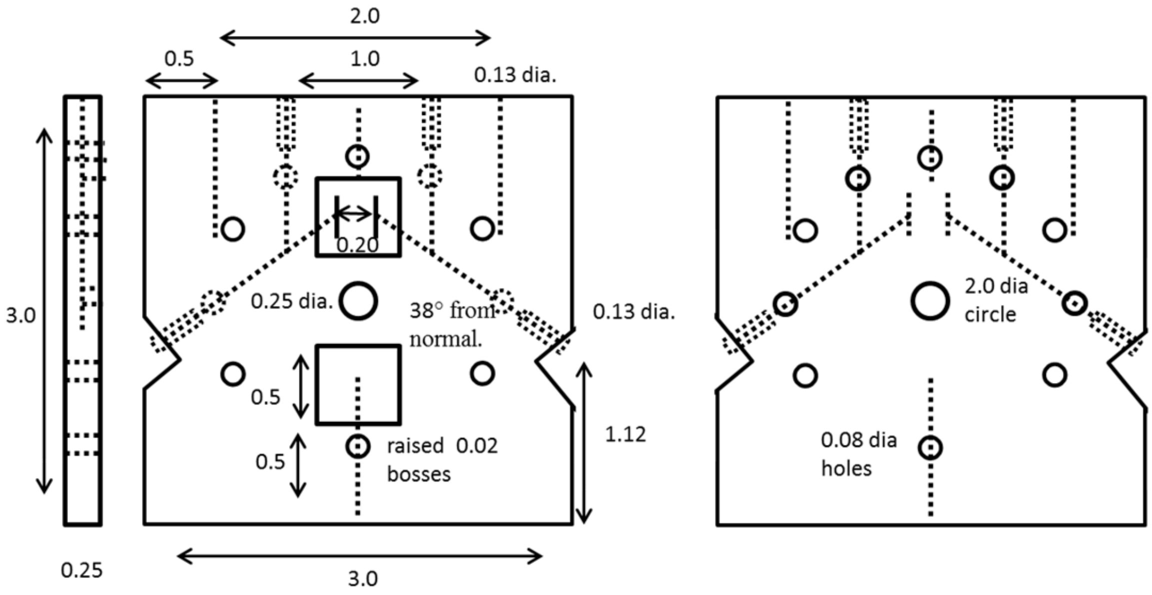

Figure C-1: Mechanical drawing of print head carrier plate. The plate features integrated channels and is made of Kovar®. Dimensions are in inches. Drillings into the front surface of the plate are arranged in a 2 in diameter clock face around a central through hole for the optical sensor. The even numbered positions are countersunk through holes to slip fit #2 screws. The 1, 3, 9, and 11 o'clock positions are bored 0.13 in into the plate to form vias that connect organic vapor sources to the channels bored into the sides of the plate. Channels are 0.08 in in diameter with 0.13 in entrances that can be sealed with 0.125 in diameter stainless steel dowel pins. Other drillings into sides of the plate accommodate heaters and thermocouples. These should be 0.13 in diameter. The angle of the diagonal channels should be chosen to connect the 3 and 9 o'clock inlets to the centers of the nozzle membrane feed trenches. The nozzle membrane is mounted on a 0.5 in square boss raised 0.02 in above the surface of the plate to facilitate lapping and polishing. A second boss is machined into the other side for symmetry while lapping and bonding.

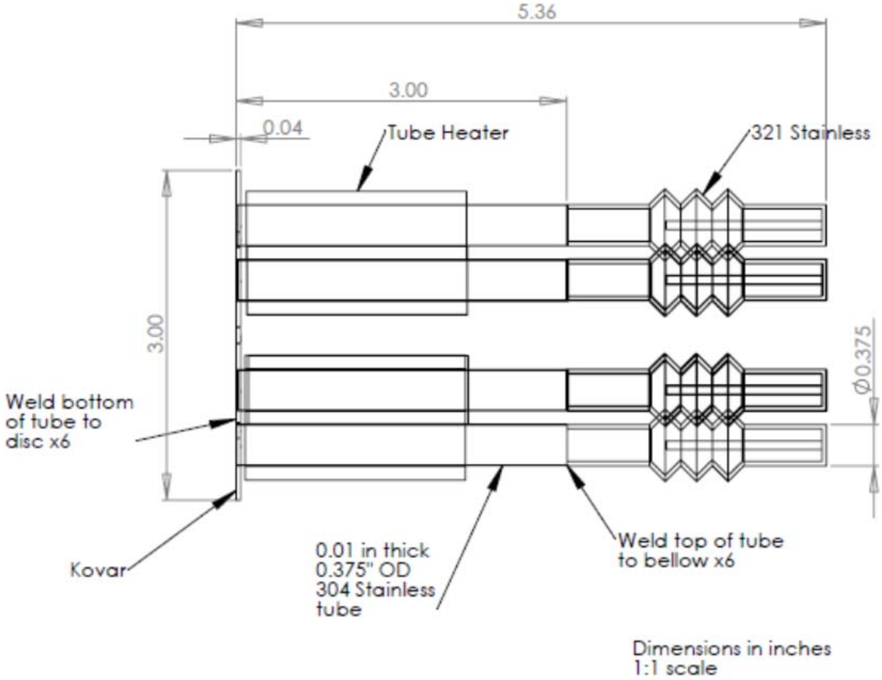

Figure C-2: Welding diagram of print head attachment manifold. The machined Kovar® disc at the base is laser welded to stainless steel source tubes. The bead is run between the inner surface of the tube and the underside of the nozzle. Source tubes are laser welded to bellows at the opposite end. Bellows can be eliminated since the Swagelok UltraTorr® fittings used to seal tubes to the feedthrough accommodate thermal expansion of the source tube. Dimensions are in inches. Note error in drawing. The actual radius of the Kovar® disc is 4 inches.

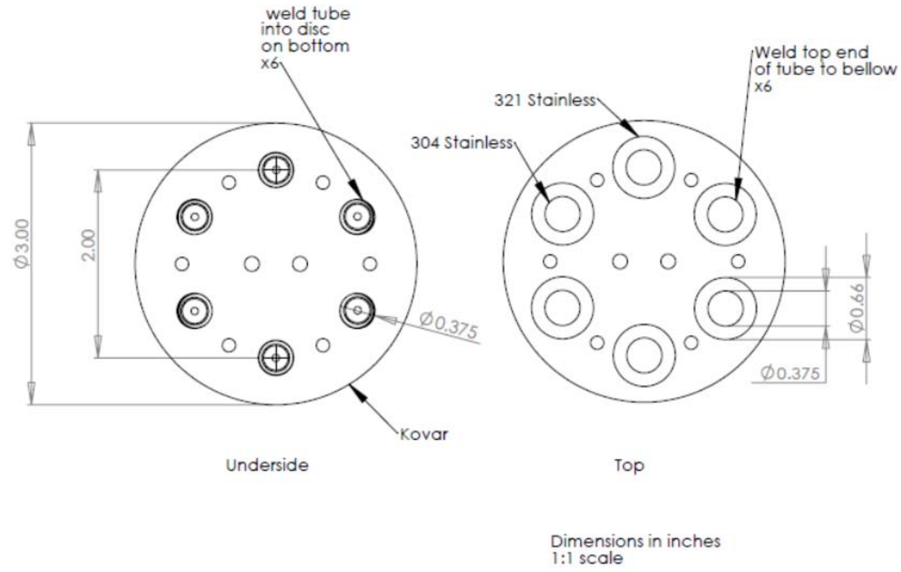

Figure C-3: Mechanical drawing of manifold flange. Dimensions are in inches. Note that this drawing has the same error as the previous structure. It is also a 4 inch disc. The other dimensions are correct. Glands on underside of the Kovar® plate are for #14 O-rings. They have 0.625 in outer diameter, 0.5 in inner diameter, and 0.057 in deep. A 0.25 in diameter cutout through the center was added later to accommodate the height sensor.

Figure C-4 (next page): Major dimensions and component list for chamber pedestal. Structure is fabricated from ¼ in cold rolled mild steel plate and rests on machine feet. It attaches to the underside of the vacuum chamber through the bolt circle of its bottom flange. A tray below the chamber provides a firm attachment point for z and θ actuators that connect to the inside of the vacuum chamber through a feedthrough. (Drawing courtesy of Diane Peters, P.E., Ph.D.)

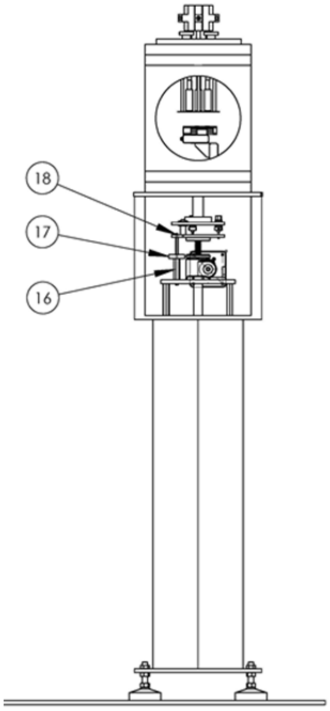

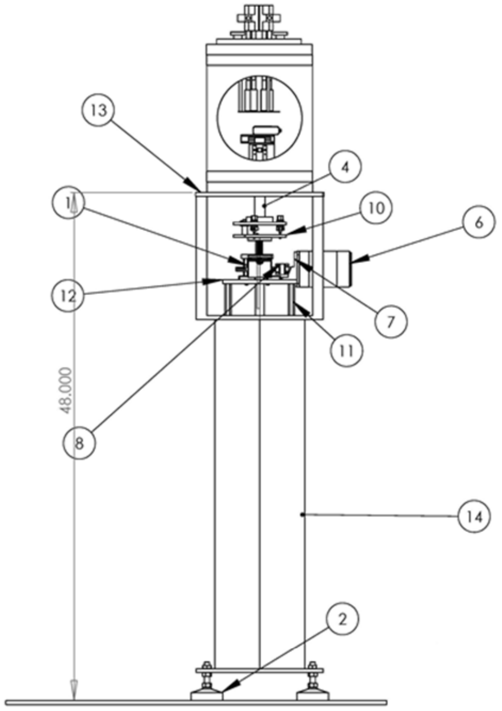

ITEM NO.	PART NUMBER	DESCRIPTION	QTY.
1	5945K370	SCREW JACK, McMASTER-CARR	1
2	AX-5	LEVELING PAD, REID TOOL	4
3	90494A033	HEX NUT, 1/2-13 UNC (SUBSTITUTIONS FOR GIVEN McMASTER NUMBER ARE PERMISSIBLE)	4
4	flangeConnector		1
5	chamber		1
6	6134K89	STEPPER MOTOR, McMASTER-CARR	1
7	bracket		1
8	CC-68	FLEXIBLE SHAFT COUPLING, REID TOOL	1
9	floor		1
10	NewLevelingAssem	SEE SEPARATE DRAWING FOR DETAILS	1
11	92230A345	SPACER, McMASTER-CARR	4
12	MountingPlate		1
13	TopPlate		1
14	NewStand		1
15	6381K413	BRONZE BEARING, McMASTER-CARR	1
16	93505A200	SPACER, McMASTER-CARR	2
17	StabilizerPlate		1
18	91259A105	SHOULDER SCREW, McMASTER-CARR	1
19	M110stage		1
20	M112stage		2
21	M-110mountingbracket		1
22	mountingbracket		1

Appendix D: Mask Designs

Mask designs used for OVJP are available in AutoCAD dxf format on the Optoelectronic Components and materials group server. Some mask layouts and descriptions are printed here. The green portions of the masks are used to expose the substrate side of the nozzle membrane. Regions inside of the lines are etched by an ethylenediamine pyrocatechol (EDP) solution as described in Chapter 7. Therefore, the edges of each green rectangle define the point at which point the <111> crystal plane of the etched trench intersects the <100> plane of the wafer surface. Etched features are narrower at their bases because the <111> crystal plane of Si remains un-etched while other planes are attacked. Red rectangles define the intersection of the <111> plane of the nozzle inlets with the <100> plane of the surface of the wafer bonded to a carrier or channel plate. In this case, etch anisotropy creates funnel shaped inlets.

Each nozzle membrane design depicted here has nozzles arranged in two banks. Each bank fits over a separate feed trench on a metal carrier plate as described in Chapter 7. This allows multiple host and dopant combinations to be deposited simultaneously, producing multicolor devices. Nozzle banks with various center to center nozzle spacing are depicted. The two nozzle banks are offset by one half center to center spacing perpendicular to the printed lines so that alternating lines of interlaced colors be deposited in a single pass.

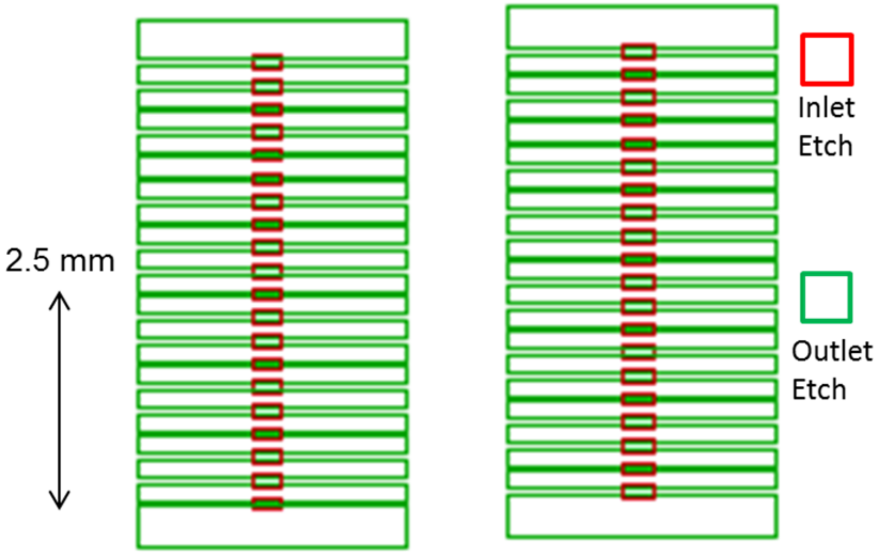

Figure D-1: Mask Design for a die with two banks of 20 converging-tapered nozzles. The enclosed area of the green rectangles defines the edges of relief structures that are etched into the underside of the nozzle membrane after the handle layer is removed. Note that the nozzle inlet is wider at its base (red rectangle) than the un-etched portion of raised Si between relief features. The relief features do not open into the nozzle inlets because the inward tapering <111> planes that defines the walls of both etched features are parallel as seen in **Fig. 5-9**. The mask design shows the extents of both features at their widest points, which are on opposite sides of the 100 µm Si membrane. Nozzles in a single bank are separated on 250 µm centers.

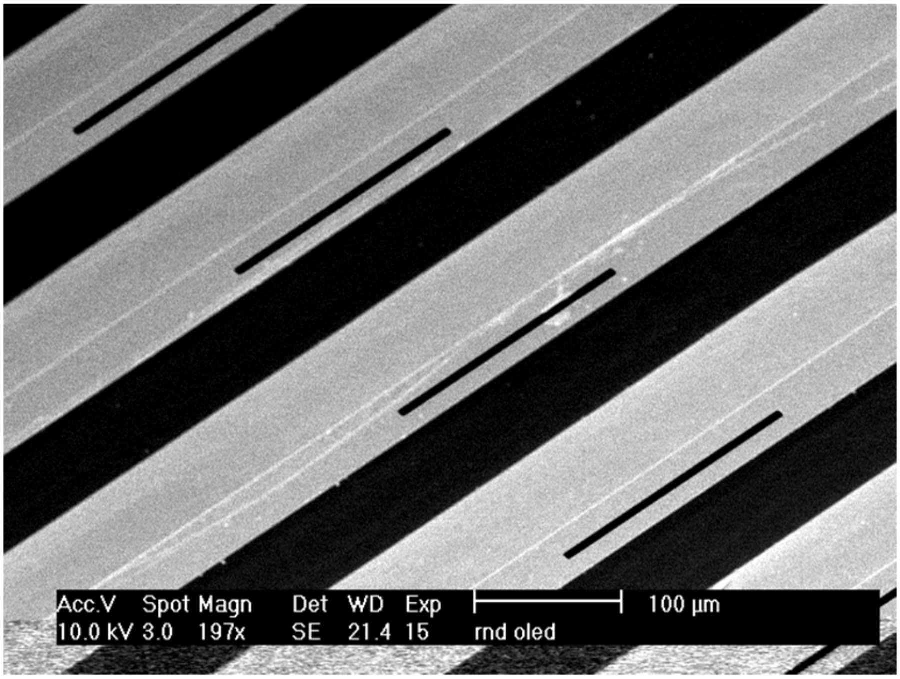

Figure D-2: SEM of structure fabricated from mask in **Fig. D-1**. It shows the underside of an array of C-T nozzles spaced 250 µm center to center.

Figure D-3: Mask for array of converging-tapered nozzles with protection structures. (Following Page) This mask makes a less densely packed array of CT nozzles than appears is **Fig. D-1**. The nozzles in a single bank are separated by 1 mm centers. The nozzle body and bumper structures are isolated islands on the surface. Therefore their corners need to be protected from an anisotropic etchant that preferentially attacks the <100> and <110> planes over the <111> plane of Si, leaving multifaceted corners. The squares at the corners of each feature are sacrificial protection structures [111] that etch away to leave a clean corner between two <111> Si planes. The red region defines nozzle inlets as in **Fig. D-1**. The region that is inside of the green square but outside of the blue polygons ($G - G \cap B$ where G and B are the areas inside the green and blue polygons) is exposed defines the etched region on the underside of the micronozzle membrane. The resulting structure is shown in **Figs. 7-6b** and **7-14**.

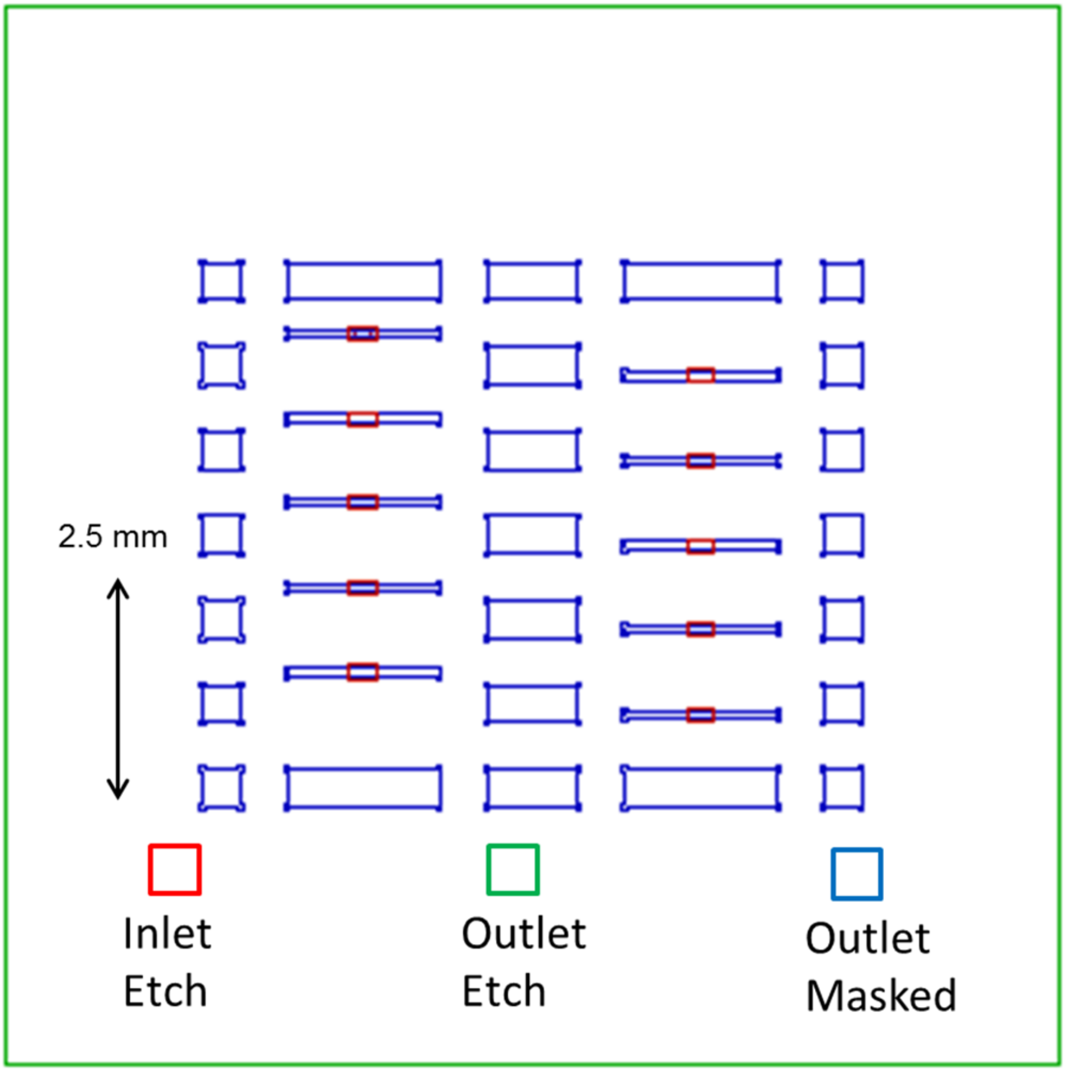
2.5 mm
Inlet Etch
Outlet Etch
Outlet Masked

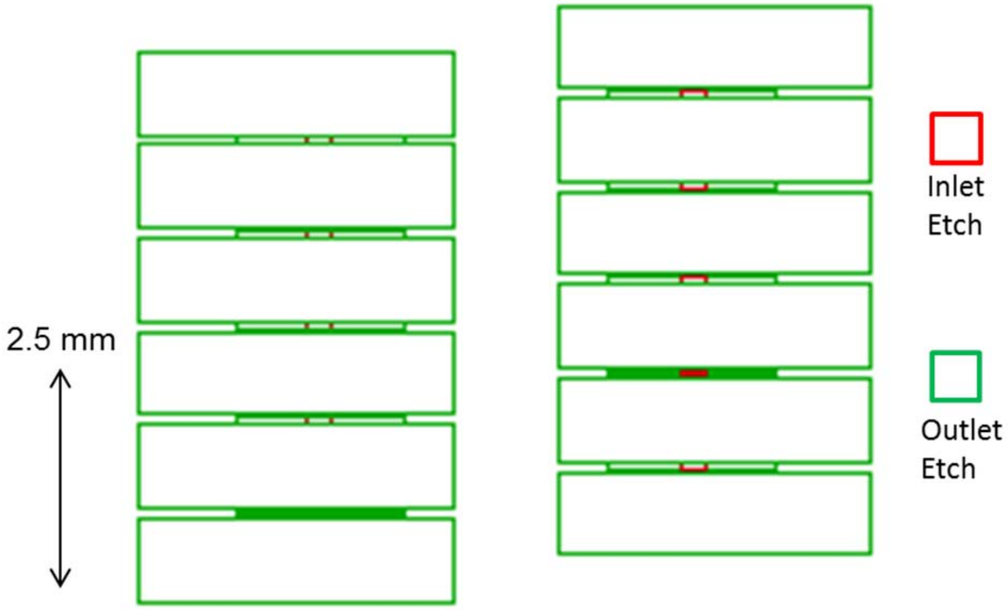

Figure D-4: Mask for an array of converging-diverging nozzles. The interior of the red rectangles define nozzle inlets. The inlets are smaller, 270 by 70 µm, since the funnel shaped converging portion only extends half way through the Si membrane. The interiors of green rectangles are exposed to define etched regions on the underside of the nozzle membrane. This mask pattern consists of an array of large rectangles with an array of much narrower rectangles in between. The large rectangles define the etched relief channels between nozzles. The narrow rectangles define the outlet of the C-D nozzle. These features taper inward into the Si membrane and intersect with the inlets to form an hourglass shaped nozzle. The outlet is elongated in the direction of printing in an attempt to produce a more diffuse carrier gas flow without broadening printed features. The raised portion is defined by the regions between the small and large rectangles. The resulting nozzles are shown in **Figs. 7-8** and **7-9**.

Appendix E: Cleanroom Fabrication Protocols

E.1 Overview

The following is a series of step by step list for procedures required to make a micronozzle array. This list is not comprehensive and it is intended to be used alongside the LNF standard operating procedures (SOPs) for each procedure. This appendix gives advice on the best tools, procedures, and supplies to use for a specific task while preserving useful and often hard won processing tricks required to fabricate nozzle membranes.

E.2 Photoresist

E.2.1 SPR 220-3.0

This resist is used for patterning nozzle inlets. Use of ACS-200 tool is strongly recommended to improve consistency. Use SPR-220-3.0 3k recipe with back side rinse (BSR). This produces a 3 μm thick photoresist layer. Priming and baking steps are automatically included. Wafers are exposed for 12 seconds with the mask aligner in soft contact mode at a lamp power of 350W. Soft contact provides sufficient resolution without fouling the photomask. The alignment gap should be set to 20 μm, although no alignment is required for the SPR-200 step. The wafer chuck should, however, be centered. The wafer is developed in the spray tank of the ACS-200 using the 35 s recipe for AZ300-MIF developer. Photoresist is removed by sonication in Acetone.

E.2.2 AZ-9260

Other photolithographic steps are performed with AZ-9260 resist. This is a thicker, more viscous resist that withstands HF and plasma more effectively than SPR-220. It is also less prone to be wicked into micronozzles which may have opened prematurely during processing. The procedure is summarized below.

1.) Set spinner for 3000 RPM, 45s.
2.) Set wafer on spinner with an appropriately sized chuck. Center.
3.) Apply ~ 5 ml of bis(trimethylesilyl)amine (HMDS) to wafer and spin coat.
4.) Liberally apply AZ-9260 to wafer with pipette. Leave a ~5 cm diameter circle of photoresist at center of wafer. Spin to produce a 9 µm film.
5.) Bake at 110°C for 2 min.
6.) Expose with 350 W lamp power for 60 s, soft contact, and 20 µm alignment.
7.) Develop with fresh AZ-400K developer, diluted 1:4 in DI H_2O. This will take 60-120s. Exposed surface will appear frosted as resist is attacked and then become specular again once the resist is fully removed. Soak until exposed resist is removed, but do not overdevelop. Do not use old developer. It loses its potency.
8.) Rinse for at least 3 min w/ DI water.
9.) Hard Bake at 110°C for 20 min. Wafer can now be etched.

E.3 Etching

E.3.1 Reactive Ion Etching

Use LAM-9400 tool to etch hard masks. Recipe LNF_Nitride_1 is used to etch the nozzle inlets. A 150s etch is sufficient to remove 100 nm of Si_3N_4. LNF_Oxide_1 is used to etch the nozzle outlets and relief trenches. A 600s etch will remove the 1 μm oxide layer from the underside of a nozzle membrane.

Obtain a 6 inch carrier wafer with a back side coating of tetraethyl orthosilicate from the LNF store. Wipe it with solvent to remove dust, paying particular attention to the back side. Place 3 drops of Krytox® grease on front surface of the carrier wafer and mount process wafer at center. Load into tool and run recipe.

E.3.2 Deep Reactive Ion Etching

Deep reactive ion (Bosch) etching steps are performed in the STS Pegasus® tool. Recipe 1 is used to etch reliefs with straight sidewalls for the underside of a nozzle membrane. The recipe is optimized for clean, high resolution patterning and high photoresist selectivity at the expense of etch rate. Recipe 3 removes bulk material more rapidly, and is therefore used to remove the handle wafer. The general procedure for using the Pegasus® is as follows.

1.) Mount wafer to carrier as prescribed by SOP for etches that thin portions of the wafer 100 μm or less.
2.) Take initial thickness measurement, either of whole wafer for handle release or of photoresist thickness for patterned etch.
3.) Carefully solvent clean back side of wafer. Guard the front side since solvent damages photoresist.
4.) Load wafer into tool. Repeat cleaning and reload if electrostatic chuck fails leak check.

5.) Set etch time and etch wafer. Look in logbook for etch rates. The first etch should be to about 66% of target depth.

6.) Confirm etch rate with measurement and go to completion. A second stop at 90% of target is advisable if etch depth is critical.

E.3.3 Hot Phosphoric Acid Etch

Phosphoric acid is used to remove the Si_3N_4 hard mask from the SOI wafer. It has extremely high selectivity between Si and Si_3N_4,[132] recovering a high quality Si surface that facilitates later bonding steps.

1.) Pour stock H_3PO_4 solution in a shallow dish on a hotplate. Place wafer in dish and cover.

2.) Heat solution to 170°C and hold for 60 min. Cool and remove.

E.3.4 Anisotropic Etches

An alkaline etch solution is used to selectively etch the <100> crystal plane, leaving the <111> plane behind so that etched features have straight 54.7° sloped sidewalls. The procedure is given for a KOH etch, which is used to fabricate concave features. Convex features such as C-T nozzles require an ethylenediamene pyrocatechol (EDP) etch. This is a much more complicated procedure outlined by its LNF SOP.

1.) Fill non-CMOS tank of wet chem base bench with 3 L H_2O. Place Teflon® displacer in tank. Set tank heater for 84°C. No need to wait for it to heat up.

2.) Gradually stir in 3 kg of KOH, adding about 0.5 kg at a time and mixing thoroughly with Teflon® spoon.

3.) Dissolving KOH is exothermic, wait for tank to cool to below 90°C.

4.) Fill tank rest of way to top with isopropanol. Tank contents should be two phase mixture.
5.) Wait for temperature to stabilize. Add wafers. Etch rate is ~1 μm/min.
6.) Check isopropanol level hourly. Verify etch progress with profilometry. Rinse wafer in DI water for 5 min after removal from bath.
7.) Etch is complete when etch stop layer is visible in microscope.
8.) Clean etched wafers with H_2SO_4:H_2O_2 in acid hood.
9.) Rinse and drain KOH etch tank 3x.

E.3.4 HF Etches

A 49% wt. HF stock solution is used to remove the glass handle layer and from nozzle membranes. It is also used to etch microchannels into the glass layer if required. Silicon is etched very slowly by HF, so there is no need to protect Si structures. The 49% wt. HF solution etches SiO_2 at ~7 μm/min. A 10% wt. HF solution can be used to remove the remaining SiO_2 from the underside of the nozzle membrane after processing. The following instructions are for the microchannel etch. This requires the two sides of the wafer to be etched to different depths. Note that concentrated HF is EXTREMELY DANGEROUS! Consult all SOPs, undergo appropriate training, and wear all recommended personal protective equipment before proceeding.

Microchannel Side:

1.) Place dummy wafer on hot plate and heat to 80°C.
2.) Melt paraffin wax over dummy wafer. Place wafer to be etched over top, microchannel side up. Make sure it is firmly seated.

3.) Remove wafer pair and allow to cool. Make sure areas to be etched are clear of wax. Use blunt tipped tweezers to gently scrape away wax if necessary.
4.) Pour HF stock solution into Teflon® beaker, immerse wafers in beaker.
5.) Wafer will etch at approximately 7 µm/s, with some variation due to factors such as room temperature. Verify etch rate at ~66% completion with stylus profilometry. Rinse wafer thoroughly before handling.
6.) Complete etch. Rinse wafer thoroughly.
7.) Heat wafers to melt wax. Flip microchannel wafer so that via side faces up and re-mount on dummy.

Via Side:

1.) Scrape wax from vias after wafer stack cools. Don't worry about wax on the masked portions. It provides an additional barrier against HF.
2.) Return wafers to HF solution. Time etch so that the depth is equal to the difference between the wafer thickness and microchannel depth.
3.) Remove wafer, rinse thoroughly. Verify that all vias are etched through the wafer. If not, etch for additional 5 min and repeat as necessary. Once vias are open, dispose of HF solution down acid drain with plenty of water.
4.) Heat wafer on hot plate to dismount from dummy wafer.
5.) Soak wafer in boiling trichloroethylene for 10 min to remove wax.
6.) Sonicate wafer in acetone for 10 min to remove photoresist.
7.) Dip wafer in Ge-48 gold etchant for 5 min to remove gold hard mask. Rinse thoroughly.

8.) Dip wafer in chrome etchant for 1 min to remove adhesion layer. Rinse thoroughly. Repeat steps 7 and 8 two additional times.

E.4 Bonding

E.4.1 Anodic Bonding

Anodic bonding is used to either seal nozzle membranes to either Pyrex® micro channel plates or to bond the membrane to Pyrex® flats for mechanical support. Either Corning 7740 glass or an equivalent product must be used. The coefficient of thermal expansion for soda lime glass is too high to permit an effective bond to Si and fused silica or quartz do not have sufficient electrolytes to permit the chemical reaction that occurs in anodic bonding. This anodic bond is performed in the Karl Suss SB-6 bonder.

1.) Clean wafers in H_2SO_4:H_2O_2

2.) Dip Si wafer in 10% HF solution for 30 s and rinse.

3.) Thoroughly dry wafers. Align by eye, load in fixture and place in bonder.

4.) Run recipe Anodic01. It goes through the following steps

    a. Evacuate bonder
    b. Kiss top platen to wafers
    c. Heat to 200°C, hold 5 min, heat to 400°C hold 5 min
    d. Apply voltage with current compliance of 10 mA, ramp to 800V.
    e. Hold voltage for 20 min.
    f. Vent chamber and raise top platen
    g. Air cool. Wafers can be removed if < 150°C

5.) RCA clean[105] wafers with $NH_4OH:H_2O_2$, HF, and $HCl:H_2O_2$ solutions to remove NaO2 precipitates on electrode side of glass.

E.4.2 Lapping carrier plate

This procedure assumes a metal carrier plate with a two 12 mm square bonding surfaces. Use more pressure for larger areas.

1.) Plate should be surface ground to ± 10 µm flatness before lapping.

2.) Follow SOP to flush mount plate to 100 mm glass plate with beeswax using aluminum mounting jig.

3.) Place carrier on polishing jig. Adjust spring for 1 kg downward force.

4.) Load lapper with 12 µm slurry. Mix slurry and adjust for 1-2 drops per second. Use slotted iron platen. Set lapper to 20 rpm. Fully wet platen with slurry and mount polishing jig. Arm should be stationary.

5.) Lap carrier plate until bonded regions have an even matte finish. Verify flatness with height gauge.

6.) Thoroughly clean carrier plate and lapping platen. Repeat lapping with 9, 3, and 1 µm slurry.

7.) Replace iron platen with black felt polishing cloth on aluminum platen. Set arm to sweep.

8.) Polish with 1 µm slurry until bonded surfaces have even specular finish.

9.) Heat glass plate and remove metal carrier plate. Sonicate in DI water, then sonicate in acetone, boil in trichloroethylene, sonicate in acetone, sonicate in DI water, flush channels with DI water, and boil in isopropanol.

E.4.3 Gold Eutectic Bonding

1.) Apply solder layers to nozzle membrane, metal carrier plate, and a dummy membrane by e-beam as described in Chapter 7.

2.) Load plate into EVG-510 bonder. Verify that the steel top platen, and not the quartz platen is installed. Center nozzle membrane over feed trenches and place a dummy membrane of the same thickness on the other raised boss to balance the force load. Place titanium disk over assembly.

3.) Close and evacuate chamber.

4.) Heat to 350°C. Apply 500 N to platen.

5.) Heat to 400°C and hold for 1 hr.

6.) Release platen pressure, vent chamber and air cool.

Appendix F: OVJP Operating Protocols

F.1 Chamber Vent

1.) Verify that relief valves are open.

2.) Move stage to load position. Minimum *z* and *x* to glovebox side.

3.) Disable z motion

4.) Verify that all heater power is off. All themocouples read < 200°C.

5.) If accessing chamber through glovebox, make sure that main chamber door is latched.

6.) Click vent valve on in control software.

7.) Click vent valve off once Baratron reads > 700 Torr.

F.2 Substrate Load and Pump Down

1.) Apply Fujipoly® or cryo grease to substrate tray.

2.) Seat substrate on heat transfer media by pressing firmly on edges.

3.) Load substrate tray by hand or using fork in glovebox. Align to dowel pins on chiller plate. Be careful not to touch print head or torque the stage actuators.

4.) Verify that tray is seated flush on chiller plate.

5.) Verify that turbo pump is on.

6.) Close chamber and open rough pump valve.

7.) Wait until Baratron reads below 50 mTorr. Then shut rough valve, open foreline valve, and open gate valve. If chamber does not reach 50 mTorr in ~15 min check for leaks.

8.) Move stage to desired warm-up position. Distance sensor must be over substrate to accurately read separation.

9.) Verify that P term of z controller is -0.8. Set steps per cycle to 100. Enable motion. Advance substrate to within 300 μm of print head.

10.) Set steps per cycle to 10 and advance to 100 μm.

F.3 Warm-Up Procedure

1.) Heat Print Head to 200 °C. Do not exceed 30W of heating during this phase.

2.) Turn on power to organic vapor source heaters. Set temperatures to 50°C less than desired processing temperature in software.

3.) Heat print head incrementally to 350°C, ramping at about 5°/min. Set final source cell temperatures in source cells once the initial setpoints are stable.

4.) Reduce nozzle to separate separation to desired *g*.

5.) Set desired MFC flow rates in software. Hit run switches in software to open MFC and close relief valve for each depositing source.

6.) Let tool equilibrate for 5 min.

F.4 Printing

1.) If *x* or *y* stage motion is controlled with National Instruments software (backup actuators), *z* motion must be disabled prior to stage translation.

2.) Move stage to desired print start position.

3.) Deposit pattern using PI Micromove software for Physik Instrumente actuators to direct substrate motion. Stepper driven backup actuators can be controlled through NI MAX if necessary.

4.) Turn organic vapor source switches to vent after the desired pattern is drawn.

F.5 Cool Down

1.) Verify *z* actuator is enabled. Retreat substrate to 300 μm from substrate.

2.) Set print head power for ~20W.

3.) Turn off power to organic vapor source heaters

4.) Move stage to load position. Disable *z* actuator.

5.) Ramp print head temperature down to 200°C

6.) Verify all power sources are off in chamber before reaching in with hand or fork.

7.) Follow vent procedure to retrieve substrate.

8.) Substrate tray may become stuck on the chiller plate dowel pins due to thermal contraction. Forcibly prying the tray off may damage the stage actuators. Increase temperature of heat exchange fluid to loosen the pins instead.

Appendix G: Direct Simulation Monte Carlo Code

G.1 Overview

The direct simulation Monte Carlo Algorithm is based on Bird[91], with random number and distribution generation functions from *Numerical Recipes in C*.[133] The DSMC procedure is outlined in Chapter 5. This appendix describes procedures for establishing boundary conditions such as inlets, outlets, and walls in greater detail. It will also address how bulk flow properties are derived for each cell by averaging the gas molecules present over time. Finally it will conclude with concepts for a more efficient code compatible with parallel computing.

A full copy of the code does not appear in this thesis, but instructions for editing it do. It is implemented in C++. The code is the property of the Optoelectronic Components and Materials (OCM) group at the University of Michigan, and is available to members on the group server. Outside researchers wishing to obtain a copy of this code should contact Prof. Stephen Forrest at stevefor@umich.edu.

G.2 General Boundaries

Particles that either enter through a reservoir boundary or diffusely reflect from a wall are assumed to enter the simulation from a reservoir of ideal gas in thermal equilibrium with the boundary. In the case of walls, a particle that crosses is redirected back into the simulation with a trajectory representative of a particle leaving a gas reservoir from a boundary coplanar to the wall at the same position.

Gas particles in thermal equilibrium obey the Boltzmann distribution. Density function *f* obeys eq. G.1. The flux, *j*, of particles is given by eqs. G.2 to 4.[91] Note that only particles moving across the barrier into the simulation are counted when integrating *f*. Variables are defined as in Chapter 5. Additionally, c_x is the *x* component of particle velocity, $\bar{c}$ is the mean particle speed, and $\hat{x}$ is the unit vector normal to the boundary.

$$f(\vec{c}) = \left(\frac{m\pi}{2k_BT}\right)^{\frac{3}{2}} exp\left(-\frac{m\vec{c}\cdot\vec{c}}{2k_BT}\right) \tag{G.1}$$

$$j_x = n\int_{-\infty}^{\infty}\int_{-\infty}^{\infty}\int_{0}^{\infty} f(\vec{c})\vec{c}\cdot\hat{x}\,dc_xdc_ydc_z \tag{G.2}$$

$$j_x = n\sqrt{\left(\frac{m\pi}{2k_BT}\right)}\int_0^{\infty} c_x exp\left(\frac{mc_x{}^2}{2k_BT}\right)dc_x \tag{G.3}$$

$$j_x = \frac{P}{\sqrt{2\pi m k_BT}} = \frac{n\bar{c}}{4} \tag{G.4}$$

$$N = \frac{\Delta^2}{F} j_x dt \tag{G.5}$$

Equation G.5 gives the quantity *N* of particles are introduced across a reservoir boundary into a cubic cell of side length *Δ* for each cycle time of time step *dt*, where each simulated particle representing *F* real particles. If *N* is fractional, it is rounded down to the nearest integer and an additional particle is randomly added with probability equal to the fractional value rounded off. Organic is added by the same rules at rate *N*S* where *S* is the seeding ratio on the inlet boundary. The number of cells for which is influx boundary condition is maintained is given by user adjustable parameters L and H in the main section, where the simulation geometry is given by **Fig. G-1**.

The velocity distribution in plane with the boundary is Gaussian. Values are assigned using the using the *gasdev* function[133] to map randomly generated numbers between 0 and 1 onto a normal distribution and then scaling with by the standard deviation of the velocity distribution, (k_BT/m)^0.5. The velocity distribution of particles normal to a boundary is given by eq. 5.9. This can be approximated as a Gaussian with centered around $(2k_BT/m)$^0.5 with standard deviation $(k_BT/(2m))$^0.5. Position parallel to the boundary is randomly assigned along the length of the cell boundary. Position normal to the boundary is chosen by starting at the boundary and moving the particle inward at its assigned velocity for a randomly determined fraction of the time step *dt*. Particles are added to the simulation by changing a vacant spot on the integer particle

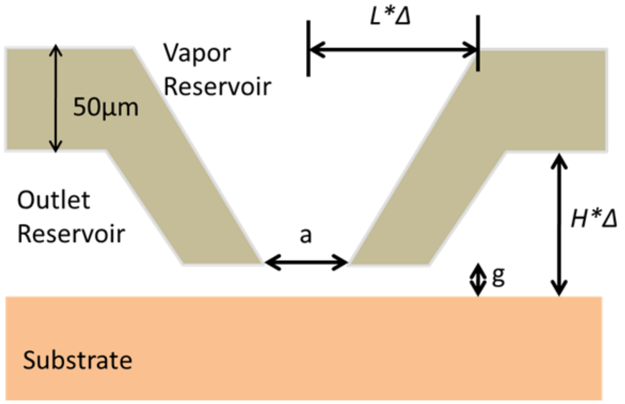

Figure G-1: Reservoir boundary conditions of a micronozzle cross section. The inlet extends L cells outward from the centerline on the top boundary. The outlet extends H cells up from the substrate along the outer boundary. Side length of each cell is Δ, denoted *delta* in the simulation code.

array, *IP[n][2]=*0, to either *IP[n][2]=1* for carrier gas or *IP[n][2]=*2 for organic. When a particle is removed, its array element reverts to 0. The code introduces new particles at the lowest available space on the integer particle array.

G.3 Walls

Determining whether a particle had crossed a wall has proven a continuing challenge in modeling OVJP by DSMC. Early versions of the code used a bitmap based system for determining whether a particle had crossed a wall. An array with the same dimension as the grid of cells was given a number 1 or 0 in each element. A 1 corresponded to cell in which particles were allowed, 0 corresponded to a cell in which they were not. If a particle was inside of a disallowed cell, i.e. behind a wall, a seek algorithm found the nearest allowed cell and placed it in there with a velocity consistent with the wall orientation and temperature. This approach was ultimately abandoned due to difficulty matching temperature and pressure boundary conditions along the walls as well as problems using the seek algorithm with convex shapes.

A vector based approach was more successful. The cross sectional boundaries of walls are input as lines. A set of criteria is established to determine whether a particle has crossed over a wall. If it does, the particle is returned to its previous, allowed position and given a new trajectory consistent with the wall boundary. Since some wall geometries may be multi-sided, the particles trajectory across the boundary must be considered as well, to determine which wall surface a particle crossed over to enter a forbidden region. The criteria used for different nozzle geometries are given in the following sections. Wall designations for different nozzle geometries are given by **Fig.**

G-2. Note that these conditions do not treat every possible particle position and trajectory correctly. They do, however, work for the vast majority of particle trajectories in the simulation and effectively shape the flow. Leakage of a few particles into the walls will sometimes produce artifactual data for cells behind the walls. Particles which leave the simulation volume entirely are removed to prevent memory errors in the assign to cell function. New wall geometries can be established by changing the comparison terms within the sequential if statements of the *wallcheck* function.

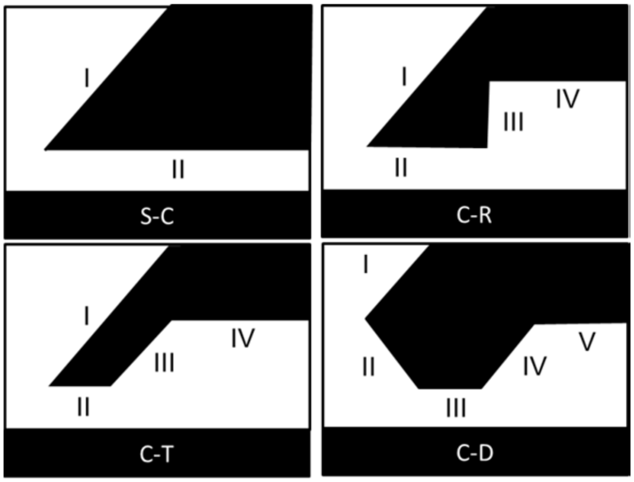

Figure G-2: Designations of boundary walls in the micronozzle model. Wall designations for the simple converging (S-C), converging-relieved (C-R), converging-tapered (C-T), and converging-diverging (C-D) nozzle geometries are indicated on their respective nozzle cross sections.

G.3.1 S-C Nozzle

Particle crosses wall I

1.) Particle is between walls I and II
2.) y velocity, $c_y < 0$

Particle crosses wall II

1.) Particle is between walls I and II
2.) $c_y > 0$

G.3.2 C-R Nozzle

Particle crosses wall I

1.) Particle is between walls I and II
2.) $c_y < 0$

Particle crosses wall II

1.) Particle is between walls I, II, and III
2.) $c_y > 0$

Particle crosses wall III

1.) Particle is between walls I, II, and III
2.) x velocity, $c_x < 0$
3.) Particle is below wall IV
4.) $c_y > 0$

Particle crosses wall IV

1.) Particle is above wall IV,
2.) Particle is under wall I,
3.) Particle is to right of wall III
4.) $c_y > 0$

G.3.3 C-T Nozzle

Particle crosses wall I

1.) Particle is between walls I, II, and III 2.)$c_y < 0$

Particle crosses wall II

1.) Particle is between walls I and II, and 3.) $c_y > 0$

2.) to the left of the bottom corner of wall III

Particle crosses wall III

1.) Particle to right of bottom corner of wall III 3.) $c_y > 0$

2.) Particle is between walls I, II, and III. 4.)Particle is below wall IV.

Particle crosses wall IV

1.) Particle to the right of the top corner of wall III 3.) $c_y > 0$

2.) Particle is below wall I and above wall IV

G.3.4 C-D Nozzle

Particle crosses wall I

1.) Particle is below wall I 3.) and above upper corner of wall II

2.) $c_y < 0$

Particle crosses wall II

1.) Particle is above wall II 3.) Particle is below upper corner of wall II

2.) Particle is left of right hand corner of wall II 4.) $c_y > 0$

Particle crosses wall III

1.) Particle above wall III 3.) $c_y > 0$

2.) Particle is between the right corner of wall II, and the left corner of wall IV.

Particle crosses wall IV

1.) Particle to the left of right corner of wall IV 3.) $c_y > 0$

2.) Particle is above wall IV

Particle crosses wall V

1.) Particle to the right of right corner of wall IV 3.) $c_y > 0$

2.) Particle is above wall V

G.4 Global Parameters

The degree of coarse graining, and consequently the precision of the simulation is controlled by a set of global parameters. Coarse graining in position space is controlled by *delta,* which gives the side length of a simulation cell. It sets the spacing of neighboring cells in the cell position, *CP*, array established by the *cell_mesh* function. Spacing is entered in microns. Graining of 2-3 μm generally offer a good compromise between fidelity and computational cost. Time step *dt* should be chosen so that a thermalized particle does not cross more than half a cell in a single cycle.

Coarse graining in momentum space is a function of *F*, the number of real particles each simulated particle represents. The value of *F* must be set sufficiently low that a statistically significant set of particles are present in the cells of interest for every cycle. Generally, 10 or more particles are desirable in a cell and this is achieved with *F* from 10^5 to 10^6.

A seeding ratio of organic into carrier gas determines composition of the simulated incoming vapor. A high seeding ratio is desirable, since it allows the code to rapidly build up a statistically significant set of organic adsorptions. Unfortunately, a significant organic fraction flowing with the simulated carrier gas changes the transport properties of the mixture. As discussed in Chapter 5, organic vapor is sufficiently dilute that it does not affect the flow properties of the carrier gas. A seeding ratio of 0.001

provides reasonable computational efficiency while not significantly affecting the carrier gas flow.

G.5 Collision Selection

The non-time counting (NTC) method[91] was discussed in Chapter 5. The number of collisions tested per cell depends on the frequency of the most probable type of collision for that cell. The acceptance probability of a collision between two particles within that cell is equal to the ratio of the frequencies of the tested and most probable collisions. This section describes the algorithm used to select particle pairs within a cell for testing and collisions.

Particles are each assigned an integer for their x coordinate and another for their y coordinate, corresponding to the coordinates of the cell each one currently occupies. These integers are recorded for each particle n in the sections *IP[n][0]* and *IP[n][1]* integer particle *IP* array. The numbers of both carrier gas and organic particles in each cell are then tallied in the *CINT* array. Maximum collision frequency for each cell is stored in the *CMAX* array. The identifier number n for each carrier gas particles occupying a given cell are recorded in the *BINC* array and the n for each organic particle are recorded in *BINO*. The occupancy in *CINT* is used to set the number of collisions to sample. The collision test number specified eq. 5.9 is rounded down to the nearest integer and an additional collision test is added with a probability equal to the rounded off portion of N_{max}. Random parings of two particles from the same cell from BINC are chosen for testing carrier gas molecule collisions. Collisions that are accepted go to the *collide* function. Random pairs of particles are then chosen from *BINC* and *BINO* to test carrier gas to organic collisions and also go to *collide* if accepted.

G.6 Simulation Outputs

The coordinates at which organic molecules cross the substrate are output to an open text file to generate a list of coordinates at which particles adsorb. The predicted thickness profiles of simulated features are given by a histogram tallied from this list with bin width equal to simulation cell width.

Average quantities for each cell are recorded in the average per cell, *APC*, array. The averages are updated every outer iteration and weighted by eq. G.6 so that each cycle of the simulation contributes equally. If A is an average quantity for a cell, eq. G.6 relates the current running average $<A>_r$ to the running average stored from the previous cycle $<A>_{r-1}$ for outer cycle r. Average occupancy for both carrier gas and organic obtained from *CINT*. This data is also used in the ongoing simulation to calculate the number of collision tests for each cell. Average velocity components v_x and v_y are recorded separately for carrier gas and organic. The *BINC* and *BINO* arrays are used to identify which particles to include in the average for each cell in each cycle. Average velocity is equivalent to bulk flow velocity for a sufficiently large sample of particles. The square of the thermal velocity of carrier gas particles for each cell is also averaged. A temperature field T is extracted from this data by eq. G.7, where *c* is the velocity of a carrier gas particle and *v* is bulk velocity, using the Equipartition Theorem.[125]

$$\langle A\rangle_r = \frac{A + r\langle A\rangle_{r-1}}{r} \tag{G.6}$$

$$\frac{1}{2}m\langle(\vec{c}-\vec{v})\cdot(\vec{c}-\vec{v})\rangle = \frac{3}{2}k_B T \tag{G.7}$$

The contents of *APC* are output into a file cellog.txt at the end of the simulation. The format of the report can be edited by changing the output commands at the end of *main*.

G.7 Extensions to Code

One of the most basic features that could be added to improve the functionality of the code is a backup file that records the positions and velocities, arrays *PP* and *PV*, of all particles currently in play in the simulation and the average occupancy and flow field data gathered in the average per cell, *APC*, array. Simulations must run long enough that data loss due to events such as power outages can be catastrophic without a backup file. A backup file would also allow a user to check on the progress of a running simulation or add additional iterations onto a completed simulation.

All DSMC simulations are inherently time dependent, as noted in Chapter 5. The imposition of boundary conditions creates a transient which dissipates over time as the system reaches a steady state. With a backup file, the simulation could be easily adapted for parallel computing, with each session loading a common backup file from a simulation that evolved to steady state and then continuing the simulation with different seed numbers loaded into their random number generators. This allows them to generate different sets of particle trajectories consistent with the steady state system. The parallel runs can then be reconciled to produce a single output.

It is assumed in the simulation that carrier gas affects the motion of organic vapor but carrier gas flow is independent of the presence of organic vapor. Since information about the distribution of organic vapor is not necessary to simulate the carrier gas flow field, the simulation can be broken into two steps. The carrier gas flow field is established in the first step and a backup file containing a large set of particle positions is generated. The flow of organic vapor can then be simulated in a second step using the backup file to generate representative collisions between the carrier gas and organic. The carrier gas flow field remains unchanged. This will be much more computationally efficient than modeling carrier gas and organic vapor simultaneously, since it eliminates the problem of organic changing the flow properties of the vapor mixture. Seeding ratio is effectively infinite once the flow field is mature. Furthermore, organic adsorption events before the simulated system reaches steady state are eliminated.

Appendix H

Motion Control

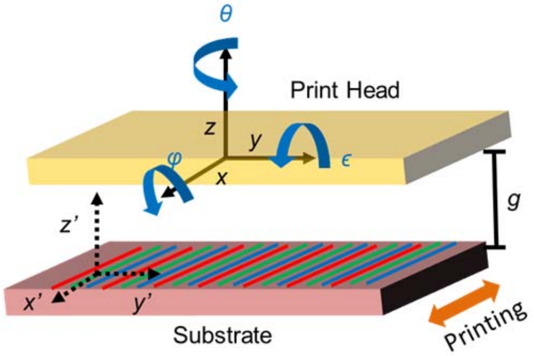

Figure H-1: Coordinate system for the print head with respect to the substrate. The direction of printed lines is parallel to *x'* and *z'* is normal to the plane of the substrate. The *y'* axis is normal to both. The orientation of the print head can be adjusted by φ, ψ, and θ so that $x||x'$, $y||y'$, and $z||z'$. Vertical axis *z* is set such that $z-z'=g$, where *g* is aperture to substrate gap and *x* and *y* are registered to desired home coordinates on the substrates

H.1 Overview

The print head must be positioned in six axes relative to the substrate. These axes are the linear displacements (x,y,z) and the angles (φ,ψ,θ) indicated in **Fig. H-1**. The alignment procedure can be broken into two steps. The first registers the print head with respect to the plane of the substrate. This is accomplished by adjusting z, φ, and ψ, where z is the vertical axis of stage motion, φ is rotation about the x axis, and ψ is rotation about the y axis. This is analogous to the wedge error correction operation on a photomask aligner. The second step registers the print head to specific features on the substrate, this requires adjusting x, y, and θ, where x and y form an orthonormal set with z and θ is a rotation about the z axis. This is the registration step.[134]

In a laboratory scale system, the wedge error correction can be performed semi-manually. An optical height sensor is used to measure z during depositions. The optical sensor is zeroed and φ and ψ are manually measured and adjusted as needed between depositions. The registration step was eliminated by designing experiments on translationally invariant substrates, although the feedthrough and manifold feature viewports to allow substrates to be optically aligned using fiducial markers on the print head. An improved method that allows for both real-time wedge error correction of and registration on substrates loaded into a vacuum chamber is required to scale-up OVJP.

H.2 Order of Actuators

The requirement that each linear axis of the print head is parallel to its counterpart in the substrate frame constrains the order in which actuators can be connected. If z' is normal to the substrate, the stage stack should be designed such that $z||z'$ over the whole range of motion of the stage once φ and ψ are properly adjusted. The φ and ψ adjustments should, therefore, be positioned to allow adjustment of the plane in which the x and y actuators move. It should be noted that other arrangements are possible, for instance if φ and ψ adjust the plane of the substrate to make it co-planar with the print head, (x,y,z,θ) can then be established by moving the print head. The θ actuator must not be positioned between the x and y actuators, since the linear axes must remain orthogonal.

Determination of the distance between the nozzle orifices and the substrate by optical reflectance is highly scalable and can be adapted for a production scale system.

Depending on the substrate thickness variation and the print speed, the *z* actuator may need to respond rapidly to changes in *g*. To keep the response time of *z* low, it should bear as little load as possible. The load on the *x* actuator should also be minimized, since the print head moves fastest relative to the substrate in the *x* direction. These actuators should be placed close to the print head so that they do not have to carry the masses of other actuators.[135]

The surface that moves the most should be the lighter one. It is the substrate for a small system, **Fig. H-2a**, and the print head in a larger system, Fig. **H-2b**. The arrangement used in the laboratory system differs from the idealized small system in **Fig H-2a**. The *z* actuator is outside of the vacuum chamber. It proved much simpler to affix the pillar holding the *x* and *y* actuators to a θ actuator beneath the chamber and then connect the θ actuator to the *z* actuator. The *z* actuator sits on a table with φ and ψ adjustments relative to the chamber stand.

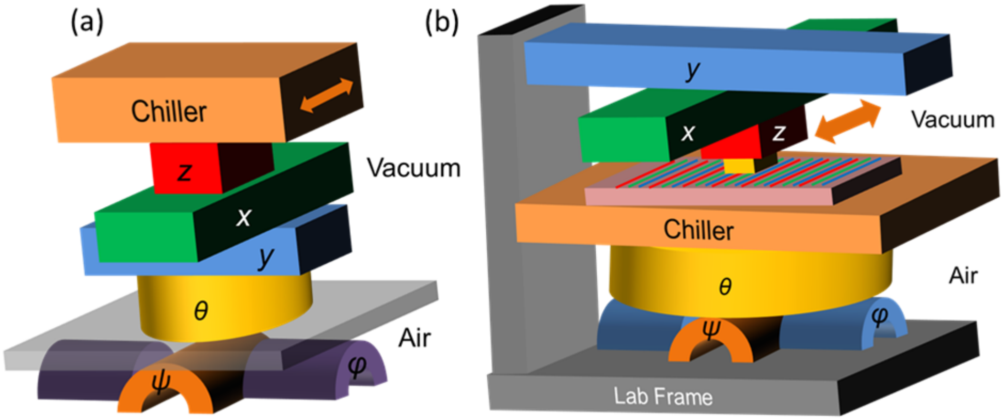

Fig H-2: Preferred actuator configurations. Sample arrangements of actuators for printing on (a) small and (b) large substrates obey the rules presented in Appendix H.2.

H.3 Capacitive Sensing

Capacitive sensing is desirable of an application like OVJP since it can measure changes in distance h between plates to within nanometers. The capacitors themselves are structurally simple, consisting of only thin film electrodes deposited on the print head and substrate. This gives them an ideal form factor for gathering information from the narrow gap between the nozzle and print head.[136] They can be made from materials that perform well at temperatures > 300°C. Finally, the capacitance between each set of electrodes can be measured by a radio-frequency signal that readily fed into and read from inside a vacuum chamber. Since the capacitors used in this application are several millimeters on a side with a gap of tens to hundreds of microns between them, they can be well approximated by parallel plates. The capacitance, C, of a set of parallel plates is related to h and the area, A, of overlap between a pair of plates conducting plates by eq. H.1, where ε_o is the permittivity of vacuum.

$$C = \frac{\varepsilon_0 A}{h} \tag{H.1}$$

If a set of grounded metal targets, set 1, is deposited onto the substrate with larger surface areas than their opposing plates on the print head, A becomes independent of the exact position of the print head. This allows h to be adjusted so it is constant for all capacitors between the print head and substrate, making the two surfaces co-planar. Another set of grounded, metallized targets, set 2, is designed to precisely overlap opposing capacitor plates on the print head. Complete overlap indicates that the print head is registered to a home position on the substrate.[134] In the context of a production system, metallization targets can be placed in a non-printed region of a mother glass, and repeated as necessary to reduce cumulative error as the print head traverses a substrate.

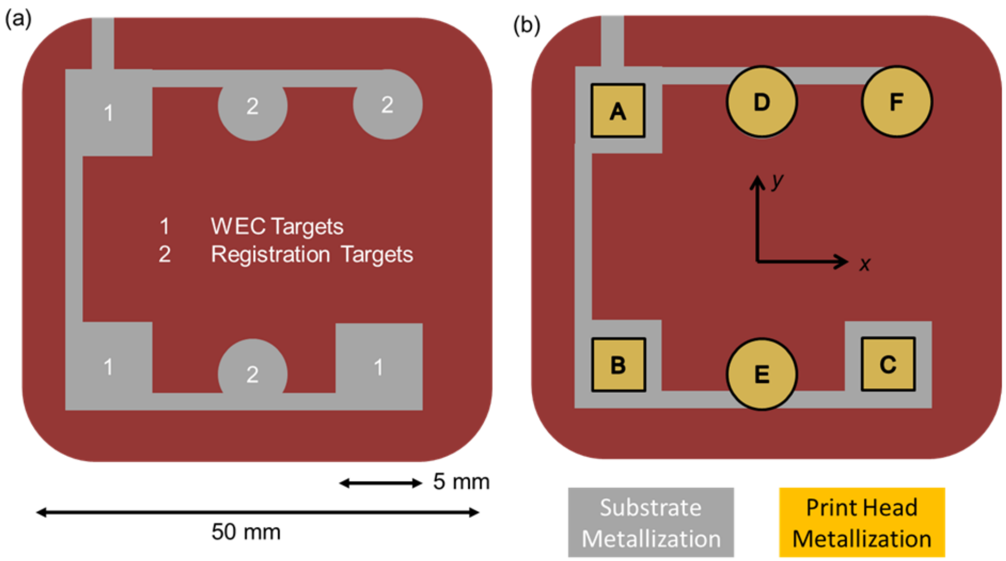

Figure H-3: Layout for capacitive sensor array and target. (a) The substrate (red) is patterned with two sets of metallized targets (gray) connected to system ground. Set 1 consists of oversized squares to permit wedge error correction (WEC) without exact registration of the substrate to the print head. Set 2 is a set of circles matched in size to mates on the print head to permit accurate registration of features once the print head and substrate are co-planar. (b) Electrodes on the print head (gold) overlay the targets on the substrate to create capacitors which generate WEC and alignment signals. (Adapted from design by Diane Peters, P.E. Ph.D.)[134]

The substrate is first positioned so that areas of electrodes A, B, and C, **Fig. H-3**, are completely overlapped by target set 1. Since target set 1 is oversized, the area A of the capacitors does not change. The angles are small enough that variation in the separation across a single pair of plates is << h. Angle φ is adjusted so to equalize the capacitance at plates B and C and ψ is adjusted to equalize the capacitance of plates A and B. At this point, h is the same for each electrode and the print head and substrate can be brought together until $h = g$.[134] The z actuator can then either be locked or slaved to a control loop with an optical sensor to compensate for local variation in substrate height.

Since h is equal for plates A, B, and C, it is also equal for D, E, and F. Since target set 2 is not oversized with respect to plates D, E, and F, the capacitance signal from each plate can be equalized and maximized by overlapping the set of plates with the set of targets on the print head. This registers the print head to the substrate in the x, y and θ directions, placing the print head into a home position that allows it to accurately print features on the substrate. Circular targets are used to generate a more straightforward homing algorithm for the print head. Plates D, E, and F have equal capacitance when θ is properly adjusted. After θ is set, x and y are set by moving each until the signals from the plates is maximized. Simulation of the WEC and registration algorithms reveal that they are stable and reliable procedures.[134]

Bibliography

[1] "LG releases new photos, details on their upcoming 55" OLED TV," *OLED-info.com*. 02-Jan-2012.

[2] C. W. Tang and S. A. VanSlyke, "Organic electroluminescent diodes," *Applied Physics Letters*, vol. 51, no. 12, pp. 913–915, Sep. 1987.

[3] H. Kim, T. Miller, E. Westerwick, Y. Kim, E. Kwock, M. Morris, and M. Cerullo, "Silicon Compatible Organic Light-Emitting Diode," *Journal of Lightwave Technology,* vol. 12, no. 12, pp. 2107–2113, Dec. 1994.

[4] G. Gu, V. Bulovic, P. E. Burrows, S. R. Forrest, and M. E. Thompson, "Transparent organic light emitting devices," *Applied Physics Letters*, vol. 68, no. 19, pp. 2606–2608, May 1996.

[5] Z. Shen, P. E. Burrows, V. Bulović, S. R. Forrest, and M. E. Thompson, "Three-Color, Tunable, Organic Light-Emitting Devices," *Science*, vol. 276, no. 5321, pp. 2009–2011, Jun. 1997.

[6] G. Grem, V. Martin, F. Meghdadi, C. Paar, J. Stampfl, J. Sturm, S. Tasch, and G. Leising, "Stable Poly(para-Phenylene)s and Their Application in Organic Light-Emitting Devices," *Synthetic Metals*, vol. 71, no. 1–3, pp. 2193–2194, Apr. 1995.

[7] M. Pope and C. E. Swenberg, *Electronic Processes in Organic Crystals and Polymers*, 2nd ed. Oxford University Press, 1999**.**

[8] N. J. Turro, J. C. Scaiano, and V. Ramamurthy, *Principles of Molecular Photochemistry: An Introduction*, 1st ed. University Science Books, 2008.

[9] W. Helfrich and W. G. Schneider, "Recombination Radiation in Anthracene Crystals," *Physical Review Letters*, vol. 14, no. 7, pp. 229–231, Feb. 1965.

[10] S. Naka, H. Okada, H. Onnagawa, Y. Yamaguchi, and T. Tsutsui, "Carrier transport properties of organic materials for EL device operation," *Synthetic Metals*, vol. 111–112, no. 0, pp. 331–333, Jun. 2000.

[11] E. Aminaka, T. Tsutsui, and S. Saito, "Effect of layered structures on the location of emissive regions in organic electroluminescent devices," *Journal of Appied Physics.*, vol. 79, no. 11, pp. 8808–8815, Jun. 1996.

[12] D. F. O'Brien, M. A. Baldo, M. E. Thompson, and S. R. Forrest, "Improved energy transfer in electrophosphorescent devices," *Applied Physics Letters*, vol. 74, no. 3, pp. 442–444, Jan. 1999.

[13] H. Kanno, Y. Sun, and S. R. Forrest, "High-efficiency top-emissive white-light-emitting organic electrophosphorescent devices," *Applied Physics Letters*, vol. 86, no. 26, Jun. 2005.

[14] V. I. Adamovich, S. R. Cordero, P. I. Djurovich, A. Tamayo, M. E. Thompson, B. W. D'Andrade, and S. R. Forrest, "New charge-carrier blocking materials for high efficiency OLEDs," *Organic Electronics*, vol. 4, no. 2–3, pp. 77–87, Sep. 2003.

[15] C. W. Tang, S. A. Vanslyke, and C. H. Chen, "Electroluminescence of doped organic thin films," *Journal of Applied Physics*, vol. 65, no. 9, pp. 3610–3616, 1989.

[16] C. Wu, P. I. Djurovich, and M. E. Thompson, “Study of energy transfer and triplet exciton diffusion in hole-transporting host materials,” *Advanced Functional Materials*, vol. 19, no. 19, pp. 3157–3164, Oct. 2009.

[17] R. J. Holmes, B. W. D’Andrade, S. R. Forrest, X. Ren, J. Li, and M. E. Thompson, “Efficient, deep-blue organic electrophosphorescence by guest charge trapping,” *Applied Physics Letters*, vol. 83, no. 18, pp. 3818–3820, Nov. 2003.

[18] M. A. Baldo, D. F. O’Brien, M. E. Thompson, and S. R. Forrest, “Excitonic singlet-triplet ratio in a semiconducting organic thin film,” *Physical Review B*, vol. 60, no. 20, pp. 14422–14428, Nov. 1999.

[19] J. S. Wilson, A. S. Dhoot, A. J. A. B. Seeley, M. S. Khan, A. Köhler, and R. H. Friend, “Spin-dependent exciton formation in π-conjugated compounds,” *Nature*, vol. 413, no. 6858, pp. 828–831, Oct. 2001.

[20] E. Merzbacher, *Quantum Mechanics*, 3rd ed. Wiley, 1997.

[21] M. A. Baldo, D. F. O’Brien, Y. You, A. Shoustikov, S. Sibley, M. E. Thompson, and S. R. Forrest, “Highly efficient phosphorescent emission from organic electroluminescent devices,” *Nature*, vol. 395, no. 6698, pp. 151–154, Sep. 1998.

[22] K.-C. Tang, K. L. Liu, and I.-C. Chen, “Rapid intersystem crossing in highly phosphorescent iridium complexes,” *Chemical Physics Letters*, vol. 386, no. 4–6, pp. 437–441, Mar. 2004.

[23] N. C. Giebink, B. W. D’Andrade, M. S. Weaver, J. J. Brown, and S. R. Forrest, “Direct evidence for degradation of polaron excited states in organic light emitting diodes,” *Journal of Applied Physics*, vol. 105, no. 12, 124514, Jun. 2009.

[24] A. B. Tamayo, B. D. Alleyne, P. I. Djurovich, S. Lamansky, I. Tsyba, N. N. Ho, R. Bau, and M. E. Thompson, "Synthesis and Characterization of Facial and Meridional Tris-cyclometalated Iridium(III) Complexes," *Journal of the American Chemical Society*, vol. 125, no. 24, pp. 7377–7387, Jun. 2003.

[25] H. Yersin, "Triplet emitters for OLED applications. Mechanisms of exciton trapping and control of emission properties," *Transition Metal and Rare Earth Compounds Iii*, vol. 241, pp. 1–26, 2004.

[26] M. A. Baldo, S. Lamansky, P. E. Burrows, M. E. Thompson, and S. R. Forrest, "Very high-efficiency green organic light-emitting devices based on electrophosphorescence," *Applied Physics Letters*, vol. 75, no. 1, pp. 4–6, Jul. 1999.

[27] T. Smith and J. Guild, "The C.I.E. colorimetric standards and their use," *Transactions of the Optical Society*, vol. 33, no. 3, pp. 73–134, Jan. 1931.

[28] J. Brooks, Y. Babayan, S. Lamansky, P. I. Djurovich, I. Tsyba, R. Bau, and M. E. Thompson, "Synthesis and characterization of phosphorescent cyclometalated platinum complexes," *Inorganic Chemistry*, vol. 41, no. 12, pp. 3055–3066, Jun. 2002.

[29] M. Shtein, "Organic Vapor Phase Deposition and Vapor Jet Printing for Electronic and Optoelectronic Device Applications," Dissertation, Princeton University, Princeton, NJ, 2004.

[30] S. M. Sze, *Physics of Semiconductor Devices*, Wiley, 2007.

[31] P. E. Burrows, G. Gu, V. Bulovic, Z. Shen, S. R. Forrest, and M. E. Thompson, "Achieving full-color organic light-emitting devices for lightweight, flat-panel

displays," *IEEE Transactions on Electron Devices,* vol. 44, no. 8, pp. 1188 –1203, Aug. 1997.

[32] G. Morrison, "What is OLED TV? | TV and Home Theater - CNET Reviews," *CNET*, 01-Mar-2012. http://reviews.cnet.com/8301-33199_7-57386898-221/what-is-oled-tv.

[33] P. F. Tian, V. Bulovic, P. E. Burrows, G. Gu, S. R. Forrest, and T. X. Zhou, "Precise, scalable shadow mask patterning of vacuum-deposited organic light emitting devices," *Journal of Vacuum Science & Technology A: Vacuum, Surfaces, and Films*, vol. 17, no. 5, pp. 2975–2981, 1999.

[34] S. R. Forrest, D. C. Bradley, and M. E. Thompson, "Measuring the Efficiency of Organic Light-Emitting Devices," *Advanced Materials*, vol. 15, no. 13, pp. 1043–1048, 2003.

[35] E. F. Schubert, *Light-Emitting Diodes*, 2nd ed. Cambridge University Press, 2006.

[36] S. Kubota, A. Taguchi, and K. Yazawa, "Thermal challenges deriving from the advances of display technologies," *Microelectronics Journal*, vol. 39, no. 7, pp. 942–949, Jul. 2008.

[37] *TV transmission standards*. United States Federal Communications Commission, 1953

[38] P. Wong, "LG 55EM9600 55-inch OLED hands-on," *CNET*, 24-May-2012. http://reviews.cnet.com/2300-6482_7-10012405-4.html.

[39] C. I. de L’Eclairage, *CIE 013.3-1995: Method of measuring and specifying colour rendering properties of light sources*. Commission Internationale de L’Eclairage, 1995.

[40] M. Thomschke, S. Reineke, B. Lüssem, and K. Leo, “Highly Efficient White Top-Emitting Organic Light-Emitting Diodes Comprising Laminated Microlens Films,” *Nano Letters*, vol. 12, no. 1, pp. 424–428, Jan. 2012.

[41] “Solid-State Lighting: World Record White OLED Performance Exceeds 100 lm/W,” *United States Department of Energy Solid-State Lighting*, 24-Dec-2008. http://www1.eere.energy.gov/buildings/ssl/highlights_udc08.html.

[42] “Lumiotec signs license agreement with UDC, to launch sample 40 lm/W panels next month,” *OLED-info.com*. http://www.oled-info.com/lumiotec-signs-license-agreement-udc-launch-sample-40-lmw-panels-next-month.

[43] K. Suzuki and N. Suzuki, “Large Gantry Table for the 10th Generation LCD Substrates,” *NTN Corp.* http://www.ntn.co.jp/english/products/review/pdf/NTN_TR76_en_p134_137.pdf.

[44] D. K. Flattery, C. R. Fincher, D. L. LeCloux, M. B. O’Regan, and J. S. Richard, “Clearing the Road to Mass Production of OLED Television,” *Information Display*, vol. 27, no. 10, pp. 8–13, Oct. 2011.

[45] J.-H. Lee, D. N. Liu, and S.-T. Wu, *Introduction to Flat Panel Displays*, 1st ed. Wiley, 2009.

[46] M. Stewart, R. S. Howell, L. Pires, and M. K. Hatalis, “Polysilicon TFT technology for active matrix OLED displays,” *IEEE Trans. Electron Devices*, vol. 48, no. 5, pp. 845–851, May 2001.

[47] A. Nathan, G. R. Chaji, and S. J. Ashtiani, “Driving Schemes for a-Si and LTPS AMOLED Displays,” *Journal of Display Technology*, vol. 1, no. 2, pp. 267–277, Dec. 2005.

[48] H. N. Lee, J. Kyung, M. C. Sung, D. Y. Kim, S. K. Kang, S. J. Kim, C. N. Kim, H. G. Kim, and S. T. Kim, “Oxide TFT with multilayer gate insulator for backplane of AMOLED device,” *Journal of the Society for Information Display*, vol. 16, no. 2, pp. 265–272, Feb. 2008.

[49] A. Mikami, T. Koshiyama, and T. Tsubokawa, “High-efficiency color and white organic light-emitting devices prepared on flexible plastic substrates,” *Japanese Journal of Applied Physics Part 1*, vol. 44, no. 1B, pp. 608–612, Jan. 2005.

[50] S. Chen, L. Deng, J. Xie, L. Peng, L. Xie, Q. Fan, and W. Huang, “Recent Developments in Top-Emitting Organic Light-Emitting Diodes,” *Advanced Materials*, vol. 22, no. 46, pp. 5227–5239, 2010.

[51] A. B. Chwang, M. Hack, and J. J. Brown, “Flexible OLED display development: Strategy and status,” *Journal of the Society for Information Display*, vol. 13, no. 6, pp. 481–486, Jun. 2005.

[52] C. C. Wu, S. D. Theiss, G. Gu, M. H. Lu, J. C. Sturm, S. Wagner, and S. R. Forrest, “Integration of organic LED’s and amorphous Si TFT’s onto flexible and lightweight metal foil substrates,” *IEEE Electron Device Lett.*, vol. 18, no. 12, pp. 609–612, Dec. 1997.

[53] B. Jones, “Apple Retina Display,” *Jonesblog*. 23-Jul-2010.

[54] M. J. Madou, *Fundamentals of Microfabrication and Nanotechnology, Third Edition, Three-Volume Set*, 3rd ed. CRC Press, 2011.

[55] M. Baldo, M. Deutsch, P. Burrows, H. Gossenberger, M. Gerstenberg, V. Ban, and S. Forrest, “Organic Vapor Phase Deposition,” *Advanced Materials*, vol. 10, no. 18, pp. 1505–1514, 1998.

[56] M. Shtein, P. Peumans, J. B. Benziger, and S. R. Forrest, “Direct, Mask- and Solvent-Free Printing of Molecular Organic Semiconductors,” *Advanced Materials*, vol. 16, no. 18, pp. 1615–1620, 2004.

[57] D. W. Gotthold, M. O’Steen, W. Luhman, S. Priddy, S. Counts, and C. Roth, “Challenges for OLED Deposition by Vacuum Thermal Evaporation.”

[58] Towne Technologies, “Design Restrictions for Chemical Milling.” http://www.townetech.com/design.htm.

[59] J.-J. Lih, C.-I. Chao, and C.-C. Lee, “Novel pixel design for high-resolution AMOLED displays with a shadow mask,” *Journal of the Society for Information Display*, vol. 15, no. 1, pp. 3–7, 2007.

[60] Y. Fukuda, T. Watanabe, T. Wakimoto, S. Miyaguchi, and M. Tsuchida, “An organic LED display exhibiting pure RGB colors,” *Synthetic Metals*, vol. 111, pp. 1–6, Jun. 2000.

[61] R. R. Lunt, B. E. Lassiter, J. B. Benziger, and S. R. Forrest, “Organic vapor phase deposition for the growth of large area organic electronic devices,” *Applied Physics Letters*, vol. 95, no. 23, 233305, 3 Dec. 2009.

[62] M. Shtein, P. Peumans, J. B. Benziger, and S. R. Forrest, “Micropatterning of small molecular weight organic semiconductor thin films using organic vapor phase deposition,” *Journal of Applied. Physics*, vol. 93, no. 7, pp. 4005–4016, Apr. 2003.

[63] G. J. McGraw, D. L. Peters, and S. R. Forrest, “Organic vapor jet printing at micrometer resolution using microfluidic nozzle arrays,” *Applied Physics Letters*, vol. 98, no. 1, 013302, Jan. 2011.

[64] G. J. McGraw and S. R. Forrest, “Fluid dynamics and mass transport in organic vapor jet printing,” *Journal of Applied Physics*, vol. 111, no. 4, pp. 043501, Feb. 2012.

[65] M. Shtein, P. Peumans, J. B. Benziger, and S. R. Forrest, “Direct mask-free patterning of molecular organic semiconductors using organic vapor jet printing,” *Journal of Applied Physics*, vol. 96, no. 8, pp. 4500–4507, Oct. 2004.

[66] Y. Sun, M. Shtein, and S. R. Forrest, “Direct patterning of organic light-emitting devices by organic-vapor jet printing,” *Applied Physics Letters*, vol. 86, no. 11, pp. 113504, Mar. 2005.

[67] S. Biswas, K. P. Pipe, and M. Shtein, “Solvent-free, direct printing of organic semiconductors in atmosphere,” *Applied Physics Letters*, vol. 96, no. 26, 263301, 2010.

[68] M. Shtein, J. Mapel, J. B. Benziger, and S. R. Forrest, “Effects of film morphology and gate dielectric surface preparation on the electrical characteristics of organic-vapor-phase-deposited pentacene thin-film transistors,” *Applied. Physics. Letters*, vol. 81, no. 2, pp. 268–270, Jul. 2002.

[69] H. W. Kang, C. Yun, S. Yoo, S. H. Ko, and H. J. Sung, “Effect of carrier gas temperature on pentacene thin film formation by organic vapor-jet printing techniques,” *Thermochimica Acta*, vol. 542, pp. 74–79, Aug. 2012.

[70] M. Voigt, S. Dorsfeld, A. Volz, and M. Sokolowski, “Nucleation and Growth of Molecular Organic Crystals in a Liquid Film under Vapor Deposition,” *Physical Review Letters*, vol. 91, no. 2, p. 026103, Jul. 2003.

[71] D. W. Shaw, K. Bufkin, A. A. Baronov, B. L. Johnson, and D. L. Patrick, “Organic-vapor-liquid-solid deposition with an impinging gas jet,” *Journal of Applied Physics*, vol. 111, no. 7, p. 074907, 2012.

[72] M. S. Arnold, G. J. McGraw, S. R. Forrest, and R. R. Lunt, “Direct vapor jet printing of three color segment organic light emitting devices for white light illumination,” *Applied Physics Letters*, vol. 92, no. 5, pp. 053301, 3 Feb. 2008.

[73] L. MacDonald and A. C. Lowe, Eds., *Display Systems: Design and Applications*, 1st ed. Wiley, 1997.

[74] C. Yun, J. Choi, H. W. Kang, M. Kim, H. Moon, H. J. Sung, and S. Yoo, “Digital-Mode Organic Vapor-Jet Printing (D-OVJP): Advanced Jet-on-Demand Control of Organic Thin-Film Deposition,” *Advanced Materials*, vol. 24, no. 21, pp. 2857–2862, 2012.

[75] M. O’Regan, *Solution Processed OLED Displays: Advances in Performance, Resolution, Lifetime and Appearance*. Campbell: Society for Information Display, 2009.

[76] J. P. Yang, Y. D. Jin, P. L. Heremans, R. Hoefnagels, P. Dieltiens, F. Blockhuys, H. J. Geise, M. Van der Auweraer, and G. Borghs, “White light emission from a single layer organic light emitting diode fabricated by spincoating,” *Chemical Physics Letters*, vol. 325, no. 1–3, pp. 251–256, Jul. 2000.

[77] C. D. Müller, A. Falcou, N. Reckefuss, M. Rojahn, V. Wiederhirn, P. Rudati, H. Frohne, O. Nuyken, H. Becker, and K. Meerholz, “Multi-colour organic light-emitting displays by solution processing,” *Nature*, vol. 421, no. 6925, pp. 829–833, Feb. 2003.

[78] S.-H. Lee, J. Y. Hwang, K. Kang, and H. Kang, *Fabrication of Organic Light Emitting Display using Inkjet Printing Technology*. New York: IEEE, 2009.

[79] D. Soltman and V. Subramanian, “Inkjet-Printed Line Morphologies and Temperature Control of the Coffee Ring Effect,” *Langmuir*, vol. 24, no. 5, pp. 2224–2231, Mar. 2008.

[80] P. Svarnas, L. Yang, M. Munz, A. J. Edwards, A. G. Shard, and J. W. Bradley, “Highly-selective wettability on organic light-emitting-diodes patterns by sequential low-power plasmas,” *Journal of Applied Physics*, vol. 107, no. 10, 103313, 2010.

[81] K. Burzac, “New Inks Could Mean Cheaper OLED Screens - Technology Review,” *Technology Review*, 17-May-2012. http://www.technologyreview.com /news/418961/new-inks-could-mean-cheaper-oled-screens/.

[82] J. H. Choi, K. H. Kim, S. J. Choi, and H. H. Lee, “Whole device printing for full colour displays with organic light emitting diodes,” *Nanotechnology*, vol. 17, no. 9, pp. 2246–2249, May 2006.

[83] T. Chen, S. S. Yang, and C. Liu, *Thermal-induced dye diffusion by laser direct-write technique*. Taipei: Society Information Display Taipei Chapter, 2005.

[84] M. B. Wolk, J. Baetzold, E. Bellmann, T. R. Hoffend, S. Lamansky, Y. B. Li, R. R. Roberts, V. Savvateev, J. S. Staral, and W. A. Tolbert, “Laser thermal patterning of OLED materials,” in *Organic Light-Emitting Materials and Devices Viii*, vol.

5519, Z. H. Kafafi and P. A. Lane, Eds. Bellingham: Spie-Int Soc Optical Engineering, 2004, pp. 12–23.

[85] V. Leblanc, J. Chen, P. Mardilovich, V. Bulovic, and M. A. Schmidt, “Evaporative Printing of Organic Materials at Ambient Pressure using a Micromachined Printhead,” in *Solid-State Sensors, Actuators and Microsystems Conference, 2007. TRANSDUCERS 2007. International*, 2007, pp. 121 –124.

[86] M. Kanellos, “Has a Startup Cracked the OLED Problem? : Greentech Media,” *greentechmedia*, 11-Sep-2009. http://www.greentechmedia.com/articles/read/has-a-start-up-cracked-the-oled-problem/

[87] F. Villani, P. Vacca, G. Nenna, O. Valentino, G. Burrasca, T. Fasolino, C. Minarini, and D. della Sala, “Inkjet Printed Polymer Layer on Flexible Substrate for OLED Applications,” *Journal of Physical Chemistry C*, vol. 113, no. 30, pp. 13398–13402, Jul. 2009.

[88] Y. S. Tsai, S. H. Wang, and S.-L. Chen, “Performance Improvement of Flexible Organic Light-Emitting Diodes with Double Hole Transport Layers by Spin-Coating and Evaporation,” *Japanese Journal of Applied Physics*, vol. 48, no. 5, May 2009.

[89] J. D. Seader, E. J. Henley, and D. K. Roper, *Separation Process Principles, 3rd Edition*, 3rd ed. John Wiley & Sons, Inc., 2010.

[90] W. M. Deen, *Analysis of Transport Phenomena*. Oxford University Press, USA, 1998.

[91] G. A. Bird, *Molecular Gas Dynamics and the Direct Simulation of Gas Flows*, 2nd ed. Oxford University Press, USA, 1994.

[92] W. G. Vincenti and C. H. Kruger, *Introduction to Physical Gas Dynamics*. Krieger Pub Co, 1975.

[93] R. B. Bird, W. E. Stewart, and E. N. Lightfoot, *Transport Phenomena, Revised 2nd Edition*, 2nd ed. John Wiley & Sons, Inc., 2006.

[94] G. K. Batchelor, *An Introduction to Fluid Dynamics*. Cambridge University Press, 2000.

[95] J. Groves, "Directed Vapor Deposition," Univeristy of Virginia, 1998.

[96] G. P. Sutton and O. Biblarz, *Rocket Propulsion Elements, 7th Edition*, 7th ed. Wiley-Interscience, 2000.

[97] J. M. Guevremont, S. Sheldon, and F. Zaera, "Design and characterization of collimated effusive gas beam sources: Effect of source dimensions and backing pressure on total flow and beam profile," *Review of Scientific Instruments*, vol. 71, no. 10, pp. 3869–3881, Oct. 2000.

[98] M. Shtein, H. F. Gossenberger, J. B. Benziger, and S. R. Forrest, "Material transport regimes and mechanisms for growth of molecular organic thin films using low-pressure organic vapor phase deposition," *Journal of Applied Physics*, vol. 89, no. 2, pp. 1470–1476, Jan. 2001.

[99] A. Amassian, T. V. Desai, S. Kowarik, S. Hong, A. R. Woll, G. G. Malliaras, F. Schreiber, and J. R. Engstrom, "Coverage dependent adsorption dynamics in hyperthermal organic thin film growth.," *The Journal of Chemical Physics*, vol. 130, no. 12, Mar. 2009.

[100] F. Sharipov and V. Seleznev, "Data on Internal Rarefied Gas Flows," *Journal of Physical and Chemical Reference Data*, vol. 27, no. 3, pp. 657–706, May 1998.

[101] J. H. Moore, C. C. Davis, M. A. Coplan, and S. C. Greer, *Building Scientific Apparatus*, 4th ed. Cambridge University Press, 2009.

[102] R. W. Schnell, “Seal Design Considerations Using KALREZ parts.” Dupont.

[103] “Kovar F15 Alloy Nickel Iron Cobalt: Glass & Ceramic Controlled Expansion Sealing Alloys",” *National Electronic Alloys*. http://www.nealloys.com/kovar.php.

[104] R. C. Weast, *CRC Handbook of Chemistry & Physics 60TH Edition*. CRC Publishing, 1979.

[105] W. Kern, *Handbook of Semiconductor Wafer Cleaning Technology: Science, Technology and Applications*. William Andrew, 1994.

[106] K. E. Bean, “Anisotropic etching of silicon,” *IEEE Transactions on Electron Devices*, vol. 25, no. 10, pp. 1185 – 1193, Oct. 1978.

[107] C. Iliescu, F. E. H. Tay, and J. Miao, “Strategies in deep wet etching of Pyrex glass,” *Sensors and Actuators A: Physical*, vol. 133, no. 2, pp. 395–400, Feb. 2007.

[108] M. A. Schmidt, “Wafer-to-wafer bonding for microstructure formation,” *Proc. IEEE*, vol. 86, no. 8, pp. 1575–1585, Aug. 1998.

[109] K. R. Williams, K. Gupta, and M. Wasilik, “Etch rates for micromachining processing - Part II,” *J. Microelectromechanical Systems*, vol. 12, no. 6, pp. 761–778, Dec. 2003.

[110] B. Schwartz and H. Robbins, “Chemical Etching of Silicon .4. Etching Technology,” *Journal of the Electrochemical Society*, vol. 123, no. 12, pp. 1903–1909, 1976.

[111] A. Reisman, M. Berkenblit, S. A. Chan, F. B. Kaufman, and D. C. Green, “The Controlled Etching of Silicon in Catalyzed Ethylenediamine-Pyrocatechol-Water

Solutions," *Journal of the Electrochemical Society*, vol. 126, no. 8, pp. 1406–1415, Aug. 1979.

[112] P. Pal, K. Sato, and S. Chandra, "Fabrication techniques of convex corners in a (100)-silicon wafer using bulk micromachining: a review," *Journal of Micromechanics and Microengineering*, vol. 17, no. 10, pp. R111–R133, Oct. 2007.

[113] G. Wallis and D. I. Pomerantz, "Field Assisted Glass-Metal Sealing," *Journal of Applied Physics*, vol. 40, no. 10, pp. 3946–3949, Sep. 1969.

[114] T. Anthony, "Anodic Bonding of Imperfect Surfaces," *Journal of Applied Physics*, vol. 54, no. 5, pp. 2419–2428, 1983.

[115] K. M. Knowles and A. T. J. van Helvoort, "Anodic bonding," *International Materials Review*, vol. 51, no. 5, pp. 273–311, Oct. 2006.

[116] M. Takahashi, H. Yasuda, and K. Ikeuchi, "Interfacial reaction in anodically bonded joints during receiving reverse voltage," *Solid State Ionics*, vol. 172, no. 1–4, pp. 335–340, Aug. 2004.

[117] K. B. Albaugh, "Electrode Phenomena during Anodic Bonding of Silicon to Sodium Borosilicate Glass," *Journal of the Electrochemical Society*, vol. 138, no. 10, pp. 3089–3094, Oct. 1991.

[118] D. Y. Sim, T. Kurabayashi, and M. Esashi, "A bakable microvalve with a Kovar - glass - silicon - glass structure," *Journal of Micromechanics and Microengineering*, vol. 6, no. 2, pp. 266–271, Jun. 1996.

[119] D. Briand, P. Weber, and N. F. de Rooij, "Integration of robust fluidic interconnects using metal to glass anodic bonding," *Journal of Micromechanics and Microengineering*, vol. 15, no. 9, pp. 1657–1663, Sep. 2005.

[120] S. Lani, A. Bosseboeuf, B. Belier, C. Clerc, C. Gousset, and J. Aubert, “Gold metallizations for eutectic bonding of silicon wafers,” *Microsystem Technologies*, vol. 12, no. 10, pp. 1021–1025, 2006.

[121] G. J. Brakenhoff, H. T. M. van Der Voort, and N. Nanninga, “High-resolution confocal scanning light microscopy in biology,” *Analytica Chimica Acta*, vol. 163, no. 0, pp. 231–236, 1984.

[122] Y. Q. Li, J. X. Tang, Z. Y. Xie, L. S. Hung, and S. S. Lau, “An efficient organic light-emitting diode with silver electrodes,” *Chemical Physics Letters*, vol. 386, no. 1–3, pp. 128–131, Mar. 2004.

[123] L. S. Hung, C. W. Tang, M. G. Mason, P. Raychaudhuri, and J. Madathil, “Application of an ultrathin LiF/Al bilayer in organic surface-emitting diodes,” *Applied Physics Letters*, vol. 78, no. 4, pp. 544–546, Jan. 2001.

[124] J. Steiger, S. Heun, and N. Tallant, “Polymer light emitting diodes made by ink jet printing,” *Journal of Imaging Science and Technology*, vol. 47, no. 6, p. 473, Dec. 2003.

[125] F. Reif, *Fundamentals of Statistical and Thermal Physics*, Waveland Press Inc., 2008.

[126] “Thermal Interface Materials from Fujipoly America | Thermal Interface Materials.” http://www.fujipoly.com/usa/.

[127] S. Forrest, P. Burrows, E. Haskal, and F. So, “Ultrahigh-Vacuum Quasiepitaxial Growth of Model Van-Der-Waals Thin-Films .2. Experiment,” *Physical Review B*, vol. 49, no. 16, pp. 11309–11321, Apr. 1994.

[128] C. Y. Kwong, A. B. Djurišić, V. A. L. Roy, P. T. Lai, and W. K. Chan, "Influence of the substrate temperature to the performance of tris (8-hydroxyquinoline) aluminum based organic light emitting diodes," *Thin Solid Films*, vol. 458, no. 1–2, pp. 281–286, Jun. 2004.

[129] M. Chan, S. Lai, F. Wong, O. Lengyel, C. Lee, and S. Lee, "Efficiency enhancement and retarded dark-spots growth of organic light-emitting devices by high-temperature processing," *Chemical Physics Letters*, vol. 371, no. 5–6, pp. 700–706, Apr. 2003.

[130] G. Wantz, O. J. Dautel, R. Almairac, L. Hirsch, F. Serein-Spirau, L. Vignau, J. P. Lere-Porte, J. P. Parneix, and J. J. E. Moreau, "Layered organic film growth by substrate temperature tuning for efficiency-enhanced OLEDs," *Organic Electronics*, vol. 7, no. 1, pp. 38–44, Feb. 2006.

[131] R. J. Holmes, S. R. Forrest, T. Sajoto, A. Tamayo, P. I. Djurovich, M. E. Thompson, J. Brooks, Y. J. Tung, B. W. D'Andrade, M. S. Weaver, R. C. Kwong, and J. J. Brown, "Saturated deep blue organic electrophosphorescence using a fluorine-free emitter," *Applied Physics Letters*, vol. 87, no. 24, Dec. 2005.

[132] K. R. Williams, K. Gupta, and M. Wasilik, "Etch rates for micromachining processing-Part II," *Journal of Microelectromechanical Systems*, vol. 12, no. 6, pp. 761–778, Dec. 2003.

[133] W. H. Press, B. P. Flannery, S. A. Teukolsky, and W. T. Vetterling, *Numerical Recipes in C: The Art of Scientific Computing, Second Edition*, 2nd ed. Cambridge University Press, 1992.

[134] D. Peters, “Leveling and Register Sensing Concept,” University of Michigan, Feb. 2011.

[135] A. H. Slocum, *Precision Machine Design*, Illustrated edition. Society of Manufacturing, 1992.

[136] R. Puers, “Capacitive sensors: When and how to use them,” *Sensors and Actuators A: Physical*, vol. 37–38, no. 0, pp. 93–105, Jun. 1993.